

# 國立交通大學

電子工程學系 電子研究所

## 博士論文

運用於微系統設計最佳化之微機電組件結構物理分析

Physical Analyses of MEMS Component Structures  
for Optimal Microsystem Design

研究生：陳健章

指導教授：鄭裕庭教授

中華民國 一 百 年 一 月

運用於微系統設計最佳化之微機電組件結構物理分析

Physical Analyses of MEMS Component Structures  
for Optimal Microsystem Design

研究生：陳健章

Student : Chien-Chang Chen

指導教授：鄭裕庭教授

Advisor : Prof. Yu-Ting Cheng



Submitted to Department of Electronics Engineering  
and Institute of Electronics  
College of Electrical and Computer Engineering  
National Chiao Tung University  
in partial Fulfillment of the Requirements  
for the Degree of  
Doctor of Philosophy  
in  
Electronics Engineering

January 2011

Hsinchu, Taiwan, Republic of China

中華民國 一 百 年 一 月

# 運用於微系統設計最佳化之 微機電組件結構物理分析

學生：陳健章

指導教授：鄭裕庭教授

國立交通大學

電子工程學系 電子研究所

## 摘要

微機電系統(Micro-Electro-Mechanical Systems, MEMS)是利用微米級立體結構實現感測和執行功能的一項關鍵技術。由於工業技術和經濟的相輔成長，使得微機電元件微型化(Miniaturization)獲得成功、能效得以提升，進而讓設計和應用層面不斷擴大，因此它們在消費性應用市場的普及率正不斷提高。其中，其應用觸角除了大量消費性電子與汽車應用，更伸及微奈米電子工業、醫療、能源、光纖通訊以及航太軍事等專門的應用領域。例如：射頻微機電(RF MEMS)元件優異性能可用於改良手機天線性能或是血糖反應與血壓偵測訊號傳輸，並在醫療影像應用中扮演連結身體各部位器官的角色，因此適合做為研究與商業應用的「人體區域網路(Body-Area Network)」元件。聲學應用層面亦有用於手機的微型麥克風與喇叭、人工電子耳、聲紋分析辨識，以及微型機械人指向元件等。於應用層面中，五種基本且實用的微機電組件結構，例如：螺旋狀結構、鰭狀結構、樞紐與梁的結構、層疊結構，以及傾面結構，業已被設計、利用且與其他微機電元件成功地相互整合。然而，整體性的微機電元件物理分析的缺乏，將導致發展高性能微系統的設計最佳化之困難，特別在於與輔助電路系統方面。為了克服此處的窘境，微機電組件分析物理模型以及其相關的元件或系統性能最佳化，包括射頻微機電式螺旋型電

感、複合型鰭狀基底、樞紐形微機電麥克風、層疊光學系統與面射型雷射，以及在矽基板上的倒金字塔型傾面中成長一維材料的方法，皆已在本論文中詳述其物理基礎與最佳化方針。Kramers-Kronig Relations 對於共振吸收的數學特性，已被運用於微機電式電感被動元件模型中用以描述電子共振行爲；nitride/oxide/nitride/air 複合鰭狀結構亦被運用在改善被動元件之基底損耗效應(Substrate Loss Effects)中。此外，一種新穎的中央懸浮結點結構亦被提出，並用於改善傳統微機電聲學結構之靈敏度與指向性。同時爲了分析並預測 MEMS 元件與後端電路上的熱淤積分佈與系統最高溫度，本論文中發展出廣義等效電熱網絡 $\pi$  模型，使結構分析得以簡化並讓模擬運算時間大幅縮減。利用 Green's Theorem 對於描述能量流(Energy Flux)的數學特性，本論文中提出了熱傳導、對流以及熱電阻的積分演算式並已經成功用於預測與描述高速光學通訊系統中的熱淤積分佈與最高溫度。亦預見三維奈米電子技術最終將成爲有效製做高密度電子產品與 MEMS 立體元件之利器，本論文中以垂直成長的奈米碳管(Vertical-Aligned Carbon Nanotubes)爲例，提出了高效率且可依 IC 設計者需求而佈局的設計方案：藉由精準控制晶種的大小與位置，來實現奈米碳管的成長位置與其單/多壁(single/multi-wall)特性。最終，本論文以材料與元件結構之觀點，提出了數項重要微機電組件結構之物理模型與分析以及清晰的設計指標，以期待得以實現微系統設計最佳化之目標。

# **Physical Analyses of MEMS Component Structures for Optimal Microsystem Design**

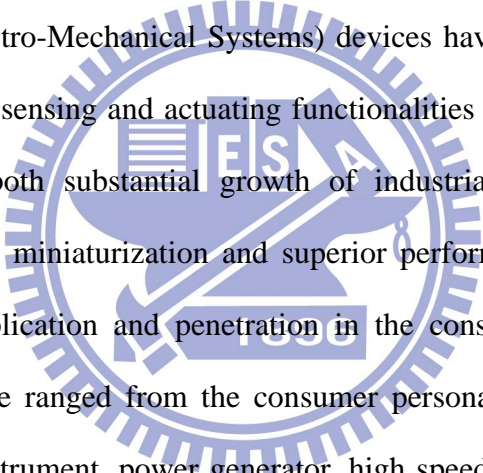
**Student: Chien-Chang Chen**

**Advisor: Prof. Yu-Ting Cheng**

**Department of Electronics Engineering and Institute of Electronics**

**National Chiao Tung University**

## **ABSTRACT**



MEMS (Micro-Electro-Mechanical Systems) devices have been the key ingredients for simultaneously realizing sensing and actuating functionalities in a system with a micro-scale structure. Due to the both substantial growth of industrial technologies and economic activities, the successive miniaturization and superior performances of the MEMS devices have extended their application and penetration in the consumer electronics market. The MEMS applications have ranged from the consumer personal portable electronics, vehicle auto-control, medical instrument, power generator, high speed data communication, military weapon, to aerospace voyage, and so on. For instance, RF MEMS passives such as inductor, capacitor, filter, and antenna, etc, have been utilized to enhance the performance of cell-phone transceiver due to their excellent performances in frontend tuning parts. MEMS acoustic components like microphone and loudspeaker have also been adopted in cell phones, cochlear prosthesis, and so on. In the applications, five fundamental and common MEMS component structures, such as spiral, fin, pivot and beam, stacking, and inclined surface structures, have been designed, utilized, and integrated with each other to form MEMS devices. Nevertheless, lack of entirely physical analyses about the devices could result in the difficulty in the design optimization for developing high performance microsystems, especially in the implementation

of circuitry design. To overcome the predicaments, the physical analyses of the MEMS components with close-form models and the corresponding optimization in device or system performance including RF MEMS passive spiral inductor, MEMS acoustic pivot-supported microphone, VCSEL in stacked optical system, and seeding control for 1-D material growth using inclined surfaces of an inverted silicon nano-pyramid are presented in this dissertation in detail. The investigation starts with the establishment of a mathematical model to depict the resonant behavior of the MEMS inductors using Kramers-Kronig Relations, and the spiral inductor can be easily and well optimized with high Q and inductance characteristics for RFIC applications. A nitride/oxide/nitride/air composited-fin structure is then presented to improve the substrate loss effects for high speed transmission applications. For sound source localization, a novel central-supported floating joint with central beams used in a hybrid microphone is proposed and presented with an analytical model to enhance the sensitivity and directivity of the conventional MEMS acoustic component structure. The biomimetic microphone design can lead the way to develop the next generation acoustic sensing and tracking microsystems like hearing aids, robots, and bionic military devices. To well analyze and predict the distribution of thermal accumulation and hottest spot occurring in a stacked optical microsystem, a general equivalent electrothermal network  $\pi$ -model is presented for simplification of the structure and saving the CPU-run-time during simulation. By means of the mathematical approach of Green's theorem for estimating energy flux inside a heating system, expressions of heat conduction, convection, and thermal resistance in view of integral forms are also presented and applied on the prediction of thermal distribution and hottest spot in a high speed optical data communication system successfully. At final, a precise seeding control scheme of vertical-aligned carbon nanotubes (CNTs) is presented for 3D nanoelectric applications, since the 1D materials have become the next generation candidate for the fabrication of nanoelectronics systems. A seeding control scheme including the physical mechanism of formation is proposed and demonstrated by employing gravitational force to

form an agglomeration of melted cobalt seeds on the inclined surface of a patterned inverted silicon nano-pyramid. It is our belief that the presented physical analyses of MEMS component structures and the establishment behavior model between device performance and related material property and geometry in this dissertation can really provide a clear design picture and analytical approach for MEMS designers and engineers to really realize the goals of microsystem optimization.





## 誌 謝

現代的藝術創作者都在創新的要求下絞盡腦汁、枯腸思索，為的就是得以發表前無古人的代表性新作。反觀在莫札特時期，他的同儕師長卻指望他在固定且共有的架構內創作，千萬不要誤了傳統的尊嚴。這是由於當時音樂家所沿用的奏鳴曲、交響樂以及歌劇的格式，早在他出生前便已確立，而且終於一生皆保持不變。如此的創作格式強加諸於莫札特身上的桎梏，就如同十四行詩的成規束縛於沙士比亞身上是相同的。然而，此種限制卻帶著既強悍又有解放的效果，因為後代的藝術評論家在這兩位創作天才的作品身上都看見了結構與奔放的共存，以及嚴謹與創意互相輝映的特質。對於老式的創造性心靈，他們在固若金湯的桎梏之下，卻能夠很含蓄地「稍微」曲解了一下規定，並偷偷游走在限制的邊緣。而如今此種的創作之樂，或許只剩科學領域中才得以窺望。

從事科學的形式與各種約束從亞理斯多德時代到今天，皆保存著一套只有科學家遵守的規矩。這不只是因為他們擁有實驗數據得以做最後防線，更因為在這圈子裡的水準比起其他領域將更為整齊、更守成規。即使在量子時代，科學家仍然可以大言不慚的討論「真實性」，也可以從容解釋何為客觀事實或是無人干擾的「視界」。這似乎就是智力世界裡，惟有科學家們才得以享有的特權了！然而，奔馳的思想雖然造就且提升了理論、技術、實驗結果以及數學架構等已知的科學要素，且使其間的關係越顯密不可分，但是如此的錯綜複雜卻也限制了科學家們以天馬行空的姿態來解決面對的問題。畢竟，我們把想像力發揮到極致，並非如同科幻小說般去夢想不存在的事物，而是去理解、分析「已經存在」的事實！

在接受高等教育十餘年之後，我有某些感觸：學習科學必須強調「自我約束」，而非放任遨遊。拿著一張白紙、空白詩句或是空白畫布然後盡情揮灑的方式，並不是科學家發揮想像力的做法。科學想像的本質本身既有一道嚴苛的準則，這個想像空間必須與所有我們知道的每件事、每件物相符合。如此保守的原則所隱含的意義是說，現存的科學知識的基礎架構基本上非常堅實，且已經可以大致反映出現實世界的實際面。此外，



與之前所提的藝術創作相似，科學家們也必須感受創新的壓力。但是在科學世界裡，創新就免不了去證明舊有的理論有點矛盾的意味。因此，科學的創新並非只是單向的往未知領域跨步邁進，而是在符合所有已知的物理定律與原則且不違背自然規則下，萌生出新點子與新物理結構。所以，我們在玩的是種頗難開始與結束的遊戲。

首先，相當感謝指導老師鄭裕庭提點了我如何走向屬於我自己的遊戲關卡。並在我深陷這遊戲的泥沼時，不吝對我伸出援手。且遇見困難關卡時，總是可以睿智、獨到的思考模式指導並提供我更為明智、果決的判斷。即便是遊戲中盤纏用盡、生病受傷或是遇上埋伏，我總是可以從他身上得到不絕的援助。同時，也必須感謝元老級的阿姐地下總司令，她所扮演的 NPC 總是能在關鍵時刻「親切」且「不求回報」的提供我不可或缺的小道消息或是人生道理。微系統整合實驗室裡的子元、喇叭昌博跟耿宇居士，都是我的道具與能力升級的最佳幫手。沒有您們的幫忙，我相信這遊戲便無法如期進展到下一層關卡。書卷大師昱賢臨門一腳的建言，總是受用不盡。同時，承蒙父母的不棄嫌，讓我在接近不惑的年紀，還可能在乎我的依賴。最後，必須感謝我的太太能夠在這孤獨的十年歲月裡，一直不嫌棄的伴我走到這裡。在我生病時，給我體貼；在我無助時，給我依靠；在我煩惱懊悔時，給我溫暖。沒有妳，我無法一個人走到這裡；這條路，還好有妳在我的身旁。也謝謝妳給我一個這麼可愛的女兒，每天入睡牽牽她的小手、捏捏她的小臉(可惜小嘴不能親親)，讓我可以擁有一夜安穩的睡眠。感謝各位！

## *Table of Contents*

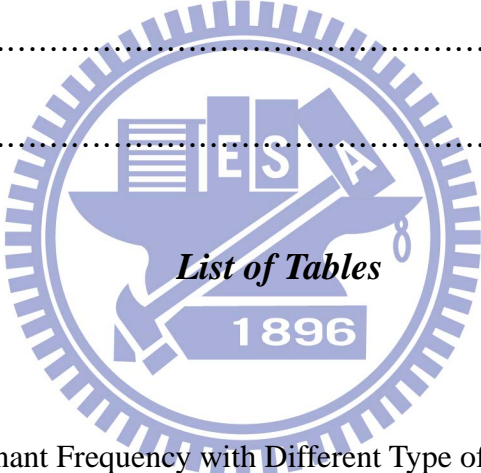
<i>Chinese Abstract</i> .....	i
<i>English Abstract</i> .....	iii
<i>Acknowledgement</i> .....	vi
<i>Table of Contents</i> .....	viii
<i>List of Tables</i> .....	xii
<i>List of Figures</i> .....	xiii
<b>Chapter 1 Introduction</b>	
<i>1.1 Overview</i> .....	1
<i>1.2 Organization of the Dissertation</i> .....	6
<b>Chapter 2 A Closed-Form Integral Model of Spiral Inductors Using the Kramers-Kronig Relations</b>	
<i>2.1 Introduction</i> .....	9
<i>2.2 Linear Response Theory, Causality, and Kramers-Kronig Relations for Metals</i> .....	11
<i>2.3 Determination of the Self-Resonant Frequency of a Spiral Inductor</i>	
<i>2.3.1 Characteristics of Anomalous Dispersion and Resonant Absorption</i> .....	14
<i>2.3.2 Kinetic Energy of Conduction Electrons in Metals</i> .....	19
<i>2.3.3 Scattering Fields and Energy Stored in Corners of a Spiral Inductor</i> .....	20
<i>2.3.4 Determination of the Self-Resonant Frequency Using Energy Conservation</i> .....	22

2.4	<i>Determination of the Inductances in View of Solid-State Physics</i>	23
2.5	<i>Determination of Boundary Condition Problems Using the Modification of Trajectory Function and the Green's Theorem</i>	
2.5.1	<i>Modification of Trajectory Function</i>	25
2.5.2	<i>The Green's Function Expression and Potential Energy</i>	28
2.5.2.1	<i>The Green's Function with a Rectangular Boundary</i>	28
2.5.2.2	<i>The Green's Function with a Circular-like Boundary</i>	29
2.6	<i>Model Validation and Discussion</i>	31
2.7	<i>Optimization of a MEMS Spiral Inductor</i>	
2.7.1	<i>Kinetic Energy, Scattering Potential, and the Kramers-Kronig Relations</i>	39
2.7.2	<i>Spiral Inductors with Magnetic Nano-Composited Material</i>	42
2.8	<i>Summary</i>	45
<b>Chapter 3</b>	<b>A Patterned Dielectric Support for High Performance MEMS Passive Component</b>	
3.1	<i>Introduction</i>	47
3.2	<i>Fabrication of Patterned Dielectric Fin-Support</i>	48
3.3	<i>Constitutive Formulation for Special Case</i>	
3.3.1	<i>The Characteristic Parameter Determination of a CPW and a Dielectric Fin-Support</i>	50
3.3.2	<i>The frequency-dependent S parameter determination for a CPW</i>	52
3.4	<i>Model Validation and Practicality in RF MEMS Optimization</i>	55
3.5	<i>Summary</i>	57

**Chapter 4 Physical Analysis of a Biomimetic Microphone with a Central-Supported (C-S) Circular Diaphragm for Sound Source Localization**

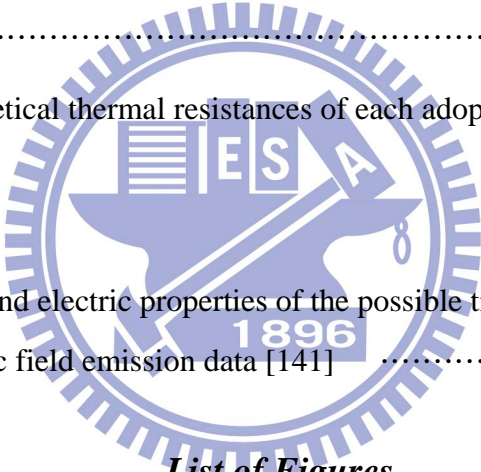
<b>4.1</b>	<b><i>Introduction</i></b>	<b>58</b>
<b>4.2</b>	<b><i>Constitutive Formulation</i></b>	
4.2.1	<i>Mechanism of Conventional C-S Design in Steady State</i>	61
4.2.2	<i>Mechanism of Hybrid C-S Design in Steady State</i>	66
4.2.3	<i>Transient State</i>	71
<b>4.3</b>	<b><i>Derivation of Quality Factors and Damping Coefficients</i></b>	
4.3.1	<i>Derivation of Quality Factors Using Squeeze Film Air Damping and Energy Transfer Models</i>	73
4.3.2	<i>Derivation of Damping Coefficients and Effective Gap Height</i>	75
<b>4.4</b>	<b><i>Model Validation</i></b>	
4.4.1	<i>Model Validation and Discussion</i>	79
4.4.2	<i>Evolution from Conventional Design to the Presented Hybrid Design</i>	83
4.4.3	<i>Comparisons Between Conventional and Hybrid C-S Designs Experimentally</i>	
4.4.3.1	<i>Processes of Microphone Fabrication</i>	85
4.4.3.2	<i>Comparisons between Measurements of Conventional and Hybrid C-S Designs</i>	87
<b>4.5</b>	<b><i>Optimized Structure of an Acoustic Sensor</i></b>	
4.5.1	<i>Rigidity and Flexibility of a Central-Supported Diaphragm</i>	91
4.5.2	<i>The Central Floating Joint</i>	93
<b>4.6</b>	<b><i>Summary</i></b>	<b>95</b>

<b>Chapter 5</b>	<b>A New Technique of Thermal Analysis for 3D-Stacking Structure Using the Green's Theorem</b>	
5.1	<i>Introduction</i>	96
5.2	<i>Case Study: Thermal Analysis of VCSELS on a SiOB</i>	100
5.3	<i>Heat Transfer Equations in Integral Form</i>	
5.3.1	<i>Steady State</i>	
5.3.1.1	<i>The Green's Theorem</i>	104
5.3.1.2	<i>Heat Conduction Equation</i>	106
5.3.1.3	<i>Heat Convection Equation</i>	108
5.3.2	<i>Transient State</i>	110
5.4	<i>Computational Algorithm in View of Integral Form</i>	113
5.5	<i>Method Validation</i>	
5.5.1	<i>Simulation Validation</i>	116
5.5.2	<i>Fabrication, Apparatus Setup, Calibration, and Experimental Validation</i>	120
5.6	<i>Thermal Optimization and Management of a Microsystem</i>	
5.6.1	<i>The Green's Theorem with Given Heating-Sources System</i>	125
5.6.2	<i>Determination of the Hottest Spot in an Unknown-Heating-Sources System</i>	129
5.7	<i>Summary</i>	131
<b>Chapter 6</b>	<b>Gravity-Assisted Seeding Control for 1D Material Growth and 3D-IC Applications</b>	
6.1	<i>Introduction</i>	132
6.2	<i>Mechanism of Motion for Liquid Drops</i>	134
6.3	<i>Seeding Control Scheme</i>	138

6.4	<i>Measurement and Discussion</i>	143
6.5	<i>A Microsystem using 1D material</i>	
6.5.1	<i>Miniaturization of the Microsystem</i>	146
6.5.2	<i>Application of 3D CNT Array</i>	147
6.6	<i>Summary</i>	153
<b>Chapter 7</b>	<b>Conclusion</b>	154
<b>Reference</b>		158
<b>Appendix A</b>		173
<b>Appendix B</b>		179
<b>Autobiography</b>		184
		
<b>Chapter 2</b>		
<b>Table 2-1</b>	Self-Resonant Frequency with Different Type of Inductors	35
<b>Table 2-2</b>	Comparison Results of the Rectangular Spiral Inductor	35
<b>Chapter 4</b>		
<b>Table 4-1</b>	Dimensional parameters of the conventional and hybrid C-S design	64
<b>Table 4-2</b>	Comparison between model prediction and simulation of the initial deformation	68
<b>Table 4-3</b>	Theoretical comparisons of the stiffness coefficients and natural resonant frequencies of the rocking and the translational modes for the conventional and	



	the hybrid C-S design, respectively .....	70
<b>Table 4-4</b>	Theoretical calculations of the quality factors for the conventional and the hybrid C-S design, respectively .....	75
<b>Table 4-5</b>	Comparisons in terms of nature frequencies and mechanical performances .....	88
<b>Table 4-6</b>	Dimensional parameters of the conventional and hybrid C-S design .....	89
 <b>Chapter 5</b>		
<b>Table 5-1</b>	The dimension parameters and thermal conductivities of the adopted materials .....	104
<b>Table 5-2</b>	The theoretical thermal resistances of each adopted material .....	118
 <b>Chapter 6</b>		
<b>Table 6-1</b>	Thermal and electric properties of the possible tip materials .....	149
<b>Table 6-2</b>	Systematic field emission data [141] .....	150



***List of Figures***

 <b>Chapter 1</b>		
<b>Figure 1-1:</b>	Embodied relations of each MEMS component and the thermal analysis in the system level morphologically .....	5
 <b>Chapter 2</b>		
<b>Figure 2-1:</b>	Real and imaginary parts of the susceptibility function in the neighborhood of two resonances. The region of anomalous dispersion is also the frequency interval where absorption occurs [27] .....	14
<b>Figure 2-2:</b>	Pauli paramagnetism at absolute zero. The orbitals in the shaded regions in (a)	

are occupied. The numbers of electrons in the "up" and "down" band will adjust to make the energies equal at the Fermi level. The chemical potential (Fermi level) of the moment up electrons is equal to that of the moment down electrons. In (b) we show the excess of moment up electrons in magnetic field [22] ..... 17

**Figure 2-3:** Schematic diagram of the two-port spiral inductor realizations: (a) rectangular, (b) octagonal, (c) circular spiral inductor. The parameters  $l_{max}$ ,  $s$ , and  $\varpi$  are the maximum edge, line spacing, and line width of the polygon inductor, respectively ..... 18

**Figure 2-4:** Band structure of the electron energy in a periodic lattice [26] ..... 20

**Figure 2-5:** Relations between distance from inductor edge to ground pad and relative error of self-resonant frequency ..... 27

**Figure 2-6:** Scheme of a circular-like freely suspended spiral inductor under a removed silicon substrate, at which a cylindrical cavity with radius of  $a$  and height  $d$  was formed ..... 30

**Figure 2-7:** Scheme of a freely suspend micromachined rectangular spiral inductor with silicon substrate underneath removed and restricting its geometric factors as  $l_{max} = 300 \mu\text{m}$ ,  $S = 5 \mu\text{m}$ , and  $\varpi = 15 \mu\text{m}$  [34] ..... 32

**Figure 2-8:** Scheme of rectangular spiral inductor with substrate removed ..... 33

**Figure 2-9:** Scheme of octagonal spiral inductor with substrate removed ..... 34

**Figure 2-10:** Scheme of circular spiral inductor with substrate removed ..... 34

**Figure 2-11:** Smith chart in which a good s-parameter match between measurement and simulation is present [4] ..... 36

**Figure 2-12:** Comparison of inductance spectrum of rectangular spiral inductors and results of simulation ..... 37

**Figure 2-13:** Comparison of inductance spectrum of octagonal spiral inductors and results of

simulation	38
<b>Figure 2-14:</b> Comparison of inductance spectrum of circular spiral inductors and results of simulation	38
<b>Figure 2-15:</b> Comparison between the theoretical calculations using Green's function in Cartesian coordinate and HFSS simulations	39
<b>Figure 2-16:</b> A flow chart presents the step to optimize the inductor model	43
 <b>Chapter 3</b>	
<b>Figure 3-1:</b> Comparison of experimental results between the losses of CPWs fabricated with and without oxide/nitride fin support on a conventional silicon substrate. The dimensions of CPW: 60 $\mu$ m strip width, 5 $\mu$ m thick, 150 $\mu$ m long and 12 $\mu$ m slot width. Both structures have the same dimensions	48
<b>Figure 3-2:</b> Fabrication process flow: (a) Deep silicon trench etching, (b) thermal oxide growth and top oxide removal, (c) ICP resident silicon etching, (d) LPCVD nitride deposition, and (e) CPW electroplating [49]	49
<b>Figure 3-3:</b> A SEM cross sectional view on the CPW deposited on the patterned nitride/oxide/nitride/air fins [49]	49
<b>Figure 3-4:</b> A SEM cross sectional view of the as-fabricated oxide-nitride islands and an enlarge view of Cu CPW fabricated on the top of oxide-nitride islands [49]	50
<b>Figure 3-5:</b> The entire spectrums of phase shift of modeling data, simulated data, and measured data with conventional and fin structure, respectively	54
<b>Figure 3-6:</b> Comparison of HFSS simulation, model analysis, and experimental results of a 150 $\mu$ m long CPW on the silicon substrate with patterned oxide-nitride fins support	55
<b>Figure 3-7:</b> Comparison of simulation results between the substrate loss of a spiral	

inductor deposited on nitride/oxide/nitride/air fins and that on conventional silicon based substrate, respectively [49] ..... 56

**Chapter 4**

**Figure 4-1:** Schemes of central-supported gimbal circular biomimetic diaphragm. The upper insertion shows the auditory organ of the parasitoid fly *Ormia ochracea* whose entire auditory organ is only 1.2 mm. The intertympanal bridge connecting two prosternal tympanal membranes (PTMs), i.e., the ipsilateral and the contralateral prosternal tympanal membranes, via the tympanal pits (TP) in a manner of flexible coupled pivot can cause the two PTMs to deflect in opposite directions. The lower insertion shows the mechanical model of the central-supported gimbal circular biomimetic diaphragm [57-66]

..... 59

**Figure 4-2:** Schematic diagrams regarding the geometrical structures for (a) the conventional and (b) the hybrid C-S designs ..... 65

**Figure 4-3:** Scheme of the hybrid biomimetic microphone with central floating gimbal design, which is hybridized by the acoustic sensing mechanism of the parasitoid fly and the flexible clover-stem-like gimbal structure. The lower insertion shows a new mechanical model with the central floating joint

..... 67

**Figure 4-4:** Comparison between the cloverleaf and the prototype of the biomimetic microphone ..... 68

**Figure 4-5:** Examples of sinusoidal driven oscillatory motion with damping. The particular solution (steady-state)  $Z_p(t)$ , the complementary function  $Z_C(t)$ , and the general solution of either ipsi- or contralateral displacement are shown in (a) driving frequency ( $\omega$ ) < damping frequency ( $\omega'$ ) and (b) driving frequency >

	damping frequency, respectively [77] .....	72
<b>Figure 4-6:</b>	(a) A photograph of fabricated diaphragm embedded in a cylindrical cavity. (b) A side view of the diaphragm [68] .....	77
<b>Figure 4-7:</b>	The comparison of the ipsilateral displacements of the conventional biomimetic microphone between the theoretical calculations with varying damping ratios and the measured data [68]. The damping ratios closed to unity indicates that the biomimetic microphone is critically damped so that the responses will directly follow the transient inputs .....	78
<b>Figure 4-8:</b>	Mechanical schemes and associated simulation results of deformation of the conventional and hybrid C-S designs due to the influences of gravitational force. The conventional C-S design of the <i>Case B</i> only has two outer beams to support the entire mass of the diaphragm, whereas the hybrid one of the <i>Case C</i> has four central beams to execute the same function .....	80
<b>Figure 4-9:</b>	Mechanical schemes and associated simulation results of deformation of the conventional and hybrid C-S designs due to the influences of sound source pressure. The hybrid C-S design of the <i>Case D</i> reveals larger displacements than that of the conventional one of the <i>Case B</i> , in which they have the same initial deformations .....	81
<b>Figure 4-10:</b>	Comparison of the (a) ipsilateral, (b) contralateral, and (c) net displacements between model analyses and experimental measurement demonstrated by Ono <i>et al.</i> [68] with applying 60 dB and 200 Hz sinusoid sound waves, respectively .....	82
<b>Figure 4-11:</b>	(a) The scheme and (b) the entire acoustic sensing system of Yu's structurally coupled design [82] .....	83
<b>Figure 4-12:</b>	The schematic process of the evolution from Yu's design to the presented hybrid design .....	85

<b>Figure 4-13:</b> Process flow of Fabrication .....	86
<b>Figure 4-14:</b> SEM photograph of the hybrid microphone [84] .....	87
<b>Figure 4-15:</b> Comparison of (a) the frequency spectra and (b) the logarithmic polar patterns of net diaphragm displacement between hybrid and conventional C-S design [84] .....	89
<b>Figure 4-16:</b> Acoustic responses of hybrid design in frequency domain in terms of (a) amplitude, and (b) phase of ipsilateral and contralateral of diaphragm, respectively [84] .....	90
<b>Figure 4-17:</b> Measured (a) ipsilateral and (b) contralateral results of hybrid and CP-S design, respectively. Comparison of model and net displacement are of (c) CP-S and (d) hybrid design, respectively .....	90

## Chapter 5

<b>Figure 5-1:</b> Scheme of the general electrothermal network $\pi$ -model for thermal management [91]. By analogizing with the common electric circuit $\pi$ -model, there are three main blocks, heating source, propagated resistance, and common base resistance, are adopted to present the thermal source, thermal flow path, and the common base, respectively .....	97
<b>Figure 5-2:</b> (a) Scheme of the 3-D stacked Vertical-Cavity Surface-Emitting Lasers (VCSELs) on a Silicon Optical Bench (SiOB). It is obviously that there should be complicated thermal behavior inside the SiOB due to its large volume and aspect ratio. The insertion of upper-right corner shows complicated structure of the VCSELs, the adjacent contact pads, and the thermal via in detail. The insertion of upper-left corner shows the bottom structure of the VCSELs and the interconnected thermal conducting channels. The detail profiles of the (b) 45° micro-reflector and the (c) V-groove array that are monolithically	



	fabricated on the SiOB .....	99
<b>Figure 5-3:</b>	A cross-section of BeamExpress's long-wavelength VCSEL [95] .....	101
<b>Figure 5-4:</b>	(a) Scheme of the modified general electrothermal network $\pi$ -model. The source of thermal flow and $Z_1$ are the components of the heating source due to the VCSELs are main heating generators themselves in our case. (b)The equivalent electrothermal circuit model of the VCSELs on the SiOB, where $Z_1$ and $Z_2$ , $Z_3$ , and $Z_4$ are thermal resistances of VCSEL ( $R_{VCSEL}$ and $R'_{VCSEL}$ ), an infinite thermal resistance due to without nature air convection here, and the thermal capacitance of SiOB ( $C_{SiOB}$ ), respectively .....	103
<b>Figure 5-5:</b>	Scheme of conduction heat transfer sphere with specified volume and surrounding surface. The parameters $q_v$ and $q_s$ are the volume power density in $W/m^3$ generated within the interesting volume and surface power density in $W/m^2$ radiated from the surrounding surface, respectively. The propagation direction of the surface power density is outward and parallel with the normal unit vector. The difference of the temperature distribution could be well determined using the derived conduction heat transfer equation in integral form .....	107
<b>Figure 5-6:</b>	Scheme of convection heat transfer sphere with specified surrounding surface. The propagation direction of the surface power density is outward and anti-parallel with the normal unit vector, $\hat{n}'$ . The difference of the temperature distribution could be well determined using the derived convection heat transfer equation in integral form .....	109
<b>Figure 5-7:</b>	Transit isothermal maps of (a) the simulation results and (b) the EETCM-based algorithm. Time interval between each map is about 30 ms and is evaluated by taking the trick that total input power within a mesh volume-element in a step of iteration divided by the power generated during 1 sec. ....	112

<b>Figure 5-8:</b>	Temperature distribution of single VCSEL realized using the presented algorithm in steady state. The bottom of SiOB is constrained at 75°C to imitate the operation environment of a typical optical transceiver system.....	115
<b>Figure 5-9:</b>	Thermal images of the optical system heated by two operated VCSELs coding by the presented algorithm .....	115
<b>Figure 5-10:</b>	The isothermal surfaces determined by means of the conduction and convection heat transfer equation. In the case, only the lateral single laser turned on where represented using the symbol “+”. The input current is limited at 8 mA and the electric-thermal energy transfer efficiency is 85.7% to meet the standard specification of the semiconductor-made VCSELs [108]. The theoretical temperature at the hottest spot is 78.4°C .....	117
<b>Figure 5-11:</b>	(a) Scheme of the simplified thermal conducting system with single operating VCSEL established by the EETCM. (b) The simulation result of simplified thermal conducting system. According the associated EETCM, the material of air and SiOB were removed in the system to reduce the required meshes as well as the CPU time and computer memory. The temperatures of node points A, B, and C are 78.9, 76.8, and 75°C while the input current is limited at 8 mA .....	119
<b>Figure 5-12:</b>	(a) Fabrication of SiOB and (b) Fabrication of High Frequency 4 Channel ×2.5 GHz Transmission Lines [94] .....	121
<b>Figure 5-13:</b>	The measured temperature distribution of SiOB heated by the operating VCSEL using IR microscope. Only a laser diode is operated by probe B with 8 mA input current and 2 V bias voltage .....	123
<b>Figure 5-14:</b>	Comparison between the EETCM with single laser turned on, measurement data, and simulated results with and without air and SiOB, respectively .....	124

**Figure 5-15:** The measured temperature distribution of SiOB heated by the operating VCSELs using IR microscope. Two laser diodes are operated with 8 mA input current and 2 V bias voltage ..... 124

**Figure 5-16:** Comparison between the EETCM with two lasers turned on, measurement data, and simulated result, respectively ..... 125

**Figure 5-17:** Scheme of Successive Over-Relaxation (SOR) with (a) red- and (b) black ordering [109]. During the first pass, the red nodes obtain the voltages as a weighted average of their original voltage, and as inputs (if any) to the six surrounding black nodes for 3D-situation. During the second pass, the black nodes obtain voltages from the six surrounding red nodes ..... 127

**Figure 5-18:** Scheme of the method for conceptually determining the temperature distribution within each volume element of the situation that (a) single, and (b) two VCSELs are turned on. Each volume enclosed by the dash-line is an “isothermal volume.” The final given temperatures on the boundary surfaces, the temperature on the bottom, could determine the really temperature within the volume elements which are sharing the given temperatures on the boundary surfaces ..... 128

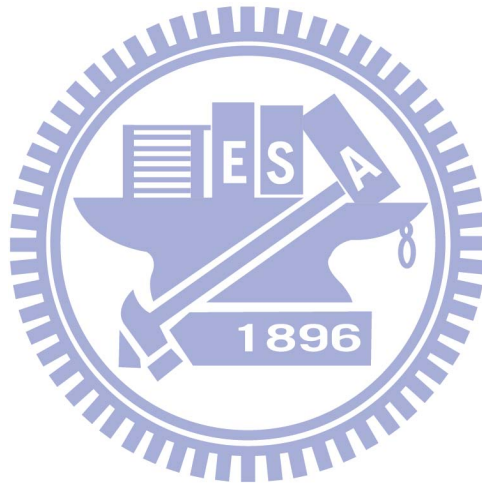
**Figure 5-19:** Scheme of the method for conceptually determining the probable path of heat flux. Four current sources enclosed by four isothermal surfaces with the same temperature difference result in a fourfold overlapped region, the hottest region in this microsystem. Any of three or two current sources also result in the three- and twofold overlapped region and cause the temperature gradients within the system. Thus, the probable path of the heat flux would follow the ideal path that has the largest temperature gradient as indicated in the figure ..... 130

## Chapter 6

- Figure 6-1:** Relations between the nominal radius, the temperature-dependent surface tension (a), and the inclined angle (b) ..... 137
- Figure 6-2:** The schemes of 1-D materials synthesis: (a) without and (b) with inclined surface of inverted pyramid on silicon substrate ..... 138
- Figure 6-3:** SEM micrographs of a 6nm thick Co film on a silicon (100) substrate after (a) 800°C and (b) 900°C thermal reflow for 10 minutes, respectively [132,133] ..... 140
- Figure 6-4:** The bottom length of inverted pyramid versus the size of agglomerated Co seed formed inside: (a) 6nm thick Co film deposition and (b) 30nm thick Co film deposition. Both substrates are thermally annealed at 900°C for 10 minutes [132,133] ..... 142
- Figure 6-5:** Auger line scanning spectrum across the region shown in the inset. The inset is an enlarged SEM view on an inverted pyramid with the bottom length of 290nm inside which a singular Co seed is formed with the size of 190nm in diameter [132,133] ..... 144
- Figure 6-6:** (a) Array of the singular CNT. (b) SEM micrograph of a singular CNT grown from a Co seed formed by the proposed seeding scheme which is reflowed with a 6nm Co seed layer. The insetted Raman spectra both in (a) and (b) indicate the CNTs are a multi-walled carbon nanotubes [133] ..... 145
- Figure 6-7:** The corresponding measured F-N plot for CNTs [129] ..... 152
- Figure 6-8:** Enhancement factor vs. the tube height for CNTs whose intertube distances are (a) 104 and (b) 65 nm [133] ..... 152

## Chapter 7

- Figure 7-1:** A flow chart of microsystem optimization using the EDA technique and the



# Chapter 1 Introduction

## 1.1 Overview

Since the concept of “infinitesimal machinery” was first proposed in 1959 by Dr. R. P. Feynman, the famous American physicist and the owner of Nobel Prize in physics, at the annual meeting of the American Physical Society at the California Institute of Technology (Caltech) [1-2], studies and techniques in the field of micro-electro-mechanical system (MEMS) regarding the integration of electrical and mechanical engineering, miniaturization, integrative fabrication method, diverse industrial and consumer applications then had been catching lots attention from the scientists and engineers. Due to the interdisciplinary MEMS technologies can inherit the advantages from solid-state material, microfabrication, and facility infrastructure, it can provide rapid pace of innovation and vast opportunities of ingenuity for a variety of applications ranging from electric, chemical, and mechanical engineering, material science, micro- and nanofabrication, life science, to civil and environment engineering, and so on.

A successful MEMS device cannot be developed without considering the varying technique connection and combination between science and engineering, thus a designer scientist or engineer who devotes in the field of MEMS would face with the inevitable challenges: the interdisciplinary design. For instance, a well-training electrical engineering designer who is developing a radio frequency (RF) antenna also might need to know the magnetic characteristics of a nanocomposite material to further enhance the performances of its passive components. A mechanical engineering designer should also have to search the fundamental knowledge about the solid state physics and corresponding fabrication skill to promote the performances of his devices efficiently. Thus, being involved in the diverse application domain, such as bioengineering, lab-on-a-chip, thermal phenomena, acoustic vibration, chemistry, nanotechnology, optical engineering, power and energy, hydrodynamics,



and wireless communication, the MEMS designers and engineers should create the desired impact with continuously developing their insight by grasping the essence in interdisciplinary design of knowledge [3]. In order to realize the connection between interdisciplinary applications, the interdisciplinary problems and challenges should be undertaken by the MEMS practitioners. In order to resolve the challenges, the physical models of every MEMS device eventually must be embedded in the technology of electronic design automation (EDA). System designers can, therefore, build their microsystem pre-designs according to the developed physical models use the hardware description language (HDL) in the EDA software platform, and then sequentially execute systematical simplification, simulations and performance predictions, systematical optimization, and layout, until achieve the goal of microsystem optimization. Thus, the EDA technique associate with the developed physical models could conveniently and conceptually provide the MEMS designers a whole picture of the microsystem design by considering the behavior dynamics of each adopted MEMS component and their cooperation, and enhance the efficiency and feasibility of the manufacture of MEMS products. Thus, in the dissertation, several MEMS component structures designed for different application have been fully analyzed for optimal microsystem designs. Five important MEMS component structures regarding a RF passive component characterized by the Kramer-Kronig relations [4,5], periodic fin support for reducing substrate loss [6], acoustic device with a specific central floating joint for sound source localization [7], 1D material for miniaturizing 3DIC applications [8], and SiOB thermal analysis using a special algorithm in view of integral form in system level for high speed data communication are presented for MEMS and NEMS devices for next generation applications [9].

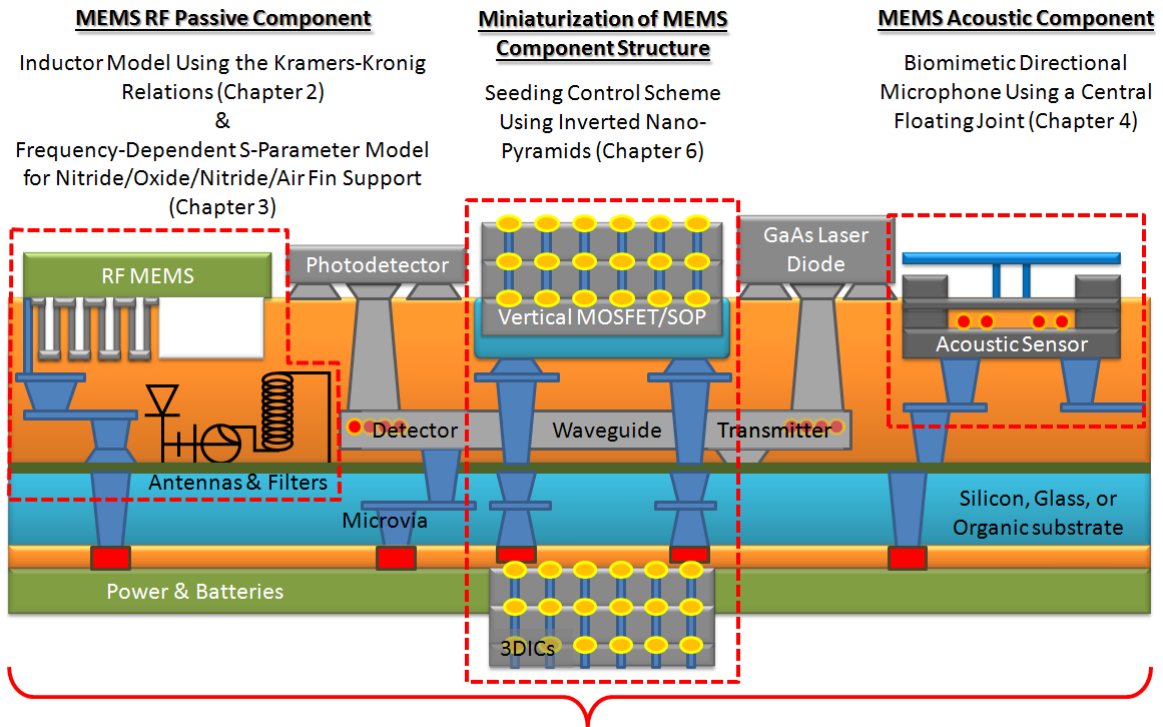
Recent advancement in the design of portable wireless communication systems has been pushed to wide bandwidth applications, in which the carrier frequencies of the systems must shift to 5~10-GHz range or even higher. Thus, the passive components, such as inductor, capacitor, and transmission line, have to be implemented in the front-end RF circuitry for

excellent signal integrity and low power consumption requirements. The on-chip micromachined spiral inductors are one of the candidates developed for the purpose. Furthermore, a closed-form inductor model adopted in the design stage would be convenient for RFIC designers to pre-design and optimize the RF passive micromachined spiral inductors in views of materials, geometries, and specially the energy interaction within the structure. To realize the energy interchange between free electrons and external electromagnetic waves within a MEMS RF passive component, freely suspended micromachining polygonal spiral inductors are investigated in detail. The resonant absorption and anomalous dispersion occurring at the self-resonance are considered as energy interchange between magnetic and electric energies. Meanwhile, a periodic structure constructed by a series of nitride/oxide/nitride/air fin support on the conventional silicon substrate is also presented to reduce the energy loss at high frequency region and reinforce the rigidity of the freely suspended component for further optimizing the performances of the MEMS RF passive components in microsystem designs.

Sound source localization is a physiological ability of animals to process sensory information regarding the orientation and magnitude of sound pressure stimulation. The source localization is achieved for a large mammal, two auditory organs are acoustically isolated by its head to have a large interaural distance (ID), via the interaural intensity difference (IID) and interaural time delay (ITD) sensed by two ears which are geometrically close but far away from the sound sources. In contrast, two auditory organs of small animals are quite close to each other, so there would be a problem for the auditory system to experience insignificant interaural differences resulted by the tiny ID, about two orders of magnitude smaller than that of large animals. Therefore, the methodology of sound source localization in the tiny auditory system could lead the way to develop the next generation acoustic sensing and tracking microsystems like hearing aids, robots, and bionic military devices. Therefore, a biomimetic directional microphone is designed to understand the

mechanical coupling between the external sound pressures, viscous air damping forces, and a specified support structure. The microphone analysis provides a mathematical approach for MEMS engineers to realize the design trade-off between the performance and miniaturization of MEMS device. Superior sensitivity and directivity can be simultaneously reached by employing a novel central-supported structure, a central floating joint. By adequately judging dimensions of central beams of the presented design, the rocking and translational modes of the will get closer to each other and then theoretically reveal better membrane displacements.

For the microsystem development, undesired non-uniformly thermal effects due to drastic increase of the power dissipation within intensively operating chipsets have become significant design problems in the 3D-Stacking Structure (3D-SS) design, such as 3DICs, Silicon Optical Bench (SiOB), and Through Silicon Vias (TSV) Interposer, and so on, and even restrained the design flexibility in terms of associated configurations of device packaging system and maximum power performance of integrated system circuits. Figure 1-1 reveals the embodied relations schematically to further illustrate the interconnections of each MEMS structure and the thermal analyses in the microsystem level. One of proposed efficient strategies to build high-performance 3D microprocessors is to introduce thermal vias through layers or dies at specific locations. However, how to effectively deploy the layers with different thermal conductivities and minimize the utilization problem of interconnect vias in the structure should be strictly considered in associated algorithms [10-12]. Additionally, thermal interface materials used in chip- and package-level for heat dissipation [10,13] will also result in inevitable 3D-SS layout complication in design stage and manufacture cost increase in mass production which should be still undertaken. Thus, to conquer the drawbacks, this dissertation will present a new technique of thermal analysis accomplished by a developed equivalent electrothermal circuit model (EETCM) and an associated mathematical algorithm in system level for next generation 3D microsystem design applications. Simplification of any 3D-SS and the corresponding thermal analysis can be efficiently and



**Thermal Analysis for MEMS Structure**

Thermal Analysis Using the Green's Theorem (Chapter 5)

Figure 1-1: Embodied relations of each MEMS component and the thermal analysis in the system level morphologically.

exactly characterized.

At final, to definitely reveal the three generic and distinct merits for MEMS devices: miniaturization, microelectronics integration, and mass fabrication with precision so that the MEMS practitioners could well follow the Moore's Law, relative methodologies for the MEMS devices and its associated implement microelectronic circuitry thus become a key point for next generation. This requirement also impacts the electromechanical devices, bio-devices, and specific microsystem, so that searches were investigated to explore the scaling effect beyond that of the traditional MEMS [14-15]. Those devices and systems are then called nano-electromechanical systems (NMES), and many of which are developed using nanostructure assembly, such as nanotubes [15-16] or nanofabricated elements [17]. In this dissertation, the miniaturization of the MEMS are realized by means of a concept of one-dimensional (1D) material, in which vertical well-aligned carbon nanotubes (CNTs) are

employed for visually constructing a three-dimensional integral circuit (3DIC) systems. Using gravitational force to trigger the metal liquids on the surfaces of inverted silicon nano-pyramids on the substrate, size and location of each vertical-aligned CNT can be well-defined. Therefore, combining with the suitable properties for microelectronics integration and ingenious seeding control scheme for precisely mass fabrication, the presented 1D material method can definitely provide an opportunity for further miniaturizing the MEMS and microelectronic devices.

## 1.2 Organization of the Dissertation

In Chapter 2, a closed-form integral model is presented for the freely suspended micromachining polygonal spiral inductor. The Kramers–Kronig relations provide an elegant theory and the causality between the interchange of magnetic and electric energies to describe the electron behavior within a polygonal spiral inductor without having complicated geometric analysis. A hypothesis built using similar mathematical approaches of the model of Pauli spin paramagnetism determines the resonant factor that described the resonant absorption of external electromagnetic energy while self-resonance occurring in the spiral inductor. Simulation and measurement results validate that the model can provide satisfactory prediction to the self-resonant frequencies and frequency-dependent inductances of on-chip freely suspended polygonal spiral inductors. Meanwhile, in Chapter 3, a structure of patterned nitride/oxide/nitride/air composited-fins on a silicon substrate with a resistivity of  $1 \Omega\text{-cm}$  is presented to effectively reduce the substrate loss. A frequency-dependent S-parameter analytical model is also developed to predict characteristics of the coplanar waveguide (CPW). Comparisons for performances of rectangular spiral inductors on the composited-fins and conventional silicon substrate, respectively, show the practicality of the composited-fins support. A physical analysis of biomimetic microphone designed with a central-supported

(C-S) diaphragm for the sound source localization is presented in Chapter 4. A clover-stem-like C-S design is then proposed and resulting in 47% improvement of net diaphragm displacement. A central floating joint is employed in the hybrid C-S design and then reveals better resistance for preventing the undesired deformation and superior sensing ability beyond the conventional C-S one. Thus, the new design can effectively not only compensate undesired deformation of sensing diaphragm due to gravity and residual stresses but also make the diaphragm more flexible for better sound pressure sensitivity.

In Chapter 5, a method combining a general electrothermal network  $\pi$ -model in system level and the associated mathematical technique, Green's theorem, in terms of the adopted materials and system geometries is presented to build up an equivalent electrothermal circuit model (EETCM) for efficient thermal analysis and behavior prediction in a thermal system. Heat conduction and convection transfer equations in integral forms are derived using the theorem and successfully applied for the thermal analysis of a 3D optical stack, VCSELs on a SiOB. The complicated stacking structure in conventional simulators can be greatly simplified using the method by well predicting probable heat flow paths, and the simplification can eventually achieve the goal of CPU time-saving without having complex mesh studying or scaling. By comparing the data from the measurement, the finite element simulation, and the method calculation, it shows that excellent temperature matching within  $\sim 0.5^{\circ}\text{C}$  and 90% CPU time-saving can be realized.

A seeding control scheme by utilizing gravitational force to form an agglomeration of melted Co seeds on a patterned inverted silicon nano-pyramid is then presented in Chapter 6. Nanometer sized melted Co seeds formed on a nonwettable inverted pyramid surface can roll along the inclination followed by aggregation to form a singular seed with the size depending on the edge length of pyramid and the thickness of as-deposited Co film inside the pyramid. The associated physical mechanism of rolling and upper and lower limits of the radius of the Co drop-like liquids on the inclination are also definitely clarified. The proposed scheme



allowing the formation of well-aligned catalytic seeds with manipulated size will promise the control growth of 1D material for practical integrated microelectronic device fabrication.

Eventually, the rest chapters summarize the developed physical analyses of the MEMS component structures and the system, and then reveal the corresponding methods for the optimal microsystem designs and the future works. It is our belief that these analyses can definitely benefit the future development of microsystem EDA.



## ***Chapter 2    A Closed-Form Integral Model of Spiral Inductors Using the Kramers-Kronig Relations***

### ***2.1 Introduction***

Researches in integral passives for the replacement of the discrete ones have shown growing importance for realizing the next generation electronics industry. The requirement for integral passives emerges from the increasing consumer demands for product miniaturization and high performance. The required components must, therefore, be reliable and controlled easily and the microelectronic industry has to respond the demands immediately. The last two decades have seen the development of personal computers, such as telecommunication, electronic equipment, devices and consumer sectors, towards product miniaturization with increasing functionality. In order to achieve the goal of miniaturization, the physical behaviors and related performance of miniaturized passive components must be understood clearly before being real products. In addition, National Electronics Manufacturing Initiative (NEMI) has well defined the integral passive as the functional elements either embedded in or incorporated on the surface of an interconnecting substrate. Since the number and areas of passive components may exceed both that of IC chips on a circuit board or a package, it is necessary to concretely estimate and predict each single device's performance and the interaction between each other. As a result, it is necessary to develop a method to well predict and then optimize the behaviors of the passive components accompanied with the benefits of smaller size, more functionality, and better performance.

The micromachined spiral inductors, one of the critical passive components, have been properly developed and widely utilized for RFIC designs. The related electric characteristics, including self- and mutual inductances, quality factors, self-resonant frequencies, and loss mechanism etc. of the inductor, have already been investigated in detail. A variety of methodologies to calculate the inductance of a spiral inductor, such as Greenhouse-based

formulations [18-20], empirical expressions [21], analysis and simulation of inductors and transformers in integrated circuits (ASITIC) [22], and several textbooks in physics and engineering, have been presented for the design principles.

Nevertheless, in order to facilitate the implementation of integrated inductors, a compact scalable physical model that can accurately predict the physical behaviors of the inductors in terms of material, geometrical, and overall configured parameters is still an important research topic for the RFIC design and optimization [21,23-27]. Conventional inductor models [21,24] could calculate inductance precisely. The applied method, however, is based on the Greenhouse algorithm [18], which has high accuracy but still relies on numerous summation steps that depend on the number of interacting segments and overall combinations of parallel segments so that a complicated geometrical analysis could not be avoided. Meanwhile, several aforementioned methods only can provide nonphysical expressions using a large number of fitting factors, the lack of sufficient physical and mathematical meanings of the presented models result in the difficulties of optimization in design stage. Since the factors are created to overcome the imperfect of the fitting function, it is also essential to create an accurate mathematical expression associated with the physical sense for predictions of the physical behaviors of a micromachined spiral inductor.

In this chapter, a closed-form integral model is presented for freely suspended micromachined polygonal spiral inductors. Based on the Kramers-Kronig relations, field theory, and solid state physics [26-28], the presented model can actually describe behaviors of free electrons in a metal to characterize physical parameters of a spiral inductor which RFIC designers could easily have the optimal design. Meanwhile, this model can exactly predict inductances and self-resonant frequencies of spiral inductors without complicated geometrical analysis. Simulation and measurement results have validated the accuracy of the model. Furthermore, unlike conventional formulations only based on circuit parameters, this model analysis provides physical intuition in terms of materials and geometry.

## 2.2 Linear Response Theory, Causality, and Kramers-Kronig Relations for Metals

An external field applies on, or more strictly perturb, an interesting system, the physical characteristics of the system, such as thermal qualities or electron distribution, would provide corresponding responses. While the quantity of external field (or say, the perturbation) is sufficient weak, the response of the system is linearly proportional to the stimulus. The proportional factor is generally called a linear response function or a generalized susceptibility that can be expressed using the Green's function. Meanwhile, two prescribed conditions should be achieved before obtaining the response function:

- (1) The external field shall be so sufficient weak that the associated Hamiltonian of the system would become perturbed equations such as the generalized form of Hook's law. Thus, the concerned physical problem would be reduced as a linear combination of linear response functions. For instance, by employing the Faltung theorem of Fourier integrals, the temporally nonlocal connection between the displacement field  $\bar{D}(\bar{x}, t)$  and the electric field  $\bar{E}(\bar{x}, t)$  can be expressed as [21]:

$$\bar{D}(\bar{x}, t) = \varepsilon_0 \left[ \bar{E}(\bar{x}, t) + \int_{-\infty}^{\infty} G(\tau) \bar{E}(\bar{x}, t - \tau) d\tau \right], \quad (2-1)$$

where  $G(\tau)$  is the Fourier transform of the electric susceptibility,  $\chi_e$ , (or the response function):

$$G(\tau) = \frac{1}{2\pi} \int_{-\infty}^{\infty} \chi_e \exp(-i\omega\tau) d\omega = \frac{1}{2\pi} \int_{-\infty}^{\infty} \left[ \frac{\varepsilon(\omega)}{\varepsilon_0} - 1 \right] \exp(-i\omega\tau) d\omega. \quad (2-2)$$

The parameters  $\varepsilon_0$  and  $\varepsilon(\omega)$  are the permittivity constant in free space and the frequency-dependent dielectric constant, respectively. The response function in (2-1) clarifies the responses of the medium, in which an electric susceptibility would be induced due to the external electric field.

(2) The responses could directly follow with the stimulus, thus the system should be assumed in an adiabatic environment. The system is in equilibrium or at ground state when the propagated time is at the condition of  $t = 0$ . To judge whether our concerning problems in the RF regime could be reduced as a linear response functions or not, we can clearly consider and examine the frequency-dependent Ohmic law in view of solid state theory [26-29]:

$$\vec{J}(\vec{x}, \omega) = \sigma(\omega) \vec{E}(\vec{x}, \omega), \quad (2-3)$$

where the electric conductivity  $\sigma(\omega)$  is a complex physical parameter:

$$\sigma(\omega) = \frac{n_e e^2 \tau_r}{m_e} \frac{1}{1 - i\omega\tau_r} = \frac{\sigma_0}{1 - i\omega\tau_r}. \quad (2-4)$$

The parameters  $n_e$ ,  $e$ ,  $\tau_r$ , and  $m_e$  are the density of free electron, the charge element, the relaxation time, and the mass of a electron, respectively. Generally, for a simple metal such as copper, the relaxation time is typically  $10^{-14}$  second [28,29]. Thus, within the RF even the terahertz radiation (TR) region, the condition  $\omega\tau_r \approx 10^{-2} \ll 1$  results in the imaginary part could be safely ignored in (2-4). The consequence indicates that the current is definitely in-phase with the associated driving time-varying electric field, and the energy of the electromagnetic field would be absorbed in form of Joule heat due to the finite resistance of the metal.

Therefore, as mentioned above, the physical behaviors and the corresponding responses due to the external frequency-dependent stimulus of the micromachined spiral inductor could be definitely clarified and analyzed based on the linear response theory. The rest problem is: can the linear response theory reveal the causality of the interaction between the stimulus and the responses in the interesting system, so that the quantitative relationships between attenuation and dispersion of the system could be uniquely determined? To overcome the risk, the

Kramers-Kronig relations are employed in this chapter. As a prescribed consequence, the Kramers-Kronig relations will be the core key to resolve the physical behaviors of the micromachined spiral inductor.

The Kramers-Kronig relations compose of one of the most elegant and general theorems in physics, because they depend only on the principle of causality for their validity: the response cannot be prior to the stimulation. Simply based on the principle, the Kramers-Kronig relations describe the interdependence of the real and imaginary parts of the generalized susceptibility  $\chi(\omega)$ . Thus, the Kramers-Kronig relations can explain in the most fundamental and general terms, completely independent of the underlying physical mechanisms, the intimate connection between refraction and absorption. In fact, given one, the other follows immediately. To evaluate the behavior of low frequency due to the singularity for a conducting medium in the case (this can be realized that the condition  $\omega\tau_r \ll 1$  is satisfied automatically), the generalized response functions derived by the Kramers-Kronig relations can be expressed as [26-30]:

$$\text{Re}[\chi_g(\omega_0)] = \frac{2}{\pi} \mathbf{P} \int_0^\infty \frac{\omega \text{Im}[\chi_g(\omega)]}{\omega^2 - \omega_0^2} d\omega, \quad (2-5)$$

and

$$\text{Im}[\chi_g(\omega_0)] = -\frac{2}{\pi} \mathbf{P} \int_0^\infty \frac{\omega_0 \text{Re}[\chi_g(\omega)]}{\omega^2 - \omega_0^2} d\omega, \quad (2-6)$$

where  $\sigma_0$  is the dc conductivity of metal as shown in (2-4), and the  $\omega_0$  is the eigen-frequency of the response functions. The detail mathematical derivation of the Kramers-Kronig relations could be found in the Reference [26-30]. Therefore, the Kramers-Kronig relations for metals are definitely presented.

## 2.3 Determination of the Self-Resonant Frequency of a Spiral Inductor

### 2.3.1 Characteristics of Anomalous Dispersion and Resonant Absorption

In this section, the concurrence relationships of the real and imaginary parts of the Kramers-Kronig relations are modified to explain certain physical characteristics. For instance, preceded with the Lorentz–Drude Model (1900) in a conducting medium, a phenomenon called anomalous dispersion occurring near a narrow absorption feature, i.e., resonant absorption in a metal vapor, can be well represented in terms of the utilization of equation (2-5) and (2-6) to describe the relation between resonant absorption and anomalous dispersion as shown in Figure 2-1. The dispersion and absorption are coupled with each other and associated with the real and imaginary parts of the susceptibility, respectively. If a medium has an imaginary component of the susceptibility at the self-resonant frequency, it must have a real component over a broad range of frequencies around the self-resonant frequency. While

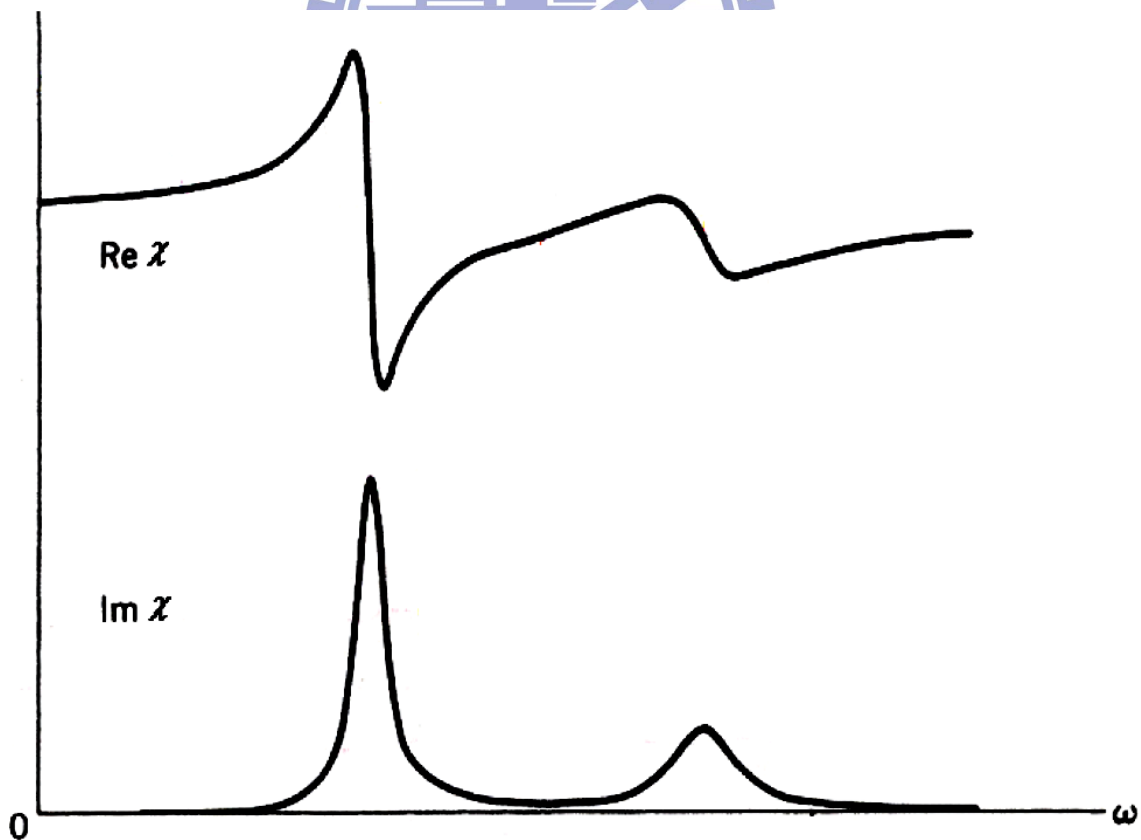


Figure 2-1: Real and imaginary parts of the susceptibility function in the neighborhood of two resonances. The region of anomalous dispersion is also the frequency interval where absorption occurs [27].



the resonance occurs, the energy of incident electromagnetic waves are fully absorbed by the free electrons inside the medium and the frequency diagram of the absorption would be peaked strongly at the resonant frequency. Similar physical behavior of the resonance should be also applicable for the case of a micromachined spiral inductor. The self-resonance occurrence of the spiral inductor would result in a complete energy transformation from stored magnetic energy into electrical energy, and vice versa. The occurrence of the energy exchange is similar to the anomalous dispersion in which the incident electromagnetic waves are totally absorbed by the conducting medium and transformed into the kinetic energy and scattering potential of the free electrons. Therefore, we can construct a physical-based inductor model using the Kramers-Kronig relations based on the mentioned linear response theory and the causality of the responses. First, we assume that the inductor is perfect for electromagnetic wave signal propagation without having any energy loss except the Joule heating. Fortunately, the Joule heating should be smaller than the kinetic and potential energies, thus it can be safely ignored in the derivation. Thus, the imaginary part, (2-6), could be rationalized as a very narrow absorption of the electromagnetic wave at self-resonant frequency,  $\omega_r$ , due to the energy transformation and it can be modified as [27]:

$$\text{Im}[\chi_d(\omega)] \approx \frac{\pi}{2} \frac{\alpha \delta(\omega - \omega_r)}{\omega_r} + \dots, \quad (2-7)$$

which is accompanied with the real part as the following:

$$\text{Re}[\chi_d(\omega)] \approx \bar{\chi}_d + \frac{\alpha}{\omega_r^2 - \omega^2}, \quad (2-8)$$

where  $\bar{\chi}_d$  is the slow part of (2-8) resulted by the more remote contributions to (2-7). The resonant factor  $\alpha$  can be evaluated by employing similar mathematical and physical approaches as the model of Pauli spin paramagnetism [28,29]. For discussion in high frequency region, the new response function can be then reduced as:

$$\text{Re}[\chi_d(\omega)] \approx \frac{\alpha}{\omega_r^2 - \omega^2}. \quad (2-9)$$

Thus, we can easily employ the equation (2-9) with a new physical mission without complicated mathematical structure. The physical meanings of resonant factor  $\alpha$  will be derived in detail as follows.

A hypothesis for deriving the resonant factor is presented: “*half of the free electrons seize all of their own energy, kinetic and magnetic, so that they stay at the inductance region, while the rest lose all of their energy and fall into the capacitance region. The energy difference of these two groups of free electrons is just the induced magnetic energy in the system.*” At this moment, in the view of similar mathematical approach, we can assume that those free electrons are divided themselves into the spin-parallel-like and spin-anti-parallel-like groups just as the model of Pauli spin paramagnetism when the self-resonance occurring. Considering the free electron density ( $n_e$ ) with magnetic moments parallel to the presented magnetic energy ( $\mu B$ ) with the conducting medium, the form is

$$n_e^+ = \frac{1}{2} \int_{-\mu B}^{\hbar \omega_r} D(\varepsilon + \mu B) d\varepsilon \cong \frac{1}{2} \int_0^{\hbar \omega_r} D(\varepsilon) d\varepsilon + \frac{1}{2} \mu B D(\hbar \omega_r), \quad (2-10)$$

where  $\hbar$  is the Planck's constant. Here  $\frac{1}{2} D(\varepsilon + \mu B)$  is the density of orbital of one spin orientation with energy  $\varepsilon + \mu B$ . The free electron density with magnetic moments anti-parallel to the presented magnetic field is

$$n_e^- = \frac{1}{2} \int_{\mu B}^{\hbar \omega_r} D(\varepsilon - \mu B) d\varepsilon \cong \frac{1}{2} \int_0^{\hbar \omega_r} D(\varepsilon) d\varepsilon - \frac{1}{2} \mu B D(\hbar \omega_r). \quad (2-11)$$

Figure 2-2 shows the schemes of the Pauli paramagnetism at absolute zero. The schemes present the total energy, kinetic and magnetic, of electrons with different spin direction relates to the density of orbital. Combining the (2-10) and (2-11), the resonant factor,  $\alpha$ , is

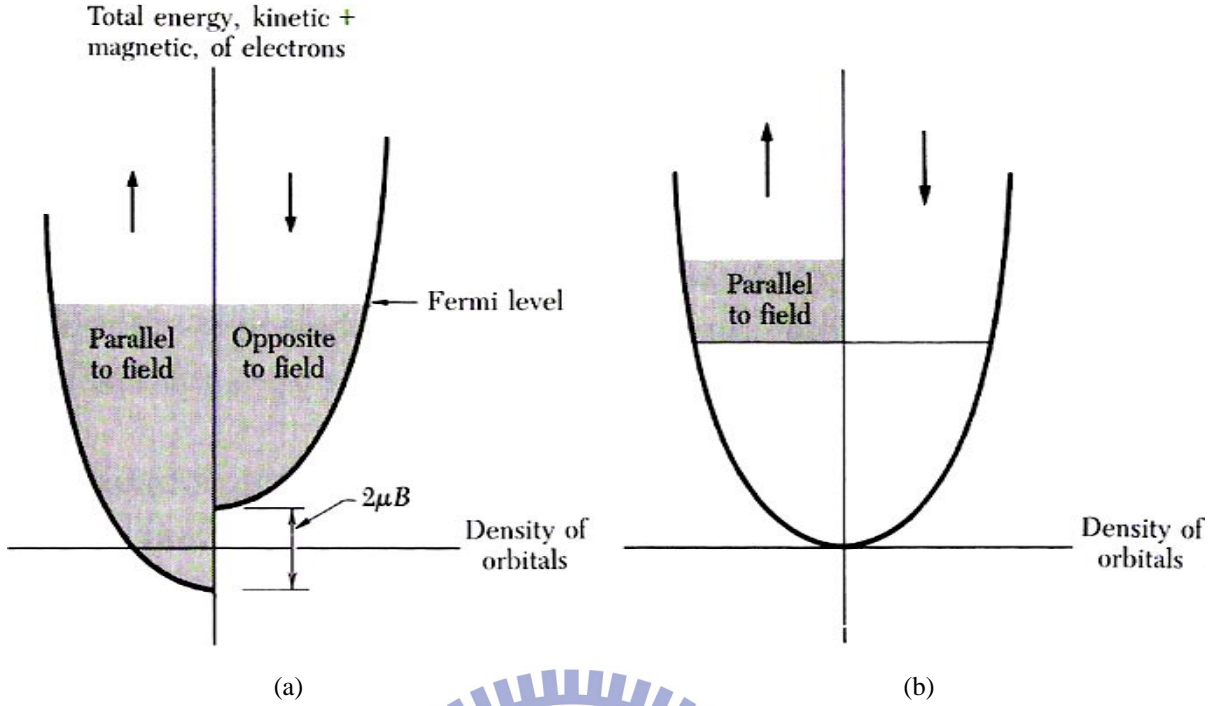


Figure 2-2: Pauli paramagnetism at absolute zero. The orbitals in the shaded regions in (a) are occupied. The numbers of electrons in the "up" and "down" band will adjust to make the energies equal at the Fermi level. The chemical potential (Fermi level) of the moment up electrons is equal to that of the moment down electrons. In (b) we show the excess of moment up electrons in magnetic field [22].

given by

$$\alpha = \mu_0 \frac{\mu \omega_r^2}{B} (n_e^+ - n_e^-) = \mu_0 \mu^2 \omega_r^2 D(\hbar \omega_r) = \mu_0 \mu^2 \omega_r^2 \frac{3}{2} \frac{n_e}{\hbar \omega_r} = \mu_0 \frac{3n_e \mu^2 \omega_r}{2\hbar}. \quad (2-12)$$

It is noted that the magnetic moment,  $\mu$ , shall be carefully defined in this case. The energy levels of the system in a presented magnetic field are

$$U = -\bar{\mu} \cdot \vec{B} = m_j g \mu_B B, \quad (2-13)$$

where  $m_j$  is the azimuthal quantum number and has the values  $J, J-1, \dots, -J$ , factor  $g$  is the spectroscopic factor, and  $\mu_B$  is the Bohr magneton. For a single spin with no orbital moment we have  $m_j = \pm \frac{1}{2}$  and  $g = 2$ , whence  $U = \pm \mu_B B$ . Thus, the paramagnetic-like factor may be modified and has the form as:

$$\alpha = \mu_0 \frac{3n_e \mu_B^2 \omega_r}{2\hbar}. \quad (2-14)$$

For a micromachined spiral inductor with the geometry as shown in Figure 2-3, the material- and geometrical-dependent resonant factor could be modified by means of different geometrical parameters and the magnetic moments of the material.

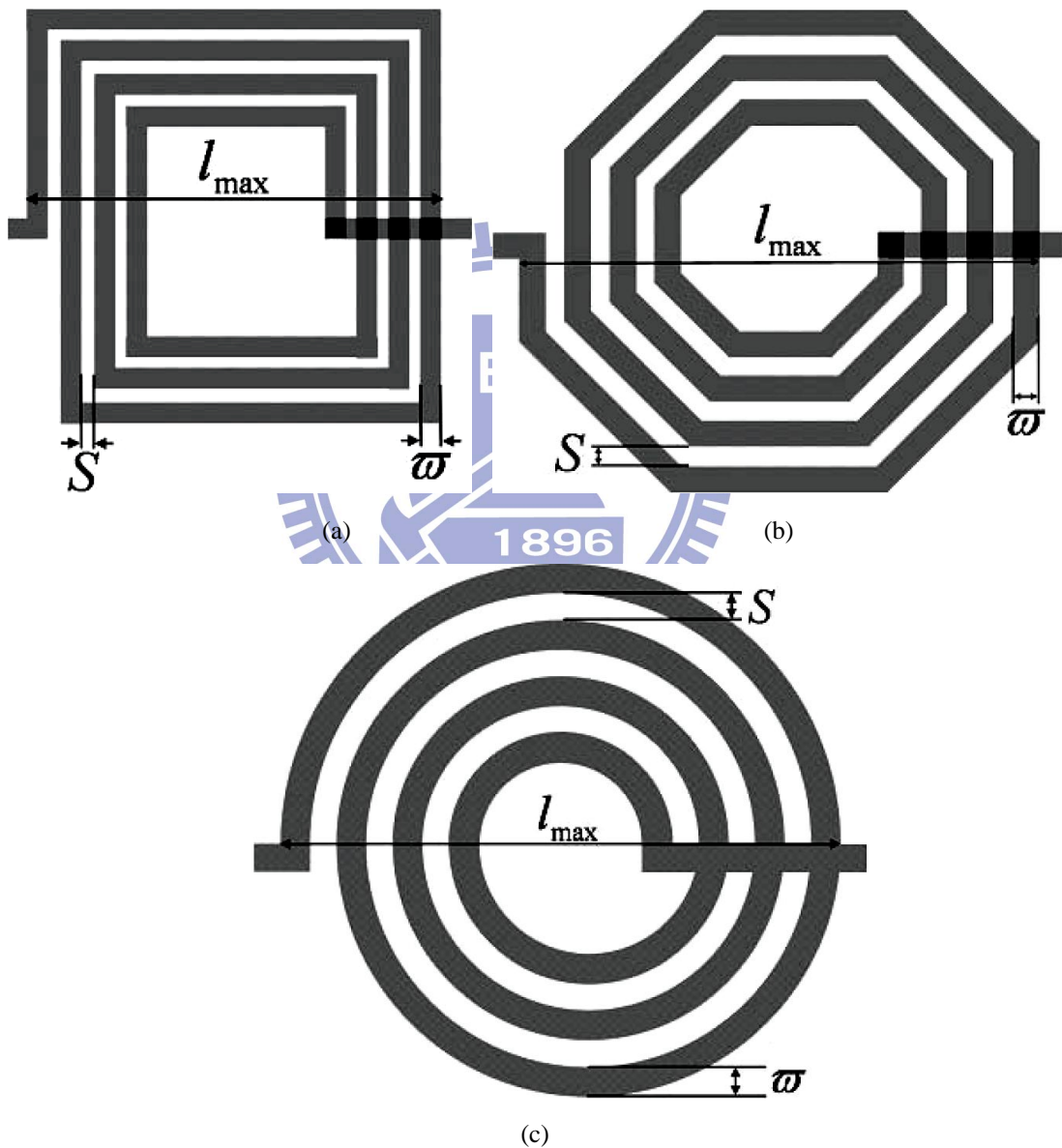


Figure 2-3: Schematic diagram of the two-port spiral polygon inductor realizations: (a) rectangular, (b) octagonal, (c) circular spiral inductor. The parameters  $l_{\max}$ ,  $s$ , and  $w$  are the maximum edge, line spacing, and line width of the polygon inductor, respectively.

### 2.3.2 Kinetic Energy of Conduction Electrons in Metals

Since high electron density would cause each wave function of an electron to be overlapped with each other, so that the quantum effects become important in metals. Quantized electrostatic oscillations of the conduction electrons in a metal ensure that their can have the energy  $E = \hbar\omega$ . Due to the exclusion principle, the electrons that move into a region that is already filled by other electrons must occupy higher energy levels lying above the Fermi level. This is equivalent, in a sense, to increase the restoring energy on the electrons that could result in an effect of the frequency increase. The kinetic energy of a free electron is described approximately by the dispersion relation [29]:

$$E_L = \sqrt{\frac{3}{5}} \frac{\hbar^2}{m_e} (3\pi^2 n_e)^{1/3} k, \quad (2-15)$$

where  $k$  is the wave number of free electrons. In metals, where the conduction band is only partially filled, the Fermi level lies somewhere in the middle of the conduction band, far from a band edge and the effective mass is very nearly that of a free electron. Figure 2-4 shows the band structure of the electron energy in a periodic lattice. The broken lines indicate the dispersion relation of free electrons.

The wave number is a critical parameter which is directly related to the self-resonant frequency of polygonal spiral inductors. In this model, the concept of standing wave is implemented to characterize the free electron behavior while the inductor starts self-resonating. The free electrons similar to the notion of standing waves move back and forth through the two terminals of the spiral inductor. Thus, the wave number,  $k$ , of the electron could be identified as  $m\pi/l_{max}$  where  $m$  represents an integral number. Once the free electrons behave like standing waves, they can effectively absorb the energy of the electromagnetic wave propagating along the metal line of the inductor. Meanwhile, since the operational frequency falls in a range of several GHzs for most of RFICs applications in

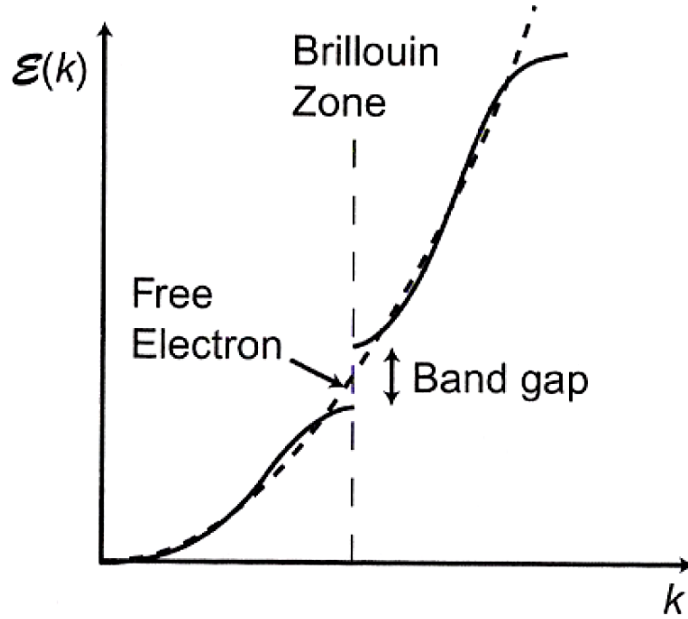


Figure 2-4: Band structure of the electron energy in a periodic lattice [26].

which the electromagnetic wavelength is about several centimeters long, the lowest mode would be the dominant one. In other words, the integral number  $m$  is equal to a unity and  $k \sim \pi/l_{max}$ . Thus, the self-resonant frequency of a spiral inductor would be equal to the frequency of the resonating electron, in which the kinetic energy could be calculated as the follows:

$$E_L = \sqrt{\frac{3}{5}} \frac{\hbar^2}{m_e} (3\pi^2 n_e)^{1/3} \frac{\pi}{l_{total}}. \quad (2-16)$$

### 2.3.3 Scattering Fields and Energy Stored in Corners of a Spiral Inductor

Another assumption is made to facilitate a mental visualization of the electron behaviors inside the polygonal spiral inductor while electromagnetic wave propagates along with the entity. Homologizing the hydromechanics that expounds the ideals about the inner corner flow, it can be hypothesized that there would be a small free vortex locally to form in each apex of



the corner while electrons travel inside the polygonal spiral inductor. Since each vortex is a closed path and its diameter is much smaller than the inductor width, it is convenient to assume that the vortex is infinitesimal in this model. The free electrons moving in a form of free vortex in each corner of the spiral inductor can be treated as a cluster of static electrons to build up a quasi-static electric field in the apex of the corner. Thus, according to theory of the quasi-static electric field [27] and the notion of hydromechanics, there will be quasi-static electric fields built up in the neighborhood of corners while an external electric field is applied on a conducting material. For a freely suspended micromachined polygonal spiral inductor with several corners in the boundary, the quasi-static electric field built up in each corner has the form as the following which is calculated by the variation principle [30]:

$$\vec{E}(\vec{r}) = \frac{1}{32\pi\epsilon_0} \frac{e[\pi + 8\sin(\pi^2/4\beta)]^2}{\beta\varpi h[\csc(\beta/2) - 1](\pi + \beta)} \hat{r}, \quad (2-17)$$

where  $\varpi$  and  $h$  are the width and height of polygon spiral inductor, respectively,  $\beta$  is the corner angle, and the field is centered at the outer apex of each corner. By considering the field scattering at the corners, the free electrons move near the corner would be scattered and change their trajectories due to the built-up electrical field. The energy lost of free electrons due to the field scattering can be then calculated using (2-17), trajectory function, and the scattering theory [31,32]:

$$E_C = \frac{\sqrt{\varpi} h [\csc(\beta/2) - 1]}{nV^{2/3} \sigma_{eff}} \left[ \left( 1 + 2 \int_{-\infty}^{\infty} \frac{d^3 r}{r^3} + \dots \right) \csc\left(\frac{\pi - \beta}{2}\right) \right]^2 e |\vec{E}(\vec{r})|$$

$$\approx \begin{cases} \frac{e^2}{16n\pi V^{2/3} \sqrt{\varpi} h \sigma_{eff}} \frac{\left(\pi + 8\sin\frac{\pi^2}{4\beta}\right)^2}{8\beta(\pi + \beta)} \csc^2\left(\frac{\pi - \beta}{2}\right), & \text{for } \beta < \pi \\ \frac{e^2}{16n\pi V^{2/3} \sqrt{\varpi} h \sigma_{eff}} \frac{(\pi + 4\sqrt{2})^2}{4\pi} \frac{\pi}{2.7}, & \text{for } \beta = \pi \text{ (circular inductor)} \end{cases}, \quad (2-18)$$



where  $V$  and  $\sigma_{eff}$  are the volume of polygon spiral inductor and the effective scattering factor of the inductor, respectively. Here, the effective scattering factors are 0.025, 0.042, and 0.049 in  $F/m^3$  for the rectangular, octagonal, and circular inductors, respectively [4,5]. In above formula, the term

$$1 + 2 \int_{-\infty}^{\infty} \frac{d^3 r}{r^3} + \dots, \quad (2-19)$$

means the trajectory function with the perturbation terms in the classical mechanism. The first term means the ideal trajectory function, and the second terms means perturbation from the near field such as the ground pad, defects in metal line, other electrons or metal lines, etc. Since we assume the perturbations from the field is far from the infinity, the integral arguments in (2-19) could be ignored theoretically. The recent investigations also reveal that the substrate coupling effects could be neglected as long as the air gap is larger than  $60\mu m$  [33]. For a micromachined spiral inductor in the RFIC design, the reference ground point would be far away from itself. Thus, infinity assumption is reasonable and practical in the model. Nevertheless, if a reference ground plane is designed to close to the inductor, the self-resonant frequency would be changed and can be calculated in (2-19) by changing the integral range  $[r_m, \infty)$  to replace  $(-\infty, \infty)$ , where the factor  $r_m$  presents a reference point for an inductor circuit. This factor indicates the loss or shift term for applying energy. We will also provide an alternative method, the Green's function, to evaluate the boundary condition problem in the later section in details.

#### **2.3.4 Determination of the Self-Resonant Frequency Using Energy Conservation**

Since the built-up electric field near the corners could modify the forward direction of the free electrons and make them move straightly down to the end of the inductor to form the standing waves, the realistic self-resonant frequency,  $\omega_r$ , of a freely suspended polygonal

spiral inductor with removed silicon substrate should be derived as the following:

$$\omega_r = (E_L + N \cdot E_C) / \hbar, \quad (2-20)$$

where  $N$  is the number of the corners within a spiral inductor. Equation (2-20) indicates that the electron starts resonating to form a standing wave as long as its energy is equal to the kinetic energy plus the total energy lost in the corner field scattering, in which the energy conservation is revealed.

#### ***2.4 Determination of the Inductances in View of Solid-State Physics***

It is noted that for a closed current-carrying circuit with arbitrary shape such as a spiral inductor, the Ampère's law will be annullable from the asymmetry of the shape. To overcome the drawback at present, there are three independent ways which can be employed. The first way is to execute the integrand along the circuit path of the spiral inductor using the Biot-Savart law. The integral of current and coordinate function, however, is very complicated, so that it only can be exactly completed by computer-based tools. The second way is to decompose the circuit path into several segments, estimate each one, and then sum over all of them. This way may be more convenient than the Biot-Savart law, but the accuracy will be lessened. The final way is based on the Greenhouse-based algorithm. Though the algorithm is very accurate, it still employs numerous summation steps that depend on the number of interacting segments and overall combinations of the parallel segments. Complicated geometrical analysis cannot be avoided. Meanwhile, there are nonphysical expressions, obtained using a large number of fitting factors. Since the factors are created to overcome the imperfection of the fitting function, it is essential to create an accurate mathematical expression associated with the physical sense for the inductance calculation.

Additionally, the frequency-independent inductance estimated using the

Greenhouse-based algorithm cannot present the resonant behaviors of the spiral inductors. On the contrary, the presented model reveals a simple method to accurately estimate the self-resonant frequency of an inductor without complicated geometrical analysis and integrand. In the following section, to overcome the predicaments from Greenhouse's method, the phenomenon of the free electron transport within the spiral inductor will be resolved by means of the Boltzmann transport equation. Associating with the self-resonant behaviors mentioned above, equation of frequency-dependent inductance will be obtained in terms of geometrical and material parameters, so that the RF circuit designer can modify the inductor circuit intuitively and rely on their physical sense to predict the performance of the inductor.

In this model, it is necessary to develop the distribution of the free electrons inside the metals by the physical statistics. Thus, the transport behavior of the free electrons should be discussed. The classical theory of transport processes is based on the Boltzmann transport equation. By working in the six-dimensional space of Cartesian coordinates  $\vec{r}$  and velocity  $\vec{v}$ , the Boltzmann transport equation can be calculated as:

$$\frac{\partial f}{\partial t} + \vec{v} \cdot \nabla_{\vec{r}} f + \frac{d\vec{v}}{dt} \cdot \nabla_{\vec{v}} f = \left( \frac{\partial f}{\partial t} \right)_{\text{collisions}}. \quad (2-21)$$

In many problems the collision term may be treated by the introduction of a relaxation time  $\tau_r(\vec{r}, \vec{v})$ , defined by the equation:

$$\left( \frac{\partial f}{\partial t} \right)_{\text{collisions}} = -\frac{f - f_0}{\tau_r}, \quad (2-22)$$

where  $f_0$  is the energy distribution function in thermal equilibrium. Thus, this result provides a way to address the distribution of free electron density with magnetic energy in the complex frequency plane, defined as:

$$f(\omega) = \frac{n_e \hbar \omega_r}{4\pi} \exp\left(-\frac{\hbar(\omega - \omega_r)}{k_B T}\right). \quad (2-23)$$

By recalling (2-20) and realizing the fact that  $\hbar(\omega - \omega_r) \ll k_B T$  in room temperature, the above equation could be further modified as a simple form:

$$f(\omega) = \frac{n_e}{4\pi} (E_L + N \cdot E_C), \quad (2-24)$$

By the normalization condition and integral the resonant energy function, the total resonant energy can be obtained:

$$F(\omega) = \left| \frac{1}{n} \int f(\omega) d^3\vec{r} \right| = \frac{n_e l_{total} \hbar \omega}{4\pi n} (E_L + N \cdot E_C). \quad (2-25)$$

After all, by employing the conception of the velocity distribution from Sommerfeld's theorem [28-29], the inductance,  $L$ , of a freely suspended micromachined polygonal spiral inductor with a removed silicon substrate underneath can be derived with the associated magnetic energy in the inductor:

$$L \equiv \frac{\int \vec{B} \cdot \vec{H}^* d^3\vec{r}}{I^2} \cong \chi_d \cdot \left[ \frac{F(\omega)}{I^2} \right] = G_S \cdot \chi_d \frac{n_e l_{total}^3}{\sigma_0^2 \hbar \omega n} (E_L + N \cdot E_C), \quad (2-26)$$

where  $G_S$  is the geometrical structure factor, that of the rectangular, octagonal, and circular spiral inductor are  $1/4\pi$ ,  $3/5\pi$ , and  $1/\pi$ , respectively. Thus, as mentioned in (2-26), the free electron density and conductivity indicated that the inductance shall depend on the characteristics of material and the dimension of the inductors strictly.

## ***2.5 Determination of Boundary Condition Problems Using the Modification of Trajectory Function and the Green's Theorem***

### ***2.5.1 Modification of Trajectory Function***

Both conceptually and physically, the influence from the grounded pad to the interesting system such as a micromachined spiral inductor that will rely on interaction of the

electromagnetic energy (or the potential energy) between them. In most engineering applications, the grounded pad of an on-chip circuitry may closely surround with the system, so that then the effects from the grounded pad cannot be ignored. In this case, detail discussion of the grounded pad issue is presented by resolving the corresponding boundary condition problems. Thus, by comparing the second term of (2-19) with the multipole expansion of the electric energy, it becomes:

$$\left| 2 \int \frac{d^3 r}{r^3} \right| = \frac{2r_{<}^2 r_{>}}{b}, \quad (2-27)$$

where  $b$ ,  $r_{<}$ , and  $r_{>}$  are the distance from the central point of the spiral inductor to the grounded pad edge, the distance from the central point to the innermost edge of the spiral inductor, and the distance from the central point to the outermost edge of the spiral inductor, respectively.

Taking 5- $\mu\text{m}$  thick micromachined freely suspended copper rectangular spiral inductors with restricting their geometric factors as  $l_{max} = 300 \mu\text{m}$ ,  $s = 5 \mu\text{m}$ , and  $\varpi = 15 \mu\text{m}$  and silicon substrate underneath removed as examples, Figure 2-5 shows the relations between equation (2-27) and relative error percentage of self-resonant frequency calculated using (2-16), (2-18) and (2-20). The details will not be discussed here because of the mathematical tools still cannot undertake the requirements of the physical problems. As presented in the presented study [33], the result of model calculation reveals the fact that the inductor can be seen as a freely system while the ground pad far from 60  $\mu\text{m}$  at least.

However, in some practical cases the relation (2-27) cannot provide correct results because of the oversimplified mathematical structure. Generally, the relation constructed by few high order terms of the multipole expansion cannot completely describe the behaviors of electric fields built up within the device structure and correlate the interaction between an arbitrary polygonal inductors and their grounded pad. Thus, it is necessary that to construct a

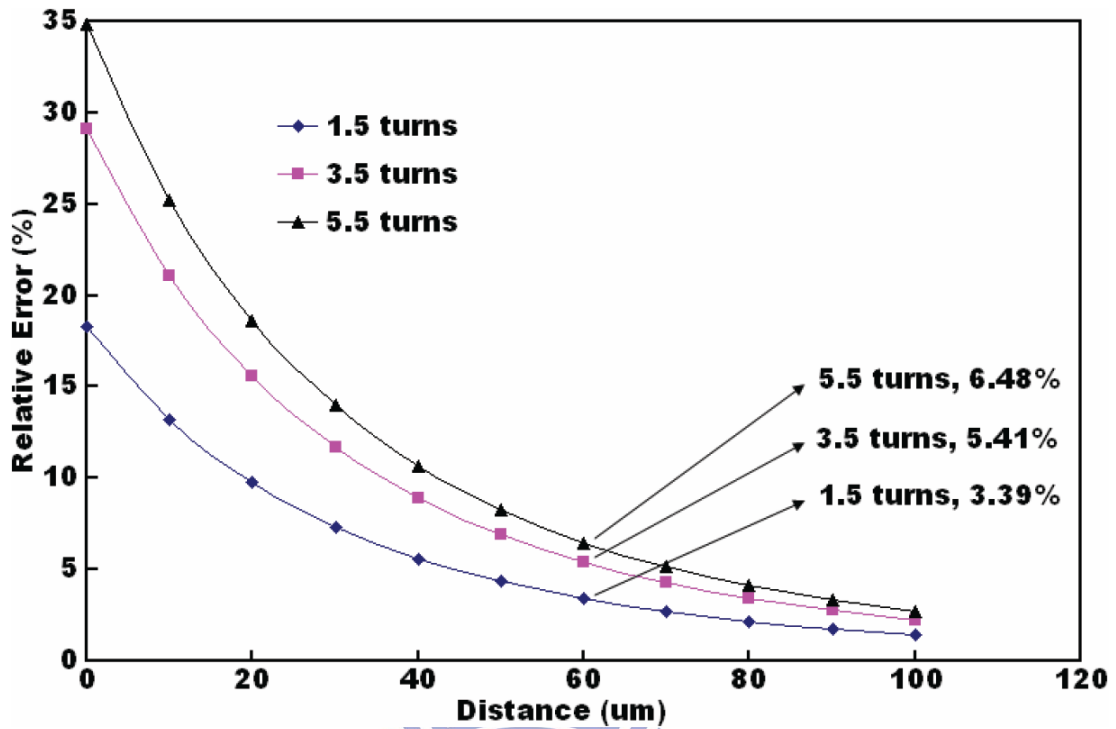


Figure 2-5: Relations between distance from inductor edge to ground pad and relative error of self-resonant frequency.

general coordinate Green's function with the Dirichlet condition to describe the field behaviors in any configuration of the device structures. Unfortunately, it is very difficult to develop the seriously mathematical and physical structures of the general coordinate Green's function. Only few configuration of micromachined polygonal spiral inductor with the associated grounded pad could be definitely constructed mathematically, and we will discuss those structures in the following section. In the drawback like this situation, an approximate method to estimate the field behaviors will help us to understand somewhere the operations of the fields within the structure.

In the next section, the rectangular and circular coordinate Green's functions are respectively developed to resolve the complicated physical and mathematical boundary condition problems resulted by the mentioned micromachined polygonal spiral inductors associated with their grounded pads.

### 2.5.2 The Green's Function Expression and Potential Energy

In order to reveal the issue of interaction from ground pad to the interesting system, to develop a proper Green's function is actually necessary, in which the Dirichlet condition is employed to describe the special situation at boundary surface. Potential energy is then presented to estimate the influence of direction from the ground pad to the spiral inductor edge side. In this section, specified solution of the potential energy will be developed for each polygonal micromachined spiral inductor mentioned above. Starting with the solutions of the potential on the boundary surface by using Dirichlet condition with source free:

$$\Phi_S(\bar{r}) = -\oint_S \Phi_S(\bar{r}') \frac{\partial G(\bar{r}, \bar{r}')}{\partial n'} dS', \quad (2-28)$$

where  $G(\bar{r}, \bar{r}')$  and  $n'$  are the response function or called the Green's function and the normal unit vector on the enclosed surface  $S$ , respectively.

#### 2.5.2.1 The Green's Function with a Rectangular Boundary

First, an expression of potential energy of a rectangular micromachined spiral inductor with a limited-distance grounded plane is derived using the Green's function in Cartesian coordinate, in which original potential of the inductor is set to be  $\Phi_0$ . Starting from the general definition of the Green's function

$$G(\bar{r}, \bar{r}') = G_0(\bar{r}, \bar{r}') + G_i(\bar{r}, \bar{r}') = \frac{1}{4\pi|\bar{r} - \bar{r}'|} + G_i(\bar{r}, \bar{r}'), \quad (2-29)$$

where  $G_0(\bar{r}, \bar{r}')$  and  $G_i(\bar{r}, \bar{r}')$  are the fields generated by the charge sources and induced by the surface charge densities on the surrounding boundary, respectively. Leaving all of the mathematical detail in Appendix A, the potential energy in any observable point outside the spiral inductor and within the grounded pad should be:



$$\Phi_s(\vec{r}) = \frac{\Phi_0}{2\pi} \sum_{\pm, \mp} \left\{ \cot^{-1} \left( \frac{(l_{\max}/2 \pm x)(l_{\max}/2 \pm y)}{z[(l_{\max}/2 \pm y)^2 + (l_{\max}/2 \pm x)^2 + z^2]^{1/2}} \right) + \cot^{-1} \left( \frac{(l_{\max}/2 \pm x)(l_{\max}/2 \mp y)}{z[(l_{\max}/2 \mp y)^2 + (l_{\max}/2 \mp x)^2 + z^2]^{1/2}} \right) \right\} = \frac{\Phi_0}{2\pi} \times G_{\text{rec}} \quad (2-30)$$

Similarly, the self-resonant energy affected by the distance of the grounded pad will be also proportional to the parameter  $G_{\text{rec}}$  in (2-30):

$$\hbar\omega_r' \Big|_{\text{rec}} \propto G_{\text{rec}} \hbar\omega_r = \alpha_{\text{rec}} G_{\text{rec}} \hbar\omega_r, \quad (2-31)$$

where the proportional factor  $\alpha_{\text{rec}}$  should be determined by both the scattering potentials and the resonant factor that after affecting by the grounded pad.

### 2.5.2.2 The Green's Function with a Circular-like Boundary

Assuming that the removed silicon substrate underneath the freely suspended polygonal spiral inductor caused a cylindrical cavity with a radius of  $a$  and a height of  $d$ , on which the radius of the circular-like spiral inductor is  $b$  as shown in Figure 2-6. It is noted that since it is difficult to deal with the boundary conditions of the octagonal spiral inductor, the boundaries of the octagonal and circular inductor were categorized as circular-like problems.

For any point source  $(\rho', \varphi', z')$  inside the cavity, the scalar Green's function satisfies the inhomogeneous equation as follows:

$$\frac{1}{\rho} \frac{\partial}{\partial \rho} \left( \rho \frac{\partial G}{\partial \rho} \right) + \frac{1}{\rho^2} \frac{\partial^2 G}{\partial \varphi^2} + \frac{\partial^2 G}{\partial z^2} = -\frac{1}{\rho'} \delta(\rho - \rho') \delta(\varphi - \varphi') \delta(z - z'), \quad (2-32)$$

where the expansions of the  $\delta(\varphi - \varphi')$  and  $\delta(z - z')$  are as follows:

$$\delta(\varphi - \varphi') = \frac{1}{2\pi} \sum_{m=-\infty}^{\infty} e^{im(\varphi - \varphi')}, \quad (2-33)$$

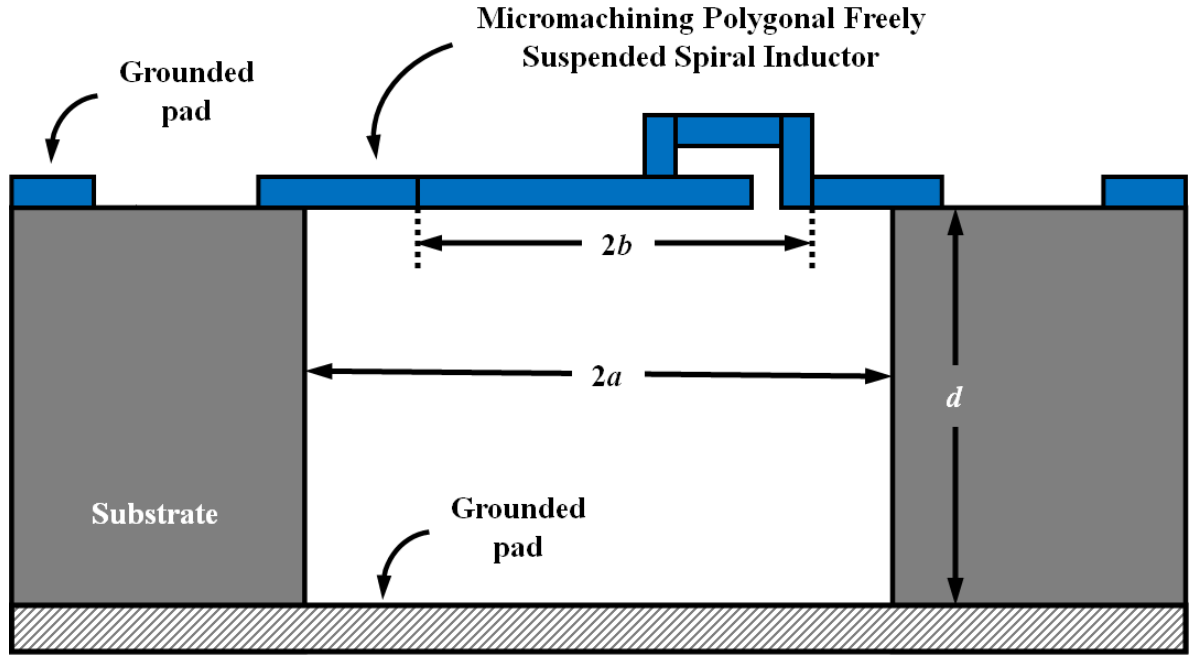


Figure 2-6: Scheme of a circular-like freely suspended spiral inductor under a removed silicon substrate, at which a cylindrical cavity with radius of  $a$  and height  $d$  was formed.

and

$$\delta(z - z') = \frac{2}{d} \sum_{n=1}^{\infty} \exp\left(\frac{n\pi}{d}(z - z')\right). \quad (2-34)$$

Thus, the generalized solution of the Green's function has the form:

$$G(\rho, \rho') = \frac{1}{d\pi} \sum_{m=-\infty}^{\infty} \sum_{n=1}^{\infty} g_{mn}(\rho, \rho') e^{im(\varphi - \varphi')} \sinh\left(\frac{n\pi}{d}z\right) \sinh\left(\frac{n\pi}{d}z'\right). \quad (2-35)$$

Leaving the all mathematical details in the Appendix A again, the special solution of the potential energy is

$$\begin{aligned} \Phi_V(\rho) &= \frac{1}{\varepsilon_0} \int_V G(\rho, \rho') \sigma(\rho') dV' \\ &= \frac{q}{\varepsilon_0 b \pi} \sum_{m=-\infty}^{\infty} \sum_{n=1}^{\infty} \exp\left(\frac{n\pi}{d}(z-d)\right) \times \frac{I_m\left(\frac{n\pi}{d}\rho\right) W_{mn}\left(a, \frac{l_{\max}}{2}\right)}{I_m\left(\frac{n\pi}{d}a\right)}, \\ &= \frac{q}{\varepsilon_0 b \pi} \times G_{\text{Circular}} \end{aligned} \quad (2-36)$$

where  $I_m$  is one of the general solutions of the modified Bessel function and  $W_{mn}$  is a combinational function defined in (A-24). Obviously, once the potential energy with the prescribed boundary conditions is clarified, the changes of the scattering potential at the corners and resonant factor could be quantitatively determined:

$$\hbar\omega_r' \Big|_{\text{Circular}} \propto G_{\text{Circular}} \hbar\omega_r = \alpha_{\text{Circular}} G_{\text{Circular}} \hbar\omega_r. \quad (2-37)$$

Comparisons between the theoretical calculations of the resonant energies affected by changing the distance of grounded pads and simulation results will be derived in next section.

The proportional factors  $\alpha_{\text{rec}}$  and  $\alpha_{\text{Circular}}$  will be also derived by adequately fitting the simulation results.

## 2.6 Model Validation and Discussion

So far, we have developed a method using the Kramers-Kronig relations for metal to character the behaviors of free electrons while the resonant absorption (or anomalous dispersion) occurring. The kinetic energy and scattering potential of the free electrons inside the freely suspended micromachined spiral inductors with silicon substrate underneath removed were calculated to achieve the prediction of the self-resonant frequency of the inductors. The hypothesis regarding the distribution of magnetic energy was presented to estimate the inductances of the polygonal spiral inductors. Furthermore, the grounded pad issue was discussed using the modified trajectory function and the Green's function. All of the significant theories were addressed above in detail. Thus, the further model validation is required to verify the hypothesis and theoretical estimation.

Considering the fabricated structure of a  $5\mu\text{m}$  thick and 3.5 turns freely suspended micromachined copper spiral inductor with silicon substrate underneath removed and

restricting its geometric factors as  $l_{max} = 300 \mu\text{m}$ ,  $S = 5 \mu\text{m}$ , and  $\varpi = 15 \mu\text{m}$ , as shown in Figure 2-7 [34]. It is noted that the rectangular spiral inductor is freely-suspended on the air gap. The substrate effect has been neglected in order to simplify the inductor model. Thus, the further work and simulations will follow this simplification in this chapter. By adding the suitable boundary condition, wave port excitation, and the grounded pad consisted of perfect conductor, the 3D structures of rectangular, octagonal, and circular spiral inductors with substrate removed were built and simulated, and as shown in Figure 2-8, 2-9, and 2-10, respectively.

In the Ansoft-HFSS simulator [35], the radiation boundary condition presents the surface that the electromagnetic wave can pass through from the region of the existence of the device

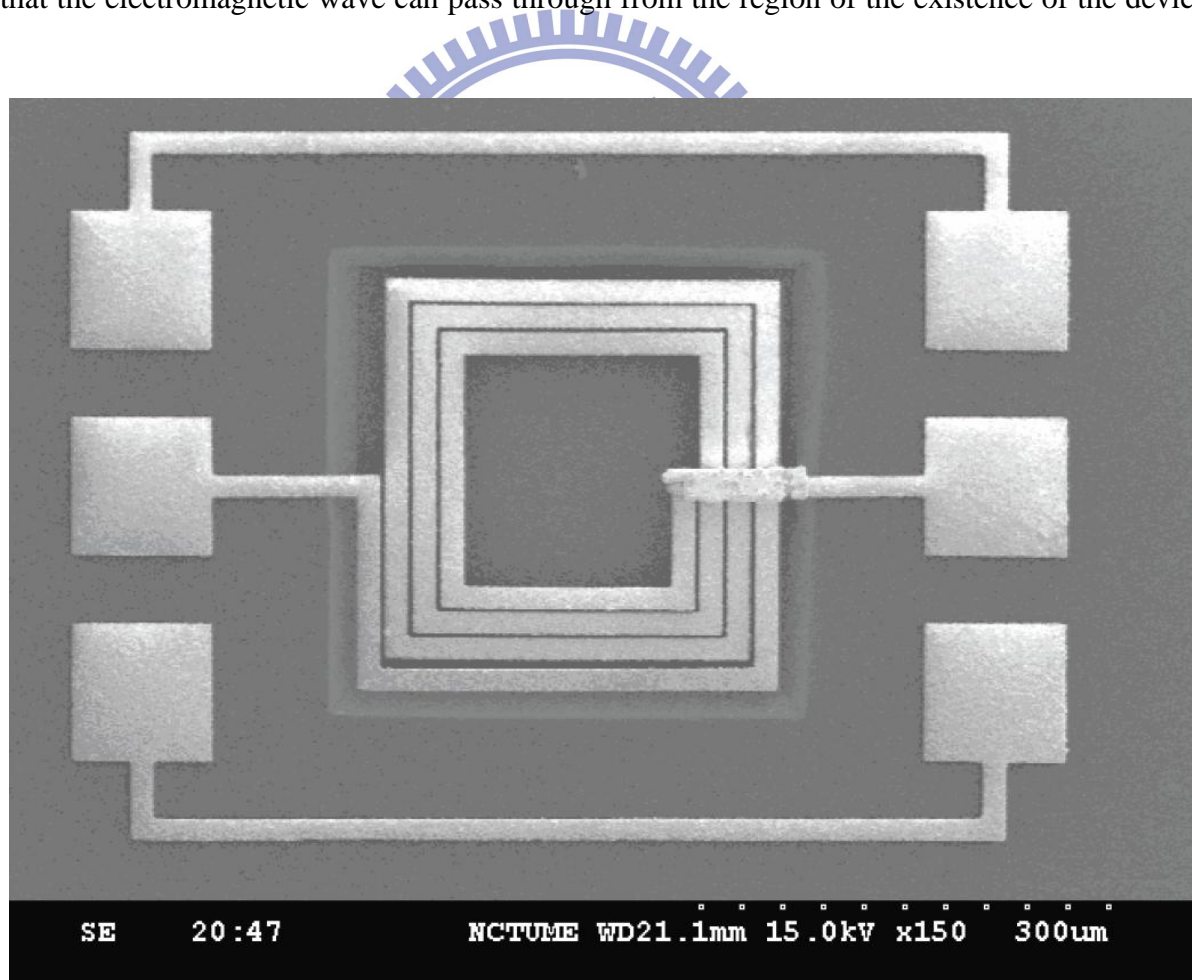


Figure 2-7: Scheme of a freely suspend micromachined rectangular spiral inductor with silicon substrate underneath removed and restricting its geometric factors as  $l_{max} = 300 \mu\text{m}$ ,  $S = 5 \mu\text{m}$ , and  $\varpi = 15 \mu\text{m}$  [34].

to the outer region but in the opposite direction. The default boundary, however, means that the electromagnetic wave may be reflected from the external region and enter the inner region. The excitation of the simulation is defined by adding semi-infinite long wave guides, wave ports and impedance lines, which are pointed from the grounded pad to one side of the wave port, on the two terminals of the spiral inductors. The employing wave guides are consisted of perfect conductors in which the skin effect may not be considered, thus the propagated electric and magnetic fields are perpendicular to the surface of the strip. In addition, the whole device is included into box, as shown associated with Figure 2-8, 2-9, and 2-10 in the right-lower corners, in which the radiation boundary condition is adopted and is filled by air.

In general, it is difficult but important to construct the step of the port-source and boundary condition for the micromachined inductors. The distance between the boundary condition and the center of inductor was set up as twelve times of the dimension of inductor. In addition, the ground-signal-ground pads, as shown in Figure 2-8, were attached to the terminals of inductor as measured pads. The scale of two square wave ports is about eight

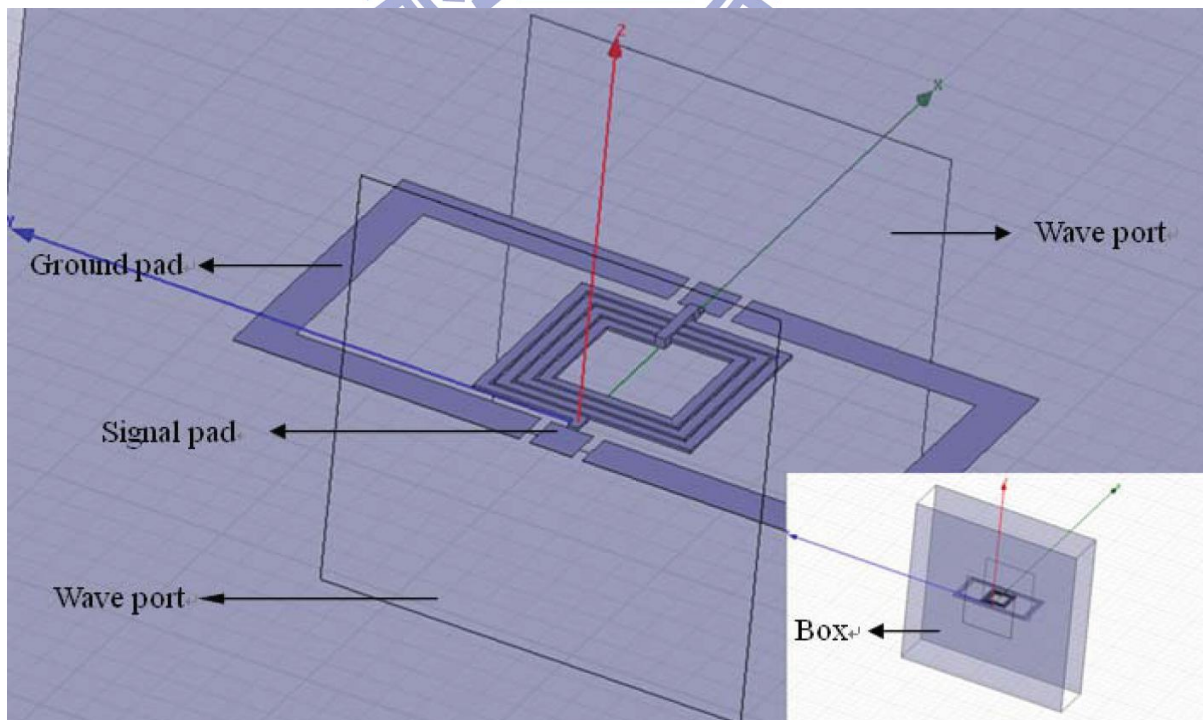


Figure 2-8: Scheme of rectangular spiral inductor with substrate removed.



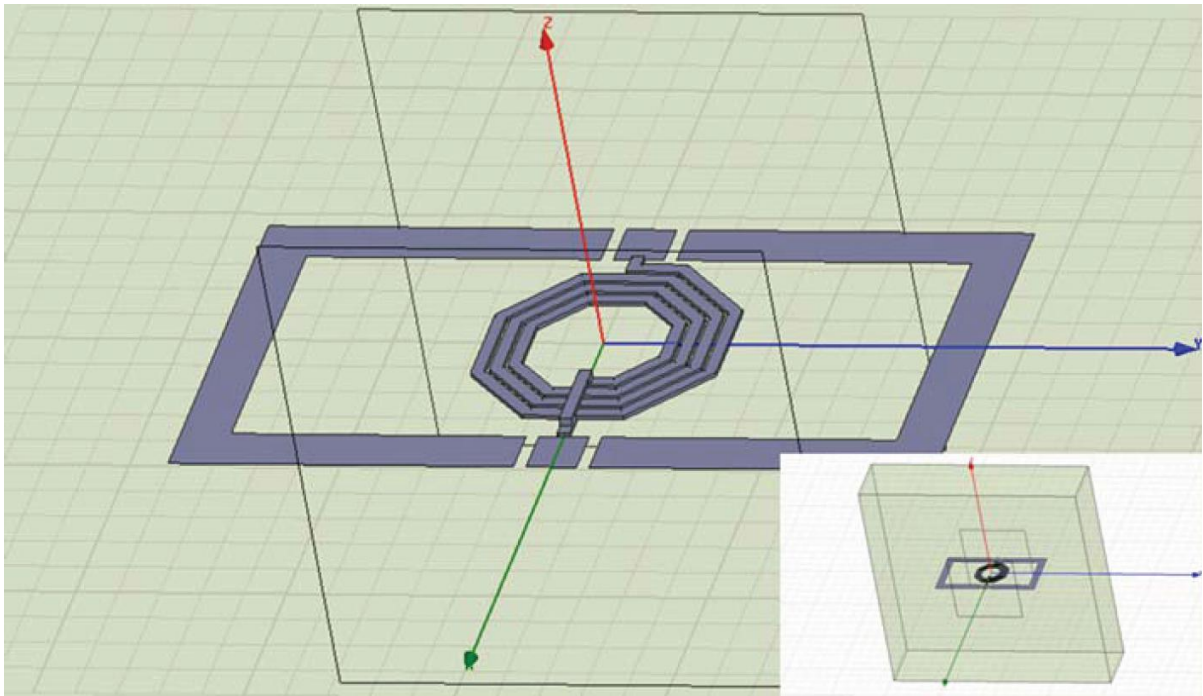


Figure 2-9: Scheme of octagonal spiral inductor with substrate removed.

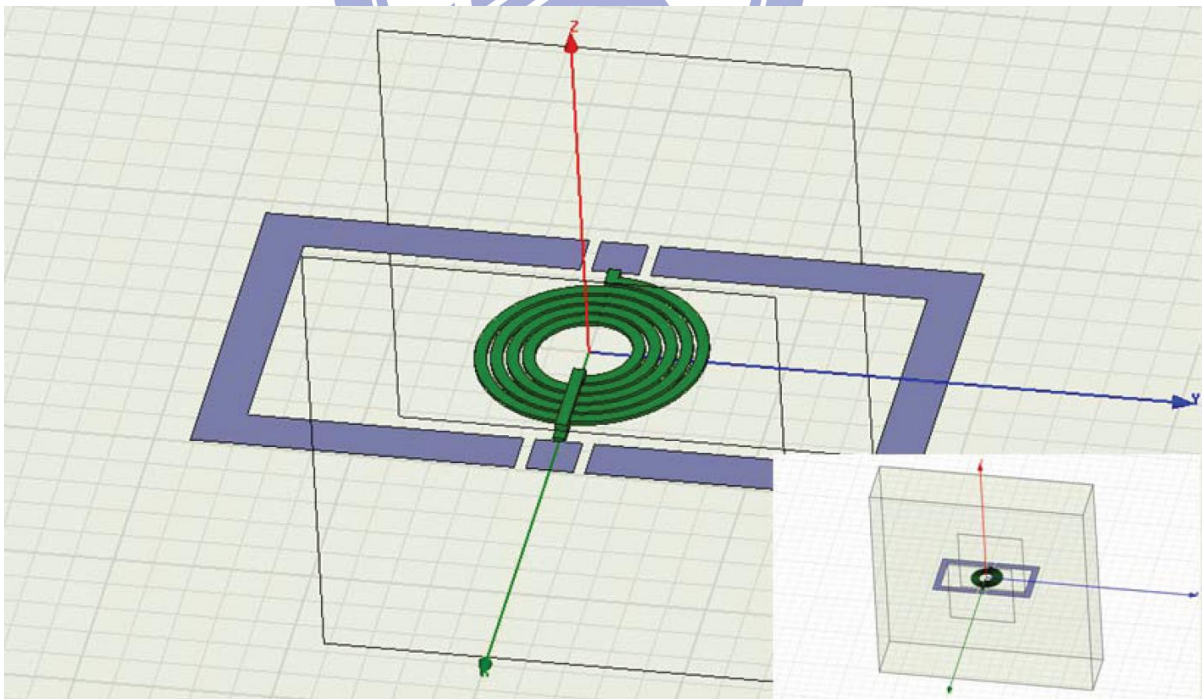


Figure 2-10: Scheme of circular spiral inductor with substrate removed.

times of the width of signal pads [36]. The results of modeling extracted from Ansoft-HSFF simulator will be de-embedded on the S-parameters.

The self-resonant frequencies of rectangular, octagonal, circular inductors could be predicted well by means of utilizing developed theoretical equations, and the values are shown in Table 2-1. Then, we could determine the required inductances at particular frequency using (2-26) for rectangular spiral inductor and the values are listed as in Table 2-2. In Table 2-1 and 2-2, our model is examined by comparing with the contemporary

Table 2-1  
Self-Resonant Frequency with Different Type of Inductors

Comparisons (n=3.5)	Self-resonant frequency based on our model (GHz)	Self-resonant frequency based on HFSS (GHz)
Rectangular inductor	23.9	22.9
Octagonal inductor	24.9	23.6
Circular inductor	25.8	24.6



Table 2-2  
Comparison Results of the Rectangular Spiral Inductor

Number of Turns Comparisons (n)	1.5	2.5	3.5	4.5	5.5
$\omega_r$ for HFSS (GHz)	39.5	27.1	22.9	20.6	19.4
$\omega_r$ for K. K. model (GHz)	38.6	28.6	23.9	21.4	19.9
$\omega_r$ for Greenhouse (GHz) based model	X	X	X	X	X
$L$ for HFSS @ 3GHz (nH)	1.58	2.94	4.27	5.31	6.01
$L$ for K. K. model @ 3GHz (nH)	1.18	2.65	4.13	5.32	5.95
$L$ for Greenhouse based model @ 3GHz (nH)	1.60	3.02	4.28	5.18	5.60
$L$ for HFSS @ 5GHz (nH)	1.58	2.99	4.38	5.49	6.21
$L$ for K. K. model @ 5GHz (nH)	1.19	2.71	4.25	5.51	6.20
$L$ for HFSS @ 9GHz (nH)	1.63	3.22	4.92	6.31	7.23
$L$ for K. K. model @ 9GHz (nH)	1.24	2.91	4.74	6.33	7.30



calculations including the results derived from Greenhouse based model [19] and Ansoft-HFSS simulator, respectively. A good S-parameter match between the measurement and HFSS simulation in a Smith chart which is shown in Figure 2-11 [4] presents the fact that the accuracy of the HFSS analysis listed in Table 2-1 and 2-2 is experimentally validated. It is noted that Greenhouse-based model does not provide the frequency dependence of the inductance. The symbol, X, used in Table 2-2 means it does not be available. The material utilized here is copper with the properties of  $n_e = 8.45 \times 10^{28} \text{ m}^{-3}$ ,  $m_e = 9.11 \times 10^{-31} \text{ kg}$ , and  $\sigma_0 = 5.6 \times 10^7 (\text{m}\Omega)^{-1}$ .

The inductance expression based on this model is closely fitted with the simulation and experimental data for the structure of the spiral inductor with substrate removed. The above

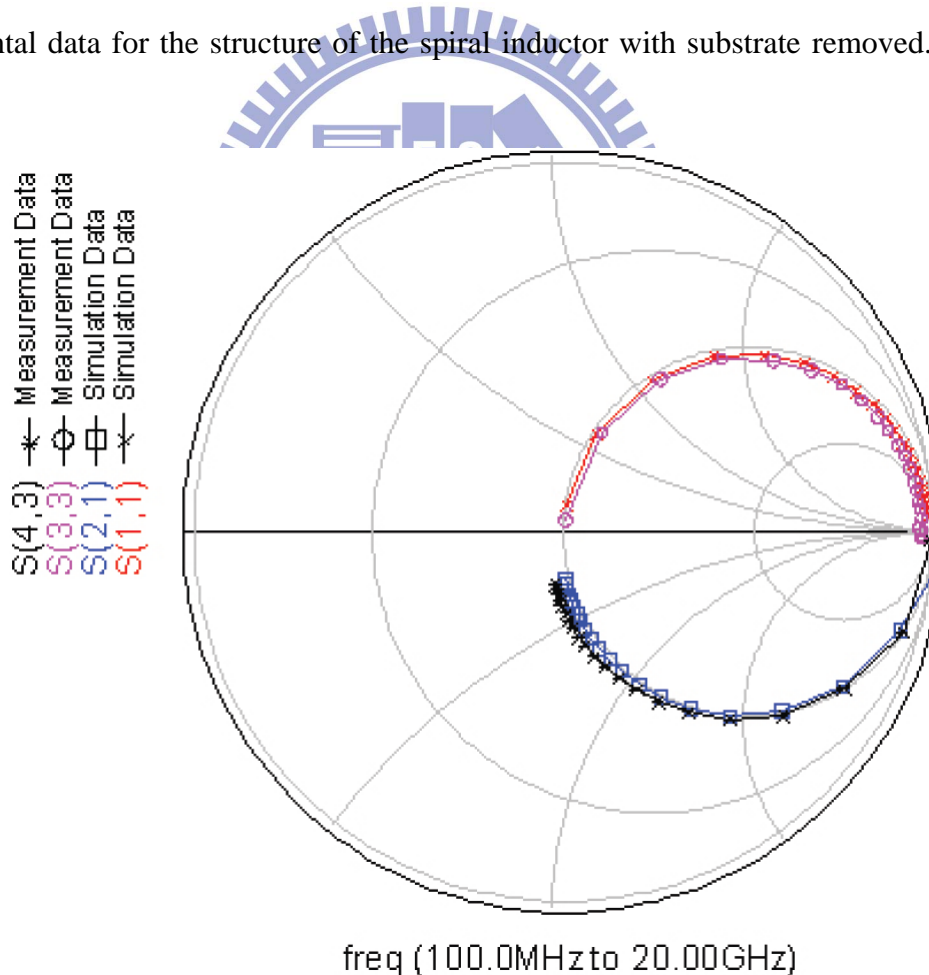


Figure 2-11: Smith chart in which a good s-parameter match between measurement and simulation is present [4].

table also indicated that the greenhouse model does not provide the self-resonant frequency itself and cannot determine the frequency-dependent inductances. The comparison of rectangular, octagonal, and circular inductance spectra are shown as Figure 2-12, 2-13, and 2-14, respectively. Note that again this inductor model could predict the self-resonant frequency and inductance of an on-chip freely suspended spiral inductor, so that the circuit designers and engineers could easily satisfy their requirements by means of modifying the geometry and material parameters in priori design stage. The analytical method based on Kramers-Kronig relations, EM field theory and solid state physics could provide us mathematically convenience for the passive design in view of physical senses.

When the grounded pad effects are considered, the developed green's function provides an alternative method to deal with the interaction between the stored energy, resonant factor, and the distance from the pads. Figure 2-15 shows the comparisons between the theoretical calculations using Green's function in Cartesian coordinate and HFSS simulations. Significant differences at the short distance from the grounded pad to the edge of the inductor

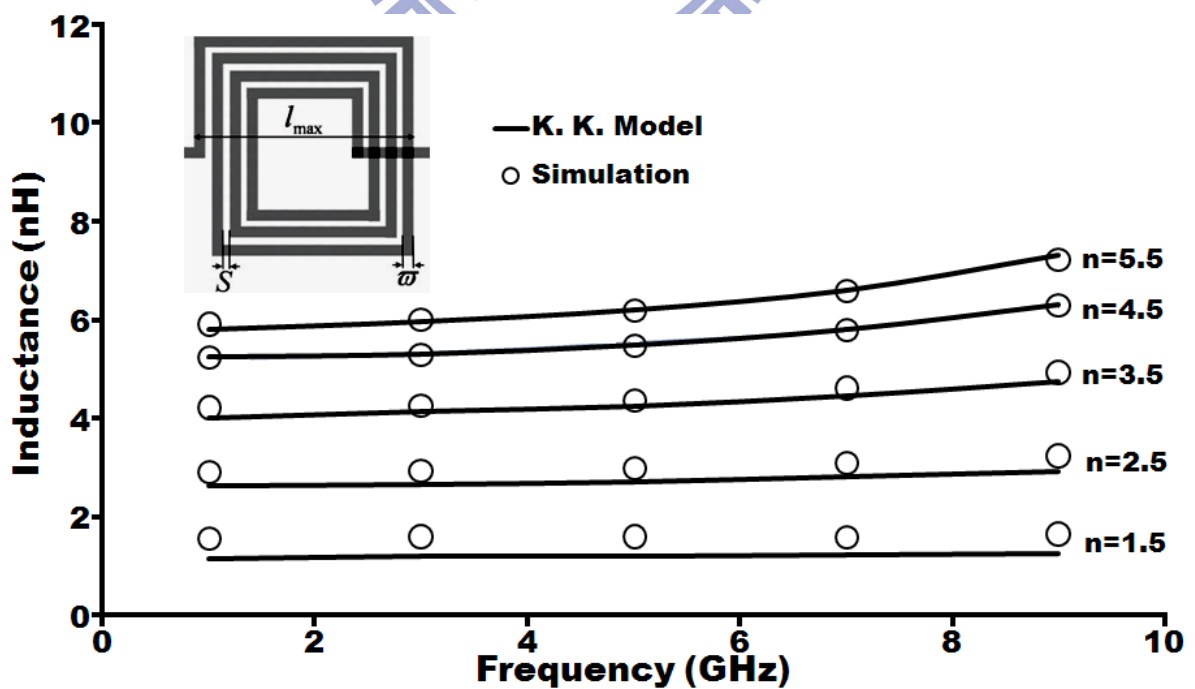


Figure 2-12: Comparison of inductance spectrum of rectangular spiral inductors and results of simulation.

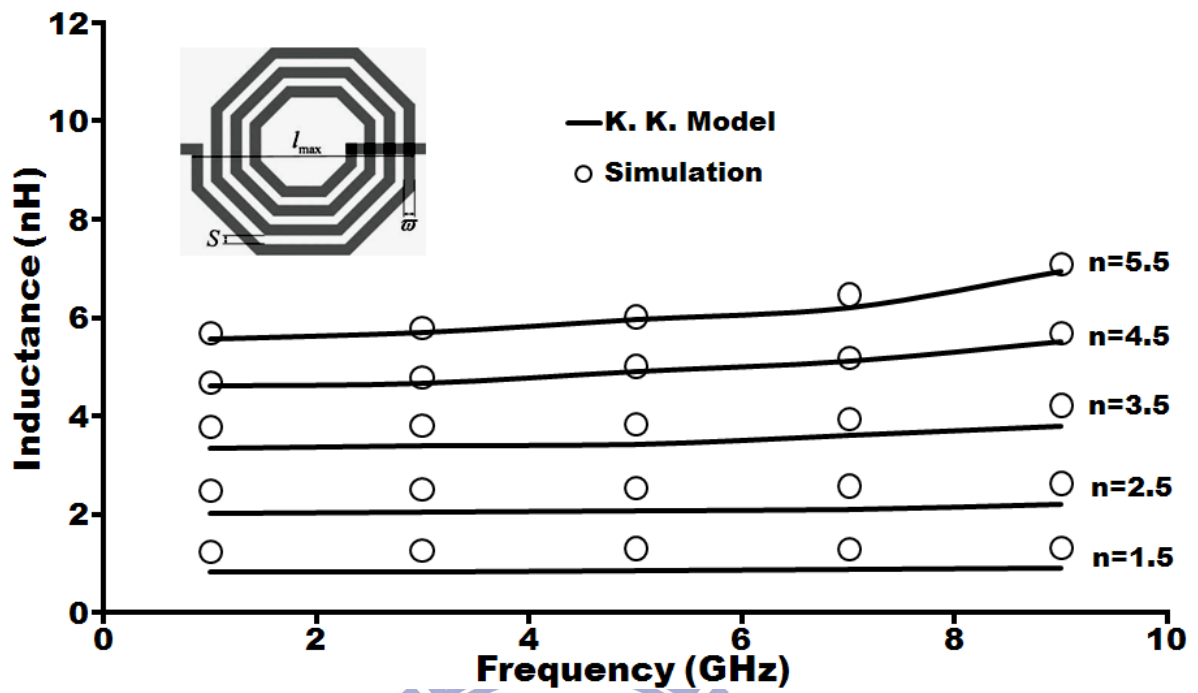


Figure 2-13: Comparison of inductance spectrum of octagonal spiral inductors and results of simulation.

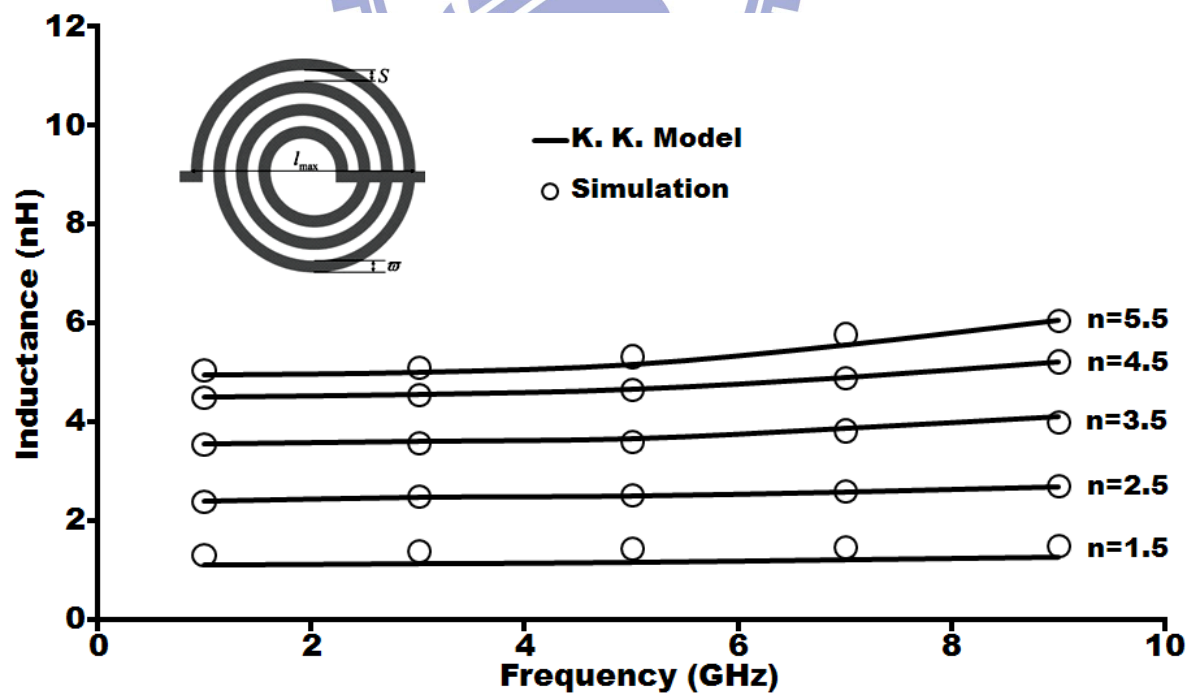


Figure 2-14: Comparison of inductance spectrum of circular spiral inductors and results of simulation.

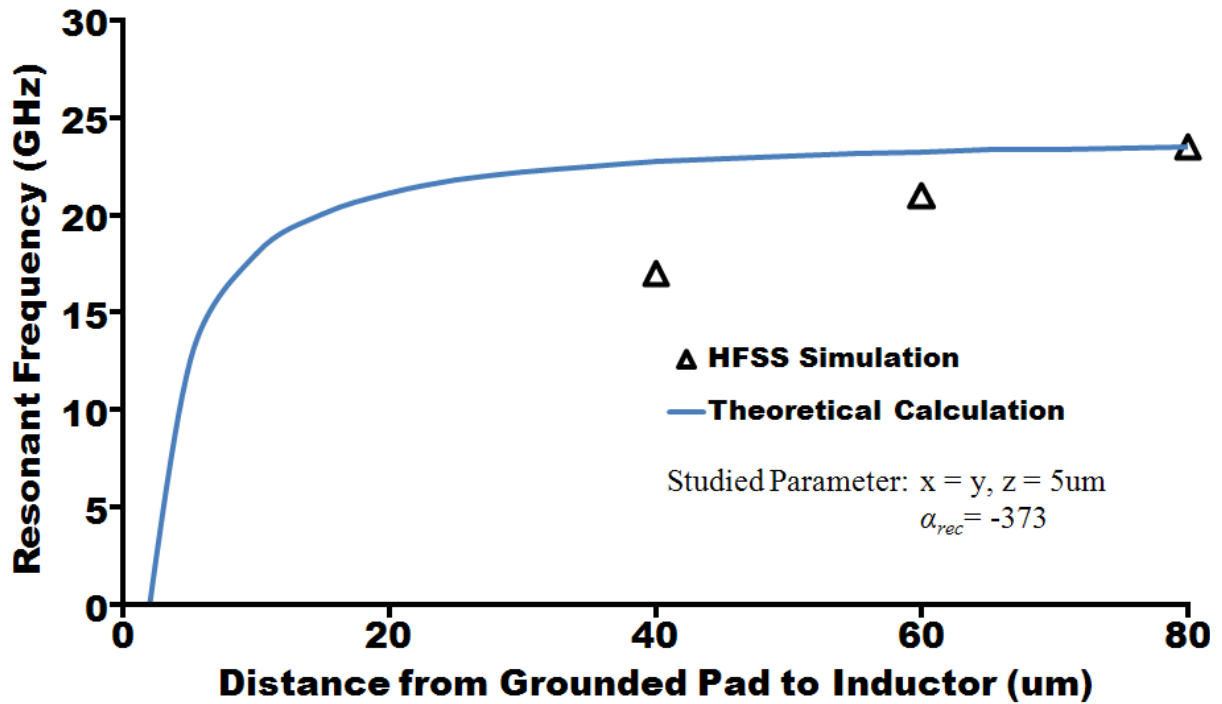


Figure 2-15: Comparison between the theoretical calculations using Green's function in Cartesian coordinate and HFSS simulations.

indicate the oversimplification of the mathematical approaches of the Green's function in steady state and the requirement of twofold-symmetry in x- and y-directions. Additionally, the value of the proportional factors  $\alpha_{rec}$  used in fitting the curve to the simulation results could not be entrusted in terms of the related physical meaning and derivation so far, and it shall be pursued as well as the frequency-dependent Green's function in future work. The resonant energy becomes zero before achieving edge of the inductor might be deduced to the dramatically near-field interactions.

## 2.7 Optimization of a MEMS Spiral Inductor

### 2.7.1 Kinetic Energy, Scattering Potential, and the Kramers-Kronig Relations

Recalling and combining the derived equations of the kinetic energy, scattering potential, and the resonant factor employed in the Kramers-Kronig relations, the expression of the

frequency-dependent inductance of a freely suspended micromachined polygonal spiral inductor can be remarked as:

$$L = G_S \cdot \chi_d \frac{n_e l_{total}^3}{\sigma_0^2 A n} (E_L + N \cdot E_C), \quad (2-38)$$

where

$$\chi_d(\omega) = \mu_0 \frac{3n_e \mu_B^2 \omega_r}{2\hbar(\omega_r^2 - \omega^2)} = \frac{3n_e \mu_B^2}{2\hbar^2(\omega_r^2 - \omega^2)} (E_L + N \cdot E_C), \quad (2-39)$$

$$E_L = \sqrt{\frac{3}{5}} \frac{\hbar^2}{m_e} (3\pi^2 n_e)^{1/3} \frac{\pi}{l_{total}}, \quad (2-40)$$

and

$$E_C = \begin{cases} \frac{e^2}{16n\pi V^{2/3} \sqrt{\omega} \hbar \sigma_{eff}} \frac{\left(\pi + 8 \sin \frac{\pi^2}{4\beta}\right)^2}{8\beta(\pi + \beta)} \csc^2\left(\frac{\pi - \beta}{2}\right), & \text{for } \beta < \pi \\ \frac{e^2}{16n\pi V^{2/3} \sqrt{\omega} \hbar \sigma_{eff}} \frac{\left(\pi + 4\sqrt{2}\right)^2}{4\pi} \frac{\pi}{2.7}, & \text{for } \beta = \pi \text{ (circular inductor)} \end{cases}. \quad (2-41)$$

Thus, the expression of the inductance eventually can be expressed as:

$$\begin{aligned} L &= \mu_0 \cdot G_S \frac{3\mu_B^2 n_e^2 l_{total}^3}{2\hbar^2(\omega_r^2 - \omega^2) \sigma_0^2 A n} (E_L + N \cdot E_C)^2 \\ &= \mu_0 \cdot G_S \cdot \frac{3\mu_B^2 n_e^2 l_{total}^3 (\hbar \omega_r)^2}{2\hbar^2(\omega_r^2 - \omega^2) \sigma_0^2 A n} \end{aligned} \quad (2-42)$$

In order to achieve optimization of the inductor model in microsystems, the dispersion relation of the inductor in frequency domain should be carefully considered in both views of material and geometrical properties.

- (1) For the case of extremely low operating frequency,  $\omega \ll \omega_r$ , (2-42) can be further simplified as:

$$L \approx \mu_0 \cdot G_s \cdot \frac{3\mu_B^2 n_e^2 l_{total}^3}{2\hbar^2 \sigma_0^2 A n} \quad (2-43)$$

Thus, the expression of the frequency-dependent inductance is retrograded as a simple constant in terms of specified material and geometrical properties. In view of the geometrical properties, the inductance in the low operating frequency region is proportional to  $G_s \frac{l_{total}^3}{nh\omega}$ , in which the total length of the metal line highly dominates the inductance. On the other hand, in view of the material properties, the inductance is proportional to  $\mu_0 \frac{n_e^2}{\sigma_0^2}$ . It is worthy to emphasized that the term  $\frac{n_e^2}{\sigma_0^2}$  can be

modified as  $\left(\frac{\tau_r}{m_e e^2}\right)^2$  using the definition of conductivity in metal, thus the inductance can be proportional to  $\mu_0 \tau_r^2$ , in which the relaxation time should be expressed as that time of those free electrons under the Fermi surface between each collision.

- (2) While the operating frequency approaches the self-resonant frequency but still lower than the frequency, the expression of the inductance has been derived as (2-42), the most complicated circumstance. Even though the inductance is proportional to  $G_s \frac{l_{total}^3}{nh\omega}$  as the behavior in extremely operating frequency region, the proportional relation  $\mu_0 \frac{\tau_r^2}{(1-\omega^2/\omega_r^2)}$  in high frequency region in view of the material properties is somehow complicated and will diverge when the two frequencies are the same. In the circumstance, the interchange of the magnetic and electric energies occurs in the spiral inductor as well as the resonant absorption of the interchange energies by the electrons.
- (3) After the operating frequency beyond the self-resonant frequency, the magnetic energy is totally transformed to the electric energy and the inductor becomes a

capacitor-like component. Thus, all incident electromagnetic energy is interchanged to electric energy and stored inside the inductor.

In order to achieve the optimization of the inductor model, the parameters employed in the model are clarified in both views of geometrical and material properties in frequency region. Three main parameters, total length of the metal line, relaxation time of the free electrons, and permeability should be adopted to realize the optimization of the model. It should be also reminded that the total length of the metal line is still limited by maximum edge length as shown in Figure 2-3 in fabrication. Additionally, the effects caused by enhancement of the permeability and patterned dielectric support for the spiral inductor by means of increasing the magnetic energy and rigidity of the structure of the freely suspended micromachined inductor will be clarified in following sections and Chapter 3, respectively. A flow chart shown in Figure 2-16 presents the steps to optimize the inductor model.

### 2.7.2 *Spiral Inductors with Magnetic Nano-Composited Material*

Obviously, the inductance is directly proportional to both the magnitude of magnetic energy and electric current. However, increasing electric current to enlarge the inductance is not a suitable approach for low-power requirement due to the formation of larger joule heating loss occurring within the metal lines [37]. An alternative approach is to introduce the composited nano-magnet-particles with high saturated magnetization ( $M_s$ ) like NiFe, CoNbZr, and  $\text{SrO}_6\text{Fe}_2\text{O}_3$  for creating large magnetic field to enhance the relative permeability of the pure Cu spiral inductors [38]. The simplest way to realize the enhancement of the inductance is to utilize conductive magnetic nano-particles for the inductor fabrication like NiFe permalloy, however, inevitable high resistivity ( $\sim 1.5 \times 10^{-5} \Omega\text{-cm}$ ) still results in large joule heating loss which deteriorates the performance of micromachined spiral inductor for low-power applications. Fortunately, the selection of suitable conductive magnetic



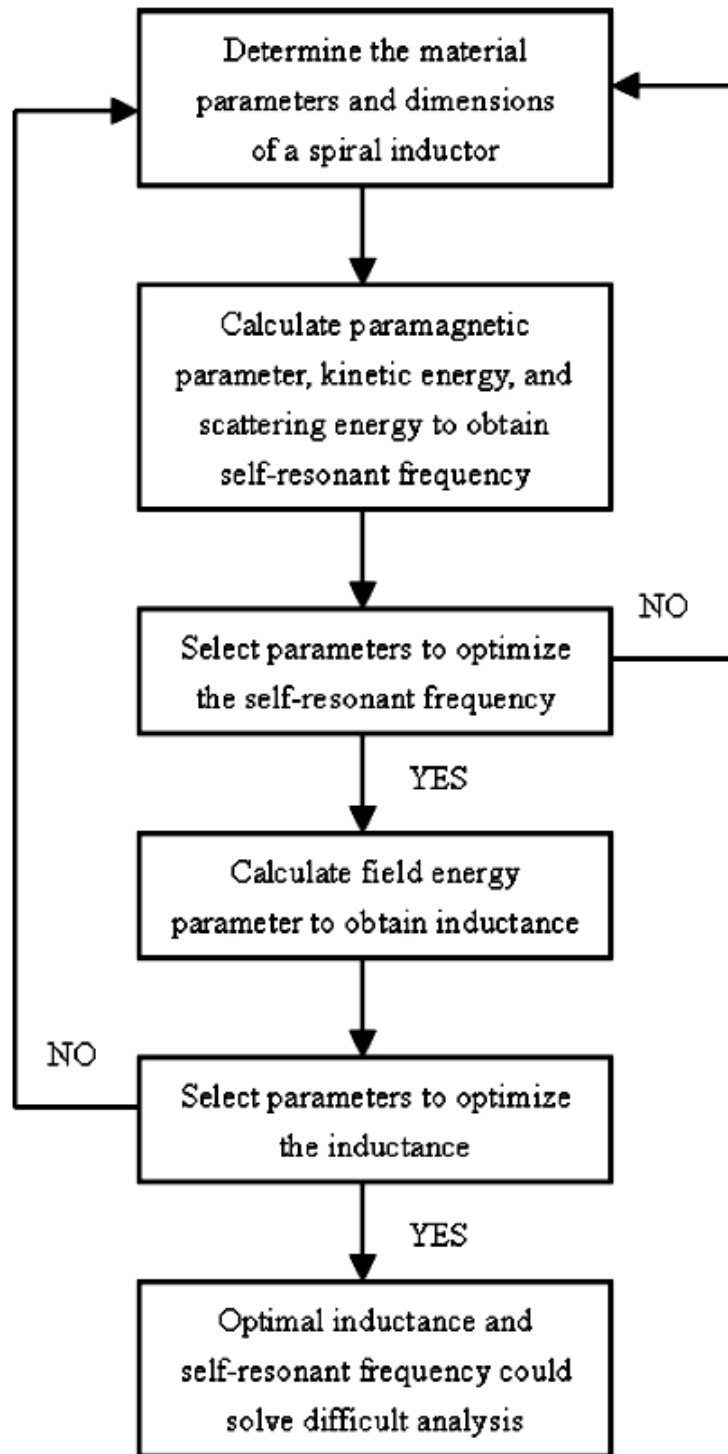


Figure 2-16: A flow chart presents the step to optimize the inductor model.

nano-particles could be achieved by means of the Maxwell Wegner equation, which is based on the model of two-phase random network and can provide good estimation and the electric conductivity of the nano-composited spiral inductor [39]. The Maxwell Wegner equation can

be calculated as the following:

$$k_c = k_m \frac{1 + 2V_f (1 - k_m/k_d)/(1 + 2k_m/k_d)}{1 - V_f (1 - k_m/k_d)/(1 + 2k_m/k_d)}, \quad (2-44)$$

where  $k_c$ ,  $k_d$ , and  $k_m$  are the electrical conductivities of the composite film, embedded secondary phase, and metal matrix, respectively, and  $V_f$  is the volume fraction of the embedded secondary phase. Meanwhile, from the rule of mixture [40], the induced magnetic moment of composite ( $M_i$ ) due to the incorporation of magnetic particles into Cu matrix can be simply estimated based on the intrinsic induced magnetic moment and the weight ratio of the magnetic particle and Cu.

$$M_i = M_c W_c + M_m W_m \quad (2-45)$$

where  $W_m$ ,  $W_c$ ,  $M_m$ , and  $M_c$  represent the weight percents and induced magnetic moment of the incorporated particle and metal matrix, respectively. Thus, according to (2-44) and (2-45), to adequately choose a composite material with large  $M_i$  and  $k_c$  can not only effectively reduce the power consumption within the spiral inductor, but also enhance the magnetic energy as well as the inductance of the MEMS passive component. Therefore, a Cu-Ni nanocomposite is proposed and synthesized here to realize the goal of enhancement of inductance of the micromachined spiral inductor. Instead of the aforementioned  $\text{CoFe}_2\text{O}_4$  or other ferromagnetic materials, Ni powders are chosen for having a nice ratio of  $k_m$  to  $k_c$  for better power efficiency since Ni has lower electrical resistivity than NiFe.

Since the dimension of the Ni particle in our case approached the critical radius of single magnetic domain, we can estimate the susceptibility by adapting the Barkhausen Effect [41]. By quantum statistical mechanics, the variation of free energy could be:

$$\frac{\partial F}{\partial x} = \frac{\gamma}{a^2} \frac{\partial S}{\partial x}, \quad (2-46)$$

where  $a$ ,  $S$ , and  $\gamma$  are the mean distance of each Ni particles, area of domain wall, and energy

density of domain wall, respectively. Thus, we can obtain the relation between mean applied field ( $H$ ) and magnetic strength ( $M_S$ ) with the associated variation of free energy

$$\langle H \rangle = \left\langle \frac{1}{2\mu_0 M_S} \left( \frac{\partial F}{\partial x} \right)_{\max} \right\rangle = \frac{3\gamma}{4\mu_0 M_S} \frac{a}{r^2} (1-n), \quad (2-47)$$

where  $r$  and  $n$  are the radius and the volumetric density of Ni particle, respectively. Thus, the mean susceptibility of Ni particle could be defined as:

$$\langle \chi \rangle = \left\langle \frac{M}{H} \right\rangle = \left\langle \frac{2M_S a S}{H} \right\rangle = \frac{6}{1-n} \left( \frac{r}{R_C} \right)^2, \quad (2-48)$$

where  $R_C$  and  $M$  are the critical radius of Ni particle and variation of magnetic. The susceptibility, therefore, could be estimate with the experimental result of  $r$  (=48nm),  $R_C$  (=41nm), and  $n$  (=1%) [42], that is,  $\chi = 8.31$ . Thus, it means relative permeability  $\mu_r$  is about 9.31, which is very close to the measured result of relative research work using SQUID [43].

Eventually, the theoretical calculations above definitely clarify the method of increasing the relative permeability as well as the inductance of a passive nano-composited microsystem. However, according to the developed (2-42) or (2-43), the risk of decrease of the relaxation time as well as the inductance due to the increasing scattering rate between the electrons and nano-particles should be undertaken in the MEMS passive nano-composited component.

## 2.8 Summary

In this chapter, a closed-form integral model is presented for the polygonal micromachined spiral inductor. The Kramers–Kronig relations provide an elegant theory to describe the inductor behavior without having complicated geometric analysis. A mathematical approach based on the Kramers-Kronig relations was then presented to

characterize electron behaviors within the polygonal micromachined spiral inductors in which self-resonance occurs. Combining with the concepts of anomalous dispersion, standing wave, and field scattering, the self-resonant frequency of the microinductors can be calculated by means of an associated analytical model. According to this model the self-resonant frequency can be derived as the “free electron” frequency of the inductor material. Simulation and measurement results validate that the model can provide satisfactory prediction to the inductance of on-chip freely-suspended spiral inductors. Meanwhile, unlike conventional Greenhouse-based formulations, the self-resonant frequency of inductor can be predicted using the integral model.



## ***Chapter 3 A Patterned Dielectric Support for High Performance MEMS Passive Component***

### ***3.1 Introduction***

Inevitable substrate loss is one of the major issues which need to be resolved in the development of CMOS-based RFIC technology for high frequency wireless communication applications. The silicon substrate loss could result in a poor circuit performance in terms of smaller dynamic range, high noise figure, and larger power consumption. Several successful investigations [44-48] have been presented to resolve the substrate loss issue, such as proton implantation, patterned ground shield, silicon trenched islands and nitride blocks, and cross membrane support. Nevertheless, while the operational frequency of circuitry approaches to or even beyond 10 GHz, only the membrane support with substrate removal and proton implanting methods can effectively eliminate the loss issue. The risks of process compatibility, unstable mechanical structure, and low reliability, however, should be undertaken.

Therefore, in the chapter, a tentative copper coplanar waveguide (CPW) directly electroplated on a silicon substrate with patterned oxide/nitride fins is utilized to demonstrate the proposed patterned dielectric support process for the fabrication of passive components with better signal isolation, structural reliability, and process practicality than those aforementioned methods. Significant air gap spacing between neighbor fins can adequately avoid the substrate loss for better transmission line performance at very high operational frequencies. Figure 3-1 shows a comparison of experimental results between the losses of CPWs deposited on oxide/nitride fins and that on conventional silicon based substrate. More than 12.40dB/cm improvements of  $S_{21}$  for the CPWs are demonstrated.

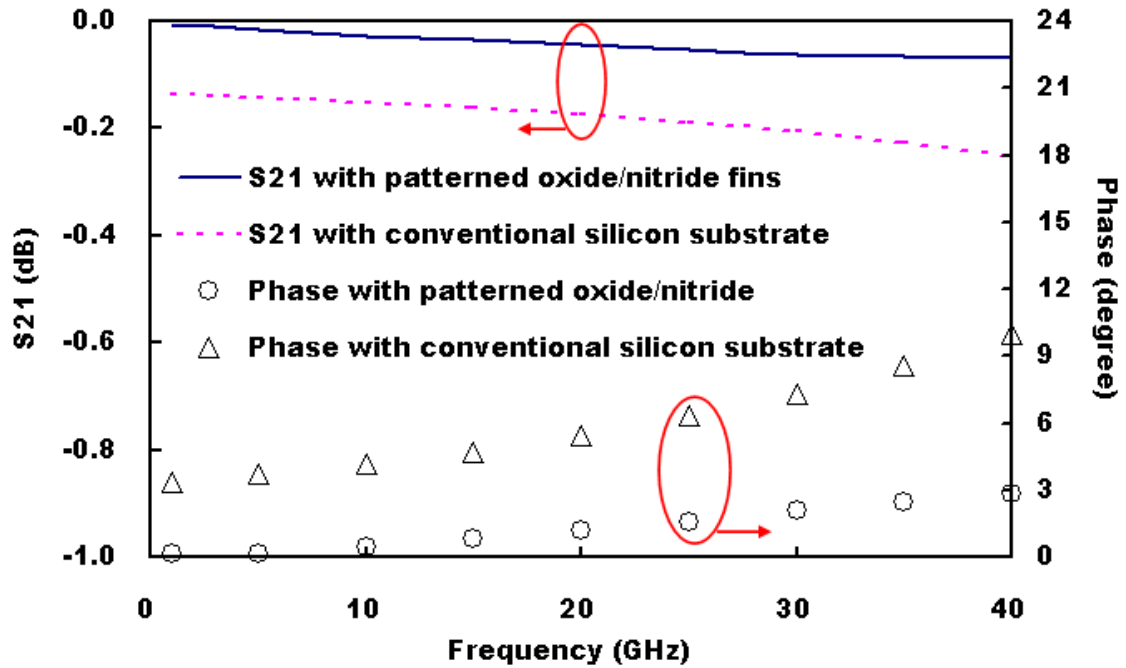


Figure 3-1: Comparison of experimental results between the losses of CPWs fabricated with and without oxide/nitride fin support on a conventional silicon substrate. The dimensions of CPW: 60 $\mu$ m strip width, 5 $\mu$ m thick, 150 $\mu$ m long and 12 $\mu$ m slot width. Both structures have the same dimensions.



### 3.2 Fabrication of Patterned Dielectric Fin-Support

Figure 3-2 shows the fabrication process flow of patterned nitride/oxide/nitride/air fins on which a CPW is deposited. 5- $\mu$ m wide silicon deep trenches with 10:1 aspect-ratio are first formed by ICP-DRIE followed by 1.5 $\mu$ m thick thermal oxidation at 1100 $^{\circ}$ C. After the removal of upper oxide layer by RIE, the residual silicon of the silicon-oxide fins is etched using ICP-DRIE again. The oxide fins are then coated with 1.5- $\mu$ m thick LPCVD silicon nitride. Once the patterned dielectric supporting structure, nitride/oxide/nitride/air fins, is made, a 90-nm Cu/10-nm Ti seed layer is then deposited for following CPW fabrication and afterwards a 5- $\mu$ m thick Cu layer is electroplated to form the CPW as shown in Figure 3-3.

Due to the hydrophilic property of metal seed layer, Cu will be electroplated into the sidewall of fins to form acicular Cu stalactites resulting in un-anticipated characteristic

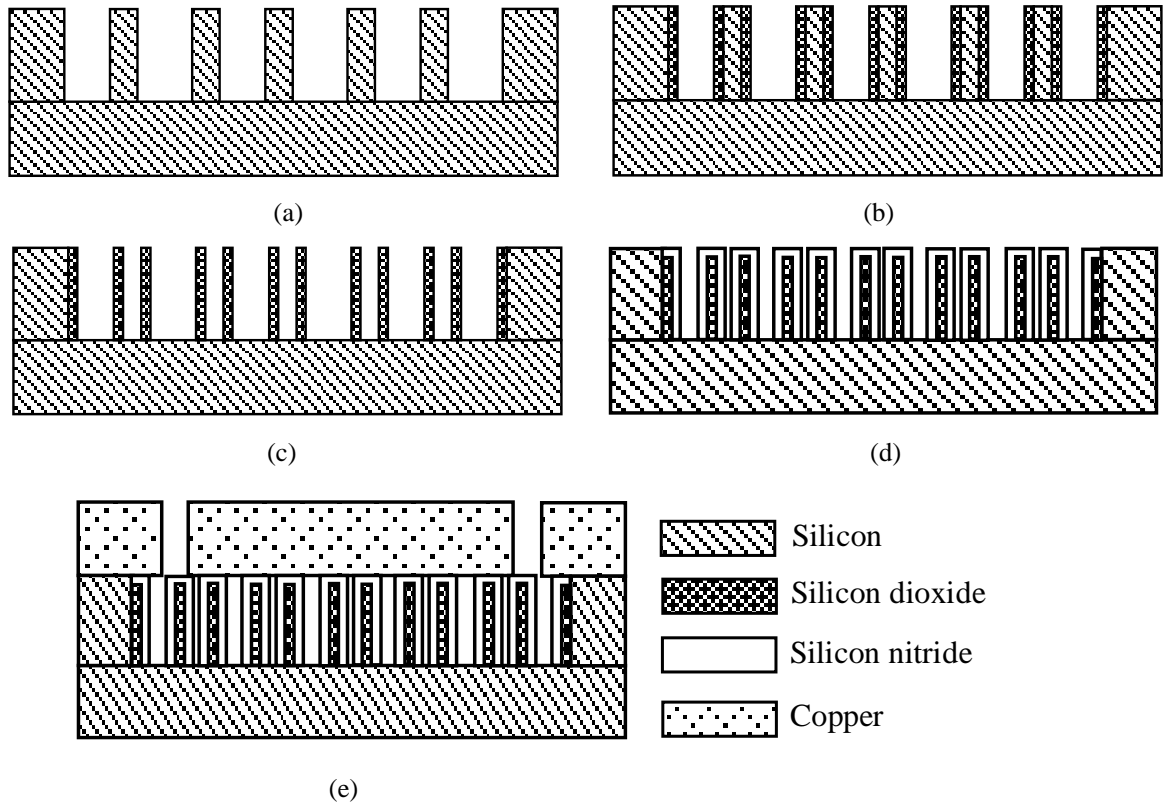


Figure 3-2: Fabrication process flow: (a) Deep silicon trench etching, (b) thermal oxide growth and top oxide removal, (c) ICP resident silicon etching, (d) LPCVD nitride deposition, and (e) CPW electroplating [49].

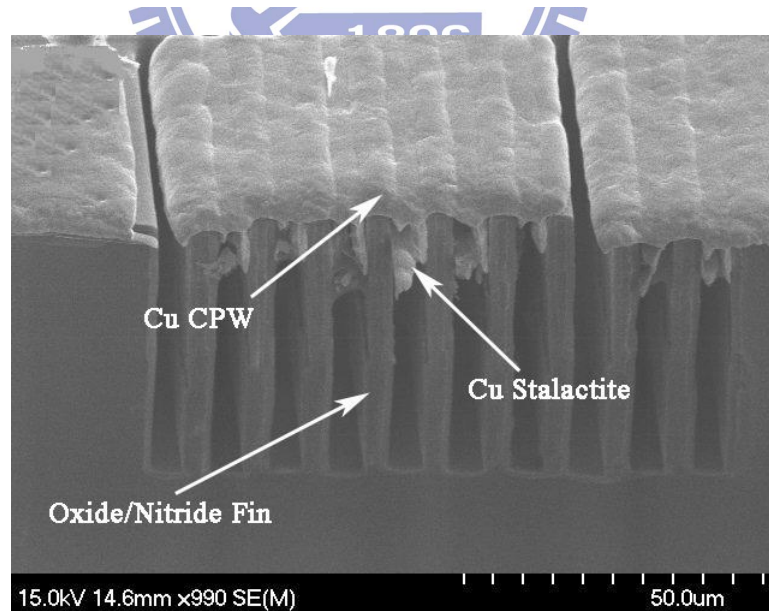


Figure 3-3: A SEM cross sectional view on the CPW deposited on the patterned nitride/oxide/nitride/air fins [49].

impedance. In order to overcome the circumstance, a 7- $\mu\text{m}$  thick AZ 4620 PR (photoresist) is



spun on the top of seed layer prior to the Cu plating. After soft baking the PR, part of PR will reflow into the trenches. Since the seed layer on the top of dielectric fins can reflect more UV light than that coated along the side wall of the trenches, the PR can be hyper-exposed and hypo-exposed, respectively, on the two aforementioned locations via well adjusting exposure time. Thus, after PR development, the sidewalls can be filled with the non-developed PR to effectively prevent the occurrence of Cu electroplating along the sidewall and no copper stalactites form within the fins. At final, the PR filled inside the trenches will be removed by acetone once the CPW is fabricated. Figure 3-4(a) shows the as-fabricated oxide-nitride islands and 3-4(b) shows an enlarge view of Cu CPW fabricated on the top of oxide-nitride islands.

### 3.3 Constitutive Formulation for Special Case

#### 3.3.1 The Characteristic Parameter Determination of a CPW and a Dielectric Fin-Support

In order to expound and popularize the benefits of patterned nitride/oxide/nitride/air fins,

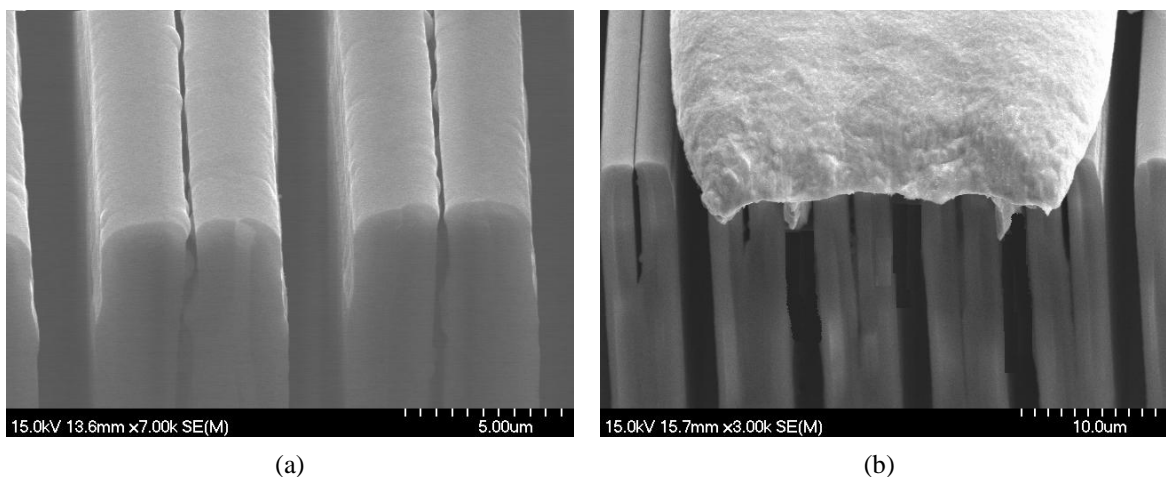


Figure 3-4: A SEM cross sectional view of the as-fabricated oxide-nitride islands and an enlarge view of Cu CPW fabricated on the top of oxide-nitride islands [49].

the CPW with symmetrical structure as shown in the Figure 3-2(e) is utilized for equivalent model analysis. By adapting the concepts of microwave engineering approach to analyze a CPW on top of a conventional substrate, the effective dielectric constant and characteristic impedance of a CPW and that of substrate could be well defined, respectively, as the following [50]:

$$\varepsilon_{eff} = \frac{\varepsilon_r + 1}{2} + \frac{\varepsilon_r - 1}{2\sqrt{1 + 12d/W_{CPW}}}, \quad (3-1)$$

$$Z_{CPW} = \frac{12\pi}{\sqrt{\varepsilon_{eff}}} \left[ \frac{1}{\pi} \ln \left( \frac{1 + \sqrt{x}}{1 - \sqrt{x}} \right) \right], \quad (3-2)$$

$$x = \frac{2\sqrt{s(s + W_{CPW})}}{W_{CPW} + 2s}, \quad (3-3)$$

and

$$Z_{sub} = \frac{30\sqrt{2}}{\sqrt{\varepsilon_{eff} + 1} \ln \left( \frac{8d}{W_{CPW}} \right)}, \quad (3-4)$$

where  $\varepsilon_r$ ,  $d$ ,  $W_{CPW}$ , and  $s$  are the dielectric constant and the thickness of substrate, the width of CPW, and slot width, respectively. For the case of patterned nitride/oxide/nitride/air fins underneath the CPW, however, the effective dielectric constant and characteristic impedance of the conventional substrate should be modified to add the employment of the fins. Both mathematically and physically being analogous with the theory of acoustic crystal for periodic materials [51], we can safely use the assumption of the perfect periodicity of the nitride/oxide/nitride/air fins to compose an effective crystal lattice. In addition, due to the repetition of each component of the dielectric support, we could estimate the contribution of a single fin into 1-dimension. Thus, by considering the integral distribution of the fin components into reciprocal lattice space [28,29], the average effective dielectric constant

should be:

$$\varepsilon_{eff} = \frac{1}{\sqrt{2\pi}} \int \varepsilon_i e^{jG \cdot R} dR = 2 \cos\left(\frac{1}{2}\right) \sum_i \left[ \frac{\varepsilon_i + 1}{2} + \frac{\varepsilon_i - 1}{2\sqrt{1 + 12d/W_i}} \right], \quad (3-5)$$

where the parameters described in integral,  $G$  and  $R$ , are reciprocal lattice and dimensional length, respectively. It should be noted that the decision of the reciprocal lattice factor relies on the composition of components in a fin, so we obtain the average factor,  $2\cos(1/2)$ , for the case presented in this section. The subscript,  $i$ , used in above formulations represents the components of each fin which are oxide, nitride, and air in turn. The parameters  $d$ ,  $\varepsilon_i$  and  $W_i$  are the fin thickness, the dielectric constant and width of  $i$ , respectively. By dealing with the parallel connection of fins underneath the CPW, the characteristic impedance of the patterned dielectric support now could be adapted from (3-4), so we can have:

$$Z_{fins} = \left( \frac{f_1}{Z_{air}} + \frac{f_2}{Z_{nitride}} + \frac{f_3}{Z_{oxide}} \right)^{-1} = \left[ \sum_i \frac{f_i \sqrt{\varepsilon_i + 1}}{30\sqrt{2} \ln[8d/W_i]} \right]^{-1}, \quad (3-6)$$

where the fractional factors,  $f_i$ , used in above formulation should be totally a unity.

### 3.3.2 The frequency-dependent $S$ parameter determination for a CPW

combining (3-2), (3-3), (3-5), and (3-6) associated with the employment of dissipation relation in a loss medium, a closed-form model to describe the frequency-dependent  $S$  parameter for the patterned dielectric support with symmetrical structure can be derived [50, 52, 53]:

$$|S_{11}| = |S_{22}| = -\frac{20}{2.25} \log \left| \frac{Z_{CPW} + (Z_{CPW} + Z_0) // Z_{fins} - Z_0}{Z_{CPW} + (Z_{CPW} + Z_0) // Z_{fins} + Z_0} \right| \cdot \log \left\{ \left[ 17.372 \sqrt{\frac{f \times \mu_0}{2\sigma_{CPW}}} \frac{L_{CPW}}{W_{CPW}} \right] [Z_{CPW} + (Z_{CPW} + Z_0) // Z_{fins}]^{-1} \right\}, \quad (3-7)$$

and

$$\begin{aligned}
|S_{12}| &= |S_{21}| \\
&= 20 \log \left[ \frac{(Z_{CPW} + Z_0) // Z_{fms}}{(Z_{CPW} + Z_0) // Z_{fms} + Z_{CPW}} \frac{1.55Z_0}{Z_0 + Z_{CPW}} \right] \\
&\quad \times \frac{7.47\pi \times f}{C} \frac{\varepsilon_{sub}^2 (\varepsilon_{eff} - 1)^2}{\varepsilon_{eff}^{2/3} (\varepsilon_{sub} - 1)^2} \cdot L_{CPW}
\end{aligned} \tag{3-8}$$

The parameters  $Z_0$ ,  $f$ ,  $\sigma_{CPW}$ ,  $L_{CPW}$ ,  $C$ , and  $\varepsilon_{sub}$  are 50-ohm, operational frequency, conductivity and length of the CPW, speed of light, and dielectric constant of silicon substrate, respectively.

In addition, the phase term could be estimated by considering the attenuation constant,  $\alpha$ , from CPW to the silicon substrate [50]:

$$\begin{aligned}
|\alpha| &= (\text{dielectric loss}) + (\text{Ohmic loss}) \\
&= 4.88 \times 10^{-4} R_s \varepsilon_{eff} Z_{CPW} \frac{P' L_{CPW}}{\pi W_{CPW}} \left( 1 + \frac{s}{W_{CPW}} \right) \left\{ \frac{1 + 1.25 \frac{t}{\pi s} + \frac{1.25}{\pi} \ln \left( \frac{4\pi s}{t} \right)}{\left[ 2 + \frac{s}{W_{CPW}} - \frac{1.25t}{\pi W_{CPW}} \left( 1 + \ln \left( \frac{4\pi s}{t} \right) \right) \right]^2} \right\},
\end{aligned} \tag{3-9}$$

where

$$P' = \frac{\pi^2}{\ln \left[ \frac{2 \left( 1 + \sqrt{\frac{s}{s + 2W_{CPW}}} \right)}{1 - \sqrt{\frac{s}{s + 2W_{CPW}}}} \right]^2} \frac{\frac{s}{s + 2W_{CPW}}}{\left( 1 - \sqrt{1 - \left( \frac{s}{s + W_{CPW}} \right)^2} \right) \left( 1 - \left( \frac{s}{s + 2W_{CPW}} \right)^2 \right)^{\frac{3}{4}}}. \tag{3-10}$$

The parameters  $R_s$  and  $t$  are surface resistivity and thickness of CPW, respectively. In more convenient way, by dividing those losses into individual parts, we can obtain:

$$\alpha_d = 2.73 \frac{\epsilon_{sub}}{\sqrt{\epsilon_{eff}}} \frac{\epsilon_{eff} - 1}{\epsilon_{sub} - 1} \frac{\sum_i \sigma_i / f_i}{2\pi\epsilon_{eff}C} L_{CPW} + (\text{Ohmic Loss}), \quad (3-11)$$

where  $\sigma_i$  represents the conductivity of each element of the patterned fins. The calculated value of phase angle by considering the attenuation constant at 40 GHz is 2.1 degree and very approaches the experimental result shown in Figure 3-1. For convenient comparison, Figure 3-5 also shows the entire spectrums of phase shift of modeling data, simulated data, and measured data with conventional and fin structure, respectively. Therefore, the patterned nitride/oxide/nitride/air fins can provide a better isolation to reduce the dielectric losses obviously.

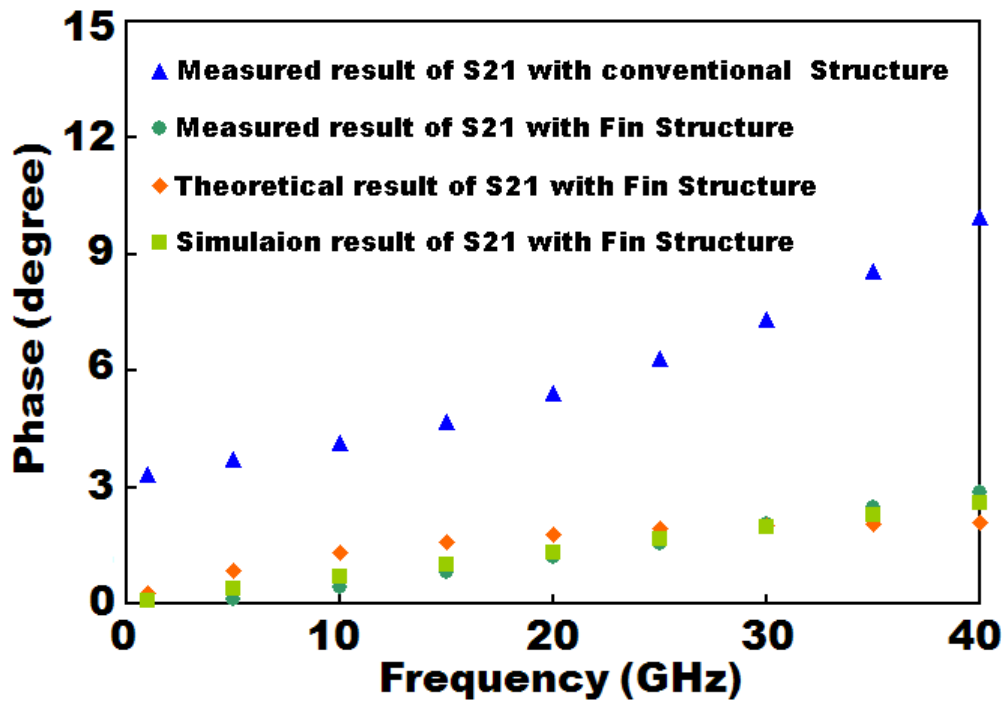


Figure 3-5: The entire spectrums of phase shift of modeling data, simulated data, and measured data with conventional and fin structure, respectively.

### 3.4 Model Validation and Practicality in RF MEMS Optimization

For the case of CPW shown in this chapter that has  $60\mu\text{m}$  strip width,  $150\mu\text{m}$  long and  $12\mu\text{m}$  slot width, the demonstrated ratio of the effective crystal lattice is designed as air: nitride: oxide= 2: 2: 1 and the thickness of dielectric support has the value of  $50\mu\text{m}$  in order to reduce the substrate loss coupling between CPW and the silicon substrate underneath the nitride/oxide/nitride/air fins [54]. The resistivity of silicon substrate is  $1\ \Omega\text{-cm}$ . Figure 3-6 shows the  $S$  parameters of the CPW with nitride/oxide/nitride/air fin support, which are extracted from HFSS simulation, model analysis, and experimental results, respectively. The developed analytical model can well predict the  $S$  parameters of CPW with a good match for the HFSS analysis. The large  $S_{11}$  (or  $S_{21}$ ) discrepancy between simulated and experimental results at high frequency range could be attributed to the process variation resulting in impedance variance from the original CPW design. Nevertheless, as aforementioned, the insertion loss of the CPW with the patterned dielectric support can have a small  $S_{21}$  with value of  $4.33\text{dB/cm}$  at  $40\text{ GHz}$ .

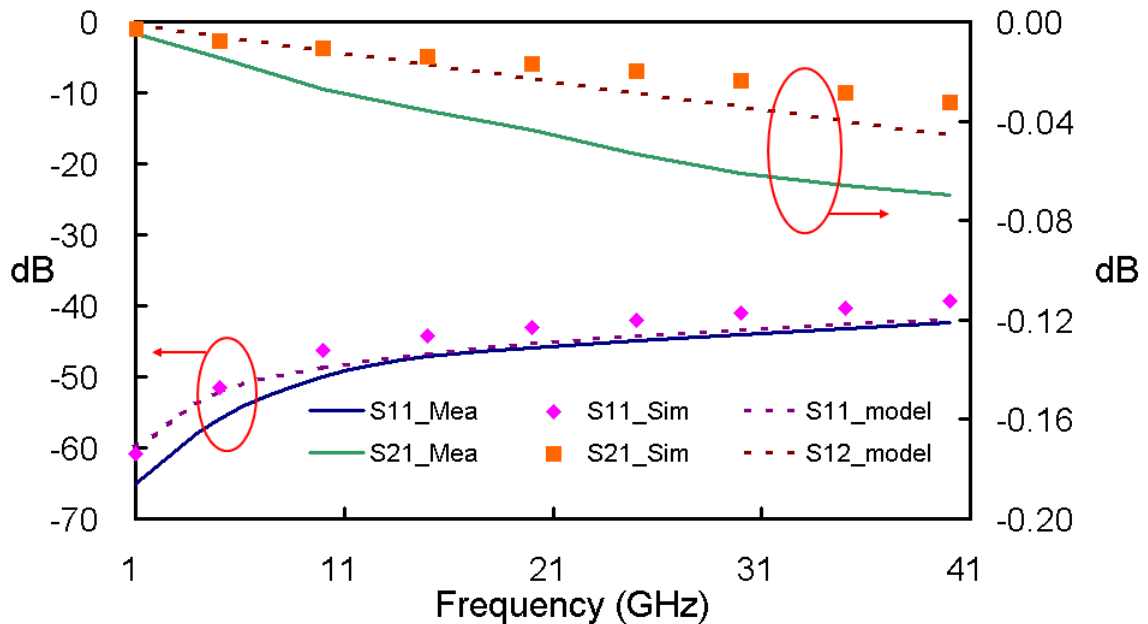


Figure 3-6: Comparison of HFSS simulation, model analysis, and experimental results of a  $150\mu\text{m}$  long CPW on the silicon substrate with patterned oxide-nitride fins support.

As we can realize that the scheme presented in this chapter can not only fit very well in the RF SOP (System-on-Package) applications [55,56], but also the proposed analytical model provides a technique in the future development of high performance passives such as high  $Q$  inductor and band-pass filter fabricated using the same approach. Figure 3-7 shows simulated comparisons of a 3.5-turn micromachining spiral inductor placed on the patterned dielectric support and the conventional silicon substrate. When the substrate replaced by trrenched oxide-nitride islands, the quality factor and self-resonance frequency of the inductor are dramatically improved.

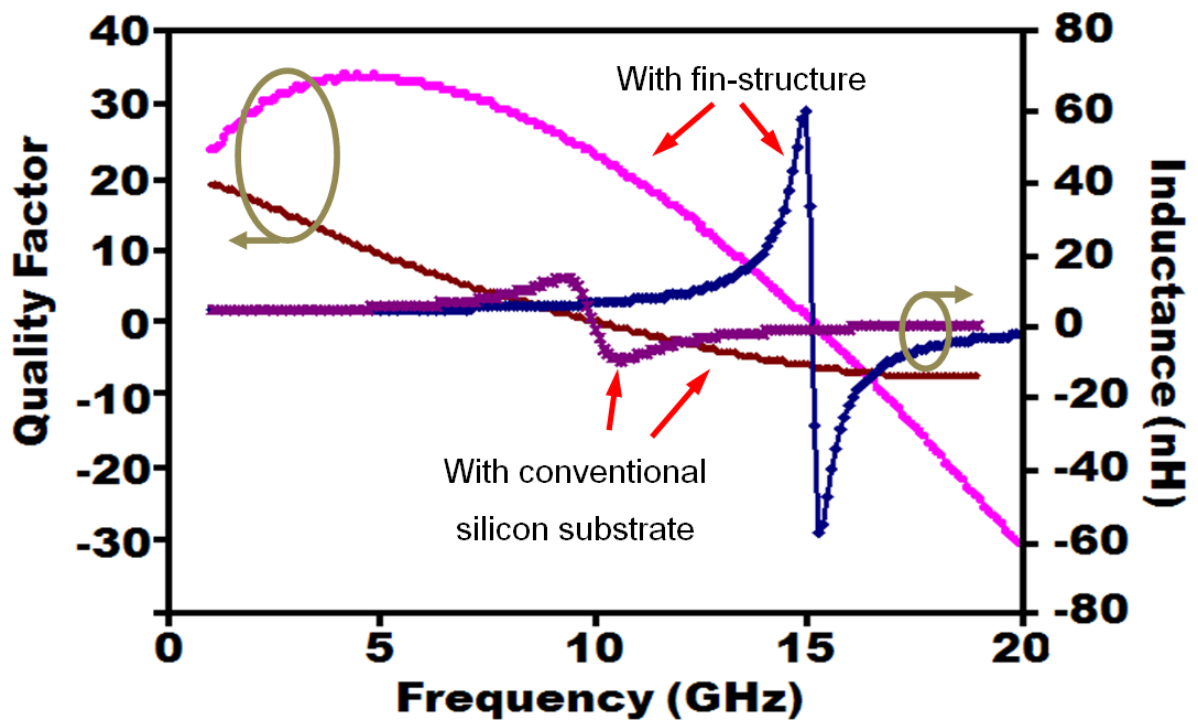


Figure 3-7: Comparison of simulation results between the substrate loss of a spiral inductor deposited on nitride/oxide/nitride/air fins and that on conventional silicon based substrate, respectively [49].



### 3.5 Summary

This chapter presents a micromachining process to effectively reduce substrate loss via a structure of patterned oxide/nitride fins on a silicon substrate with a resistivity of 1  $\Omega$ -cm. Experimental results demonstrate that the insertion loss of a coplanar waveguide deposited on the structure can be lowered to the value of 4.33 dB/cm at 40 GHz. Meanwhile, an analytical model is developed to predict the characteristics of the CPW.



## ***Chapter 4 Physical Analysis of a Biomimetic Microphone with a Central-Supported (C-S) Circular Diaphragm for Sound Source Localization***

### ***4.1 Introduction***

Sound source localization is a physiological ability of animals to process sensory information regarding the orientation and magnitude of sound pressure stimulation. The source localization is achieved via the differences of sound intensity and arrival time sensed by two ears which are geometrically close but far away from the sound sources. For a large mammal, two auditory organs are acoustically isolated by its head to have a large interaural distance (ID). For instance, the auditory system of an adult human with an ID of 20 cm can have an interaural time delay (ITD) of 600  $\mu$ s and interaural intensity difference (IID) of about 16 dB between the ears with a 5 KHz tone sound pressure stimulation. Such minute ITD and IID are adequate for reliable time coding and processing in auditory nervous systems for sound source detection [57]. In contrast, two auditory organs of small animals are quite close to each other, so there would be a problem for the auditory system to experience insignificant interaural differences resulted by the tiny ID, about two orders of magnitude smaller than that of large animals. Therefore, the methodology of sound source localization in the tiny auditory system could lead the way to develop the next generation acoustic sensing and tracking microsystems like hearing aids, robots, and bionic military devices. In recent two decades, the acoustic sensing mechanism and auditory behavior of the parasitoid fly (*Ormia ochracea*) whose entire auditory organ is only 1.2 mm, as shown in Figure 4-1, have been thoroughly investigated. Several studies demonstrated that the acoustic interaction between ipsilateral and contralateral prosternal tympanal membranes (PTMs) can effectively increase the interaural differences for locating sound sources by means of an intertympanal bridge structure as a mechanically coupled pivot [57-66]. The ipsilateral and contralateral

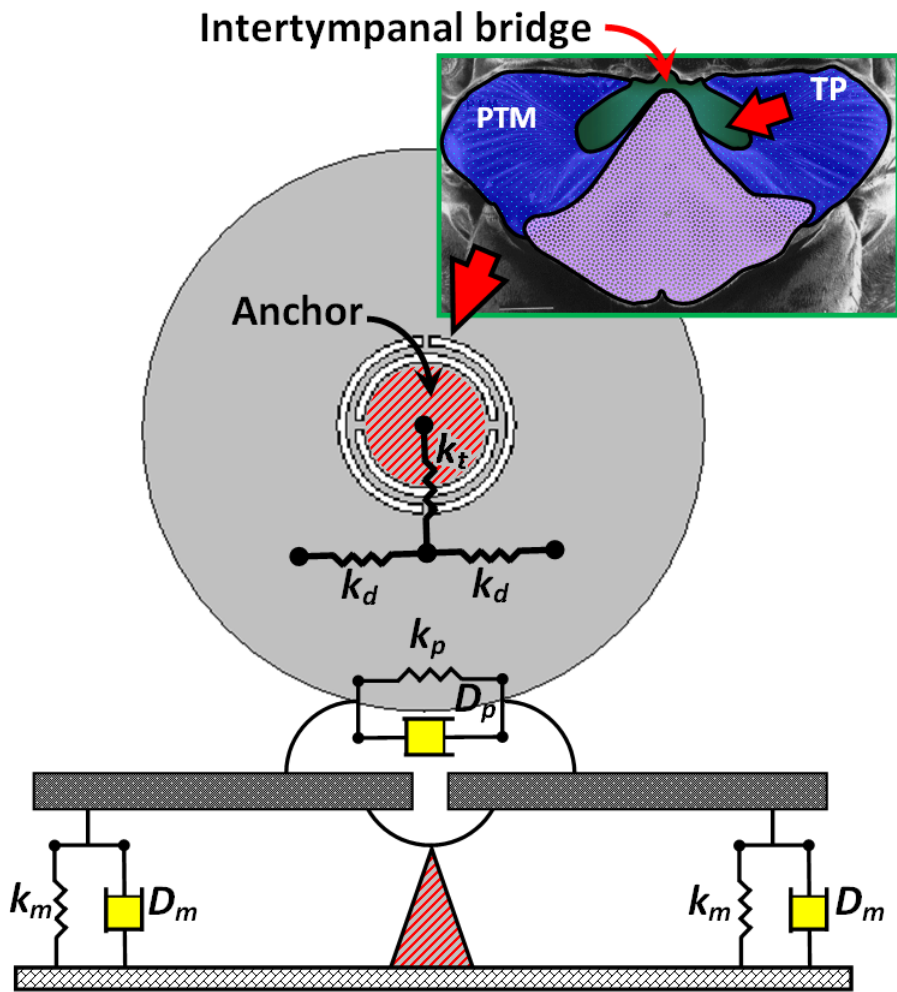


Figure 4-1: Schemes of central-supported gimbal circular biomimetic diaphragm. The upper insertion shows the auditory organ of the parasitoid fly *Ormia ochracea* whose entire auditory organ is only 1.2 mm. The intertympanal bridge connecting two prosternal tympanal membranes (PTMs), i.e., the ipsilateral and the contralateral prosternal tympanal membranes, via the tympanal pits (TP) in a manner of flexible coupled pivot can cause the two PTMs to deflect in opposite directions. The lower insertion shows the mechanical model of the central-supported gimbal circular biomimetic diaphragm [57-66].

membranes are defined as the membrane on the same side as and the one on the opposite side to the sound source, respectively.

The intertympanal bridge connecting the two PTMs via the tympanal pits (TP) functions like a flexible coupled pivot that can cause the PTMs to deflect in opposite direction. In other words, under an insignificant IID stimulation, the two fly ears constrained by the

intertympanal bridge will move in the opposite direction with roughly equal amplitudes. It indicates that an interaural phase difference (IPD) of  $180^\circ$  would be formed in all frequency spectra [58]. The mechanical time delay (MTD) between the ipsi- and contralateral ears then can be equivalent to a half of the stimulation period due to the IPD of  $180^\circ$ . For instance, the MTD between the ipsi- and contralateral fly-ears will be equivalent to  $100 \mu\text{s}$  under a 5 kHz tone sound pressure stimulation with corresponding wavelength and period of 6.8 cm and  $200 \mu\text{s}$ , respectively. Since the net displacement of the contralateral membrane would be a superposition of the displacements caused by the ipsilateral mechanical coupling via the intertympanal bridge and by the delayed sound pressure, the net displacement differences resulted by the two causes within the two PTMs could make the parasitoid fly easily detect the sound sources.

As an incident sound wave with an angle  $\varphi$  relative to longitudinal axis of an auditory system is applied on the system, the ITD between the ipsi- and contralateral auditory organs should be expressed as [58]:

$$\text{ITD} = (D/v) \cdot \sin \varphi, \quad (4-1)$$

where  $v$  is the sound propagating speed with a value of 344 m/s at room temperature. For instance, the ITD is about  $7 \mu\text{s}$  to either the parasitoid fly or any specific animal with the same auditory system size as the fly but without the mechanically coupled pivot, when an incident sound wave hits with  $\varphi = 90^\circ$ . With a 5 KHz tone sound pressure stimulation, the tiny ITDs of the fly or the specific animal can only result in the same amplitudes of the PTMs as well as the same oscillating direction with slight phase difference. Fortunately, by considering the aforementioned mechanism of the MTD, the time delay caused by the mechanically coupled pivot of the fly will dominant with a larger value which is about 14 times of the ITD ( $\sim 100 \mu\text{s}/7 \mu\text{s}$ ) and the PTMs can move in the opposite direction simultaneously. Thus, the employment of the mechanically coupled pivot indeed can raise the ability of the tiny auditory

system for sound source localization. In a nutshell, the concept of the tiny auditory system with such a mechanically coupled pivot can provide an important design feature for Micro Electro-Mechanical Systems (MEMS) microphones for hearing aid applications in terms of sound source localization [67-71].

Previously, an acoustical structure with a central-supported (C-S) sensing diaphragm in microscale as shown in Figure 4-1 was proposed for sound source localization by imitating the aforementioned auditory mechanically coupled principle of the parasitoid fly [67,68,71]. The proposed design had drawn lots of attention due to the characteristics of simple fabrication process, easy sensing circuit implementation, and excellent directional identification as well as spatial resolution in comparison with the other biomimetic designs [69,70]. However, lacking of physical intuition and complete theoretical model in terms of material and dimensional characteristics has caused the difficulty in design optimization of the C-S diaphragm for device designers. Further investigation is required to reveal the mechanical dynamics with significant physical explanations for sound source localization. In this chapter, we construct a corresponding physical response model with air damping effects from which the auditory dynamical behaviors of the C-S diaphragm can be fully elucidated.

## ***4.2 Constitutive Formulation***

### ***4.2.1 Mechanism of Conventional C-S Design in Steady State***

By considering the conventional C-S design as shown in Fig. 1 with the detail schematic diaphragm and mechanical configuration, the corresponding equation of motion for the ipsi- and contralateral displacements of the diaphragm could be derived as follows [58,71]:

$$\begin{aligned}
& \begin{bmatrix} k_m + k_p & k_p \\ k_p & k_m + k_p \end{bmatrix} \begin{bmatrix} Z_{ipsi} \\ Z_{contra} \end{bmatrix} \\
& + \begin{bmatrix} D_m + D_p & D_p \\ D_p & D_m + D_p \end{bmatrix} \frac{d}{dt} \begin{bmatrix} Z_{ipsi} \\ Z_{contra} \end{bmatrix} \\
& + \begin{bmatrix} m/2 & 0 \\ 0 & m/2 \end{bmatrix} \frac{d^2}{dt^2} \begin{bmatrix} Z_{ipsi} \\ Z_{contra} \end{bmatrix} = \begin{bmatrix} F_{ipsi} \\ F_{contra} \end{bmatrix}
\end{aligned} \tag{4-2}$$

where  $k_m$  and  $k_p$ ,  $Z_{ipsi}$  and  $Z_{contra}$ ,  $D_m$  and  $D_p$ ,  $m$ ,  $F_{ipsi}$  and  $F_{contra}$  are the stiffness coefficients of the membrane and the coupled pivot, the displacements of ipsi- and contralateral membranes, the damping coefficients of the membrane and the coupled pivot, the mass of entire diaphragm, and the driving force loaded onto the ipsi- and contralateral membranes, respectively. According to the mechanical model as shown in Figure 4-1, the parameter  $k_p$  is physically equivalent to the linear combination of the spring constant of deflection and two times that of twist, i.e.  $k_d + 2k_t$ . The parameter  $k_m$  is equivalent to the spring constants of deflection  $k_d$ . In general, the corresponding displacements of the ipsi- and contralateral membranes in steady state can be expressed by a linear combination of the displacements of translational and rocking modes in time domain [58]:

$$\begin{aligned}
Z_{ipsi}(t) &= A_t \sin(\omega t + \phi_t) + A_r \cos(\omega t + \phi_r), \\
Z_{contra}(t) &= A_t \sin(\omega t) - A_r \cos(\omega t),
\end{aligned} \tag{4-3}$$

where  $A_t$  and  $A_r$  are the amplitudes of translational and rocking modes, respectively. Meanwhile, by physically considering the angle of twist and deflection of the diaphragm caused by the time-variant sound pressure, these amplitudes can be expressed in terms of operating frequency  $\omega$  and material characteristics:

$$\begin{aligned}
A_t &= \frac{P(t) \cdot A}{m} \frac{\cos(\omega\tau/2)}{\sqrt{(\omega_t^2 - \omega^2)^2 + (2\omega_t\eta_t\omega)^2}}, \\
A_r &= \frac{P(t) \cdot A}{m} \frac{\sin(\omega\tau/2)}{\sqrt{(\omega_r^2 - \omega^2)^2 + (2\omega_r\eta_r\omega)^2}},
\end{aligned} \tag{4-4}$$

where



$$\begin{aligned}
A &= 2\pi(a^2 - c^2), \\
\omega_t &= \sqrt{\frac{k_m + 2k_p}{m}}, \quad \eta_t = \frac{D_m + 2D_p}{\omega_t m}, \\
\omega_r &= \sqrt{\frac{k_m}{m}}, \quad \eta_r = \frac{D_m}{\omega_r m}, \\
k_m = k_d &= \frac{8E(a-c)T^3}{\pi^2(a+c)^3}, \\
k_p = k_d + 2k_t &= \frac{8(a-c)T^3}{\pi^2(a+c)^2} \left( \frac{E}{(a+c)} + \frac{G}{3a} \right) + \frac{8GWT^3}{3(a-c)^3}.
\end{aligned} \tag{4-5}$$

The parameters  $a$ ,  $c$ ,  $\tau$ ,  $W$ ,  $T$ ,  $G$  and  $E$ , and  $P(t)$  are outer radius of the diaphragm, inner radius of the diaphragm, the ITD derived in (4-1), width of the beam, thickness of the diaphragm, shearing modulus and Young's modulus of the structural material, and magnitude of time-variant sound pressure applied on the membranes, respectively. The phase coefficients mentioned in (4-3) are described as follows:

$$\begin{aligned}
\phi_t &= -\arctan\left(\frac{2\omega_t \eta_t \omega}{\omega_t^2 - \omega^2}\right), \\
\phi_r &= -\arctan\left(\frac{2\omega_r \eta_r \omega}{\omega_r^2 - \omega^2}\right).
\end{aligned} \tag{4-6}$$

In (4-4) and (4-5), the  $\omega_t$  and  $\omega_r$ , and  $\eta_t$  and  $\eta_r$  are the natural resonant frequencies and the damping ratios of the translational and rocking modes, respectively [58]. Table 4-1 shows the dimensional parameters of the C-S diaphragm microphones. According to (4-5), the corresponding theoretical calculations of the resonant frequencies of the rocking and translational modes are about 621Hz and 1186Hz, respectively, which are very close to the results of finite element analysis (FEA) simulation presented by the previous study in Case A listed in Table 4-1 [67]. Figure 4-2 shows the schematic diagrams regarding the geometrical structures of the structurally coupled C-S designs.

Obviously, the conventional C-S design can be mechanically divided into two regions, i.e. the central-supported region and the diaphragm, that are connected to each other using an

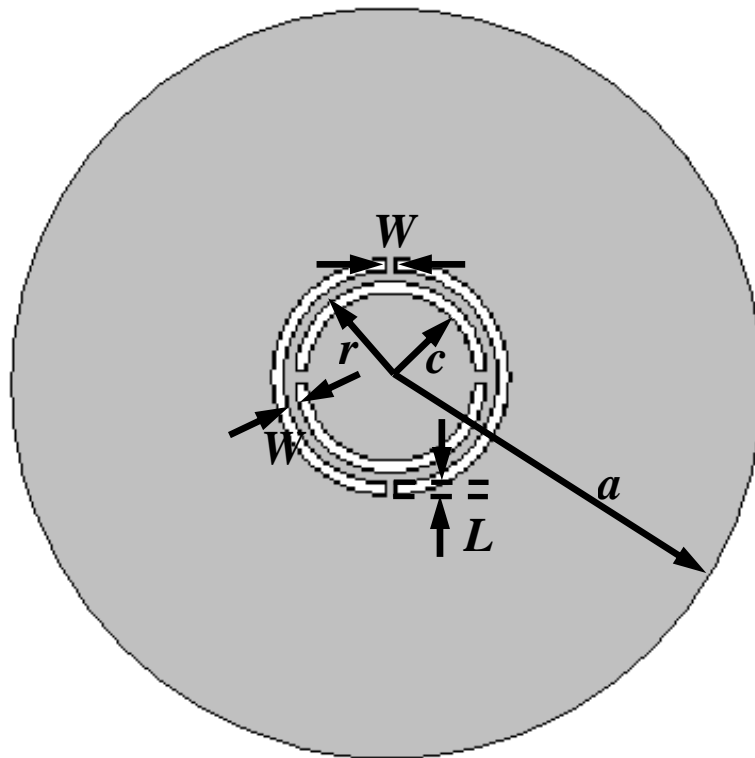
Table 4-1  
Dimensional parameters of the conventional and hybrid C-S design

Conventional C-S design ( $\mu\text{m}$ )		
	Case A [67]	Case B [68]
Radius of diaphragm ( $a$ )	1700	10800
Thickness of diaphragm ( $T$ )	5	30
Radius of central-supported region ( $c$ )	100	1500
Radius of ring ( $r$ )	175	1800
Width of ring ( $W$ )	50	200
Length of beam ( $L$ )	50	200
Width of beam ( $W$ )	50	200
Gap height ( $h$ )	10	8000
Hybrid C-S design ( $\mu\text{m}$ )		
	Case C	Case D
Radius of diaphragm ( $a$ )	10800	10800
Thickness of diaphragm ( $T$ )	30	30
Length of end-clamped supporting beam ( $L$ )	200	1700
Length of central beam ( $L$ )	200	1700
Width of beam ( $W$ )	200	100
Spacing between beams ( $b$ )	100	100
Gap height ( $h$ )	8000	8000

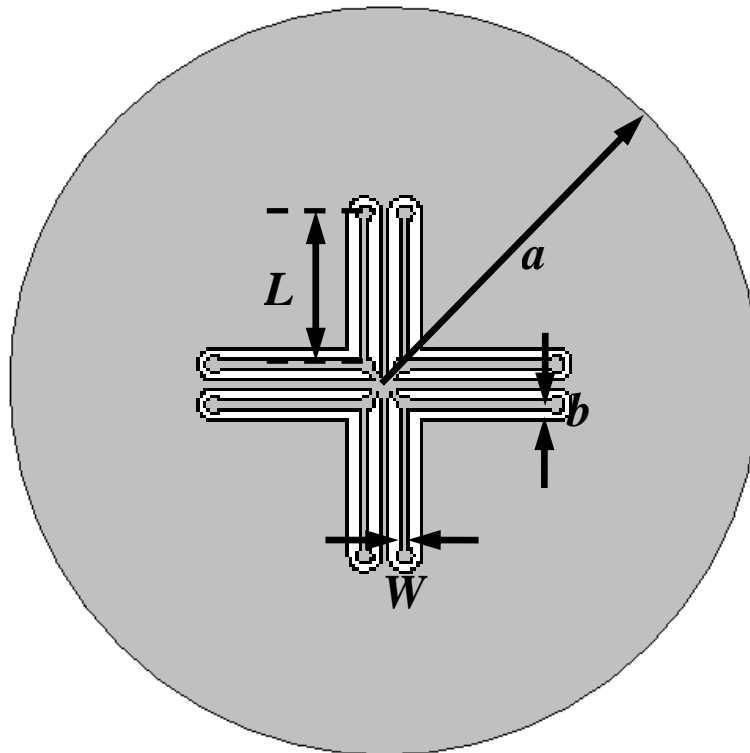
asymmetrical beam structure as shown in Figure 4-1. The design of the asymmetrical beam structure with a large aspect ratio of the outer radius to the thickness ( $\sim 200$  to 1) usually accompanies with an undesired diaphragm deflection caused by the gravitational force. For instance, the torque contributed by the gravitational force applied on the outer beams will lead to drastic deflections on the edges of the ipsilateral and contralateral diaphragms and should be considered in the design. Thus, the induced deflection,  $Z_g$ , caused by the gravitational force is calculated as the superposition of the deflections of diaphragm and that of the asymmetrical beams:

$$Z_g = \frac{3mg(a-c)^3(a+3c)}{8ET^3(a^2-c^2)} + \frac{4mg[(2+\pi/2)L+(2+\pi/4)W]^3}{EWT^3}, \quad (4-7)$$

where  $g$  and  $L$  are the gravitational acceleration constant and length of the beam, respectively. By employing the undesired gravitational effect into the equation of diaphragm motion, the



(a)



(b)

Figure 4-2: Schematic diagrams regarding the geometrical structures for (a) the conventional and (b) the hybrid C-S designs.

net ipsi- and contralateral displacements can be expressed as  $Z_{ipsi}(t) + Z_g$  and  $Z_{contra}(t) + Z_g$ , respectively. For the capacitive biomimetic microphones for sound source localization, the net displacements should be the indicators to identify the sensitivity of the device [72]. The designers can, therefore, determine minimum gap height between the diaphragm and the substrate as well as the maximum capacitances by considering the net displacements caused by the summation of the applied sound pressures and the gravitational effect in design stage using the derived equation of diaphragm motion.

#### **4.2.2 Mechanism of Hybrid C-S Design in Steady State**

In the prior analysis, (4-4) and (4-5) disclose a new finding in terms of biomimetic microphone structure: net displacements of a C-S diaphragm will be increased with the decrease of the radius of central-supported region. On the other hand, from the (4-7) the undesired deformation due to the gravitational force could be also increased. In order to further realize the improvement of the net displacements but simultaneously conquer the undesired deformation, a new central floating gimbal structure as shown in Figure 4-3 is demonstrated for the biomimetic C-S microphone design in the next generation. To imitate the flexible stem of a cloverleaf supporting four independent leaves as shown in Figure 4-4, the conventional central anchor was replaced by a central floating joint. The four central beams with two ends connected to the central floating joint and membrane, respectively, are similar to the four independent leaves of the cloverleaf. Thus, the structure of the biomimetic microphone becomes a fourfold rotation axial symmetry. In order to enhance the acoustic response of the central beams to sound pressure, eight end-clamped supporting beams are also adopted to enhance the twist angles. Nevertheless, the weak interactions between each independent membrane could not efficiently carry out the force transferring from the ipsilateral side to the contralateral one. Thus, the mechanical characteristics from the

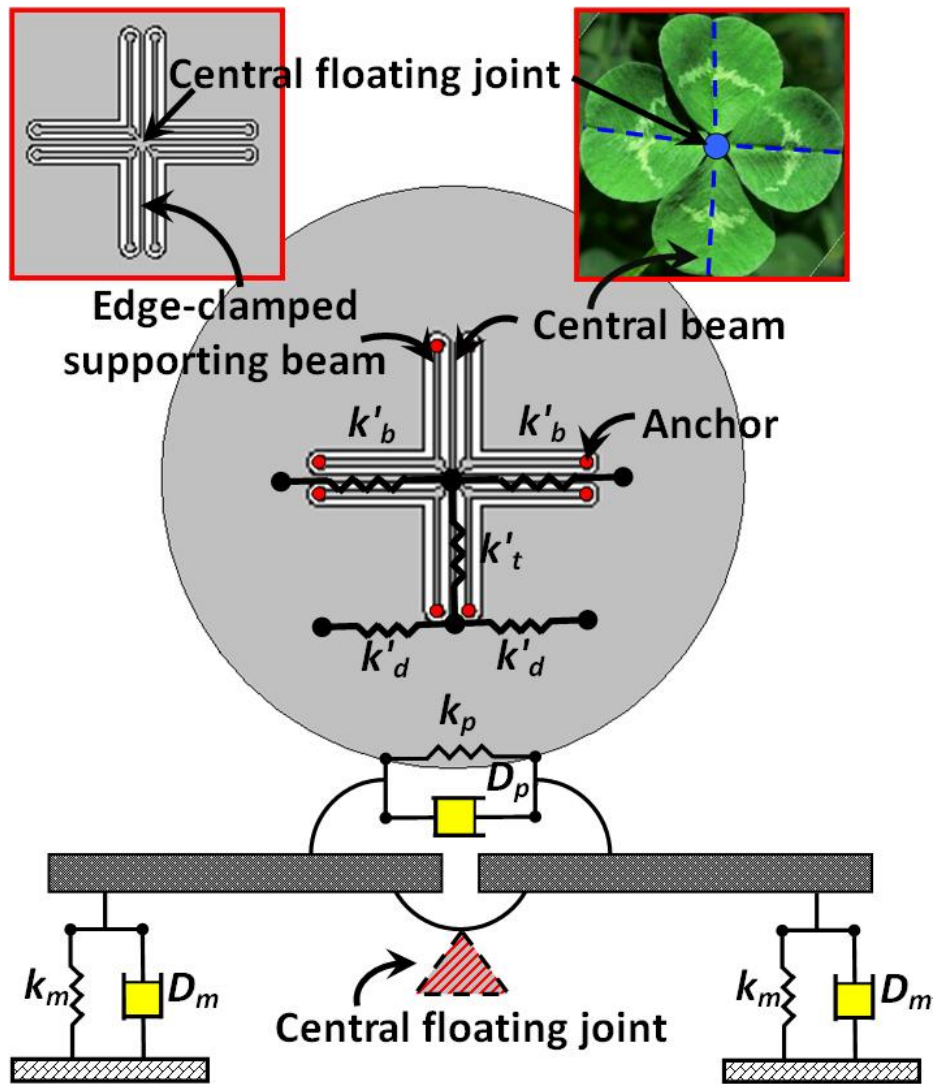


Figure 4-3: Scheme of the hybrid biomimetic microphone with central floating gimbal design, which is hybridized by the acoustic sensing mechanism of the parasitoid fly and the flexible clover-stem-like gimbal structure. The lower insertion shows a new mechanical model with the central floating joint.

parasitoid fly are further employed. By hybridizing the mechanical characteristics of the sensing mechanism of the parasitoid fly and the clover-stem-like gimbal structure, the conventional C-S structure is further modified using eight end-clamped supporting beams connected to a central floating joint. Fourfold-rotation axial symmetry of the clover-stem-like gimbal structure is adopted to replace the conventional asymmetrical beam structure. The entire mass of the diaphragm is supported by four central beams whose ends are connected to

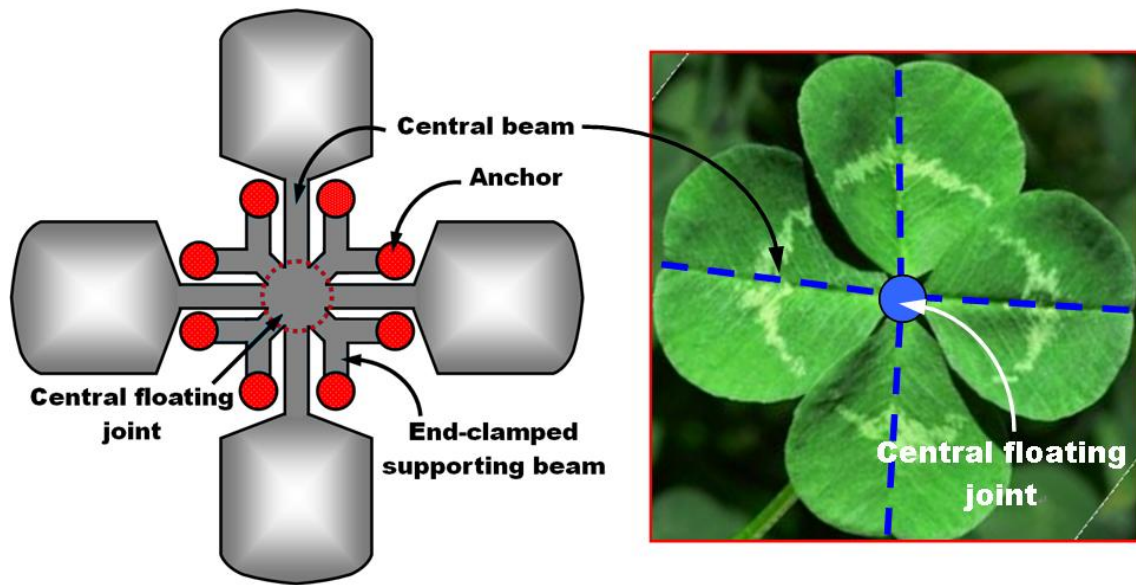


Figure 4-4: Comparison between the cloverleaf and the prototype of the biomimetic microphone.

form the central floating joint which performs like a freely suspended support. Thus, while the diaphragm is released from the substrate underneath itself, the effects of gravitational force or residual stress on the displacement of the diaphragm can be effectively compensated by the concentrated moments which are resulted by the reaction forces and applied to the joint [73,74]. In comparison with the theoretical calculations using the dimensional parameters listed in Table 4-1, the results of the initial deformation shown in Table 4-2 indicate that the hybrid C-S design could have better resistance to the undesired deformation. It is also validated by ConventorWare simulations [75]. Meanwhile, the net displacement of the hybrid C-S design can not only have the typically acoustic responses resulted by the twist of the

Table 4-2  
Comparison between model prediction and simulation of the initial deformation

Comparison				
Case	A	B	C	D
Modeling prediction ( $\mu\text{m}$ )	0.05	4.44	2.39	4.31
Simulation [75] ( $\mu\text{m}$ )	0.02	3.96	2.11	3.89

beams perpendicular to the direction of incident sound pressure and the deflection of the diaphragm along the direction of wave propagation but also have additional responses caused by the deflection of the central beams along the direction of propagation which can greatly enlarge the displacement of the diaphragm.

Thus, the parameters  $k_p$  and  $k_m$  of the hybrid C-S design should be structurally modified through the linear combination of the spring constants of the deflection of the membrane, that of the central beam, and that of the twist of the central beam, i.e.  $k'_d + k'_b + 4k'_t$ , and  $k'_d + k'_b/2 - 4k'_t$ , respectively. Eq. (4-4) and (4-5) can be likewise modified as follows:

$$\begin{aligned} A_t^{Hybrid} &= \frac{3}{2} \frac{a^2}{a^2 - c^2} A_t \Big|_{\omega_t \rightarrow \omega_t^{Hybrid}}, \\ A_r^{Hybrid} &= \frac{3}{2} \frac{a^2}{a^2 - c^2} A_r \Big|_{\omega_r \rightarrow \omega_r^{Hybrid}}, \end{aligned} \quad (4-8)$$

where

$$\begin{aligned} \omega_{in}^{Hybrid} &= \sqrt{\frac{k_m^{Hybrid} + 2k_p^{Hybrid}}{m}}, \quad \omega_{reversed}^{Hybrid} = \sqrt{\frac{k_m^{Hybrid}}{m}}, \\ k_m^{Hybrid} &= k'_d + \frac{k'_b}{2} - 4k'_t \\ &= k_m \Big|_{c \rightarrow L+2W} + \frac{EWT^3}{2a^3} - \frac{16\sqrt{2}G[a - (L+2W)]T^3}{3\pi^2 a[a + (L+2W)]^2}, \\ k_p^{Hybrid} &= k'_d + k'_b + 4k'_t \\ &= k_m \Big|_{c \rightarrow L+2W} + \frac{EWT^3}{a^3} + \frac{16\sqrt{2}G[a - (L+2W)]T^3}{3\pi^2 a[a + (L+2W)]^2}. \end{aligned} \quad (4-9)$$

Meanwhile, the initial deflection caused by the gravitational force should be also mechanically and structurally modified as follows:

$$Z_g^{Hybrid} = \frac{3mg[a - (L+2W)]^3[a + 3(L+2W)]}{8ET^3[a^2 - (L+2W)^2]} + \frac{mg(L-W)^3}{EWT^3}. \quad (4-10)$$

Table 4-3 lists the theoretical comparisons of the stiffness coefficients of the rocking and



Table 4-3

Theoretical comparisons of the stiffness coefficients and natural resonant frequencies of the rocking and the translational modes for the conventional and the hybrid C-S design, respectively.

Parameters	Conventional C-S design (Case B)	Hybrid C-S design (Case D)
$k_p$ (Nt/m)	18.1	20.4
$k_m$ (Nt/m)	13.1	2.8
$k_m+2k_p$ (Nt/m)	49.2	43.6
$\omega_r$ (Rad/Hz)	372.0	170.4
$\omega_t$ (Rad/Hz)	720.3	671.4

translational modes in the conventional and the hybrid C-S designs, respectively. It is obvious that both stiffness coefficients of the rocking ( $k_m$ ) and translational ( $k_m+2k_p$ ) modes of the hybrid C-S design are smaller than that of the conventional design as well as the natural resonant frequencies in both modes. According to the derived (4-4) and the two-degree-of-freedom (2-DOF) model [76], the smaller the natural resonant frequencies are, the larger the displacements of the diaphragm will be. The sensitivity and directivity of the biomimetic microphone will be also enhanced. It is noted that the rocking-mode frequency of the hybrid C-S design has about a 50% reduction, so the amplitude of rocking mode can be effectively increased using the hybrid C-S design.

Additionally, the performances of biomimetic microphones can be also strictly compared using two mechanical indicators, the mechanical interaural intensity difference (mIID) and the mechanical interaural phase difference (mIPD) [76], which can be expressed as follows:

$$\text{mIID} = 20 \log_{10} \frac{|Z_{\text{ipsi}}|}{|Z_{\text{contra}}|}, \quad (4-11)$$

and

$$\text{mIPD} = \cos^{-1} \left( \frac{Z_{\text{ipsi}}}{Z_{\text{contra}}} \right). \quad (4-12)$$

For the case of sound source localization via the biomimetic microphone, the ipsi- and contralateral membranes moving in the opposite direction with equal amplitudes must have the mIID and mIPD with the values of near 0 dB and 180°, respectively. According to the theoretical calculations, the values of the mIID and mIPD for both the conventional and the hybrid C-S designs are 16.1 dB and 99.1°, and 16.6 dB and 98.5°, respectively. In a nutshell, as compared with the mIID and mIPD of the conventional C-S design, the hybrid C-S design can be enhanced with the displacement increase of the diaphragm without any mechanical performance degradation by means of dramatically decreasing the rocking-mode stiffness.

#### 4.2.3 Transient State

By recalling the equation of motion (4-2), the solution should actually consist of two parts, a complementary function  $Z_C(t)$ , which is the solution of (4-2) with right-hand side set equal to zero, and a particular solution  $Z_P(t)$ , which reproduces the right-hand side. The particular solution has been derived as (4-3), and the complementary function has the form:

$$Z_C(t) = \begin{cases} e^{-\omega_r \eta_r t} A_r \sin(\omega t + \phi_r) + e^{-\omega_i \eta_i t} A_i \cos(\omega t + \phi_i) \\ e^{-\omega_r \eta_r t} A_r \sin(\omega t) - e^{-\omega_i \eta_i t} A_i \cos(\omega t) \end{cases}. \quad (4-13)$$

Thus, the general solution of either ipsi- or contralateral displacement is

$$\begin{aligned} Z(t) &= Z_C(t) + Z_P(t) \\ &= \begin{cases} (1 + e^{-\omega_r \eta_r t}) A_r \sin(\omega t + \phi_r) + (1 + e^{-\omega_i \eta_i t}) A_i \cos(\omega t + \phi_i) \\ (1 + e^{-\omega_r \eta_r t}) A_r \sin(\omega t) - (1 + e^{-\omega_i \eta_i t}) A_i \cos(\omega t) \end{cases}. \end{aligned} \quad (4-14)$$

It is obvious that  $Z_C(t)$  here represents transient effect, i.e., effects that die out soon, and the terms contained in the solution damp out with time due to the factor  $e^{-\omega_r \eta_r t}$  and  $e^{-\omega_i \eta_i t}$ .

Meanwhile, the second term  $Z_p(t)$  represents the steady-state effects and contains all the information for operating time larger than  $1/\beta$ , where  $\beta$  represents either  $\omega_t \eta_t$  or  $\omega_r \eta_r$  in translational- or rocking-mode motion, respectively. Thus, the steady-state solutions have widely functionalities in many physical, mechanical, and engineering applications.

The detail of the motion in the duration of the transient region strongly depend on the oscillator's conditions at the moment that the driving force is first applied on and also on the relative magnitude of the driving frequency and the damping frequencies  $\omega_t \sqrt{1-\eta_t^2}$  and  $\omega_r \sqrt{1-\eta_r^2}$ , respectively. Figure 4-5 reveals the oscillation motions of the transient state and

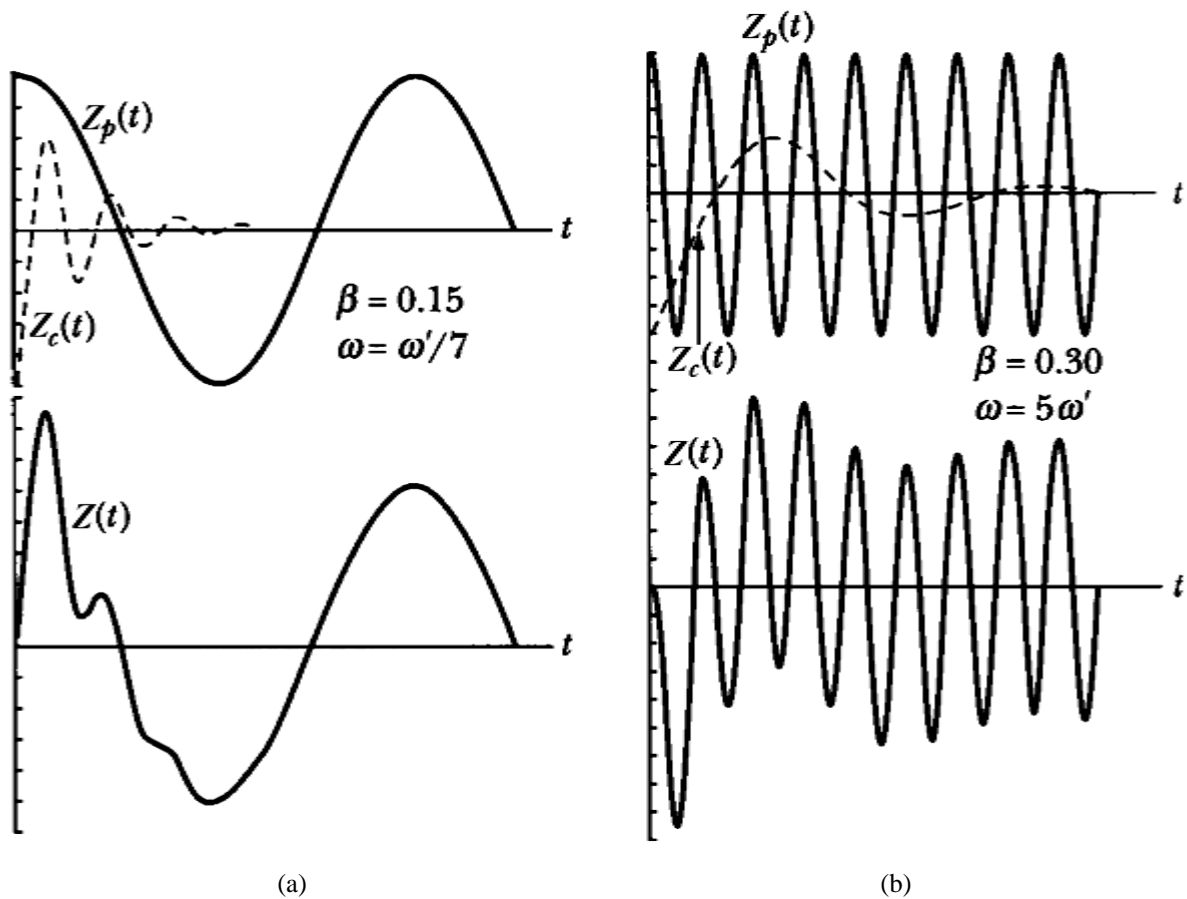


Figure 4-5: Examples of sinusoidal driven oscillatory motion with damping. The particular solution (steady-state)  $Z_p(t)$ , the complementary function  $Z_c(t)$ , and the general solution of either ipsi- or contralateral displacement are shown in (a) driving frequency ( $\omega$ ) < damping frequency ( $\omega'$ ) and (b) driving frequency > damping frequency, respectively [77].

steady state with specified conditions, respectively [77]. It is obvious that when the driving frequency is small than the damping frequency, the transient response of the system greatly distorts the sinusoidal shape of the driving forcing function immediately as shown in Figure 4-5(a). On the contrary, when the driving frequency is larger than the damping frequency, there will be a modulation of the driving forcing function with slight distortion in the high frequency region as shown in Figure 4-5(b).

In the case, both the damping ratios in the translational and rocking modes of the *Case B* and *D* will be theoretically calculated using the method of squeeze film air damping (the detail derivation will be described in the next chapter), by which they have the values of  $\eta_r = 0.39$  and  $\eta_t = 2.31$ , and  $\eta_r = 0.83$  and  $\eta_t = 2.43$ , respectively. By recalling the theoretically estimated natural resonant frequencies of translational and rocking modes listed in Table 4-3, the values of  $\beta$  of each mode are 952 and 91 for conventional C-S design and are 847 and 38 for the hybrid C-S design, respectively. Thus, the transient effects are so insignificant in both cases that the (4-14) used to describe the responses of the oscillating system can be reduced to (4-3) reasonably. In a nutshell, the dynamic responses of the C-S designs can directly follow the periods of the driving forces.

### 4.3 Derivation of Quality Factors and Damping Coefficients

#### 4.3.1 Derivation of Quality Factors Using Squeeze Film Air Damping and Energy Transfer Models

The “quality factor”  $Q$  of an oscillating system can be approximately and typically described as follows [77,78]:

$$Q = 2\pi \frac{\text{energy}}{\text{energy lost per cycle}} = \sqrt{\frac{1}{\eta_R} - \frac{1}{2}}, \quad (4-15)$$

where  $\eta_R$  is the damping ratio of either rocking or translational mode. According to the extraction of the damping coefficients from the previous experiments [78], the value of  $\eta_R$  is roughly larger than unity. Thus, in the case, the  $Q$  factor is a poor value or even an imaginary number. At the moment, the microphone performs in either a critical-damping or an over-damping mode.

The oversimplified (4-15), however, does not completely reveal the detail relationship between the acoustic dynamics of the microphone and the air damping effect [79-81]. Thereby, the squeeze film air damping model and the energy transfer model are adopted for revealing the interaction between microphone diaphragm and air. Additionally, since there are two obvious motion mechanisms occur while the diaphragm is loaded by sound pressure: normal motion and rotation of the diaphragm, there will be two independent energy-loss mechanisms removing energy from each single mode. Therefore, by means of the energy transfer model, the quality factors should be obtained in terms of the quality factor of the normal motion,  $Q_N$ , and that of the rotation,  $Q_R$ , for each single mode and can be expressed as [79-81]:

$$Q = \left( \frac{1}{Q_N} + \frac{1}{Q_R} \right)^{-1}, \quad (4-16)$$

where

$$Q_N = (2\pi)^{3/2} \left( \frac{\rho Th}{2\pi a} \right) \sqrt{\frac{RT_R}{M_{air}}} \frac{\omega_R}{P(t)}, \quad (4-17)$$

and

$$Q_R = \frac{1}{\eta_R} \sqrt{\frac{I_p}{mLW}}. \quad (4-18)$$

The parameters  $\rho$ ,  $h$ ,  $R$ ,  $M_{air}$ ,  $T_R$ , and  $I_p$  are mass density of the diaphragm, gap height, universal molar gas constant, molar mass of air, ambient temperature, and the moment of

inertia of supporting beam, respectively. Eq. (4-18) obviously reveals that the damping ratios as well as the damping coefficients are significant parameters for deriving the quality factors. Thus, a complete discussion of the damping coefficients can helpfully clarify the interaction between the viscous air and the diaphragm. Table 4-4 lists the theoretical calculations of the quality factors of both rocking and translational modes in the conventional and the hybrid C-S designs, respectively.

#### 4.3.2 Derivation of Damping Coefficients and Effective Gap Height

The viscous damping indeed affects the dynamic responses of the acoustic sensors as well as the quality factor. Although several researches regarding the effects of squeeze film air damping have been investigated and provided with detail physical and mathematical models [79-81], there is still no exact solution to well model the C-S structures of the acoustic sensors. Therefore, for the demand of the solution at this stage, the damping effect of the C-S structure will be discussed and established as follows. For the circular diaphragm of the C-S design, the nonlinear Reynolds equation can be introduced for describing the air damping effect in a cylindrical coordinate [80,81]:

$$\frac{1}{r} \frac{\partial}{\partial r} \left( r \frac{\partial}{\partial r} p_d(r) \right) = -\frac{12\mu}{h^3} r \frac{d\alpha}{dt}, \quad (4-19)$$

Table 4-4  
Theoretical calculations of the quality factors for the conventional and the hybrid C-S design, respectively.

Quality factors	Conventional C-S design (case B)	Hybrid C-S design (case D)
Q for rocking mode	20.2	18.2
Q for translational mode	6.7	6.2

with the specified boundary conditions:

$$p_d(a) = 0, \text{ and } \frac{dp_d(0)}{dr} = 0, \quad (4-20)$$

where  $p_d$ ,  $\mu$ , and  $a$  are the damping pressure, the air viscosity, and the tilting angle, respectively. By integrating (4-19) with the boundary conditions (4-20), the damping pressure can be expressed:

$$p_d(r) = \frac{4\mu}{3h^3} (a^3 - r^3) \frac{d\alpha}{dt}. \quad (4-21)$$

The torque of the damping force can be then calculated as follows:

$$T_d = 2 \int_{r=0}^{r=a} \int_{\theta=0}^{\theta=\pi} p_d(r) \cdot r^2 \sin \theta \cdot dr d\theta = \frac{4\mu a^4}{9h^3} \cdot (2a) \cdot \left( a \frac{d\alpha}{dt} \right). \quad (4-22)$$

By realizing the Newton's mechanics, the damping coefficient of the membrane is the proportional constant of (4-22) and can be eventually derived as:

$$D_m = \frac{4\mu a^4}{9h^3}. \quad (4-23)$$

Similarly, by considering the similar mathematical approaches of the nonlinear Reynolds equation with specified boundary conditions to the normal motion, damping force on the diaphragm is then calculated as follows:

$$F = \int_0^a p(r) \cdot \pi r \cdot dr = -\frac{3\pi\mu a^4}{4h^3} \frac{dh}{dt}. \quad (4-24)$$

The damping coefficient of the coupled pivot is the proportional constant of the damping force and can be derived as:

$$D_p = \frac{3\pi\mu a^4}{4h^3}. \quad (4-25)$$

Generally, the sensing diaphragm is embedded in a cavity for preventing the incident sound pressure from leaking to the back [68] as shown in Figure 4-6, in which the trapped air



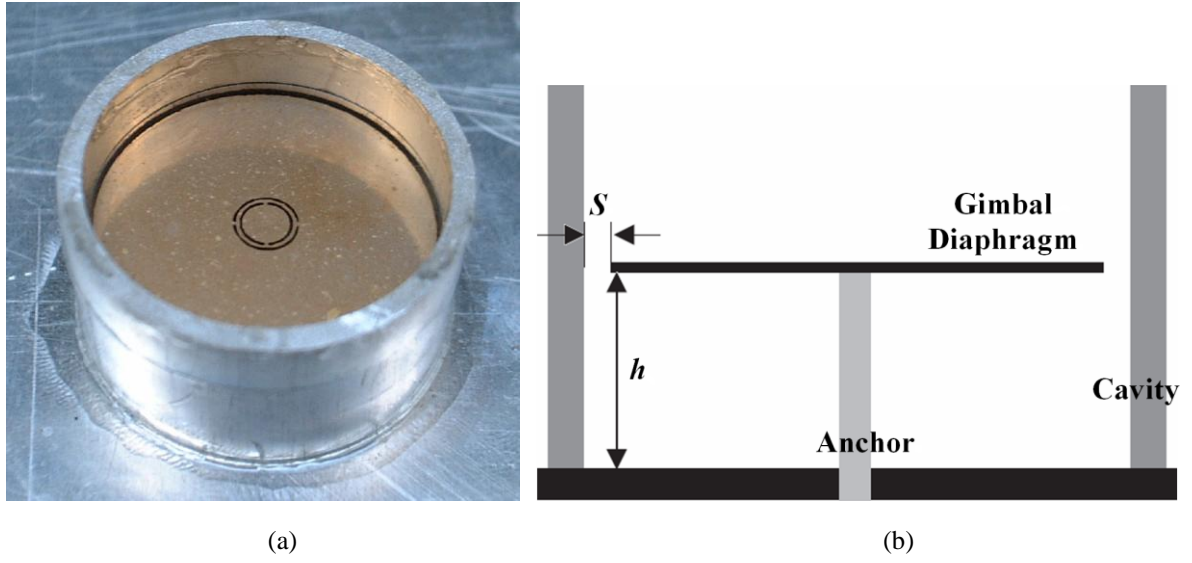


Figure 4-6: (a) A photograph of fabricated diaphragm embedded in a cylindrical cavity. (b) A side view of the diaphragm [68].

is difficult to escape to infinite space [79,82]. The air damping effect on the edge of the diaphragm from sidewalls of the cavity should be also specified. By expressing the nonlinear Reynolds equation in a three-dimensional space, (4-19) in a cylindrical coordinate can be approximately modified as [80,81]:

$$\nabla^2 p_d \approx \frac{6\mu}{h^3} \frac{dh}{dt} + \frac{12\mu}{S} \frac{dS}{dt} \approx 12\mu \left( \frac{1}{2h^3} + \frac{1}{S^3} \right) \frac{dh}{dt}, \quad (4-26)$$

where  $S$  is the distance from the sidewall of the cavity to the edge of the diaphragm and  $dS/dt$  approaches to  $dh/dt$  under the condition of small angular amplitude. Thus, the gap height mentioned in (4-23) and (4-25) should be modified as follow, while the diaphragm is embedded in the cavity:

$$h \rightarrow \left( \frac{1}{2h^3} + \frac{1}{S^3} \right)^{-\frac{1}{3}} \equiv h^*. \quad (4-27)$$

In the studied case [68], the  $h$  and  $S$  are 8000  $\mu\text{m}$  and 200  $\mu\text{m}$ , respectively, so the effective gap height  $h^*$  is about 200  $\mu\text{m}$ . The damping coefficients as well as the damping ratios for

both rocking and translational modes can then be well derived by combining (4-5), (4-23), and (4-25).

Figure 4-7 shows the comparison of the ipsilateral displacements of the conventional C-S microphone between the theoretical calculations with varying damping ratios and the measured data [68]. The measured data with the damping ratios close to unity indicates that the biomimetic microphone is critically damped. In a nutshell, the critical damping motion of the microphone leads to that the responses will directly follow the transient inputs. It should be also emphasized that even though the quality factors and the damping coefficients are derived theoretically and can well describe the responses of the conventional C-S design, the strictly experimental validations are definitely required in the further research studies.

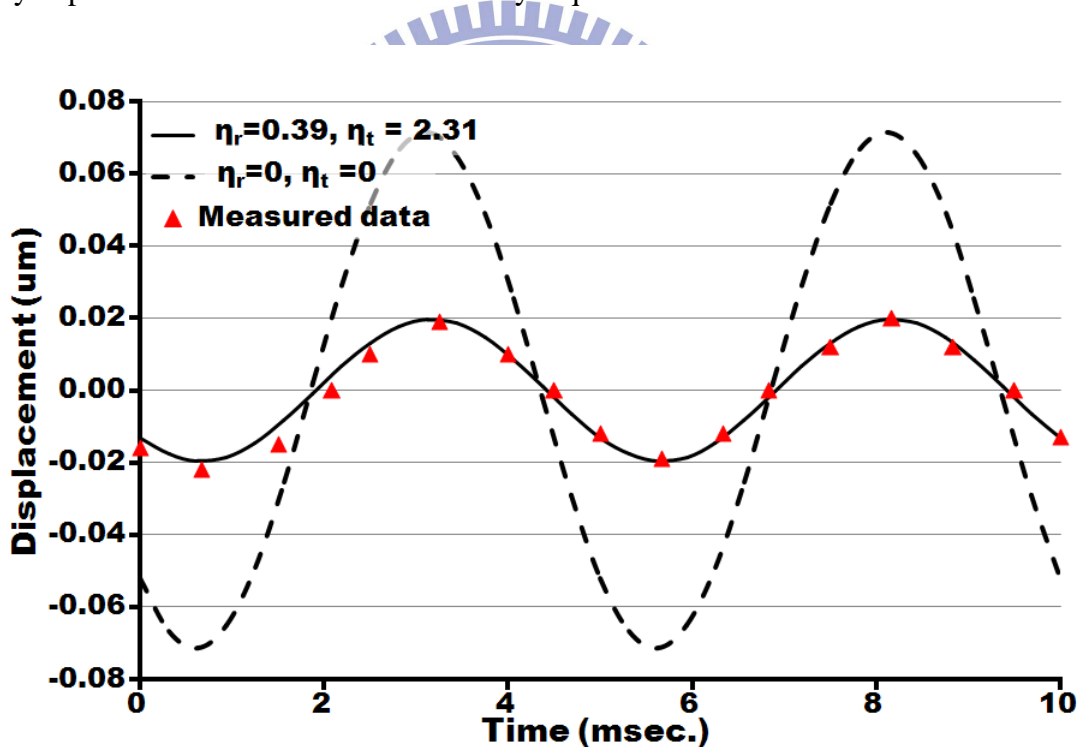


Figure 4-7: The comparison of the ipsilateral displacements of the conventional biomimetic microphone between the theoretical calculations with varying damping ratios and the measured data [68]. The damping ratios closed to unity indicates that the biomimetic microphone is critically damped so that the responses will directly follow the transient inputs.

## 4.4 Method Validation

### 4.4.1 Model Validation and Discussion

For a fair comparison of functionality between the conventional and the hybrid C-S designs, it is convenient to make  $Z_g = Z_g^{Hybrid}$  artificially, that would lead the length, thickness, and width of all beams used in the hybrid C-S design to be 8.5, 1, and 0.5 times that of the conventional design, respectively. The new structure is denoted as the *Case D* listed in Table 4-1. The comparison between the theoretical calculations and the ConventorWare simulation [75] of the  $Z_g$  and the  $Z_g^{Hybrid}$  for these two designs are respectively revealed in Table 4-2. Good data agreement also reveals the accuracy of the physical model for prediction of the undesired deflection. According to the theoretical calculations, the hybrid C-S design can enhance the amplitude of the rocking mode due to the reduction of the associated stiffness coefficient. In other words, the hybrid design exhibits better ability for the cancellation of the effect resulted by the delayed pressure received by the contralateral membrane, so it is very suitable for the applications of differential capacitive microphones. Figure 4-8 and 4-9 show the mechanical schemes with the corresponding simulation results of the conventional and the hybrid C-S designs under external influences, respectively. Obviously, the conventional C-S design of the *Case B* only has two outer beams to support the entire mass of the diaphragm as shown in Figure 4-8, whereas the hybrid design of the *Case C* has four central beams to execute the same function. Meanwhile, the hybrid C-S design of the *Case D* also reveals larger displacements than that of the conventional design of the *Case B* shown in Figure 4-9. The structure of the central floating joint accompanied with the central beams indeed provides better coupled mechanisms for improving sound source sensitivity and the resistance to undesired deformation. Therefore, the employment of the clover-stem-like gimbal structure can not only conquer the undesired gravitational force as aforementioned due to the torques of the central beams resulted by their reaction forces in the opposite direction, but also improve

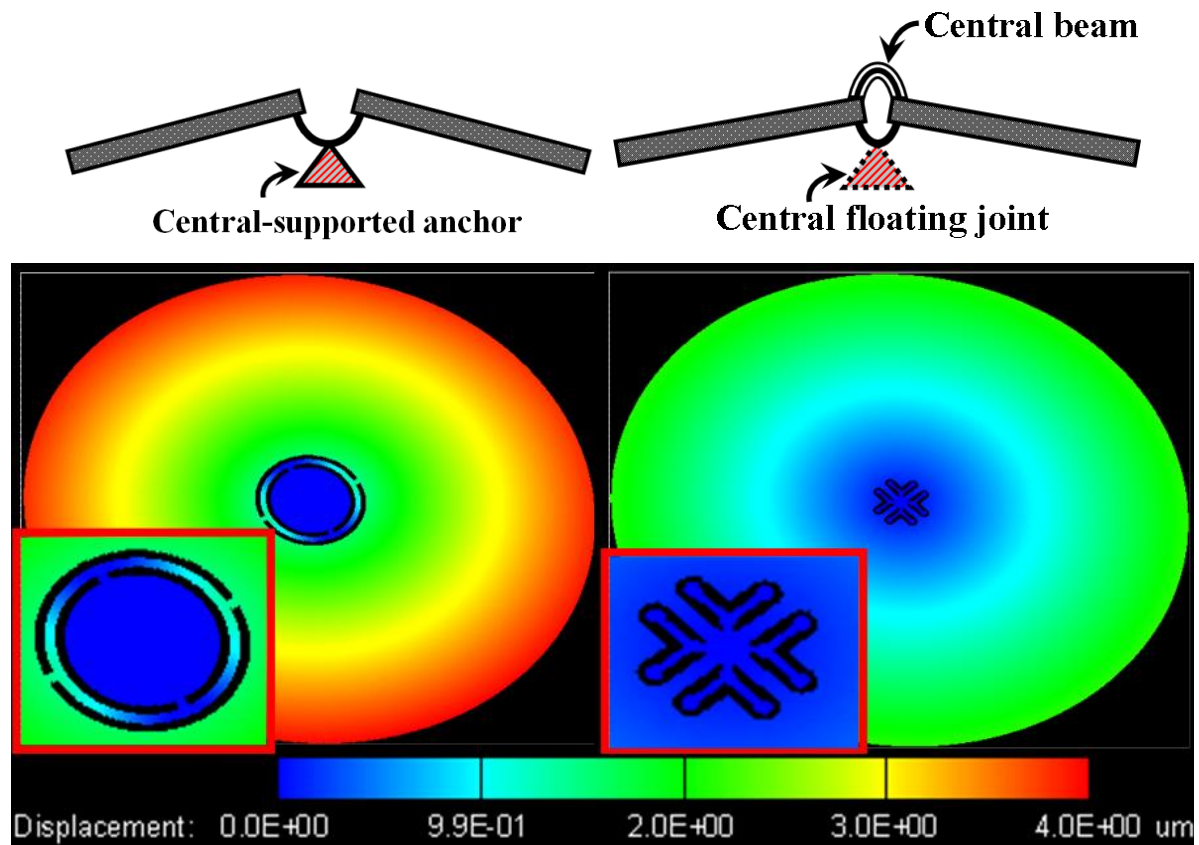


Figure 4-8: Mechanical schemes and associated simulation results of deformation of the conventional and hybrid C-S designs due to the influences of gravitational force. The conventional C-S design of the *Case B* only has two outer beams to support the entire mass of the diaphragm, whereas the hybrid one of the *Case C* has four central beams to execute the same function.

the displacement of the diaphragm by means of its mechanical coupled structure.

Figure 4-10 shows the comparison results of the measured data of the previous study [68] with the associated theoretical calculations in both of the *Case B*, and the hybrid design which is the *Case D* with specified dimensional parameters listed in Table 4-1. The stimulations of 60 dB and 200 Hz sinusoidal sound waves are employed as the loading sound source for the comparison. Two sets of the damping ratios, i.e.  $\eta_r=0.39$  and  $\eta_t=2.31$ , and  $\eta_r=0.83$  and  $\eta_t=2.43$ , respectively, are estimated and adopted in theoretical calculations of the conventional and the hybrid C-S designs, respectively. Excellent data match between the theoretical calculations and the measurement results of the conventional C-S design of the *Case B* shows the accuracy of presented physical model and further indicates that the hybrid C-S design can

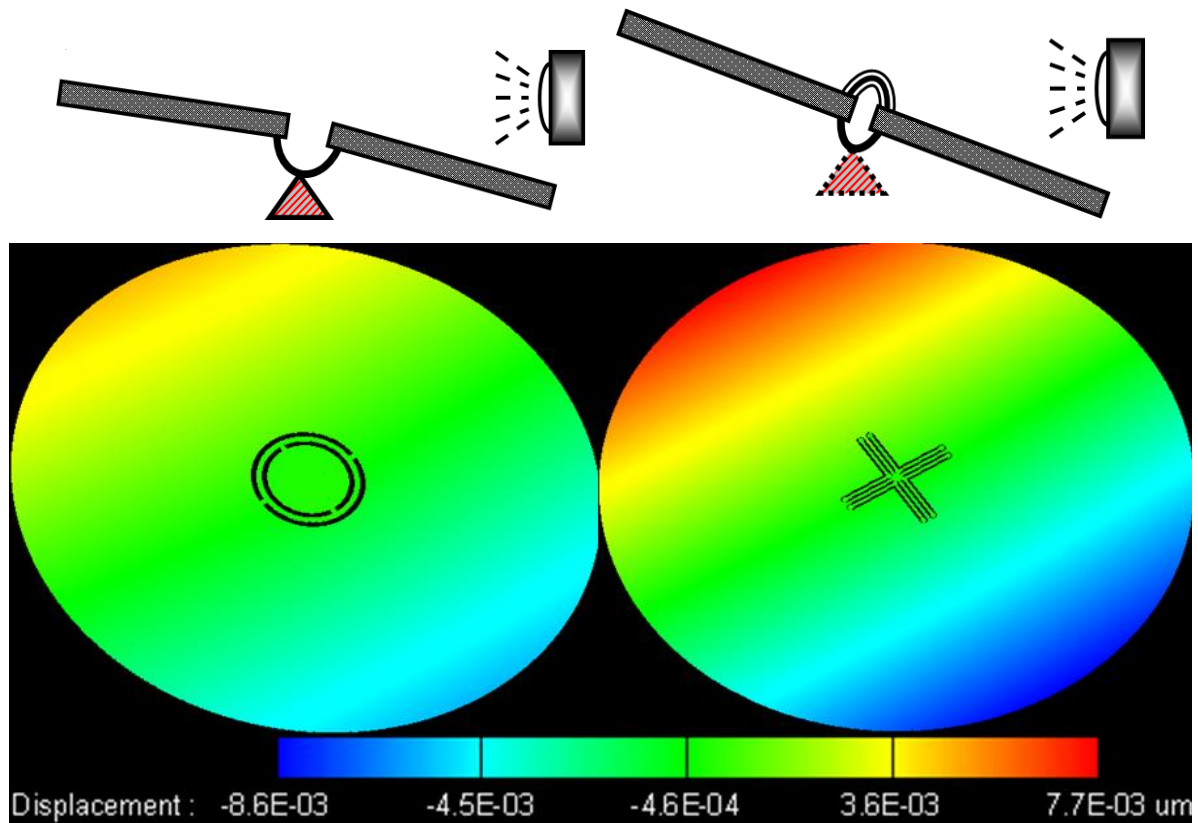
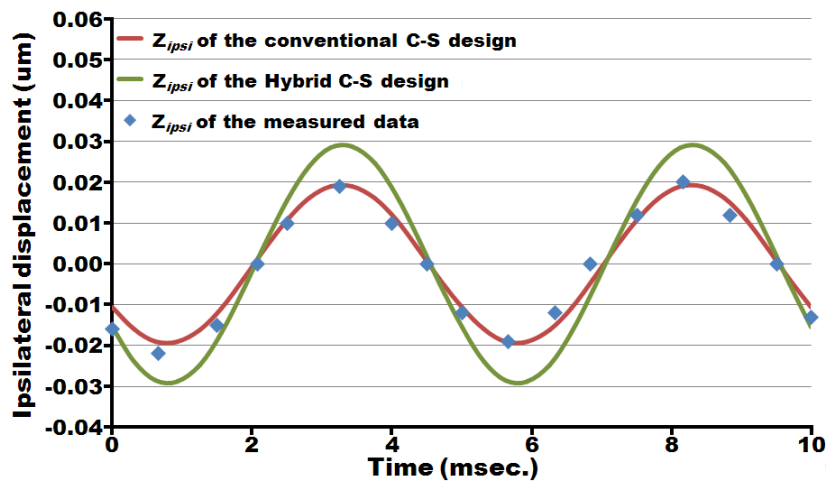


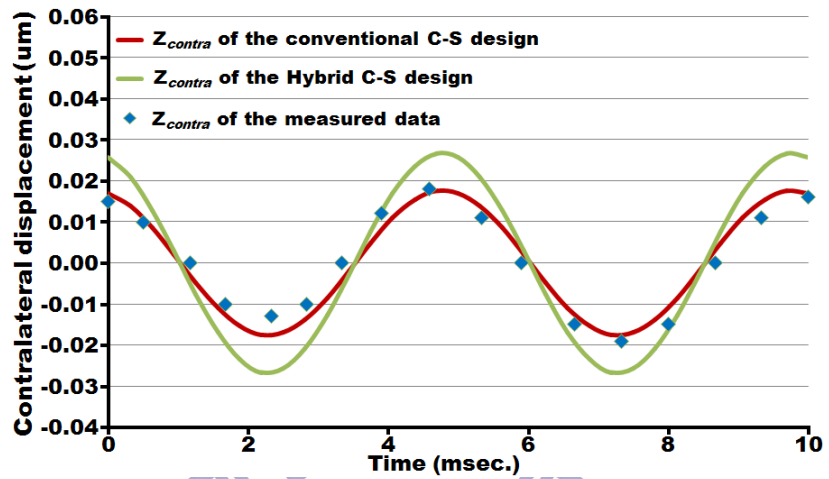
Figure 4-9: Mechanical schemes and associated simulation results of deformation of the conventional and hybrid C-S designs due to the influences of sound source pressure. The hybrid C-S design of the *Case D* reveals larger displacements than that of the conventional one of the *Case B*, in which they have the same initial deformations.

have about 47% improvement of the net diaphragm displacement. Therefore, higher sensitivity as well as directivity improvement can be realized by the proposed hybrid design in comparison with the conventional one [67,68].

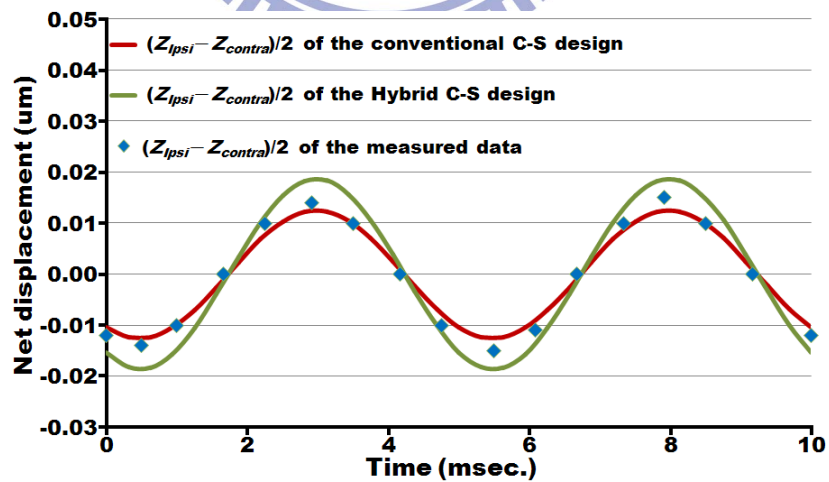
The derived model physically and mechanically reveals a finding with significant physical meanings: Based on (4-3), the displacement of the either ipsi- or contralateral membranes is dominated by the amplitude of the translational mode. The superposition of the rocking-mode motion with the amplitude of the translational mode can enhance the microphone performances. Therefore, we can safely assume that the optimal performance should happen when the resonant frequency of the translational mode nears that of the rocking mode. Meanwhile, according to a series of extensive parametrical studies from Yu's group



(a)



(b)



(c)

Figure 4-10: Comparison of the (a) ipsilateral, (b) contralateral, and (c) net displacements between model analyses and experimental measurement demonstrated by Ono *et al.* [68] with applying 60 dB and 200 Hz sinusoid sound waves, respectively.



[76,82,83] with the fly-ear and the associated structurally coupled diaphragm, they demonstrated that the fly-ear may have to use a combination of the rocking and the translational modes to achieve the high performance of sound source localization [82]. The finding is definitely a solid evidence of the result inferred from the presented acoustic model.

#### 4.4.2 Evolution from Conventional Design to the Presented Hybrid Design

It is worthy to mention that the groundbreaking research works of Miles, Hoy, and Yu indeed dramatically affect the designs of the MEMS miniature biomimetic microphones, which had been well cited as Ref. [57-61], [65], and [69-71]. The novelty of the research work from Yu's group regarding the combination of the rocking and translational modes for improving the responses of the oscillation system is indeed similar with our investigation. Different from conventional un-coupled sensors, the Yu's group also proposed a continuum-mechanical model based on the structurally coupled diaphragm by studying the sensing mechanism of the fly-ear. Figure 4-11 shows the Yu's structurally coupled design [82] and the presented hybrid CP-S design:

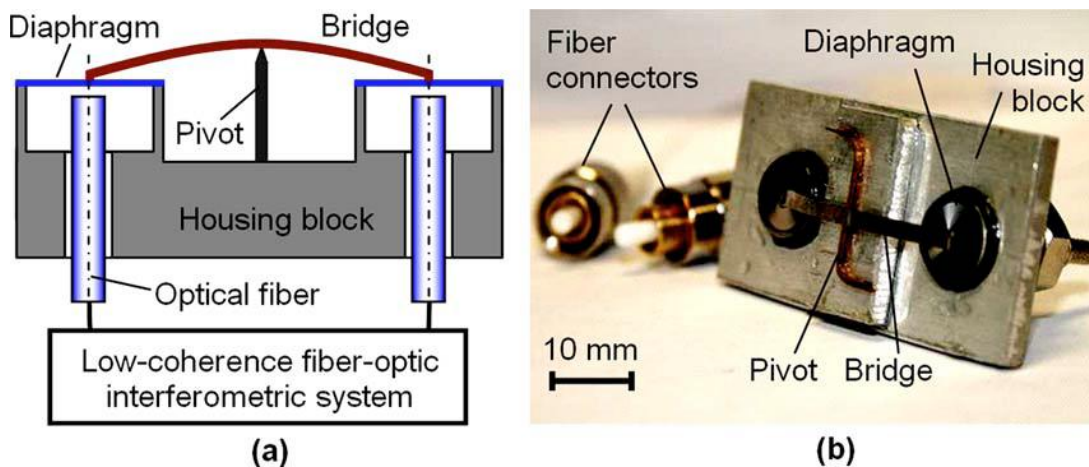


Figure 4-11: (a) The scheme and (b) the entire acoustic sensing system of Yu's structurally coupled design [82].



Morphologically and mechanically, it is obviously that the presented hybrid design has several unique progressions from the Yu's design. Figure 4-12 shows the scheme of progressive evolution.

The evolutionary processes are depicted as the follows:

- (a) Identify the fly-ear structurally coupled diaphragms from the Yu's design. Figure 4-12(a) shows the Yu's design can effectively detect the sound pressures in the X-direction.
- (b) For extending the sensing region from 1 axis to 2 axes, we consider that two Yu's designs should be combined with the same pivot for both X- and Y-directions, respectively, as shown in Figure 4-12(b).
- (c) For increasing the differentiation of the displacement between the ipsi- and contralateral diaphragms as well as reinforcing the structurally coupled mechanism, we can merge all of the discrete diaphragms and make them as an entity, as shown in Figure 4-13(c).
- (d) For conquering the residual stresses, improving the flexibility, and maintaining the sensitivity, we consider that hybridize the clover leaf, in which the four leaves are connected to the central flexible stem, with the fly-ear structurally coupled design, move out and divide the original pivot into four parts around the "floating pivot," as shown in Figure 4-14(d), would achieve all of the goals.

Therefore, by hybridizing the characteristics of the clover leaf, we proposed a new hybrid C-S design for full space detection associated with the physical acoustic model. In the new design, the conventional C-S is replaced by a structure of "floating C-S connected to four central beams." The ends of the beams do not connect to an unmovable C-S; On the contrary, they are connected to a "floating C-S" which means two ends of each beam are freely to make them more flexible. The complete physical analysis and the associated evidences by the other proposed research works listed in the Ref. and simulation have been sufficiently discussed in

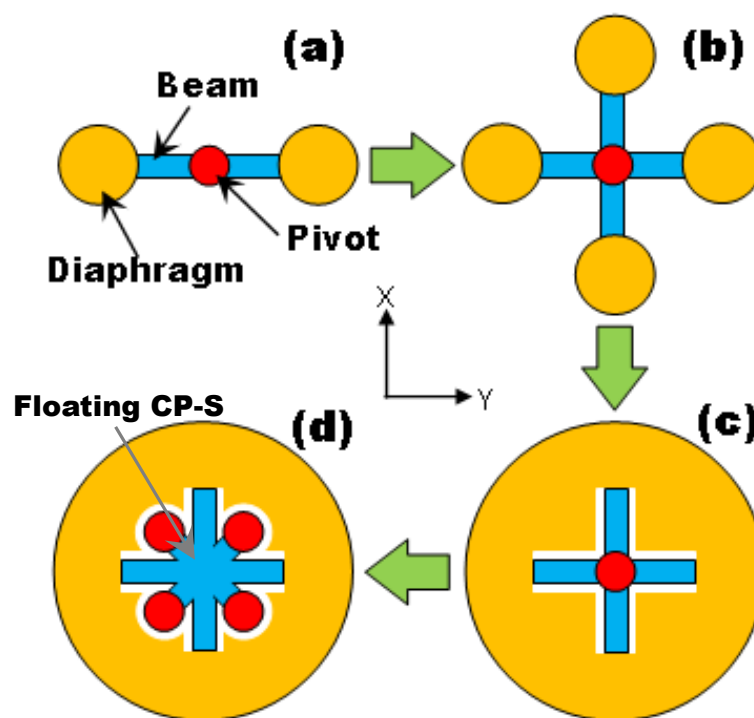


Figure 4-12: The schematic process of the evolution from Yu's design to the presented hybrid design.

detail above. The hybrid C-S design can not only inherit the merit of aforementioned research work, but also reveal the superior abilities regarding the sensitivity and directivity. The design indeed realizes the demand of full space detection.

#### 4.4.3 Comparisons Between Conventional and Hybrid C-S Designs Experimentally

##### 4.4.3.1 Processes of Microphone Fabrication

Instead of polysilicon using in the conventional biomimetic microphone, copper material reveals better electrical conductivity and lower Young's modulus than polysilicon for low power application and enhancement of sensitivity. Additionally, lower manufacturing cost and less process complexity of electroplated copper also indicate copper would be one of candidate for biomimetic microphone process. As shown in Figure 4-13, the microphone fabrication begins on a 4" silicon wafer with 0.7  $\mu\text{m}$  silicon oxide and 0.6  $\mu\text{m}$  silicon nitride

deposited on the substrate. A Cr/Cu (30nm/90nm) composited layer was employed to be the adhesion/seed layer and was sputtered on the surface. AZ4620 photoresist is spin-coated and patterned to define the area of bottom electrode and then 2 $\mu\text{m}$ -thick Cu is electroplated. After removing the photoresist by acetone, 8 $\mu\text{m}$ -thick AZ4620 is patterned as the sacrificial layer to define the region of support pillar. Another Cu electroplating is filled the region, and then 150 nm Cu layer is sputtered for the fabrication of sensing diaphragm. AZ4620 is spin-coated again to define the top electrode area follows a 5 $\mu\text{m}$ -thick Cu layer electroplating. Eventually,

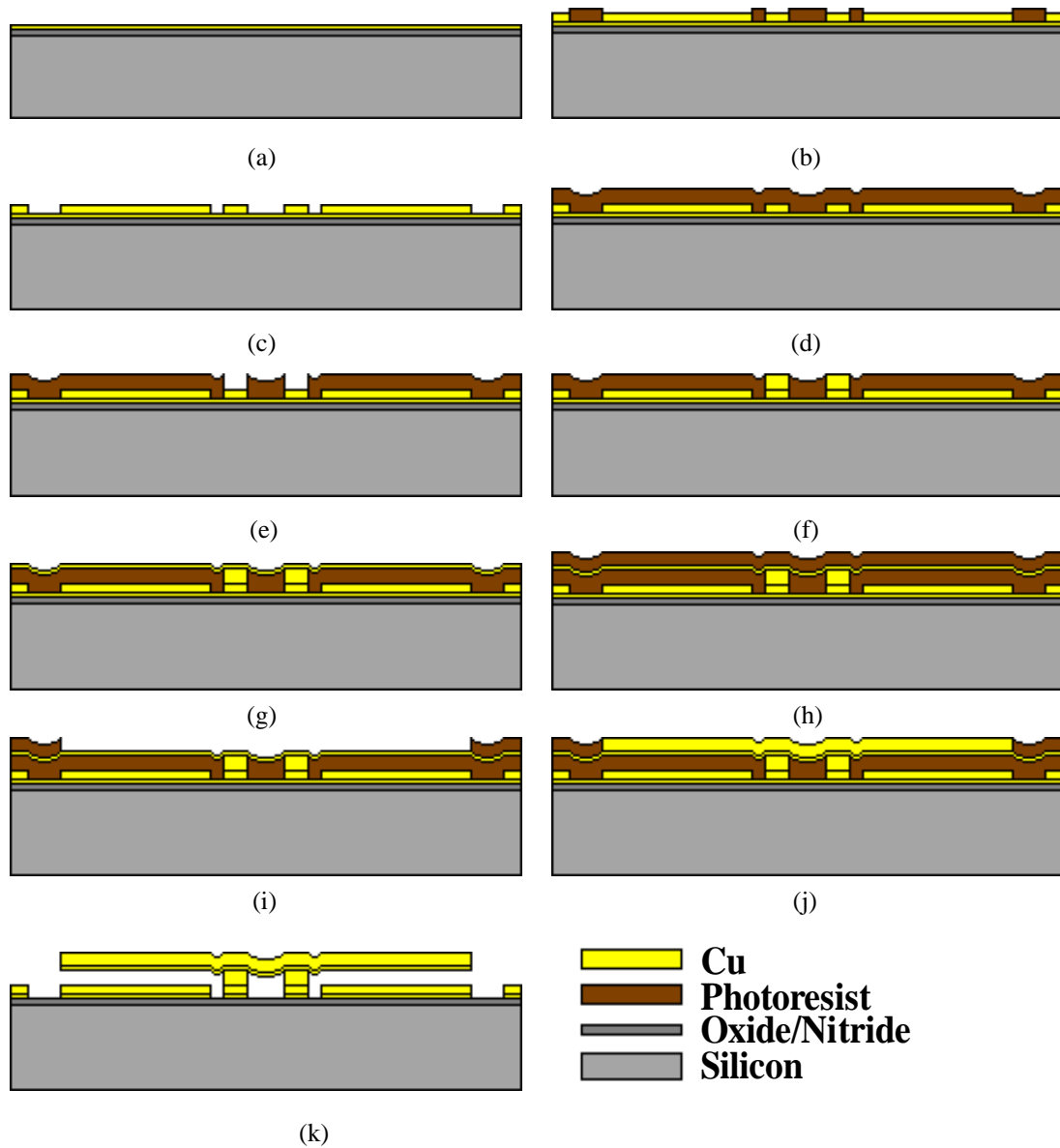


Figure 4-13: Process flow of Fabrication.

photoresist, Cu/Cr seed/adhesion layer is removed by acetone, Cu etchant, and Cr<sub>7</sub>T, respectively. To reduce the stiction effect between the sensing membrane and the bottom layer, the substrate is dipped in ethanol solution and then put on a 40°C hotplate to evaporate ethanol quickly. Therefore, the release process is completed, and Figure 4-14 shows the optical photograph of the microphone. Contact pads are reserved for the capacitance measurements [84].

#### 4.4.3.2 Comparisons between Measurements of Conventional and Hybrid C-S Designs

Table 4-5 shows the comparisons in terms of nature frequencies and mechanical performances between the parasitoid fly [76], the conventional designs [67,70,82] and the new structure. The presented hybrid design with the state-of-the-art characteristics of mIIDpA 2.7dB/mm<sup>2</sup> and mIPD 155° has shown highly potential applications for the directional microphone with full space sensitivity.

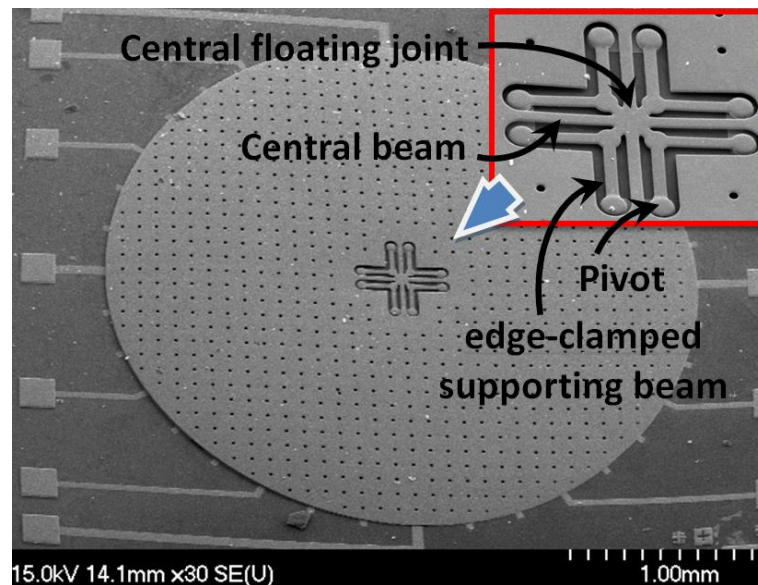


Figure 4-14: SEM photograph of the hybrid microphone [84].

Table 4-5  
Comparisons in terms of nature frequencies and mechanical performances

Comparison	First translational mode frequency	First rocking mode frequency	mIIDpA (dB/ mm <sup>2</sup> )	mIPD (deg)	Full space sensing
Parasitoid fly [76]	31KHz	7.1KHz	10.0	80	Yes
Ref. [82]	2.0KHz	1.2KHz	0.5	95	No
Ref. [67]	0.7KHz*	0.2KHz*	2.7	135	Yes
Ref. [70]	2.0KHz	X	10.5	X	No
Hybrid design	1.8KHz*	0.7KHz*	2.7	155	Yes

\* : theoretical derivation; X: not available

Meanwhile, for fairly comparison, two microphones with the hybrid and CP-S designs both having the same structure parameters listed in Table 4-6 are fabricated using a three-layer copper electroplating process [84] respectively to validate device performance. Measured resonant frequencies of the hybrid and C-S designs are about 10 and 12 KHz, respectively, close to the CoventorWare simulation as shown in Fig. 4-15(a) [84]. Better directivity and larger net displacement in the polar plot as shown in Fig. 4-15(b) reveal that the hybrid design has a superior ability in sound source localization, i.e. about 36% sensitivity and 34% directivity improvements in comparison with that of the CP-S design [84]. Figure 4-16 shows measured acoustic responses of the hybrid microphone applied with 80dB sound waves in frequency domain and it evidences that the hybrid design has well-performance at 200Hz with significant phase difference [84]. Figure 4-17 shows diaphragm displacement of the two kinds of microphones driven by a 80dB and 200Hz sinusoidal sound wave located at  $(r, \theta, \varphi) = (24\text{cm}, 37^\circ, 0^\circ)$ . The theoretical model for elaborating the dynamic response is likewise verified by experimental measurements depicted in Figure 4-17. Excellence match between calculation and measurement results indicates the accuracy of presented model and about 30% net diaphragm displacement improvement.

Table 4-6

Dimensional parameters of the conventional and hybrid C-S design

Conventional C-S design ( $\mu\text{m}$ )	
Radius of diaphragm ( $a$ )	1500
Thickness of diaphragm ( $T$ )	5
Radius of central-supported region ( $c$ )	225
Radius of ring ( $r$ )	270
Width of ring ( $W$ )	30
Length of beam ( $L$ )	30
Width of beam ( $W$ )	30
Gap height ( $h$ )	7
Hybrid C-S design ( $\mu\text{m}$ )	
Radius of diaphragm ( $a$ )	1500
Thickness of diaphragm ( $T$ )	5
Length of end-clamped supporting beam ( $L$ )	250
Length of central beam ( $L$ )	250
Width of beam ( $W$ )	15
Spacing between beams ( $b$ )	15
Gap height ( $h$ )	7

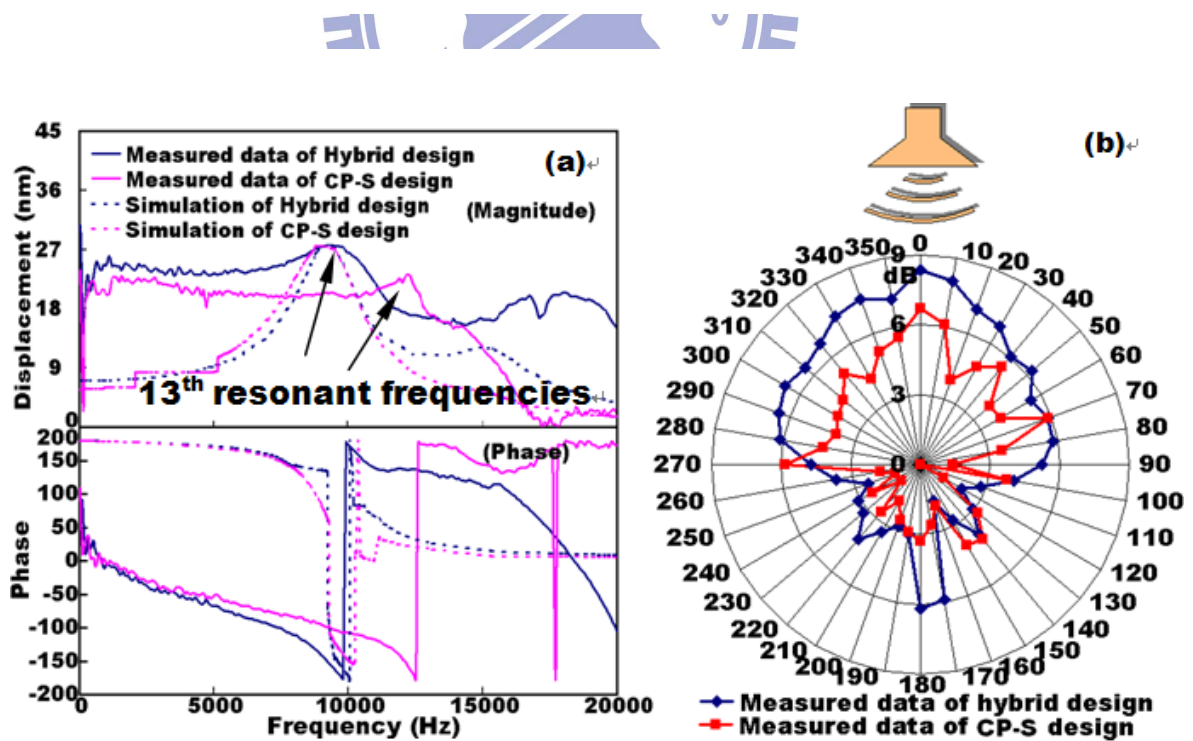


Figure 4-15: Comparison of (a) the frequency spectra and (b) the logarithmic polar patterns of net diaphragm displacement between hybrid and conventional C-S design [84].



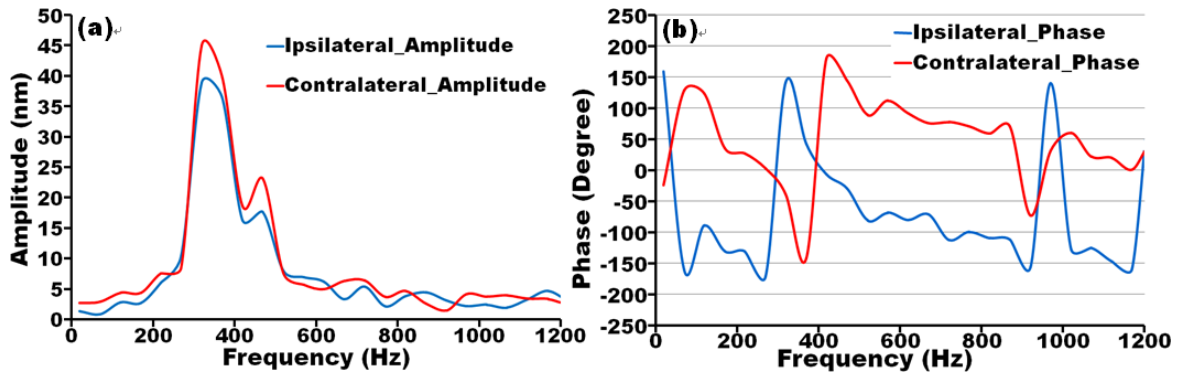


Figure 4-16: Acoustic responses of hybrid design in frequency domain in terms of (a) amplitude, and (b) phase of ipsilateral and contralateral of diaphragm, respectively [84].

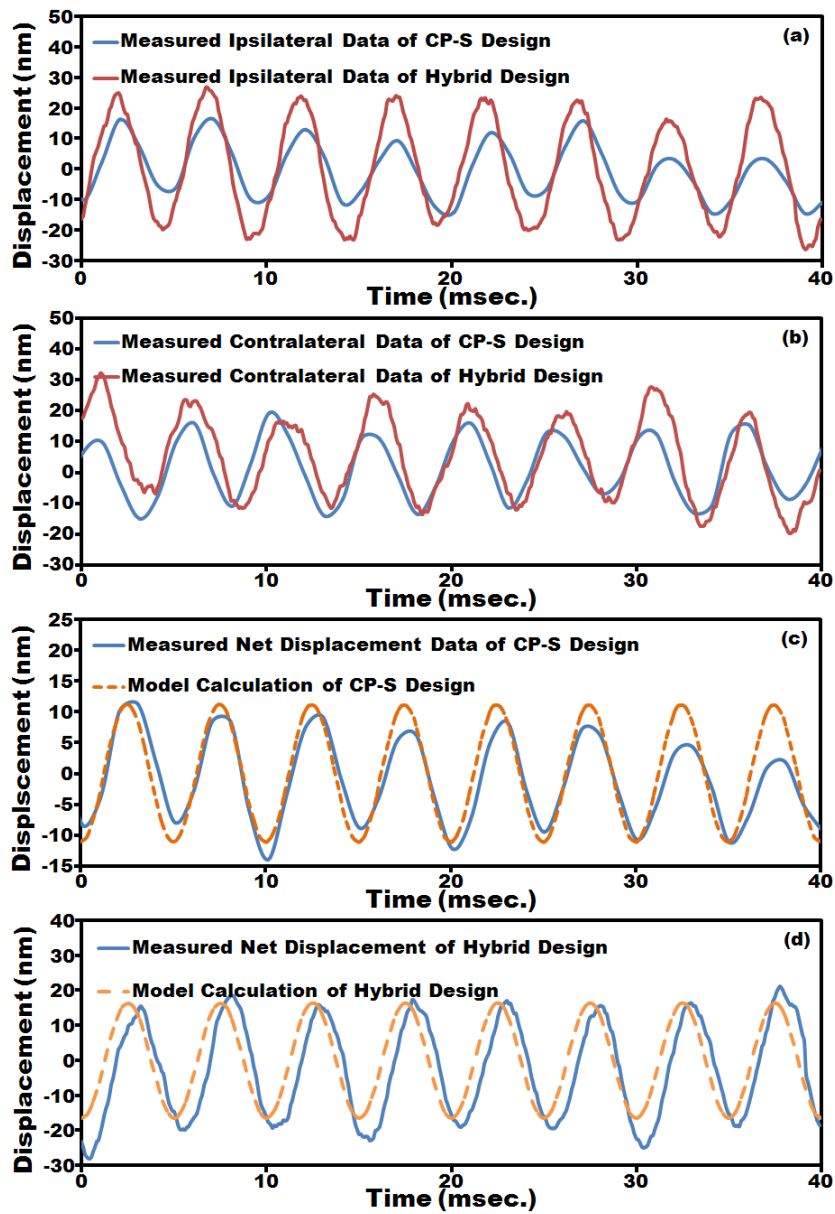


Figure 4-17: Measured (a) ipsilateral and (b) contralateral results of hybrid and CP-S design, respectively. Comparison of model and net displacement are of (c) CP-S and (d) hybrid design, respectively.



Thus, we develop a hybrid biomimetic microphone with a central floating support. Better acoustic sensitivity and directivity can be realized theoretically and experimentally. The hybrid structure can not only inherit the advantages from conventional C-S design, but also promote sound source localization sensitivity for MEMS microphones with a potential application for hearing aid devices [82].

#### ***4.5 Optimized Structure of an Acoustic Sensor***

##### ***4.5.1 Rigidity and Flexibility of a Central-Supported Diaphragm***

Newton's laws of motion are the foundation for analyzing the static and dynamic behaviors of MEMS devices under loading. For any dynamic sensor operated in steady state, one of the most expectantly encountered consequences of Newton's laws is that the vector sum of forces and torque on any part of the sensor must directly follow the transient external stimulations. For instance, the dynamic responses of developed MEMS acoustic sensor, biomimetic directional microphone, presented in Chapter 3 can directly follow the transient sound pressure input. Additionally, the gravitational force also applies on each part of the microphone and might caused undesired deformation of the diaphragm. Even though the deformation due to the gravitational force might not dramatically affect the electric signals sensed by the capacitive microphone, the gap height is limited and should be larger than the summation of the deformation due to gravitational force and the displacements caused by the external sound pressure. Larger the gap height is, smaller the capacitance is. Thus, one of the goals for optimizing a capacitive microphone is to increase its rigidity for resisting the undesired deformation resulted by the gravitational force. Nevertheless, excessive rigidity of structure of the microphone will degrade the flexibility of the diaphragm and then decrease the sensed capacitances as well as the sensitivity. The derived theoretical equations can reveal this fact in detail.

For a conventional central-supported microphone, the dynamic responses and initial deformation due to the gravitational force derived previously are

$$\begin{aligned}
Z_{ipsi}(t) &= \frac{P(t) \cdot 2\pi(a^2 - c^2)}{m} \\
&\quad \times \left[ \frac{\cos(\omega\tau/2)\sin(\omega t + \phi_i)}{\sqrt{(\omega_i^2 - \omega^2)^2 + (2\omega_i\eta_i\omega)^2}} + \frac{\sin(\omega\tau/2)\cos(\omega t + \phi_r)}{\sqrt{(\omega_r^2 - \omega^2)^2 + (2\omega_r\eta_r\omega)^2}} \right], \\
Z_{contra}(t) &= \frac{P(t) \cdot 2\pi(a^2 - c^2)}{m} \\
&\quad \times \left[ \frac{\cos(\omega\tau/2)\sin(\omega t)}{\sqrt{(\omega_i^2 - \omega^2)^2 + (2\omega_i\eta_i\omega)^2}} - \frac{\sin(\omega\tau/2)\cos(\omega t)}{\sqrt{(\omega_r^2 - \omega^2)^2 + (2\omega_r\eta_r\omega)^2}} \right],
\end{aligned} \tag{4-28}$$

and

$$Z_g = \frac{3mg(a-c)^3(a+3c)}{8ET^3(a^2-c^2)} + \frac{4mg[(2+\pi/2)L+(2+\pi/4)W]^3}{EWT^3}, \tag{4-29}$$

where

$$\begin{aligned}
\omega_i &= \sqrt{\frac{k_m + 2k_p}{m}}, & \eta_i &= \frac{D_m + 2D_p}{\omega_i m}, \\
\omega_r &= \sqrt{\frac{k_m}{m}}, & \eta_r &= \frac{D_m}{\omega_r m}, \\
k_m &= \frac{8E(a-c)T^3}{\pi^2(a+c)^3}, \\
k_p &= \frac{8(a-c)T^3}{\pi^2(a+c)^2} \left( \frac{E}{(a+c)} + \frac{G}{3a} \right) + \frac{8GWT^3}{3(a-c)^3}.
\end{aligned} \tag{4-30}$$

According to (4-28), both the ipsi- and contralateral displacements could be increased by decreasing the natural self-resonant frequencies and the damping ratios or increasing the ITD derived in (4-1). Since the operational environment is limited by the sensor packaging and the roadmap of miniaturization, the damping ratios should be determined by the squeeze film air damping effect caused in the packaging or s cavity and the ITD should be minimizing. The only way for optimizing the MEMS acoustic component is to lower the natural resonant

frequencies by considering the stiffness coefficients of the membrane and the coupled pivot in (4-30) carefully. Unfortunately, either adopting a material with lower Young's modulus or decreasing the thickness and width of the beams, all the employed ways will lead to a larger undesired deformation as indicated in (4-29). Thus, in order to overcome the drawbacks of the conventional MEMS central-supported microphone, a new design using a central floating joint has been presented in this chapter.

#### 4.5.2 The Central Floating Joint

By hybridizing the sensing mechanism of the parasitoid fly *Ormia ochracea* and flexible structure of the clover stem with four independent leaves, a new design using the central floating joint had been developed as shown in Figure 3-3. The corresponding theoretical equations for describing the dynamic responses and the initial deformation due to the gravitational force are also developed and recalled as follows:

$$\begin{aligned}
 Z_{ipsi}(t) &= \frac{P(t) \cdot 3\pi a^2}{m} \\
 &\times \left[ \frac{\cos(\omega\tau/2)\sin(\omega t + \phi_i)}{\sqrt{(\omega_i^{Hybrid}{}^2 - \omega^2)^2 + (2\omega_i^{Hybrid}\eta_i^{Hybrid}\omega)^2}} + \frac{\sin(\omega\tau/2)\cos(\omega t + \phi_r)}{\sqrt{(\omega_r^{Hybrid}{}^2 - \omega^2)^2 + (2\omega_r^{Hybrid}\eta_r^{Hybrid}\omega)^2}} \right], \\
 Z_{contra}(t) &= \frac{P(t) \cdot 2\pi(a^2 - c^2)}{m} \\
 &\times \left[ \frac{\cos(\omega\tau/2)\sin(\omega t)}{\sqrt{(\omega_i^{Hybrid}{}^2 - \omega^2)^2 + (2\omega_i^{Hybrid}\eta_i^{Hybrid}\omega)^2}} - \frac{\sin(\omega\tau/2)\cos(\omega t)}{\sqrt{(\omega_r^{Hybrid}{}^2 - \omega^2)^2 + (2\omega_r^{Hybrid}\eta_r^{Hybrid}\omega)^2}} \right],
 \end{aligned} \tag{4-31}$$

and

$$Z_g^{Hybrid} = \frac{3mg[a - (L + 2W)]^3[a + 3(L + 2W)]}{8ET^3[a^2 - (L + 2W)^2]} + \frac{mg(L - W)^3}{EWT^3}, \tag{4-32}$$

where

$$\begin{aligned}
 \omega_{in}^{Hybrid} &= \sqrt{\frac{k_m^{Hybrid} + 2k_p^{Hybrid}}{m}}, & \omega_{reversed}^{Hybrid} &= \sqrt{\frac{k_m^{Hybrid}}{m}}, \\
 k_m^{Hybrid} &= k'_d + \frac{k'_b}{2} - 4k'_t = k_m|_{c \rightarrow L+2W} + \frac{EWT^3}{2a^3} - \frac{16\sqrt{2}G[a - (L + 2W)]T^3}{3\pi^2 a[a + (L + 2W)]^2}, \\
 k_p^{Hybrid} &= k'_d + k'_b + 4k'_t = k_m|_{c \rightarrow L+2W} + \frac{EWT^3}{a^3} + \frac{16\sqrt{2}G[a - (L + 2W)]T^3}{3\pi^2 a[a + (L + 2W)]^2}.
 \end{aligned} \tag{4-33}$$

It is noted that the two parts derived in (4-29) and (4-32) present the deflection of entire diaphragms and that of beams, respectively. Meanwhile, by comparing (4-32) with (4-29), it is obvious that the value of second term of (4-32) is roughly about a quarter of that of (4-29) due to there are four central beams to support entire diaphragm in the hybrid design whereas only two beams used in the conventional design. Thus, with the same geometrical parameters, the hybrid C-S design has comparable sensitivity with but four times rigidity of structure than that of the conventional C-S design. This fact provides an advantage for further optimization using the hybrid C-S design in view of the resistance of gravity.

For fairly comparison, the geometrical parameters of the hybrid C-S design are artificially modified so that these two designs could have roughly the same initial deformations. Thus, the beams of the hybrid C-S design will much longer than that of it has previously and of the conventional C-S design. The modifications also lead to a clever consequence that the stiffness coefficients of the membrane and the coupled pivot will get closer to each other as well as the natural resonant frequencies of translational and rocking modes. Since these two designs have roughly the same stiffness coefficient of the membrane as well as the rocking-mode frequency, the translational-mode frequency of the hybrid C-S design should be decreased and then the amplitude of the mode be increased. Thus, the hybrid design has better displacements than that of the conventional one as well as better capacitance and sensitivity. Eventually, the central floating joint can not only inherit the merits of the

conventional central-supported design, but also further become the optimizing design of the central-supported one for MEMS acoustic applications.

#### **4.6 Summary**

This chapter presents a physical analysis of biomimetic microphone designed with a central-supported (C-S) diaphragm for the sound source localization. A clover-stem-like C-S design is then proposed and resulting in 47% improvement of net diaphragm displacement. The new design can effectively not only compensate undesired deformation of sensing diaphragm due to gravity and residual stresses but also make the diaphragm more flexible for better sound pressure sensitivity.



## ***Chapter 5 A New Technique of Thermal Analysis for 3D-Stacking Structure Using the Green's Theorem***

### ***5.1 Introduction***

High speed, low power consumption, robust performance, and small form factor, are four primary design issues in development of the next generation microelectronic systems [85,86]. However, undesired non-uniformly thermal effects due to drastic increase of the power dissipation within intensively operating chipsets have become significant design problems in the system development [85-88] and even restrained the design flexibility in terms of associated configurations of device packaging system and maximum power performance of integrated system circuits [85]. Several strategies and techniques concerned with predictions of the undesired thermal effects on the microsystem performance and reliability have been presented to conquer the circumstance [75,85-91]. So far, the establishment of equivalent electrothermal circuit model (EETCM) is the most efficient thermal analysis scheme which can be easily implemented in computer-aided design (CAD) programs for optimal system-IC designs to avoid undesired system functionality degradation and device failure resulted by the excess thermal accumulation. In comparison with the other analytical methods for the prediction of non-uniformly thermal effects, such as numerical solutions based on Laplace's equation [85], finite-element analysis (FEA), or boundary element method (BEM) for computer simulators [75,89,90], the EETCM can also effectively prevent data unwieldiness and time-consuming in the thermal analysis resulted by the complicated boundary conditions (BCS) associated with a system configuration. The complexity of BCS will cause a large amount of meshing work in CAD simulation which would affect the accuracy of outcomes and raise the analysis time and cost.

Therefore, for developing an efficient method for the thermal analysis of a microelectronic system with corresponding behavior predictions, this chapter will introduce a

general electrothermal network  $\pi$ -model in the system level [91] as shown in Figure 5-1. By employing the concept of the  $\pi$ -model in electronic transistors, a thermal conducting system can be decomposed into three main subcomponents which are heating source, propagated resistances, and common base resistances, respectively. From the model, the thermal interconnects from one component to the others or to external boundaries can be definitely clarified, and the external boundaries connected to the main components can be decomposed into several thermal paths to simplify the boundary conditions. Meanwhile, by introducing Green's theorem for resolving the boundary problems in the Poisson's equation of power density and heat flux gradient, new heat conduction and convection equations in an integral form can be derived to clearly specify the thermal propagations within the system and the thermal interactions between the system and its surrounding environment. Therefore, the thermal fields within the system and on the external surfaces under the prescribed thermal-field-boundary-conditions can be defined as well as the temperature distribution of the system, which can help designers easily identify the hottest spot and the primary conducting paths of the heat flux in the system.

Since late 1980's, it has been proposed to utilize silicon substrate as a cost-effective optical bench to integrate optical and microelectronic components for gigabit per second

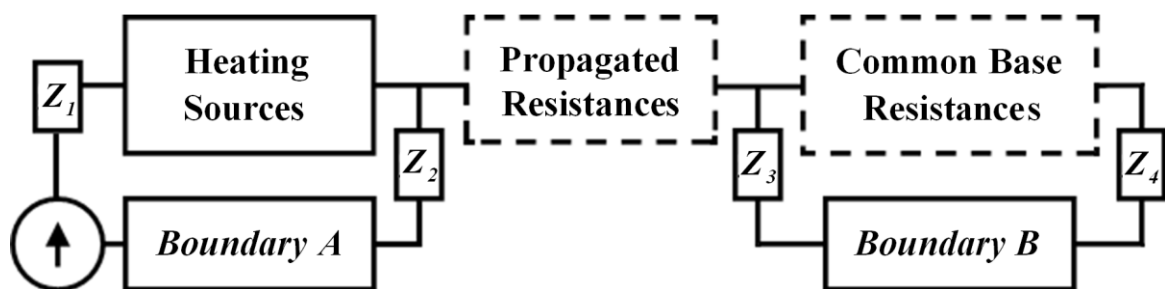


Figure 5-1: Scheme of the general electrothermal network  $\pi$ -model for thermal management [91]. By analogizing with the common electric circuit  $\pi$ -model, there are three main blocks, heating source, propagated resistance, and common base resistance, are adopted to present the thermal source, thermal flow path, and the common base, respectively.



(Gbps) high speed optical data communication applications [92-94]. The implementation of the silicon optical bench (SiOB) can greatly shrink package size and electrical interconnection length accompanying the reduction of parasitic effects in the optical transceiver system for high-speed data communication applications. Meanwhile, the SiOB can provide several unique packaging characteristics including precise optical alignment for low coupling loss from optical components to fiber cores, small thermal mismatch between the components for high reliability of the chip system, excellent thermal conductivity of silicon substrate for good chip performance with better cooling, and exact passive fabrication for good impedance matching of signal transmission within components. Nevertheless, SiOB still has its intrinsic shortcoming. Silicon is a lossy substrate material in the RF/microwave/millimeter wave regime. Electrical signals transmitted between on-chip circuitries can be easily coupled into silicon substrate to generate substrate noise. Electrical loss resulted by induced eddy current in the substrate would degrade the performance of passive components in the circuitry. In order to resolve the issue, a thick layer of dielectric, such as silicon oxide, nitride or benzo-cyclo-butene (BCB), is utilized as an electrical insulator for passive device fabrication where the loss can be greatly reduced [91]. Owing to high thermal-resist characteristic of the dielectrics, laser diode directly mounted on the top of them would have an inevitable working temperature raise that could affect the laser performance.

In the chapter, an EETCM established according to the network  $\pi$ -model is presented for the thermal behavior analysis of the silicon optical bench (SiOB). A 4-channel vertical-cavity surface-emitting laser (5G-1013nm VCSEL, BeamExpress, SA.) array is flip-chip bonded using Au-Sn solder with the SiOB as a Gbps optical transmitter where transmission lines are fabricated as electric interconnects as shown in Figure 5-2. The SiOB is monolithically fabricated with a 45° micro-reflector (see Figure 5-2(b)) and a V-groove array that can incorporate optical fibers with itself (see Figure 5-2(c)). The reflectors and V-grooves can provide precise optical alignment and coupling between fibers and VCSELs, simultaneously.

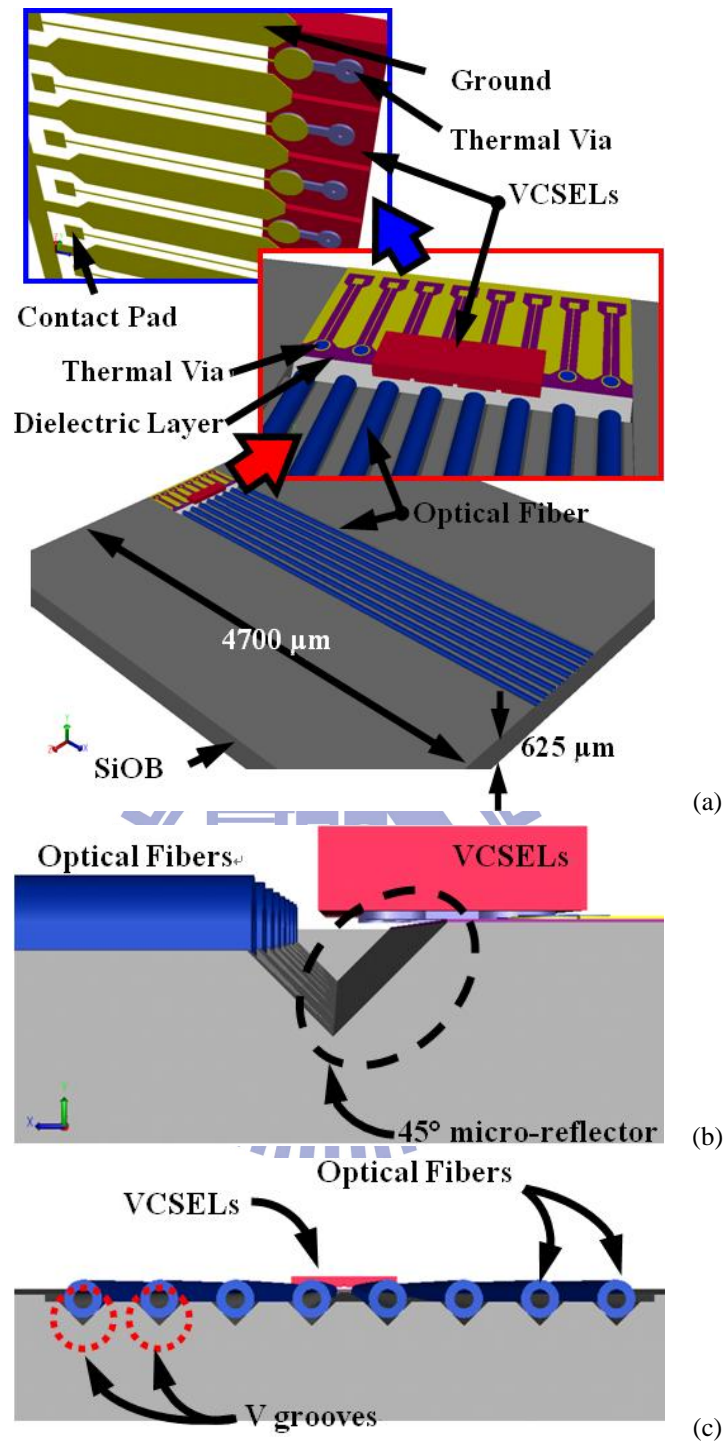


Figure 5-2: (a) Scheme of the 3-D stacked Vertical-Cavity Surface-Emitting Lasers (VCSELs) on a Silicon Optical Bench (SiOB). It is obviously that there should be complicated thermal behavior inside the SiOB due to its large volume and aspect ratio. The insertion of upper-right corner shows complicated structure of the VCSELs, the adjacent contact pads, and the thermal via in detail. The insertion of upper-left corner shows the bottom structure of the VCSELs and the interconnected thermal conducting channels. The detail profiles of the (b) 45° micro-reflector and the (c) V-groove array that are monolithically fabricated on the SiOB.

Detail SiOB design consideration and fabrication process will be discussed in the following section. Using the presented network  $\pi$ -model and the EETCM, the thermal behavior in the system and the interaction between the system and the surrounding environment can be well predicted, and the simplification of the geometrical structure used in the simulators is likewise achieved to provide a quick solution for the optical system optimization as well as thermal management.

## 5.2 Case Study: Thermal Analysis of VCSELS on a SiOB

Three main blocks labeled with heating source, propagated resistances, and common base resistances in the general electrothermal network  $\pi$ -model as shown in Figure 5-1 represent the thermal sources, the thermal flow paths, and the common base of thermal conducting system, respectively. The dash-lines enclosing each presented blocks in the network  $\pi$ -model as shown in Figure 5-1 represent an adiabatic surface [85]. The impedance parameters  $Z_i$ , where  $i$  represents 1, 2, 3, and 4, can be defined as the thermal resistance of heating source itself, nature or forced air convection, thermal capacitance, and other specified boundary conditions, and so on. *Boundary A* and *B* can be the common base of the thermal flows, other heating components of thermal conducting system with specified thermal conditions, external boundaries, or interconnections between different systems. It should be noted that icons of the source of thermal flow and the block of heating source represent the thermal generation and flow and the main heated component, respectively. As the three main blocks are definitely determined, the impedance parameters and boundaries can be specified and derived according to the configuration of the thermal system. The analysis model can provide the flexibility in resolving the analysis complexity of the thermal impedance and the external boundary problems. Additionally, the boundary conditions associated with their thermal behaviors could be further substituted by the presented thermal impedances or

*Boundary A* (or *B*). Thus, the thermal behaviors could be likewise calculated qualitatively and quantitatively by means of the Fourier's law or the following Green's theorem in terms of temperature distribution.

Thermal phenomena of a long-wavelength VCSEL are complicated due to its complex multi-layered configuration, containing an InP-based active region with several strained InAlGaAs quantum wells and followed by a composited layer in which a heavily doped p-n tunnel junction is embedded in sandwiched between two GaAs-based distributed Bragg reflectors (DBRs) in our case [95] and as shown in Figure 5-3. Thus, the thermal phenomena take place within the volume during operation will include the mutually interrelated optical, electrical, thermal and electron-hole recombination phenomena [96-98]. Meanwhile, anisotropic thermal behaviors from the non-uniform multi-layered configuration are limited by the structural geometry of the VCSEL, so an effective thermal conductivity should be adopted for replacing the conventional values of each layers in the configuration [99,100]. In addition, the nature and location of heat sources in the VCSEL are also critical characteristics, because the Joule heating is equally as important as the active region and DBRs heating in a

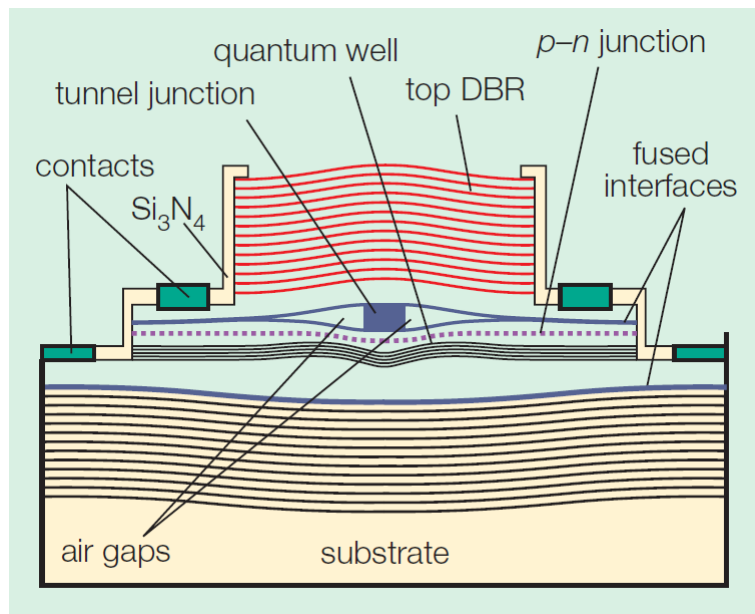


Figure 5-3: A cross-section of BeamExpress's long-wavelength VCSEL [95].

VCSEL [101,102]. Therefore, the source of thermal flow and the  $Z_1$  as shown in Figure 5-1 are merged into the block of heating source for definitely specifying the exact location of the heating source. The location of the thermal flow source is assumed at the geometrical center of the VCSEL. Meanwhile, the complicated mutually interrelated thermal phenomena will be tentatively substituted with an electric-thermal energy transfer efficiency coefficient for the steady state in the system level. In the work, an effective thermal conductivity of the VCSEL with the value of 44 W/m-K is utilized for the EECTM model for the thermal analysis.

Figure 5-4(a) and (b) show the electrothermal network  $\pi$ -model and the associated EETCM of the aforementioned 3-dimensional (3-D) stacked VCSELs on the SiOB, respectively. The two parameters, the source of thermal flow and the  $Z_1$ , are the components of the heating source in the network  $\pi$ -model since the VCSELs are the main thermal generators and also the main heated components in the case. The parameters  $Z_1$  and  $Z_2$ ,  $Z_3$ , and  $Z_4$  are thermal resistances of the 3-D stacked VCSEL ( $R_{VCSEL}$  and  $R'_{VCSEL}$ ), an infinite thermal resistance due to the negligence of nature air convection, and the thermal capacitance of SiOB ( $C_{SiOB}$ ), respectively. Both the *Boundary A* and *B* are the common bases of thermal flows for the entire thermal conducting system. Additionally, the blocks of propagated resistances are represented by a serial connection of gold ( $R_{Gold}$ ) and BCB ( $R_{BCB}$ ) layer which is parallel connected with air ( $R_{Air}$ ). The common base resistor is SiOB ( $R_{SiOB}$ ). Four switches adopted for the sources of thermal flow indicate the VCSELs can be operated individually. In fact, it is the degree of freedom in arranging the thermal impedances in the model as aforementioned. According to the Fourier's conduction law,  $R_{VCSEL}$ ,  $R_{Gold}$ ,  $R_{Air}$ , and  $R_{BCB}$  can be easily calculated as  $t_j/k_jS_j$ , where  $j$ ,  $t$ ,  $k$ , and  $S$  are adopted material, thickness, thermal conductivity, and contact area of the materials, respectively.  $C_{SiOB}$  is equal to  $Q/\Delta T$  where  $Q$  and  $\Delta T$  represent dissipated power and temperature difference between the bottom of the SiOB and ambient environment, respectively. For the purpose of convenient and fair comparison, Table 5-1 shows the dimensions and thermal conductivities of each adopted

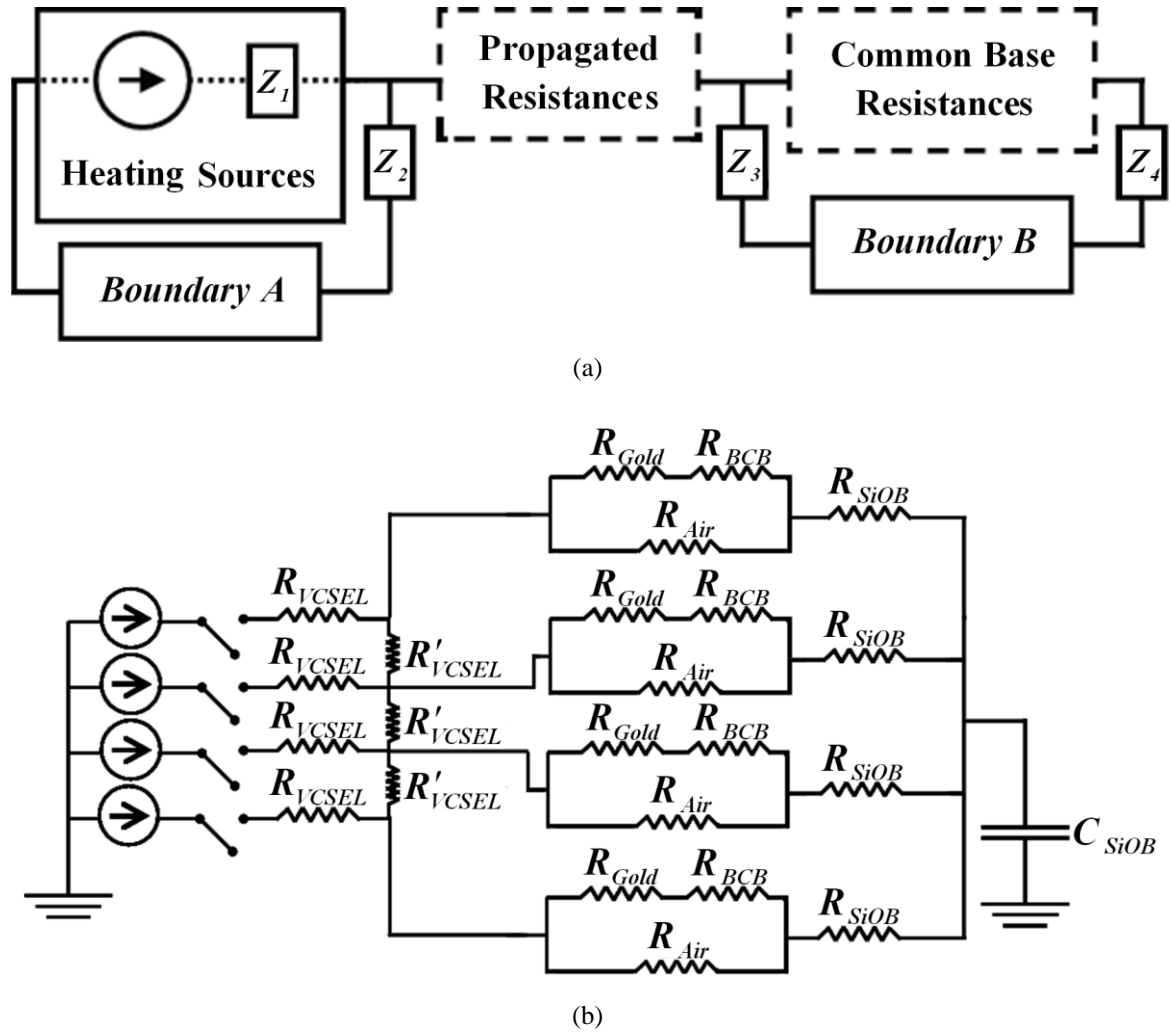


Figure 5-4: (a) Scheme of the modified general electrothermal network  $\pi$ -model. The source of thermal flow and  $Z_1$  are the components of the heating source due to the VCSELs are main heating generators themselves in our case. (b)The equivalent electrothermal circuit model of the VCSELs on the SiOB, where  $Z_1$  and  $Z_2$ ,  $Z_3$ , and  $Z_4$  are thermal resistances of VCSEL ( $R_{VCSEL}$  and  $R'_{VCSEL}$ ), an infinite thermal resistance due to without nature air convection here, and the thermal capacitance of SiOB ( $C_{SiOB}$ ), respectively.

material utilized in both of the model calculation and the simulation.

Generally, after obtaining all thermal characteristics of the components in the thermal conducting system, paths of thermal flux and highest temperature on the system can be uniquely and rapidly determined using the presented EETCM. However, the thermal behaviors within the heating sources (the 3-D stacked VCSEL) are always more complicated than the other components since they are also the power generators in the system and



Table 5-1

The Dimension Parameters and Thermal Conductivities of the Adopted Materials

Layer	Material	Thickness ( $\mu\text{m}$ )	Area ( $\mu\text{m}^2$ )	Thermal Conductivity (W/m-K)
SiOB	Silicon	625	$4.7 \times 10^7$	148
Dielectric layer	BCB	3	$2000 \times 1070$	0.29
Thermal via	Gold	12	$45 \times 45 \times \pi$	318
Contact pad	Gold	10	$3.2 \times 10^4$	318
VCSEL	GaAs	150	$250 \times 350$	44 [100]
Ground	Gold	10	$1.6 \times 10^6$	318

simultaneously contact the surfaces of the internal system and the external environment. Thus, it is necessary to employ a new mathematical technique to evaluate the temperature distribution on these contacted surfaces exactly. By realizing the requirement, the mathematical technique of the Green's theorem is adopted in this chapter to sufficiently and qualitatively describe the thermal characteristics of the 3-D stacked optical transmitter.

### 5.3 Heat Transfer Equations in Integral Form

#### 5.3.1 Steady State

##### 5.3.1.1 The Green's Theorem

Green's theorem is a mathematical tool for dealing with the problems of specified boundary conditions fixing the field values at all points in the interesting volume [103-106]. As long as field sources within the volume and net field flux on the surfaces enclosed the volume are known, the physical characteristics of the field inside the volume can be uniquely determined as well as the thermal transfer properties on the surrounding surfaces. Differing



from the previously presented graphical method of the finite-difference equations [107], Green's theorem provides more degrees of freedom for dealing with the problems of isothermal surfaces. Once isothermal surfaces of a heating system are predicted, conduction heat flux as well as adiabatic surfaces could be likewise quantitatively determined. Thus, Green's theorem is mathematically and physically one of the candidates to define the thermal characteristics of the presented EETCM of the 3-D stacked optical transmitter.

Starting from the second Green's theorem [105]:

$$\int_V [\varphi(\bar{r}') \nabla'^2 \psi(\bar{r}') - \psi(\bar{r}') \nabla'^2 \varphi(\bar{r}')] dV' = \oint_S [\varphi(\bar{r}') \nabla' \psi(\bar{r}') - \psi(\bar{r}') \nabla' \varphi(\bar{r}')] \cdot \hat{n} da' , \quad (5-1)$$

where  $\varphi(\bar{r}')$  and  $\psi(\bar{r}')$  are two arbitrary scalar fields. The parameters  $\bar{r}'$ ,  $V'$ ,  $\hat{n}$ , and  $a'$  are the position of the field source, the interesting volume, the normal unit vector of the surrounding surface enclosing the volume, and the surrounding surface, respectively. In order to describe the temperature distribution of the thermal characteristics of the heating system by means of the Green's theorem, the two scalar fields should be chosen artificially:

$$\varphi(\bar{r}') = \frac{1}{|\bar{r} - \bar{r}'|} , \quad (5-2)$$

and

$$\psi(\bar{r}') = T(\bar{r}') , \quad (5-3)$$

where  $T$  and  $\bar{r}$  are the temperature distribution and the observed point, respectively. By substituting (5-2) and (5-3) into (5-1) and using the identity:

$$\nabla'^2 \varphi(\bar{r}') = \nabla'^2 \frac{1}{|\bar{r} - \bar{r}'|} = -4\pi \delta(\bar{r} - \bar{r}') , \quad (5-4)$$

the temperature distribution is then calculated as follows:

$$T(\bar{r}) = -\frac{1}{4\pi} \int_V \frac{\nabla'^2 T(\bar{r}')}{|\bar{r} - \bar{r}'|} dV' + \frac{1}{4\pi} \oint_S \left[ \frac{\nabla' T(\bar{r}')}{|\bar{r} - \bar{r}'|} - T(\bar{r}') \nabla' \left( \frac{1}{|\bar{r} - \bar{r}'|} \right) \right] \cdot \hat{n} da'. \quad (5-5)$$

For simplifying the prescribed boundary conditions, the surrounding surface,  $a'$ , can be flexibly assumed as an isothermal surface. Thus, temperature distribution of the third term in (5-5) becomes a constant distribution, and the Green's theorem for the temperature distribution can be further modified as a temperature difference:

$$T(\bar{r}) - T(\bar{r}') \equiv \Delta T = -\frac{1}{4\pi} \int_V \frac{\nabla'^2 T(\bar{r}')}{|\bar{r} - \bar{r}'|} dV' + \frac{1}{4\pi} \oint_S \frac{\nabla' T(\bar{r}')}{|\bar{r} - \bar{r}'|} \cdot \hat{n} da'. \quad (5-6)$$

Eventually, the difference of temperature distribution for a heating system with prescribed boundary conditions could be clarified in detail by treating the volume and surface integrals in (5-6) carefully.

### 5.3.1.2 Heat Conduction Equation

Being analogy with the Poisson equation and electric-field equation in a steady state [105], the temperature sources in the volume and surface integral in (5-6) can be modified as follows:

$$\nabla'^2 T(\bar{r}') = -\frac{q_V}{k_V}, \quad (5-7)$$

and

$$\nabla' T(\bar{r}') = -\frac{q_S}{k_S} (\hat{r} - \hat{r}'), \quad (5-8)$$

where  $q_V$  and  $q_S$  are the volume power density in  $\text{W/m}^3$  generated within the interesting volume and the surface power density in  $\text{W/m}^2$  radiated from the surrounding surface, respectively. The  $k_V$  and  $k_S$  are the thermal conductivity in  $\text{W/m-K}$  for volume and surface

integrals, respectively. As the physical meanings of the conduction, the power densities mentioned in (5-7) and (5-8) represent the volume and surface densities of the thermal sources at specified points, respectively. Therefore, they indicate that the power densities of the conduction heat transfer also obey the Gauss's law.

By substituting (5-7) and (5-8) into (5-6), the difference of temperature distribution for the heat conduction as shown in Figure 5-5 can be derived as follows:

$$\Delta T = \frac{1}{4\pi} \int_V \frac{q_V}{k_V |\vec{r} - \vec{r}'|} dV' - \frac{1}{4\pi} \oint_S \frac{q_S (\hat{r} - \hat{r}') \cdot \hat{n}}{k_S |\vec{r} - \vec{r}'|} da' . \quad (5-9)$$

For constant power density and isotropic thermal conductivity, (5-9) could be further simplified by setting the field source on the original point:

$$\Delta T = \frac{q_V}{3k_V} |\vec{r} - \vec{r}'|^2 - \frac{q_S}{k_S} |\vec{r} - \vec{r}'| (\hat{r} - \hat{r}') \cdot \hat{n} . \quad (5-10)$$

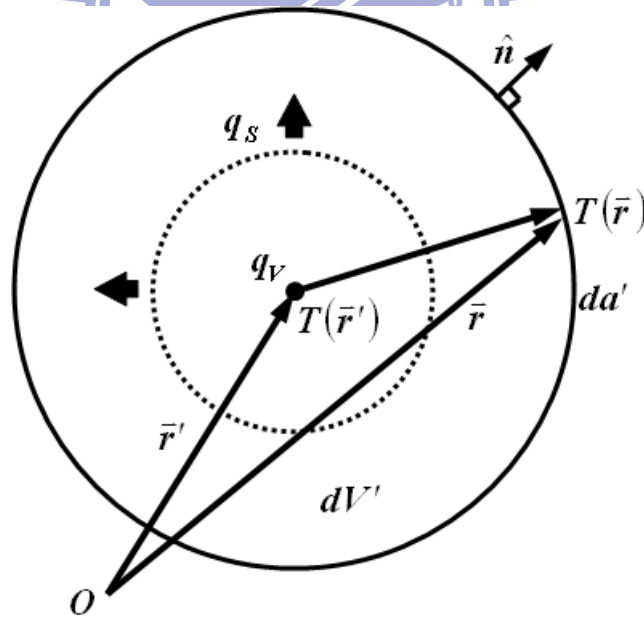


Figure 5-5: Scheme of conduction heat transfer sphere with specified volume and surrounding surface. The parameters  $q_V$  and  $q_S$  are the volume power density in  $\text{W/m}^3$  generated within the interesting volume and surface power density in  $\text{W/m}^2$  radiated from the surrounding surface, respectively. The propagation direction of the surface power density is outward and parallel with the normal unit vector. The difference of the temperature distribution could be well determined using the derived conduction heat transfer equation in integral form.

Physically and conceptually, (5-10) could be simply tackled as a one-dimension problem by assuming  $3k_v = k_s = k$  and realizing the vector difference to be the thermal conducting path,  $\Delta L$ , and it will become:

$$\Delta T = \frac{q_v}{k} \Delta L^2 - \frac{q_s}{k} \Delta L (\vec{r} - \vec{r}') \cdot \hat{n}, \quad (5-11)$$

or

$$k \frac{\Delta T}{\Delta L} = q_v \Delta L - q_s (\hat{r} - \hat{r}') \cdot \hat{n} \equiv q \Delta L - q_n. \quad (5-12)$$

Eq. (5-11) indicates that the subtraction of the power density radiated from the surrounding surface from the power density generated within the interesting volume will be equal to the product of the temperature gradient and the thermal conductivity in one-dimension for the case in a steady state. In a source free volume, (5-12) definitely becomes the so-called Fourier's Law in heat conduction [107], that also validates the correction of the equality assumption of  $3k_v = k_s = k$ . The aforementioned (5-9) is, thus, the integral form of the heat conduction equation. Meanwhile, the thermal resistances specified in the EETCM shown in Figure 5-3(b) can be derived as:

$$R = \frac{3q \int_V \frac{dV'}{|\vec{r} - \vec{r}'|} - q_n \oint_S \frac{da'}{|\vec{r} - \vec{r}'|}}{4\pi k q_n \int_S (\hat{r} - \hat{r}') \cdot \hat{n} da'}. \quad (5-13)$$

### 5.3.1.3 Heat Convection Equation

By recalling (5-6) and considering that there is no power source in the mechanism of heat convection, the temperature difference resulted by the convection as shown in Figure 5-6 can be described as follows:

$$\Delta T = \frac{1}{4\pi} \oint_S \frac{\nabla' T(\bar{r}')}{|\bar{r} - \bar{r}'|} \cdot \hat{n}' da' . \quad (5-14)$$

Slightly different from the definition of the surrounding surface in (5-9), the surface of heat convection mechanism could be extended to the surrounding where the surface temperature,  $T_\infty$ , maintains as a constant and will not be influenced by the internal heating systems. Thus, by substituting (5-8) into (5-14), the temperature distribution resulted by the heat convection can be obtained by the derived temperature difference. Using similar approaches of (5-10) and (5-11), the temperature difference can be simplified as follows:

$$\Delta T = -\frac{q_s}{k} \Delta L(\bar{r} - \bar{r}') \cdot \hat{n}' = \frac{q_n}{h} , \quad (5-15)$$

or

$$q_n = h\Delta T = h[T(\bar{r}') - T_\infty] , \quad (5-16)$$

where  $h$  is  $k/\Delta L$  and called the convection heat transfer coefficient in  $W/m^2\cdot K$ . It is noted that

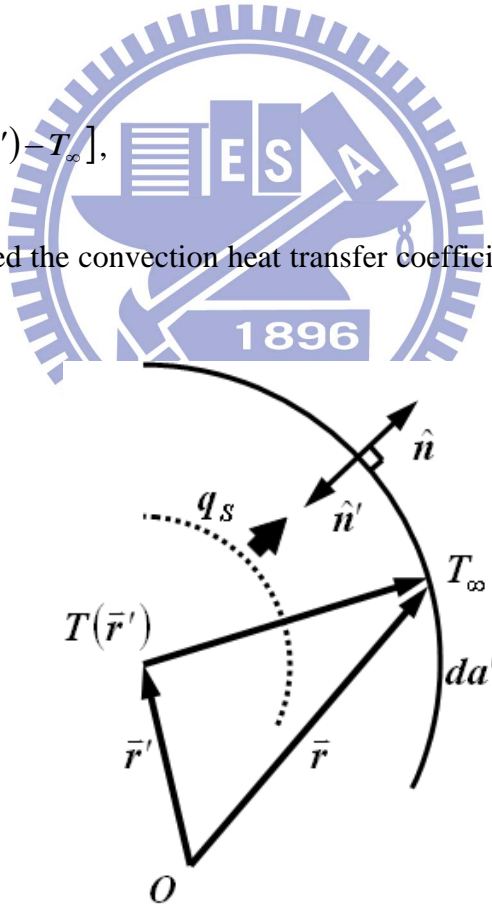


Figure 5-6: Scheme of convection heat transfer sphere with specified surrounding surface. The propagation direction of the surface power density is outward and anti-parallel with the normal unit vector,  $\hat{n}'$ . The difference of the temperature distribution could be well determined using the derived convection heat transfer equation in integral form.

the direction of the normal unit vector,  $\hat{n}'$ , is inward to surface and opposite to the direction of the  $\hat{n}$ . Eq. (5-16), therefore, becomes the so-called Newton's Law of cooling [107], and then (5-14) is the integral form of the heat convection equation.

It is noted that there are three physical mechanisms of heat transfer for the heating system, conduction, convection, and radiation. Although the integral forms of the conduction and convection mechanisms have been qualitatively derived above, the mechanism of the radiation is still not clearly defined in this section. The difficulty to definitely determine the integral form of the radiation is due to its nature of the heat transfer. Being different from the mechanisms of the conduction and convection, i.e. random molecular motion and bulk motion of fluid, only an isothermal surface should be undertaken in the integral. The mechanism of the radiation has to deal with the energy interchanges between two surfaces from the system and the surrounding environment, respectively. Thus, it needs the Green's theorem with more complicated configuration. Fortunately, according to the Stefan-Boltzmann law, the radiation mechanism only can dominate at a very high temperature region, so the mechanism can be neglected in the case concerned in the microelectronic systems [107]. At final, it is more convenient to use the integral forms for the thermal analysis rather than the conventional Fourier's Law and Newton's Law of cooling since these forms could easily elucidate the associated characteristics between the isothermal surface and the power density simultaneously in all thermal conducting components.

### **5.3.2 Transient State**

Transient time is a critical value in the high speed optical data communication applications. As the switching time of data communication is close to thermal transient time, thermal noises could be hybridized into the original signals. Meanwhile, high-frequency signals transmitted within multi-channels might be even mixed each other due to the drastic

thermal cross talks. Thus, it is necessary to convert the mentioned steady-state equations into the transient state to organize the transient time occurring in a heating high speed communication system. Since the above heat conduction and convection equations developed by the Green's theorem have been verified to obey the Gauss's law, the Laplace heat transfer equation, and the Newton's law of cooling, (5-7) and (5-8) should also follow to the heat transfer equation. Thus, (5-7) could be modified as:

$$\nabla'^2 T(\vec{r}') + \frac{q_V}{k_V} = \frac{\rho c_p}{k_V} \frac{\partial T(\vec{r}')}{\partial t}, \quad (5-17)$$

where the term right-hand side is time rate of change of the sensible (thermal) energy of the medium per unit volume. The product of mass density  $\rho$  and specific heat  $c_p$  (J/m<sup>3</sup>K), commonly termed the volumetric heat capacity, measures the ability of a material to store thermal energy. The (5-9) and (5-13) eventually in the transient state should be modified respectively as:

$$\Delta T = \frac{1}{4\pi} \int_V \frac{q_V}{k_V |\vec{r} - \vec{r}'|} dV' - \frac{1}{4\pi} \oint_S \frac{q_S (\hat{r} - \hat{r}') \cdot \hat{n}}{k_S |\vec{r} - \vec{r}'|} da' - \frac{1}{4\pi} \int_V \frac{\rho c_p}{k_V |\vec{r} - \vec{r}'|} \frac{\partial T(\vec{r}')}{\partial t} dV', \quad (5-18)$$

and

$$R = \frac{3q \int_V \frac{dV'}{|\vec{r} - \vec{r}'|} - 3q_n \rho c_p \int_V \frac{\partial T(\vec{r}')}{\partial t} \frac{dV'}{|\vec{r} - \vec{r}'|} - q_n \oint_S \frac{da'}{|\vec{r} - \vec{r}'|}}{4\pi k q_n \int_S (\hat{r} - \hat{r}') \cdot \hat{n} da'}. \quad (5-19)$$

Thus, according the time-dependent equations mentioned above, an algorithm coding by employing MATLAB compiler is developed. Therefore, the corresponding transient isothermal maps of the VCSELs obtained used FEM simulation and EETCM-based algorithm are revealed physically and mathematically as shown in Figure 5-7 with a 30 ms time interval



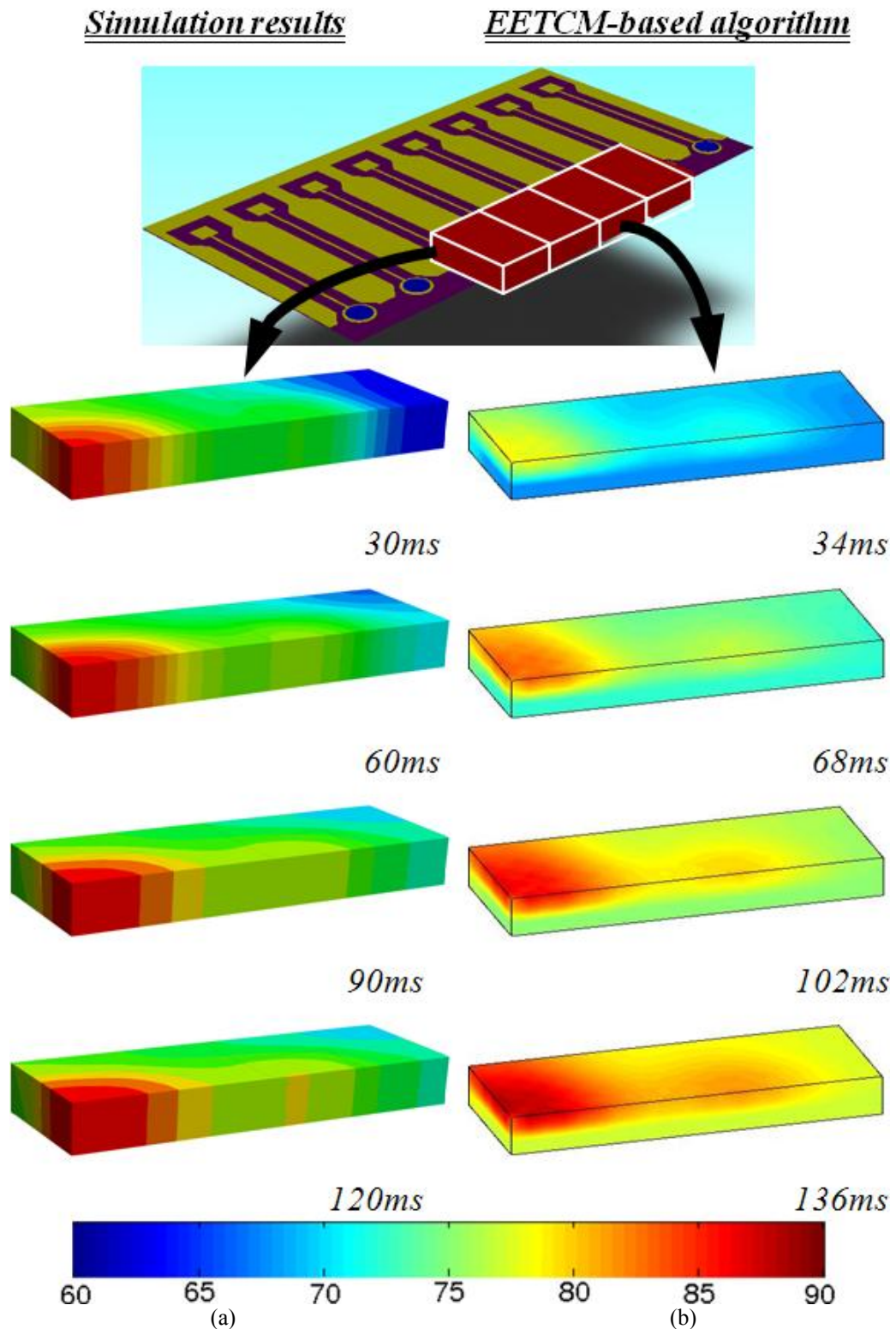


Figure 5-7: Transit isothermal maps of (a) the simulation results and (b) the EETCM-based algorithm. Time interval between each map is about 30 ms and is evaluated by taking the trick that total input power within a mesh volume-element in a step of iteration divided by the power generated during 1 sec.

for two VCSELs turn-on situations, respectively. The transit time is evaluated by taking the trick that total input power within a mesh volume-element in iteration is divided by the power

generated during 1 sec. The first step of the map starts with 30 ms. At the stage, the temperature covered each VCSEL is almost the same as that at bottom of the SiOB and indicates the good thermal conducting ability of thermal vias underneath. In the case, the total transient time obtained used FEM simulation is about 120 ms and used EETCM-based algorithm is about 136 ms, respectively. The prior analysis using the presented time-dependent algorithm is necessary. Thus, the presented algorithm can be one of the candidates for predicting the thermal phenomena in high speed data communication applications.

#### ***5.4 Computational Algorithm in View of Integral Form***

Undesired thermal impact is indeed one of main issues in the technology development of 3D-Stacking Structure (3D-SS) design, such as 3D Integrated Circuits (3DICs), optical data communication on the SiOB, and Through Silicon Vias (TSV) Interposer, and so on. For instance, one of proposed efficient strategies to build high-performance 3D microprocessors is to introduce thermal vias through layers or dies at specific locations. However, effectively deployment of the layers with varied thermal conductivities and minimization of the utilization of interconnect vias in the structure should be strictly considered in associated algorithms [10-12]. Additionally, thermal interface material used in chip- and package-level for heat dissipation [10,13] will also result in inevitable 3D-SS layout complication in design stage and manufacture cost increase which should be still undertaken. To conquer the aforementioned drawbacks and consider the transient effect in the high speed data communication applications, a tentative algorithm in view of integral form is developed to describe the path of thermal flow and temperature distribution for any heating stacked system or structure.

As mentioned previously, the general electrothermal network  $\pi$ -model as shown in

Figure 5-1 could be employed for simplifying complicated configuration and thermal boundary conditions of powered 3D-SS by means of decomposing the structure into three main components, heating sources, propagated resistances, and common base resistances, respectively. However, there is so far no sufficient algorithm which can efficiently and simultaneously resolve the presented problems, such as prediction of hottest temperature, description of thermal cross talks, arrangement of the thermal vias as well as their dimensions, employment of suitable material for thermal conduction in chip- and package-level, device optimization with physical intuition, responses during transit region, and so on. To achieve all of the requirements, a new algorithm in viewing of integral forms based on the Green's theorem is presented by dealing with the problems of specified boundary conditions fixing the field values at all points in the interesting volume. As long as thermal field sources within the volume and net field flux on the surfaces enclosed the volume are known, physical characteristics of thermal field inside the volume can be uniquely determined as well as the transfer properties on the surrounding surfaces. Meanwhile, volume and surface integrals reveal new treatments of the heating sources and isothermal surfaces, respectively. Once isothermal surfaces of a heating system are predicted, conduction heat flux as well as temperature distribution could be likewise quantitatively determined. The time-dependent temperature distribution and thermal resistance in integral forms that built by the Green's theorem have been developed as (5-18) and (5-19) above.

Figure 5-8 and 5-9 show the temperature distributions of single VCSEL and two VCSELs realized using the presented algorithm coding by MATLAB compiler. Each laser diode is operated with 8 mA input current and 2 V bias. Good mapping agreements between the image and the isothermal map verify practicality of the presented technique. The isothermal map can definitely point out the locations of the heating sources in the operated VCSEL and main paths of thermal flux. The inclined surfaces with slight curvature in the isothermal maps indicate the locations of interfaces between heating sources and surrounding

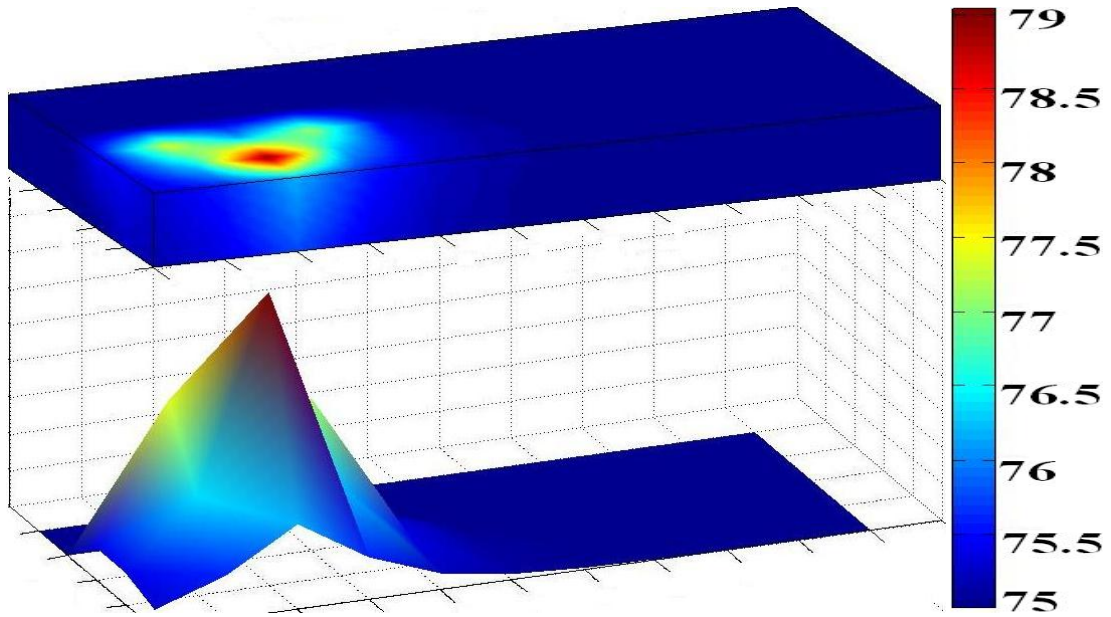


Figure 5-8: Temperature distribution of single VCSEL realized using the presented algorithm in steady state. The bottom of SiOB is constrained at 75°C to imitate the operation environment of a typical optical transceiver system.

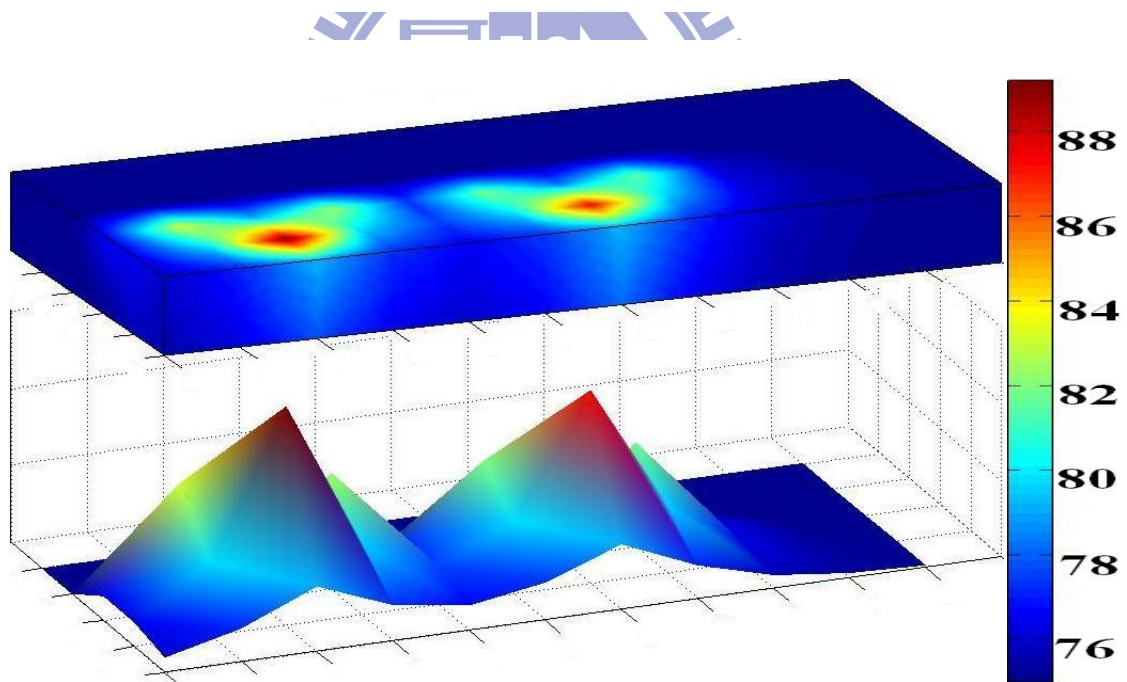


Figure 5-9: Thermal images of the optical system heated by two operated VCSELs coding by the presented algorithm.

materials. Regions of the isothermal maps also reveal the extent of thermal dissipations propagating from heating sources. Thermal cross talks as shown in Figure 5-9 resulted by the thermal accumulation between the two heating sources is embodied in the corresponding isothermal map. Higher and sharper isothermal tip of the lateral heating source indicate the



associated thermal dissipation is constrained by the adjacent heating source. Since the transient time is comparable with switching time of a 10 Gbps SiOB-based optical transmitter, it is necessary to develop a corresponding algorithm using in high speed optical data communication applications. The relative codes of the algorithm are referred to Appendix B.

## **5.5 Method Validation**

### **5.5.1 Simulation Validation**

Four VCSELs are stacked on a 625  $\mu\text{m}$  thick SiOB which is operated in the air without having artificial convection. The bottom of the SiOB is an isothermal surface where is setting at 75°C to imitate the operation environment of a typical optical transceiver system. All other surfaces are adiabatic, where no heat flux is allowed as mentioned by the EETCM for the thermal analysis. According to the presented EETCM as shown in Figure 5-3(b), the contributions of thermal resistances of air within the components, of propagated resistances, and of SiOB within the common base resistances could be ignored since they have a large thermal resistance values in the part of parallel connection and a small resistance value in the part of serial connection, respectively. The materials of air and SiOB could be reasonably removed both in the model calculation and the CoventorWare simulation [75], so more than 80% reduction of required meshes can be achieved as well as the requirements of CPU time and memory operation in this case.

In the system, the hottest spot should be determined for realizing a reliable 3-D optical stack. Using the derived heat conduction and convection equations, the isothermal surface surrounding the source could be uniquely determined. The value of the volume power density in the source can be obtained by means of the product of the input power of the VCSEL per volume and its efficiency:

$$q_v = \frac{I^2 R_h}{V_h} \times \eta \quad (5-20)$$

where  $I$ ,  $R_h$ ,  $V_h$ ,  $\eta$  are the input current, electric resistance of the heating source, volume of the heating source, and the electric-thermal energy transfer efficiency coefficient, respectively. As shown in Figure 5-10, while the lateral single laser is turned on, the configuration of the isothermal surfaces reveals the probable location of the hottest spot according to the calculation of the EETCM. Table 5-2 listed the theoretical thermal resistances of each adopted material. After determining the hottest spot within or on the surface of the heating source, the temperature distribution could then be determined using (5-9) and (5-14) by evaluating the thermal distribution from the other two main components and the external boundary conditions, which are surrounded by free air without artificial convection. The thermal resistance of each component can be also derived using (5-13). Figure 5-11 shows the

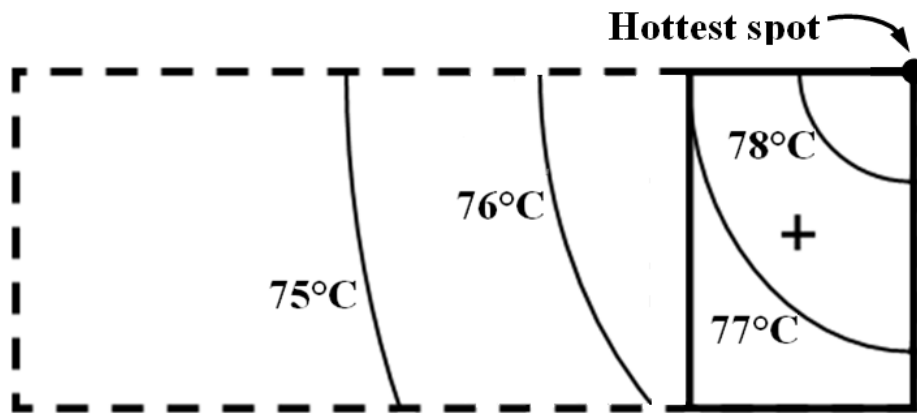


Figure 5-10: The isothermal surfaces determined by means of the conduction and convection heat transfer equation. In the case, only the lateral single laser turned on where represented using the symbol “+”. The input current is limited at 8 mA and the electric-thermal energy transfer efficiency is 85.7% to meet the standard specification of the semiconductor-made VCSELs [108]. The theoretical temperature at the hottest spot is 78.4°C.

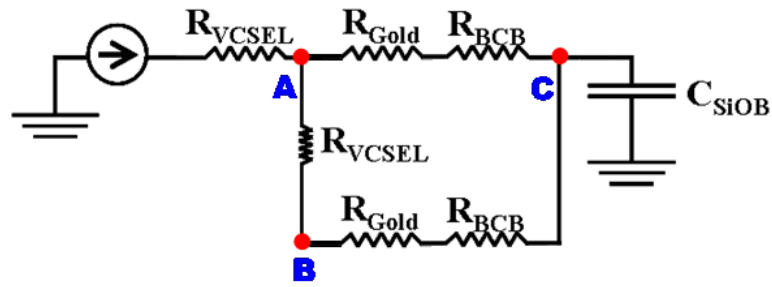
Table 5-2  
The Theoretical Thermal Resistances of Each Adopted Material

Layer	Thermal Resistance (K/W)
$R_{VCSEL}$	19.48
$R'_{VCSEL}$	54.11
$R_{Gold}$	1.47
$R_{Air}$	Infinity
$R_{BCB}$	1.20
$R_{SiOB}$	$7.91 \times 10^{-2}$

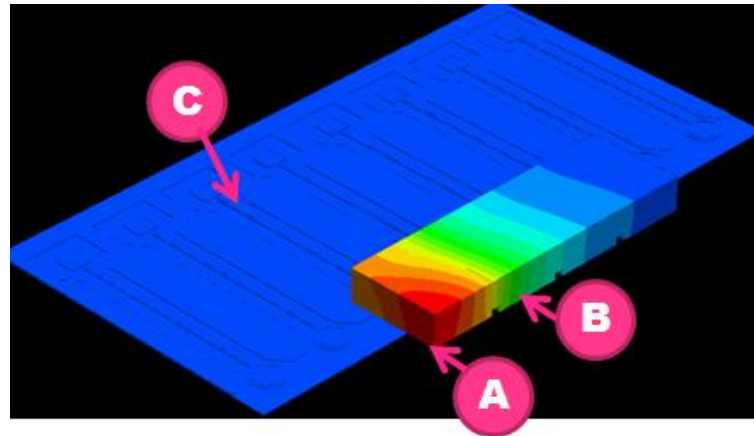
associated EETCMs and the simulation results after removing the air and SiOB in the thermal conducting system. Since the VCSELs have poor thermal conductivity than that of the thermal vias (see Table. 1) and the thickness of the operating VCSEL and the adjacent one can have two-order magnitudes larger than that of thermal vias, the thermal vias would become the main path of the thermal flow as expected in this associated EETCM.

Meanwhile, the paths of the thermal flow depicted in Figure 5-11 extracted from the simplified thermal conducting system constructed in the simulation verify the validation of the EETCM by showing the possible paths of thermal flows on the main components. The simulation results can not only obviously present the main paths of thermal flow as the prediction of the EETCM, but also indicate the hottest spot is at the outermost corner of the operating VCSEL. In the design and optimization stage, it is important to find out the hottest spot caused by a great quantity of thermal accumulation due to its direct correlation to undesired functionality degradation or even failure of the VCSELs in the optical system. In fact, according to the indications of the derived EETCM, the hottest spot could always take place at the joints of the heating source to the source of thermal flow, and the temperature in the spot strongly correlates to the characteristics of device material and geometry of  $Z_1$  and the conditions of *Boundary A* as shown in Figure 5-11(a). Figure 5-11(b) shows the simulation results where the lateral VCSEL is operated with 8 mA input current and 2 V bias voltage.





(a)



(b)

Figure 5-11: (a) Scheme of the simplified thermal conducting system with single operating VCSEL established by the EETCM. (b) The simulation result of simplified thermal conducting system. According to the associated EETCM, the material of air and SiOB were removed in the system to reduce the required meshes as well as the CPU time and computer memory. The temperatures of node points A, B, and C are 78.9, 76.8, and 75°C while the input current is limited at 8 mA.

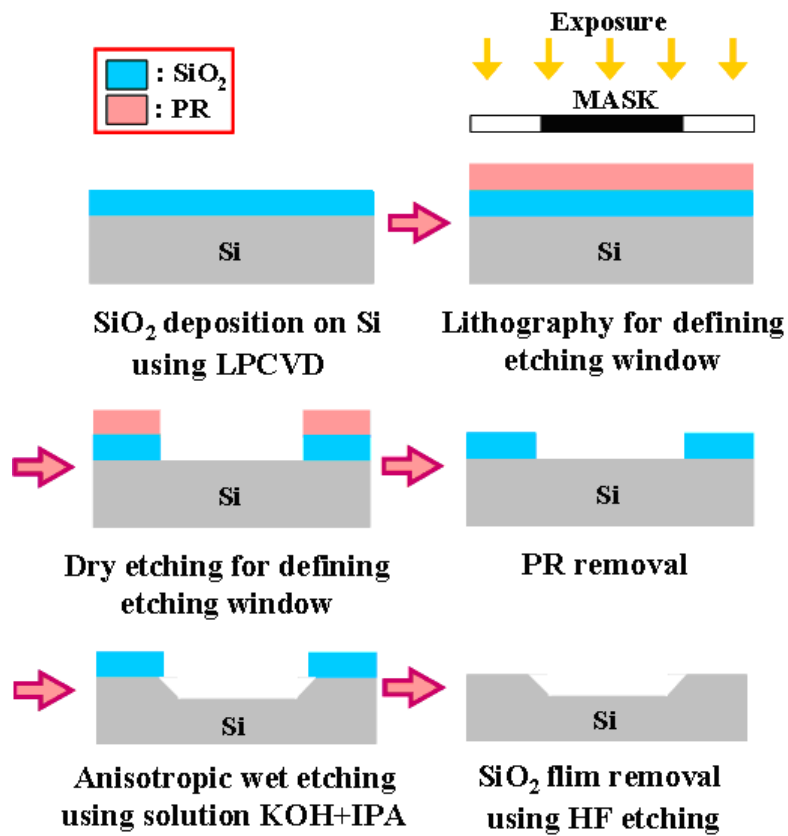
The temperatures show at node points A, B, and C are 78.9, 76.8, and 75°C, respectively. The hottest temperature at node A is close to the result that on the isothermal surfaces calculated by the EETCM as shown in Figure 5-10. The results reveal that the hottest temperature happens at node A and the main path of thermal flow is from node A to C which is the same as the simulation demonstration as shown in Figure 5-11(b) and has an excellent match with the prediction of the simplified EETCM as shown in Figure 5-11(a). Therefore, for system-IC designers and engineers, the EETCM derived based on the electrothermal network  $\pi$ -model can indeed provide a quick and accurate way to analyze the worsen cases at those joints by further investigating the thermal behaviors of  $Z_1$  and *Boundary A*.

### 5.5.2 *Fabrication, Apparatus Setup, Calibration, and Experimental Validation*

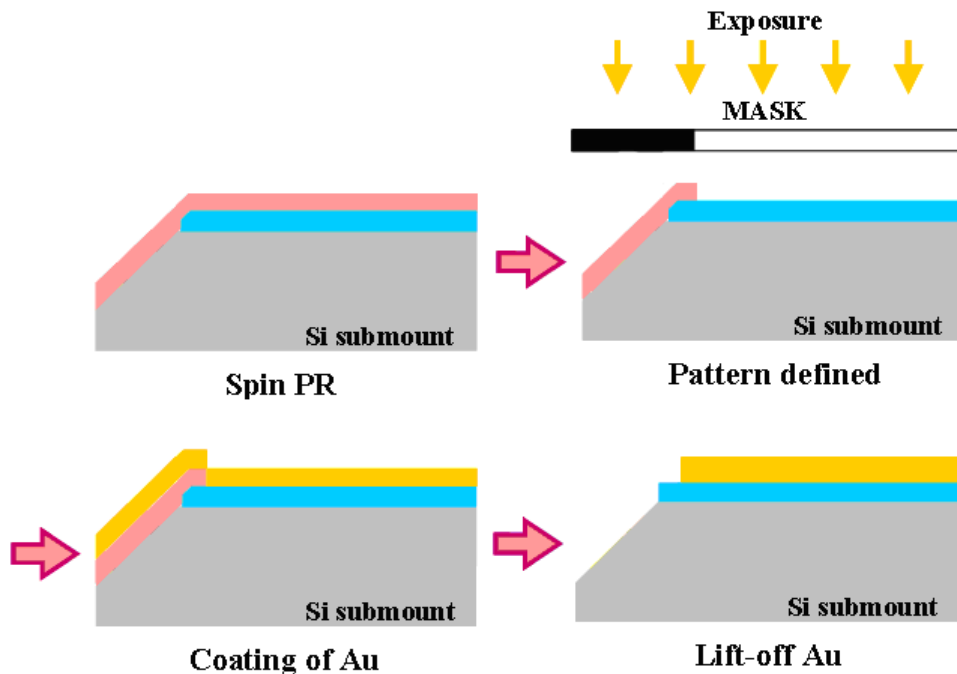
For the completeness and fair comparison between theoretically and experimentally discussion, the entire fabrication procedures of SiOB and transmitter assembly, including the manufacturing of 45°micro-reflectors, V-groove arrays, high frequency transmission lines that connected with 4-channel VCSEL array and bonding pads are demonstrated and shown in Figure 5-12 [94]. It should be emphasized that the 45°micro-reflectors and V-groove arrays did not be employed in the simulation and model analysis due to they are not main components of paths of thermal flow and furthermore for the first structure simplification.

Additionally, since the fiber assembly of proposed modules used for the optical interconnection is passively aligned, the V-groove array is designed to assemble the multimode fiber (MMF) array. The SiOB is monolithically fabricated with a 45° micro-reflector and the V-groove array. In order to etch the bench that can incorporate the optic fiber with the V-groove and provide the reflection surface for optical coupling between fiber and VCSEL simultaneously, a two-step anisotropic wet etching is developed using KOH solution. SiO<sub>2</sub> film is deposited on a (100) silicon substrate and used as a hard mask for anisotropic wet etching. Dedicated patterns for etching trenches are formed using photo-lithography and dry etching on the SiO<sub>2</sub> film to define patterns. The anisotropic wet etching using KOH solution mixed with IPA is applied to form the 45° micro-reflector and the V-groove array. After that, the photolithography is adopted again to fabricate transmission lines. Ti/Au (500/9500 Å) layers are deposited on the SiO<sub>2</sub> layer by E-Gun Evaporator. Transmission lines (TMLs) are then formed using lift-off process. For flip-chip bonding VCSEL onto the as-fabricated TMLs, Au-Sn patterns of 1µm are defined by photolithography and thermal evaporator deposition. Finally, once the 4-channel VCSEL array is flip-chip bonded onto the Au/Sn pads, the SiOB transmission module is fabricated with a position accuracy of 1µm.

Furthermore, InfraScope II, Thermal Imaging Microscope, (Quantum Focus Instruments



(a)



(b)

Figure 5-12: (a) Fabrication of SiOB and (b) Fabrication of High Frequency 4 Channel  $\times 2.5$  GHz Transmission Lines [94].

Corp, Vista, CA USA) is employed for both thermal mapping and hot spot detection in the measurement. Two main effects, vibration coupling and thermal air current, that could degrade the measured accuracy have been carefully considered and controlled. The InfraScope is mounted on a vibration-isolated table and the measurement environment is located away from air flux. The entire 3-D VCSELs optical stack is fixed on the thermal stage of the InfraScope, where a bias temperature is set at 75°C to imitate the conventional operation environment of typical optical transceiver systems. The optical stack starts with an unpowered state for measurement calibration. Radiance calibration is adopted to create the correlation between the output of infrared detector and the infrared radiance. The reference established in the unpowered state is used to calibrate the radiance units by accurately measuring the infrared radiation emitted by each pixel area of the optical stack. Then, the extracted emissivity map is utilized as a reference frame for each of the subsequent thermal images from the powered 3-D optical stack. Thus, the map can be processed immediately for the temperature acquisitions. At final, by means of zooming in the region of the heating source adequately, i.e. the region of the VCSELs, the temperature distribution of the hot spot can be definitely determined as well as the hottest temperature on the surface of the VCSELs.

Figure 5-13 is the detected infrared-ray (IR) thermal image which shows the temperature distribution of the SiOB heated by the singly operated VCSEL. The bottom of SiOB is constrained with a bias temperature of 75°C for fair comparison. Only a laser diode is operated by probe B with 8 mA input current and 2 V bias voltage. The measured hottest temperature shown in Figure 5-14 validates the simulation and model predictions as shown in Figure 5-10 and 5-11, respectively. The comparison between the CoventorWare simulation results with and without air and SiOB, respectively, also verify the simplification indicated by the EETCM. In order to further show the model accuracy in dealing with the thermal cross-talk between two operated lasers, Figure 5-15 shows the thermal image of the optical transmitter where two lasers are operated simultaneously. Each laser diode is operated with 8

mA input current and 2 V bias voltage. Figure 5-16 shows the comparison between the measured data, simulation, and the EETCM. Excellent temperature matches within  $\sim 0.5^{\circ}\text{C}$  verify the EETCM and show the practicality of the simplified structure in which we can have 90% CPU operation time saving due to 80% mesh number reduction. In addition, the slight temperature mismatch should be caused by the thermal impedance mismatch between the interfaces and the phonon vibration. Further investigation and model improvement are still undergoing.

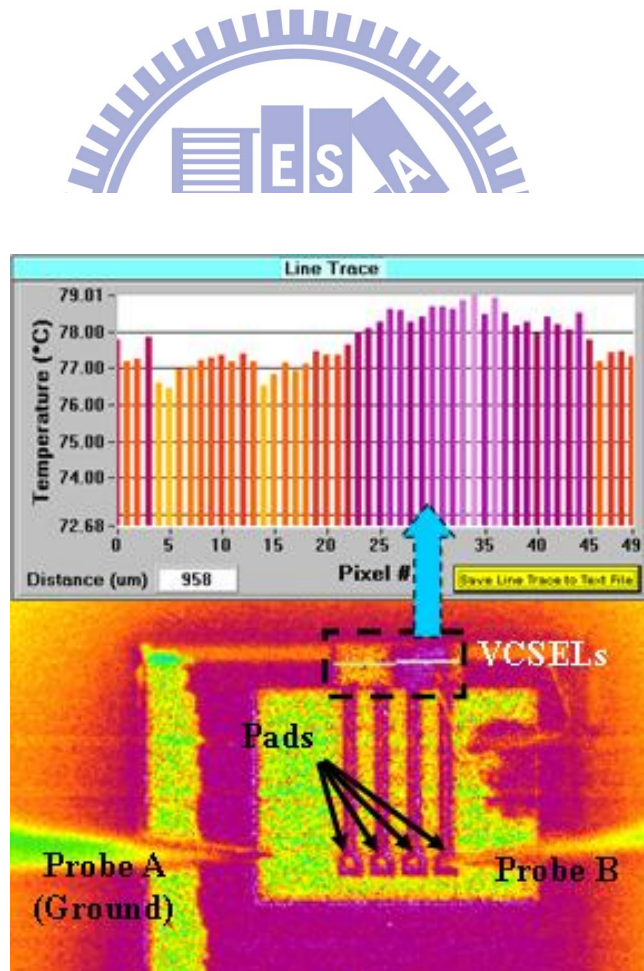


Figure 5-13: The measured temperature distribution of SiOB heated by the operating VCSEL using IR microscope. Only a laser diode is operated by probe B with 8 mA input current and 2 V bias voltage.

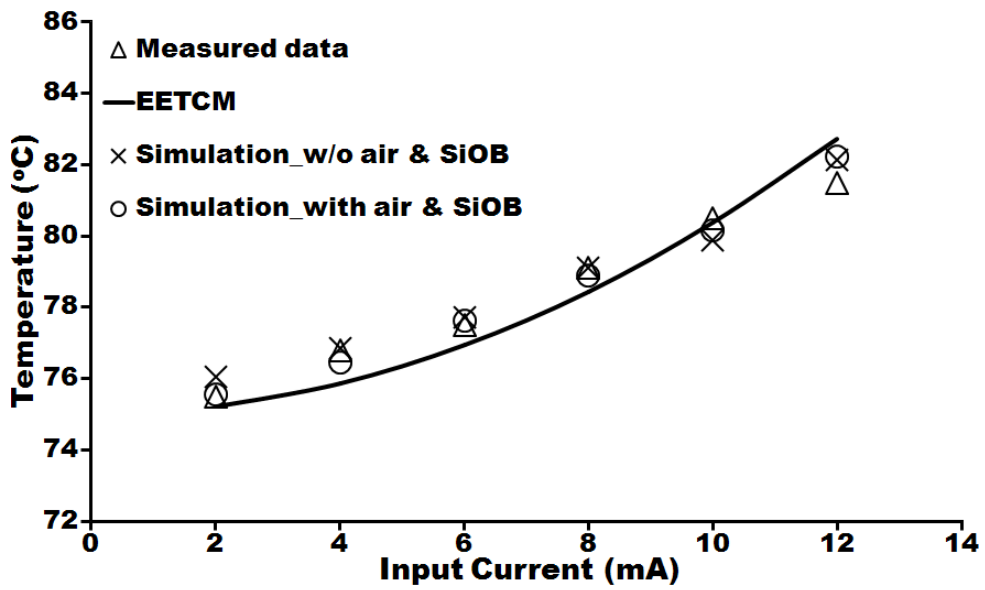


Figure 5-14: Comparison between the EETCM with single laser turned on, measurement data, and simulated results with and without air and SiOB, respectively.

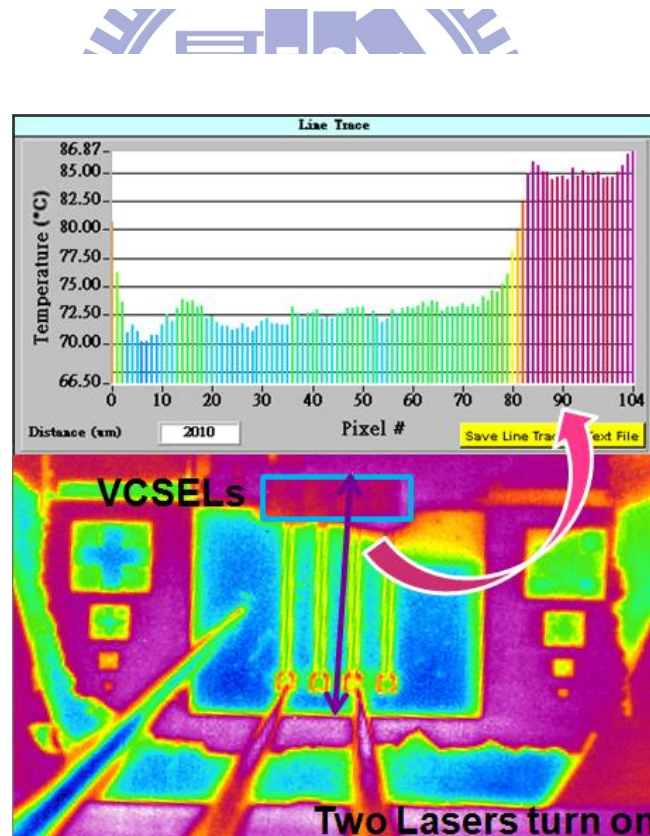


Figure 5-15: The measured temperature distribution of SiOB heated by the operating VCSELs using IR microscope. Two laser diodes are operated with 8 mA input current and 2 V bias voltage.

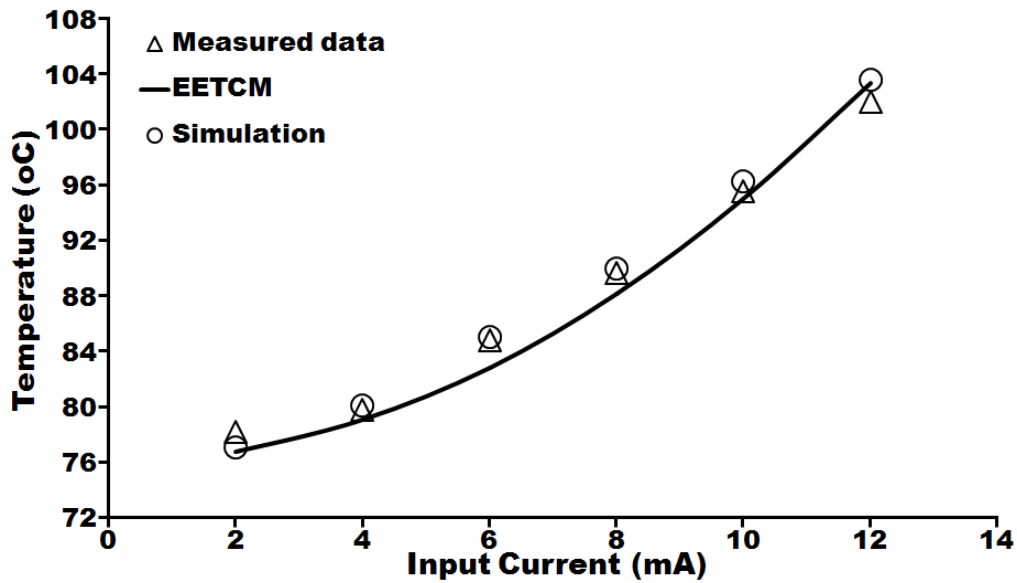


Figure 5-16: Comparison between the EETCM with two lasers turned on, measurement data, and simulated result, respectively.



## 5.6 Thermal Optimization and Management of a Microsystem

### 5.6.1 The Green's Theorem with Given Heating-Sources System

As mentioned the classical Green's theorem above, mathematical characteristics of the specified heat conduction and convection equations can be derived as the Green's function and also can deal with given geometry and boundary conditions of a heating system even though the heating sources are unknown. Additionally, in order to introduce the Green's function into the algorithm conveniently, a numerical analysis, successive over-relaxation (SOR) with red-black ordering [109], is also employed. This is certainly not the fastest way to solve the problem, but it does illustrate many important programming ideas. Nodes employed in this analysis are divided in half into red nodes and black nodes. During the first pass, the red nodes obtain the voltages as a weighted average of their original voltage, and as inputs (if any) to the six surrounding black nodes for 3D-situation. During the second pass, the black



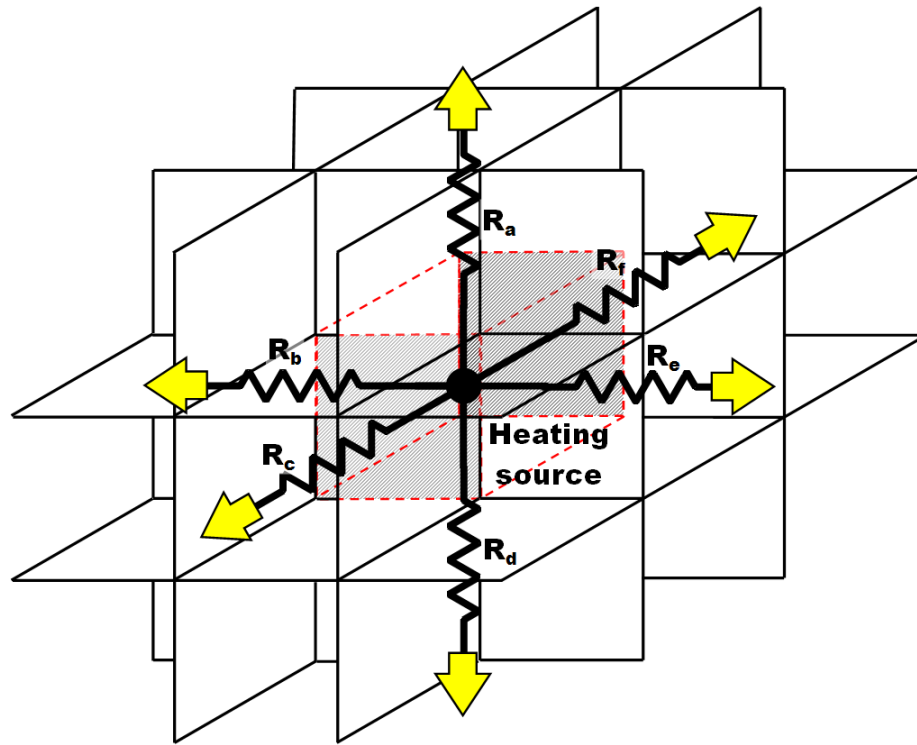
nodes obtain voltages from the six surrounding red nodes. The process converges in the limit to the correct answer for the finite grid. By realizing and transferring the physical meanings from electric to thermal characteristics, the voltages and electric resistances using in the red-black ordering become temperature differences and thermal resistances in our algorithm. Detail codes are derived in the Appendix B.

The benefit using the SOR with red-black ordering is that each thermal resistance within the associated volume element could be linked with a simple way as shown in Figure 5-17, where the processes of thermal transferring from one volume element to another by means of the prescribed thermal resistances derived in (5-19) are clarified. The thermal flux generated by the heating source could be transferred through the surrounding six thermal resistances outward (the red ordering) as shown in Figure 5-17(a), and each of the thermal resistance could use the same way to obtain thermal energy from other surrounding resistances (the black ordering) as shown in Figure 5-17(b). The governing equation is as the follows:

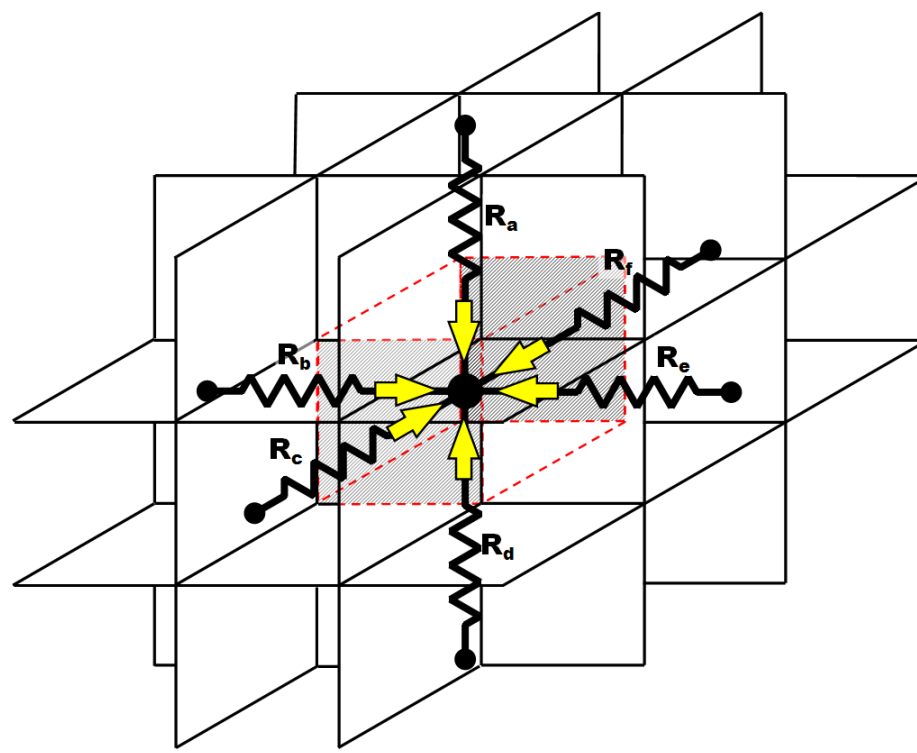
$$\Delta T_{\text{central}} = \sum_{i=a}^f \frac{\Delta T_i}{R_i} / \sum_{i=a}^f \frac{1}{R_i}, \quad (5-21)$$

where  $\Delta T_{\text{central}}$ ,  $T_i$ , and  $R_i$  are temperature difference in the central point, temperature difference at  $i$ th thermal resistance, and the  $i$ th thermal resistance, respectively. The parameter  $i$  is a symbol labeled from  $a$  to  $f$ . In the studied cases, either single or two VCSELs were turned on, the entire volume of the VCSELs on the SiOB are decomposed into several volume elements with each edge length of which is less than 100  $\mu\text{m}$ .

Since the thermal transmission within the volume elements due to the temperature differences could be well defined by means of the SOR with red-black ordering, the temperature distribution of an entire heating system could be also defined eventually according to the prescribed boundary conditions, i.e. the given temperatures, using (5-9), (5-13), and (5-14) in steady state. Figure 5-18 conceptually shows the method for determining



(a)



(b)

Figure 5-17: Scheme of Successive Over-Relaxation (SOR) with (a) red- and (b) black ordering [109]. During the first pass, the red nodes obtain the voltages as a weighted average of their original voltage, and as inputs (if any) to the six surrounding black nodes for 3D-situation. During the second pass, the black nodes obtain voltages from the six surrounding red nodes.

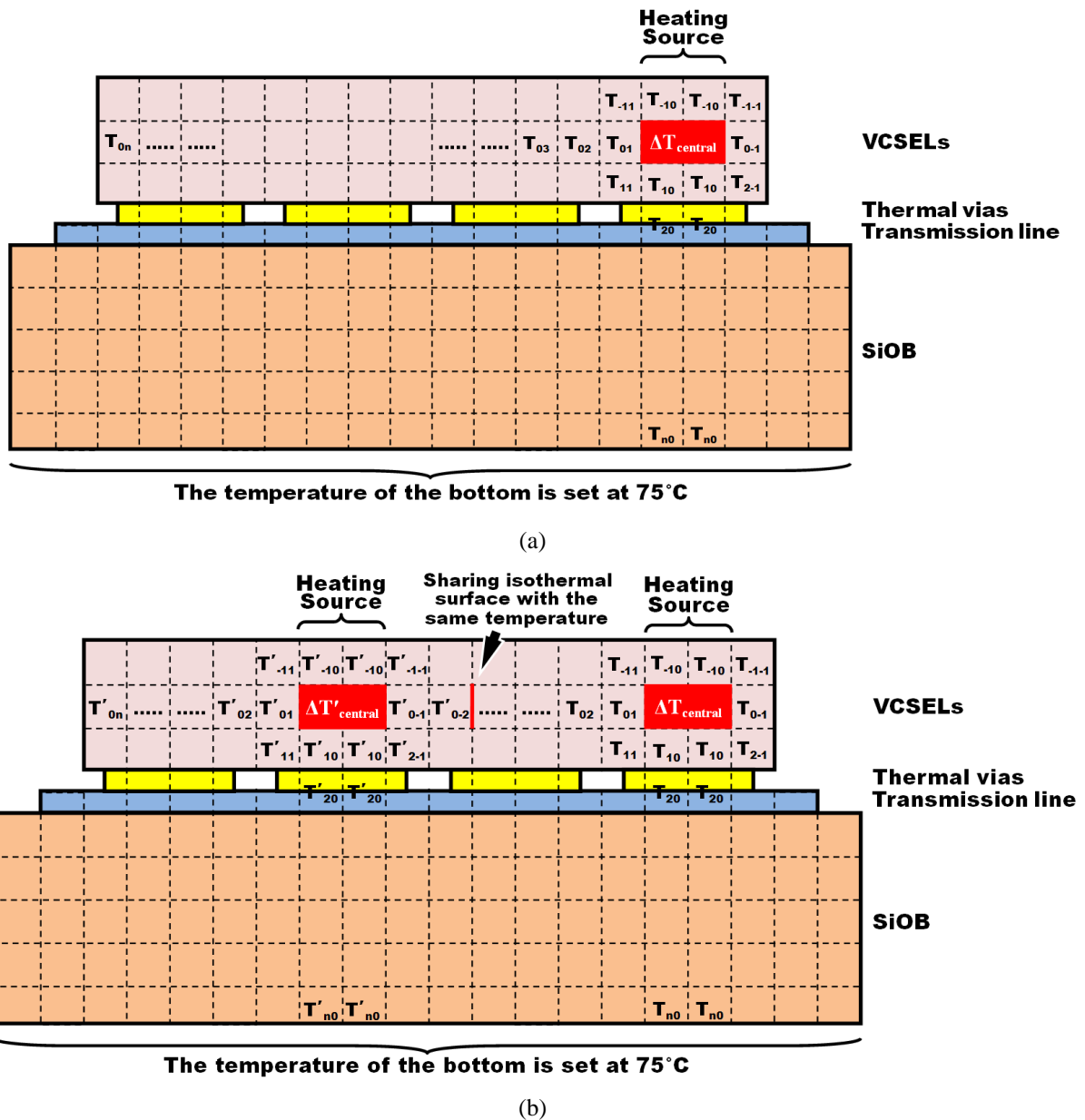


Figure 5-18: Scheme of the method for conceptually determining the temperature distribution within each volume element of the situation that (a) single, and (b) two VCSELS are turned on. Each volume enclosed by the dash-line is an “isothermal volume.” The final given temperatures on the boundary surfaces, the temperature on the bottom, could determine the really temperature within the volume elements which are sharing the given temperatures on the boundary surfaces.

the temperature distribution within each volume element. Although only the temperature differences within those volume elements so far, the final given temperatures on the boundary surfaces could determine the really temperature within the volume elements which are sharing with the given temperatures on the boundary surfaces. Thus, the whole picture of the

temperature distribution of the entire heating system can definitely be clarified including the hottest spot on the surface of the heating system. It is noted that the hottest point of temperature is not necessarily located on the surface of the heating system; it might exist inside the system.

For a thermal system optimization, the IC-designers, engineers, and scientists should carefully consider the sharing volumes that several isothermal surfaces surround. According to the definition regarding the heat flux and the associated isothermal surface, the direction of the heat flux is always orthogonal to the surface that enclosed it. Therefore, the sharing volumes that several isothermal surfaces surround indicate that amount of thermal accumulation will happen there and the added vector is the final direction of thermal flux.

#### **5.6.2 *Determination of the Hottest Spot in an Unknown-Heating-Sources System***

Inevitable non-uniformly thermal effects indeed dramatically affect performances of a micro- and nano-electronic system. Undesired thermal accumulations within the intensive electronic devices could cause the device degradation and damage. Even though the MEMS sensors or actuators can perform ideally well, the degradation and failure of implemental circuitry or passive components due to the undesired thermal accumulation eventually cannot provide the required performance. Fortunately, the previously developed EETCM and the mathematical technique, the Green's theorem-based heat transfer equations, successfully provides a precise method for predicting the temperature distribution and the most probable path of thermal flux in a heating system with given characteristics of the heating sources. The arrangements of thermal vias or thermal interface material can be realized after determining all of the isothermal surfaces in the heating system.

A system, however, with unknown heating sources seems to be a problem to use the presented technique. Without knowing the heating sources, the system seems to be also cannot

decompose it into the three blocks mentioned previously, heating sources, propagated resistances, and the common base resistances. To overcome this predicament, the Green's theorem-based heat transfer equations provide a simple way to determine the locations of thermal flux convergence and the probable path and direction of the flux. By means of applying the isothermal surfaces to enclosed each current source, the volume (or volumes) enclosed by the most of the surfaces in the heating system with unknown heating sources should be the hottest region due to most of the heat flux will path through there. Furthermore, the sum of vector of the flux will indicate the probable path and the direction of them as shown in Figure 5-19. Eventually, the IC-designers or engineers could pre-arrange the thermal vias and thermal interface material in their microsystem for system optimization.

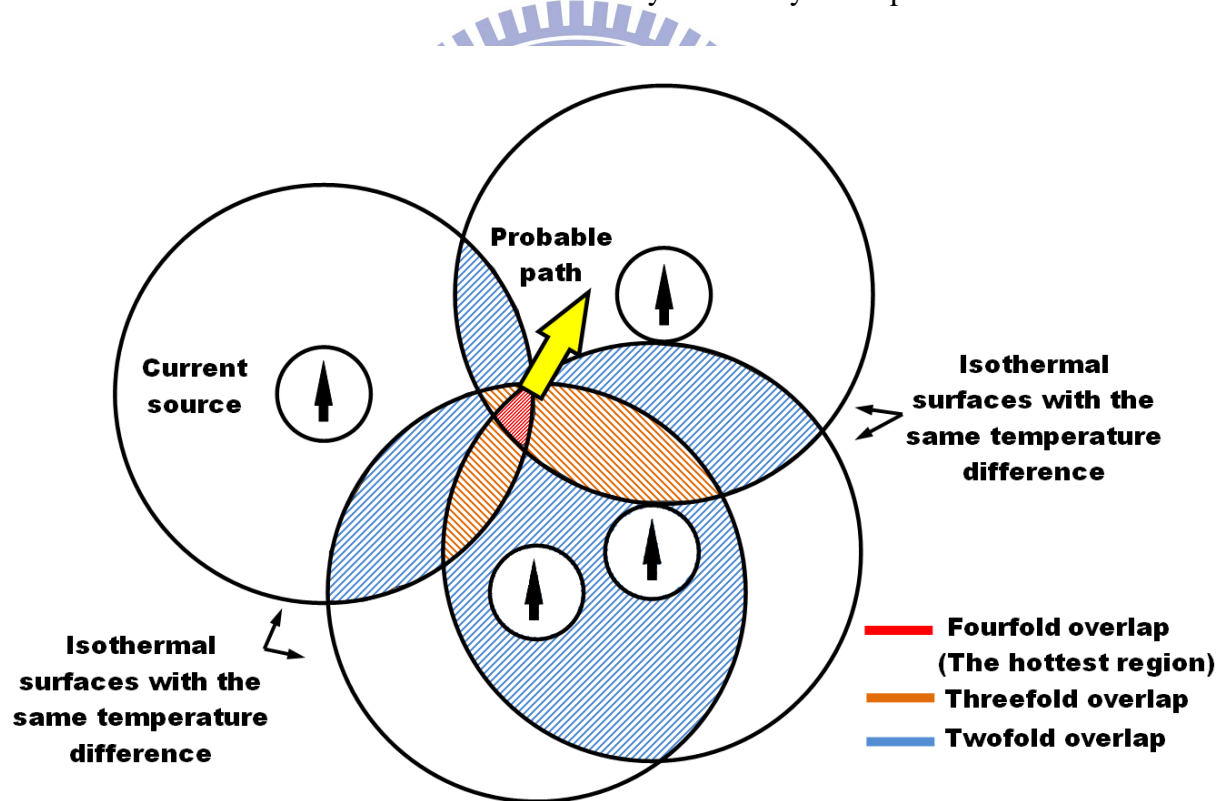
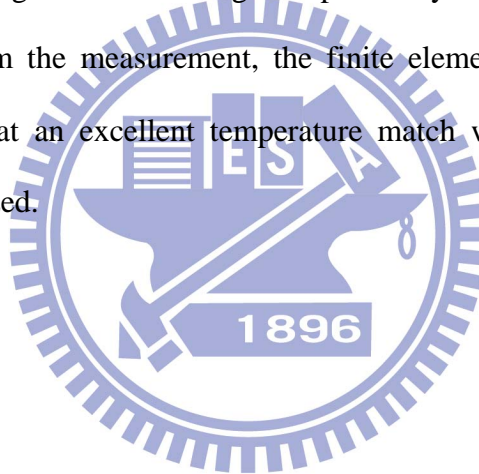


Figure 5-19: Scheme of the method for conceptually determining the probable path of heat flux. Four current sources enclosed by four isothermal surfaces with the same temperature difference result in a fourfold overlapped region, the hottest region in this microsystem. Any of three or two current sources also result in the three- and twofold overlapped region and cause the temperature gradients within the system. Thus, the probable path of the heat flux would follow the ideal path that has the largest temperature gradient as indicated in the figure.

## 5.7 Summary

The chapter introduces a method combining a general electrothermal network  $\pi$ -model in system level and the associated mathematical technique, Green's theorem, in terms of the adopted materials and system geometries to build up an equivalent electrothermal circuit model (EETCM) for efficient thermal analysis and behavior prediction in a thermal system. Heat conduction and convection equations in integral forms are derived using the theorem and successfully applied for the thermal analysis of a 3-D optical stack, VCSELs on a SiOB. The complex stack structure in conventional simulators can be greatly simplified using the method by well predicting probable heat flow paths, and the simplification can eventually achieve the goal of CPU time-saving without having complicatedly mesh designing or scaling. By comparing the data from the measurement, the finite element simulation, and the method calculation, it shows that an excellent temperature match within  $\pm\sim 0.5^{\circ}\text{C}$  and 90% CPU time-saving can be realized.



## **Chapter 6     Gravity-Assisted Seeding Control for 1D Material Growth and 3D-IC Applications**

### **6.1 Introduction**

Recent research progress in the synthesis and characterization of one-dimensional (1D) materials has disclosed the potential nanoelectronic device fabrication using the materials, such as zinc oxide nanowire with negative electron affinity suitable for room temperature field emitter application [110], carbon nanotube (CNT) with ballistic conductance good for nanoscale field effect transistor fabrication [111], tin oxide nanowire with surface state dependent conductance right for chemical sensor device making [112], and so on. So far, most of the 1D materials can be massively produced by chemical vapor phase deposition with appropriate catalytic seeds whose size, composition, and formation have been found as deterministic factors to the microstructure and physical property of the 1D materials [113,114]. Because precisely catalytic seed sizing and positioning control would be the next deterministic factors to facilitate device fabrication using the typical “top-down” IC manufacturing approach, i.e. the synthetic control in forming a group of stand-alone and well-aligned 1D material on a substrate with well defined positions for device fabrication, it is still desirable to develop a seeding control method to pave the way for the future integrated nanoelectronic application of 1D materials.

Several methods, such as Fe catalyst positioning on a Si pillar array [115], Ni catalytic seed locating in a non-lithographic anodized aluminum oxide (AAO) nanopore template [116], and electron-beam (EB) lithographically seed size and location defining on a blank silicon substrate [117], etc., have been developed and proposed for the selective growth application of 1D materials. However, at present, most of the approaches except the EB defining still cannot effectively achieve the required “precise” control in terms of the size, number, and location of catalytic seeds. Even in the EB method, a special lab-made photoresist is still required and

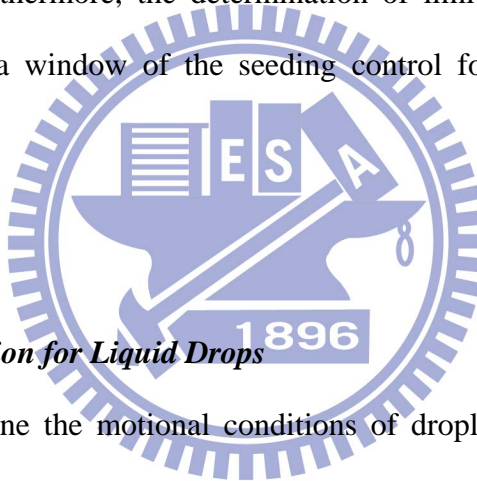


approximate 10% of the catalyst can be activated for subsequent material growth. Thus, in this chapter, a seeding control scheme including the physical mechanism of formation is proposed and demonstrated by employing gravitational force to form an agglomeration of melted cobalt seeds within a patterned inverted silicon nano-pyramid. Because this approach could ensure a group of well-aligned catalytic seeds with fixed size and designated location, it is our belief that this technique will be useful for future 1D material growth control and practical for integrated nanoelectronic device fabrication.

The first task should be overcome is to realize how to perform a seed precisely within a designated location. In the chapter, a seeding control scheme is proposed and demonstrated by employing gravitational force to form an agglomeration of molten Co seeds within a patterned inverted silicon nano-pyramid. Because this approach could ensure a group of well-aligned catalytic seeds with fixed size, it is our belief that this technique will be useful for future 1D material growth control and practical for integrated nanoelectronic device fabrication. Therefore, the physical behaviors and motional mechanisms of the melted Co seeds on the inclined surfaces of the nano-pyramids should be definitely clarified first. Several proposed schemes of motional mechanisms for liquid droplets on an inclined solid could be conceptually and physically realized to have three motional categories: rolling [118,119], sliding [120,121], and mixed modes. For a rolling case, surface tension of a small enough droplet will dominate its gravitational force and can be interpreted by means of specified Bond, nominal Reynolds, and Capillary numbers [119], whereas for a sliding case the gravitational force of a large enough one will dominate and make itself to be spreading [122]. Meanwhile, the mixed mode indicates that the surface of drops may slide down along the inclination with the fluid inside rolling, and then trace will be left behind the drops after run-off [123]. In fact, complicated dynamics of droplets associated internal fluid motion on an inclination have been developed to well determine behaviors of droplets in terms of size, mass

density, viscosity, surface tension, contact angle, and properties of interfaces, etc. [119,123,124].

This chapter derives the upper limitation of nominal radius of nanometer sized melted Co seeds formed on a nonwettable silicon inverted pyramid {111} surface in which the seeds can purely roll down along the inclination due to gravitational force and then agglomerate to become a singular seed on the bottom of the inverted pyramid by employing the specified dimensionless Bond number,. Additionally, by considering the relations between the Gibbs free energy, inclined angle, and the contact angle, mechanism of formation of the Co seeds, called nucleation, on an inclination can also character the lower limitation of the nominal radius of the seeds. Furthermore, the determination of limitary nominal radius for rolling mechanism will reveal a window of the seeding control for the demanding selective 1D material growth.



## 6.2 Mechanism of Motion for Liquid Drops

In order to determine the motional conditions of droplets, it is first to determine the dimensionless Bond number,  $B_0$ , which could be as an indicator to recognize the modes of motion [118,119,125]:

$$B_0 = \frac{\rho g R^2 \sin \phi}{\pi \gamma (\cos \theta_r - \cos \theta_a)}, \quad (6-1)$$

where  $\rho$ ,  $g$ ,  $R$ ,  $\phi$ ,  $\gamma$ ,  $\theta_r$  and  $\theta_a$  are mass density of droplet, acceleration of gravity, nominal radius, inclined angle, surface tension, receding angle, and advancing angle, respectively.

The numerator and denominator of the Bond number represent the component of gravitational force per characteristic length along the inclination and the difference of surface tension between the upper half of the droplet and the lower one, respectively. The characteristic

length is the physical radius of the contact line. It is noted that for a droplet on an inclined plane to the threshold of motion, the relations between the associated Bond numbers can be summarized as the follows [118-121,124]:

$$B_0 \begin{cases} \ll 1, & \text{for rolling mode} \\ \geq 1, & \text{for sliding mode.} \\ \text{otherwise,} & \text{for mixed mode} \end{cases} \quad (6-2)$$

Thus, as long as the condition of  $B_0 \ll 1$  is satisfied, in which the difference of the surface tension dominate the gravitational force, the nanometer sized melted Co seeds might move down to the bottom of the patterned inverted silicon nano-pyramid with purely rolling motion and then agglomerated to become a singular seed due to its tiny mass density in our case.

Since Carter *et al.* have reported that silicon surface is hydrophobic to melted Co [126], the shape of the nm-sized Co droplet on a horizontal surface can be assumed to be nearly spherical and the contact length of the droplet to silicon substrate,  $l$ , is

$$l \cong \left(\frac{\rho g}{\gamma}\right)^{1/2} R^2. \quad (6-3)$$

On the inclination, however, small deformation of the seed-droplet shape would occur, and it is necessary to introduce the receding angle, advancing angle, and the characteristic length for describing the rolling motion in detail. Based on the force equilibrium and the geometrical shape of the deformed drop, the relations between gravitational force and surface tension can be expressed as follows:

$$\rho \frac{4\pi}{3} R^3 g \sin \phi = \frac{\pi \gamma R}{2} (\cos 2\theta_r - \cos 2\theta_a) - \pi \rho g R^3 \cos \phi, \quad (6-4)$$

and

$$\rho \frac{4\pi}{3} R^3 g \cos \phi = \frac{\pi \gamma R}{2} (\sin 2\theta_a + \sin 2\theta_r) - \pi \rho g R^3 \sin \phi. \quad (6-5)$$

The terms on the right hand sides of (6-4) or (6-5) represent the difference of surface tensions of the drops between on the inclination and on the horizontal surface. Thus, by combining (6-4) and (6-5) mathematically and the governing rule from (6-2), the upper limitations of nominal radius of liquid drops for rolling mechanism can be well defined.

Meanwhile, the exceed surface Gibbs free energy of the melted Co liquids on the inclination,  $\Delta g_s$ , derived from the relation between the nominal radius and the deformation of drop-liked liquids on the inclination in the duration of nucleation can be further depicted by the original surface free energy on a plane times the modified function in terms of the receding and advancing angles [127]:

$$\Delta g_s = \frac{4}{3} \pi R^2 \gamma [f(\theta_a) + f(\theta_r)], \quad (6-6)$$

The functions of receding and advancing angles,  $\theta_r$  and  $\theta_a$ , mentioned above can be calculated as follows [120,127]:

$$f(\theta_i) = \frac{(2 + \cos \theta_i)(1 - \cos \theta_i)^2}{4}, \quad (6-7)$$

where  $i$  represents  $a$  and  $r$ , which are advancing and receding angle, respectively. By introducing critical Gibbs free energy of nucleation [127], the size of the atomic cluster with maximum free energy can be determined as well as the minimum nominal radius of the seed-droplet on the inclination. Therefore, by combining the solutions derived from (6-4) to (6-7), the upper and lower limits of the radius of liquid droplet rolling along the inclination of an inverted silicon pyramid will be triggered while the following condition is satisfied [119,127]:

$$\frac{\sqrt{2}g_s}{g_v} \sqrt{f(\theta_a) + f(\theta_r)} \leq R \leq \frac{1}{3\sqrt{5}} \sqrt{\frac{\gamma}{\rho g}} \sqrt{\frac{\sin 2\theta}{13 + 12 \sin \phi}}, \quad (6-8)$$

where  $\theta$ ,  $g_s$ , and  $g_v$  are the contact angle of the melted Co on silicon substrate, interface

energy per area, and Gibbs free energy per volume, respectively. For the case of the melted Co seeds, the calculated upper and lower limits of the nominal radius roughly fall in the regime of  $10^{-8}$  meters  $< R < 10^{-4}$  meters [114,115], where the seed droplet is expectably satisfied the required condition of  $B_0 \ll 1$  in (6-2) [119]. It indicates that the Co droplets with a size within the limitation can directly roll down to the bottom of inverted silicon nano-pyramid with the inclination of  $54.7^\circ$ . For instance, with the measured value of surface tension and contact angle of the melted Co on silicon substrate at 1514K, which are 0.23 N/m and  $121^\circ$  respectively [128,129], the maximum radius of liquid droplet for rolling along the Si (111) plane ( $\phi=54.7^\circ$ ) is about 0.1mm which is much larger than the size of the Co droplets formed on the surface of inverted silicon pyramid, indicating that all Co droplets can roll down to the bottom of the pyramid for aggregation.

Owing to the temperature-dependent property of the surface tension, the relations between the nominal radius, inclined angle, and surface tension can be further calculated by means of the following equation [130]:

$$\gamma = 1.93 - 0.00033(T - T_m), \quad (6-9)$$

where, as an example, the  $T_m$  is melting temperature of Co with the value of 1768K. Figure 6-1 shows that the nominal radius would be decreasing with the environmental temperature

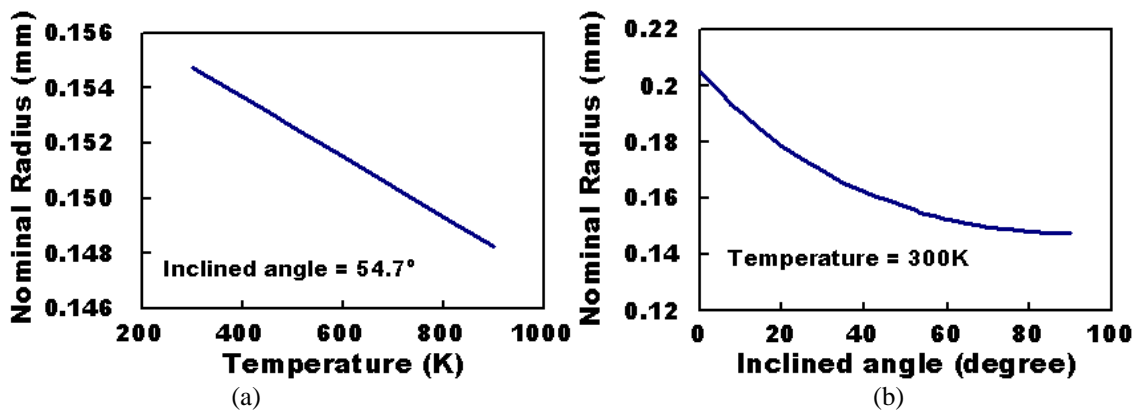


Figure 6-1: Relations between the nominal radius, the temperature-dependent surface tension (a), and the inclined angle (b).

and with the inclined angle increase, respectively. The result might be deduced from the drastic thermal and gravitational force influence within the Co-Si interface and the Co seed along inclination, respectively.

### 6.3 Seeding Control Scheme

Figure 6-2 conceptually illustrates the seeding control scheme. For 1D material synthesis, a metal layer is deposited first and then thermally reflowed to form melted seeds on substrate surface [131] for following material synthesis as shown in Figure 6-2(a). On the contrary, if

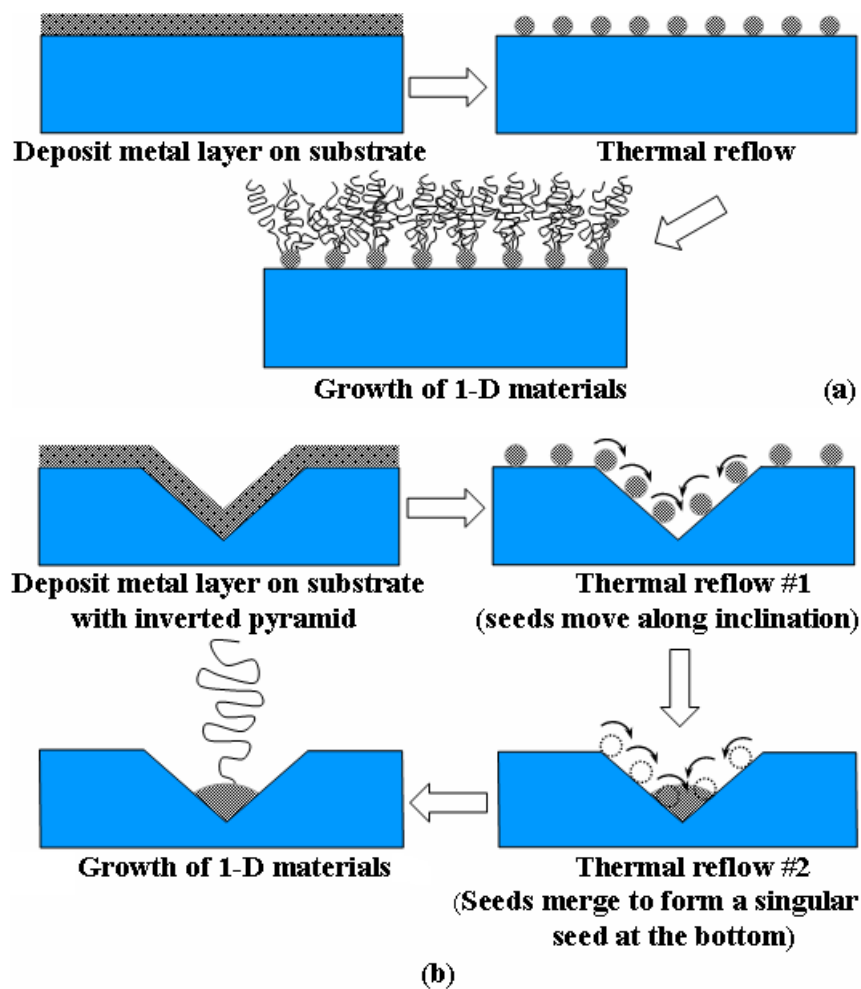


Figure 6-2: The schemes of 1D materials synthesis: (a) without and (b) with inclined surface of inverted pyramid on silicon substrate.

the seeds are just formed on inclined surfaces of inverted pyramid, gravitational field could force each seed to move along the inclination and make them merged to form a singular seed at the bottom as shown in Figure 6-2(b). Thus, the phenomenon of liquid rolling on the inclination can only happen while the melted seeds exhibit hydrophobic characteristic to the surface.

Figure 6-3 shows SEM micrographs of a 6nm thick Co film on a silicon (100) substrate after 800°C and 900°C thermal reflow for 10 minutes, respectively, in a chamber purged with Ar/H<sub>2</sub> mixture [132,133]. The silicon substrate has been micromachined to form inverted 400x400nm<sup>2</sup> nano-pyramids with 1µm spacing in between. In general, a catalytic metal film should be deposited followed by a thermal reflow on a substrate prior to the growth of 1D materials from the chemical vapor deposition [113,134]. During reflowing, the catalytic film would form a group of tiny droplet-like seeds or the coalescence of seeds randomly dispersed on the substrate. However, if these seeds are just formed on the inclined surface of the inverted nano-pyramids, which is Si {111} plane with a slope of 54.7°, and then the gravitational field would exert a force on each seed along the inclination and possibly make the seeds merged to form a large seed right at the bottom of the pyramid. For a several or several dozens-nm thick catalytic seed layers, the average seed size right after thermal reflowing is around 45nm [134]. Meanwhile, for the case of rolling droplet, the speed of droplet moving along an inclination can be calculated as follows:

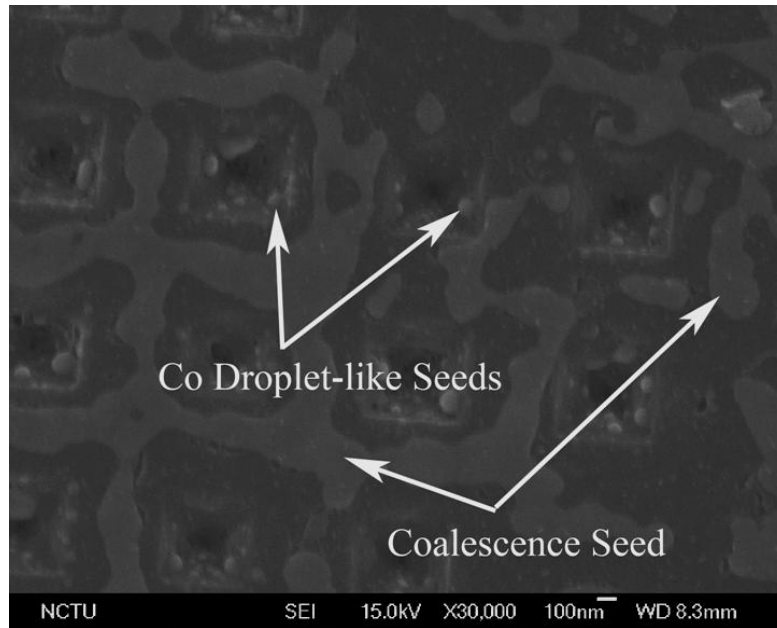
$$v \sim \frac{\gamma^{3/2} \sin \phi}{\mu R (\rho g)^{1/2}}, \quad (6-10)$$

where  $v$  is the viscosity of the Co droplet and can be estimated using the following equation [128]:

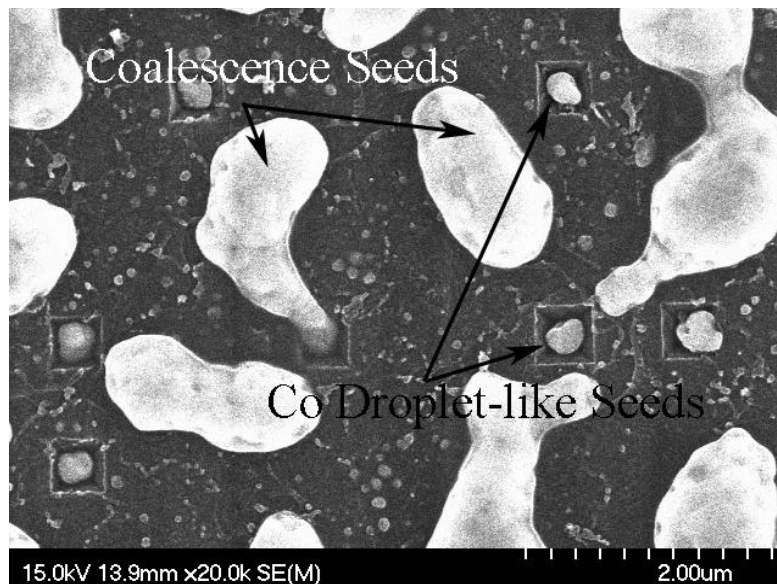
$$\mu \sim 0.033 \exp\left(\frac{8.2 \times 10^5}{RT}\right) \text{ mPa} \cdot \text{s}, \quad (6-11)$$

Therefore, the rolling speed could be enhanced by slightly raising the reflowing temperature





(a)



(b)

Figure 6-3: SEM micrographs of a 6nm thick Co film on a silicon (100) substrate after (a) 800°C and (b) 900°C thermal reflow for 10 minutes, respectively [132,133].

for a shorter reflow time for the seed aggregation. In comparison with the two morphologies as shown in Figure 6-3(a) and (b), the appearance of large coalescences of seeds in the inverted pyramid confirms the tendency via 100°C reflowing temperature increase.

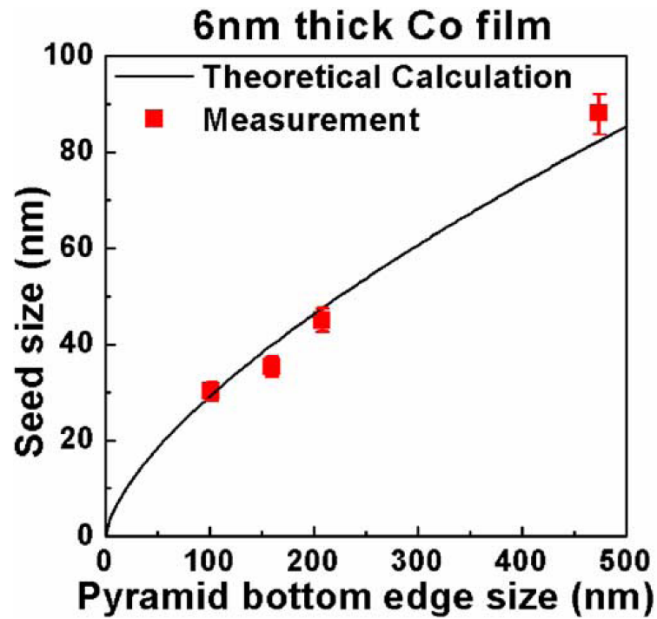
In addition to the coalescence of seeds at the bottom of the inverted pyramid to achieve

the unity and localization of catalytic seed, the seed size should be controlled by the thickness of the deposited Co and the size of the inverted pyramid. In the experiment, a variety of inverted pyramids whose bottom edge lengths ranging from 100 to 500 nm are fabricated on a silicon (100) substrate using KOH silicon etching technique [135]. The silicon substrate is then deposited with a either 6 or 30 nm thick Co film for characterizing the correlation between the average size of Co seed, the size of inverted pyramid, and the thickness of deposited Co. Figure 6-4 shows the experimental results in which both types of silicon substrates are thermally annealed at 900°C for 10 minutes [132,133]. The results indicate that thinner Co film (6nm, Figure 6-4(a)) deposited on a smaller pyramid produces a smaller catalytic seed, which is about 30 nm in radius in an inverted pyramid with a bottom edge of 100nm. The seed size is estimated by the law of mass conservation. It is assumed that all the coated Co film on the surface of inverted pyramid would melt, reflow, and agglomerate to form a singular seed at the bottom of the pyramid. Thus, the radius of seed coalescence ( $R_C$ ) can be calculated as follows:

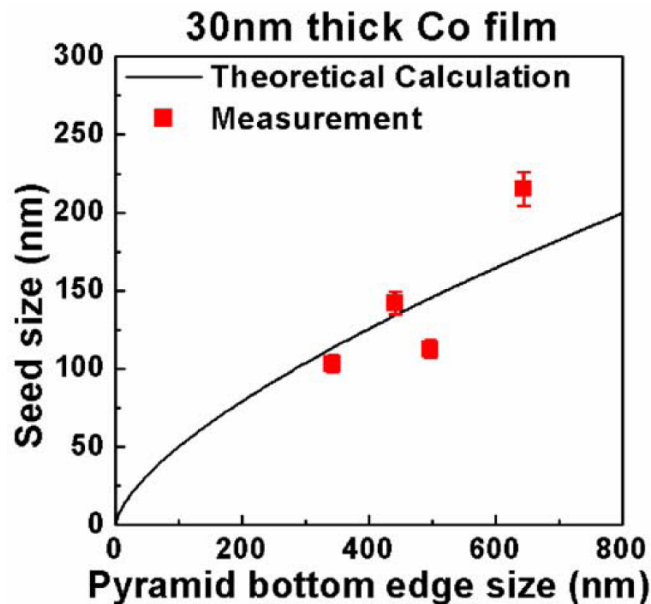
$$R_C = \left[ \frac{3\sqrt{3}}{4\pi} \cdot t \cdot L^2 \right]^{\frac{1}{3}}, \quad (6-12)$$

where  $L$  and  $t$  are the bottom edge length of inverted pyramid and the thickness of deposited Co film, respectively. As shown in Figure 6-4, the calculation provides a good size prediction suggesting the seed size can be further reduced by reducing the thickness of deposited Co and the size of pyramid.

Thus, a seeding control scheme from the aforementioned inferences is proposed as follows: A 500nm thick PECVD oxide deposited on a (100) Si wafer is coated with a 200nm thick ZEP520A photoresist lithographically patterned by e-beam followed by RIE oxide etching to form an opening for following KOH anisotropic silicon etching. The size of oxide opening which is related to the lower limit of bottom length of the inverted pyramid should be



(a)



(b)

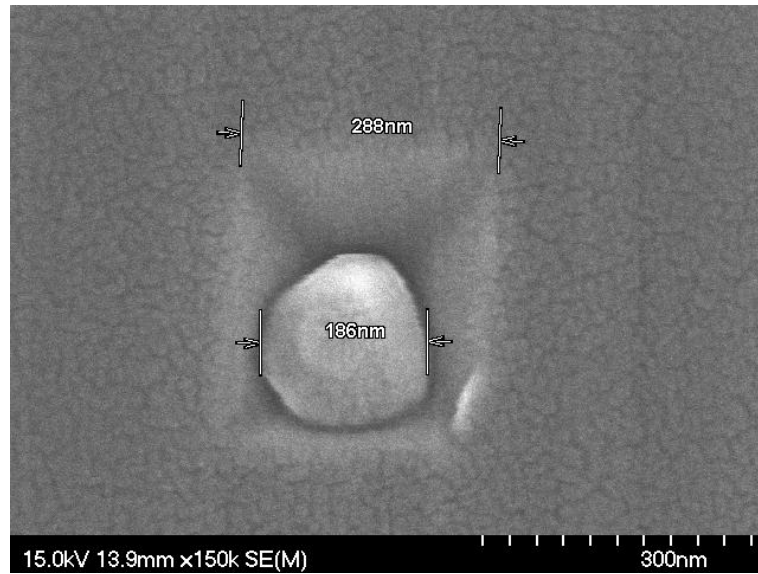
Figure 6-4: The bottom length of inverted pyramid versus the size of agglomerated Co seed formed inside: (a) 6nm thick Co film deposition and (b) 30nm thick Co film deposition. Both substrates are thermally annealed at 900°C for 10 minutes [132,133].

controlled as smaller as possible. After KOH silicon etching, the substrate is then sputtered by a layer of Co film followed by thermal anneal at high temperatures with a reasonable time frame (e.g. 1050°C, 10 mins). Eventually, a singular Co seed can form right at the bottom of the inverted pyramid after removing the surface oxide mask by HF etching.

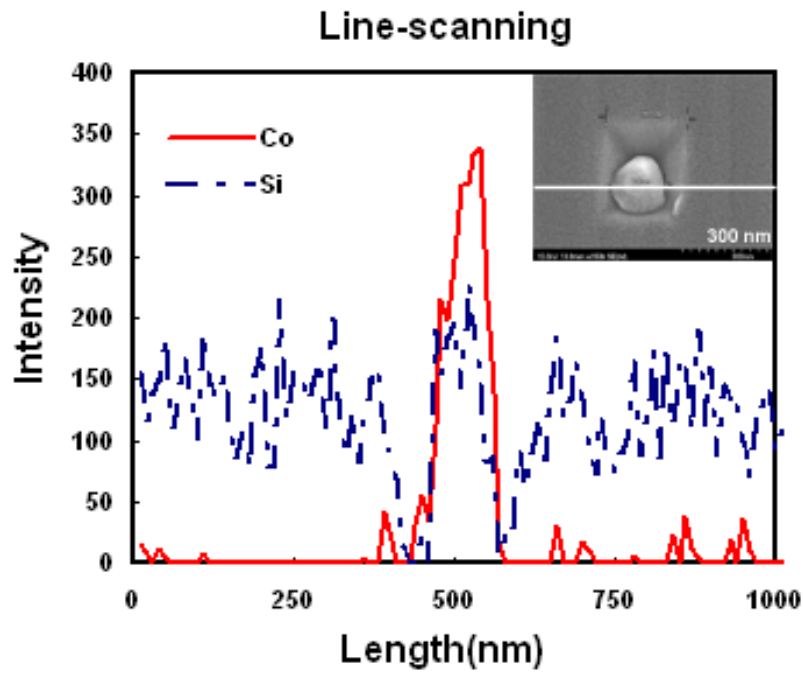
#### 6.4 Measurement and Discussion

Figure 6-5 shows the Auger line scanning spectrum across a singular Co seed at the bottom of the inverted pyramid formed by the proposed seeding control scheme reflowed with a 30nm Co seed layer [132,133]. The detected 774eV of Co and 1617eV of Si signals shown in the spectrum as well as the SEM inset validate the seeding control scheme confirming a singular Co seed with the size of 190nm in diameter located inside an inverted pyramid with a bottom length of 290nm. Figure 6-6 shows the array of the singular CNT at designated locations and the SEM micrograph of a singular CNT grown from a Co seed formed by the proposed seeding scheme which is reflowed with a 6nm Co seed layer [133]. The CNT is grown under the conditions of a reduction treatment at 600 °C for 10 minutes with mixed gases of H<sub>2</sub> (250ml/min) and Ar (250ml/min). Then, C<sub>2</sub>H<sub>4</sub> is introduced for another 2 minutes for CNT synthesis at 850°C. The respective flow rates for the Ar, H<sub>2</sub>, and C<sub>2</sub>H<sub>4</sub> are 375, 100, and 25ml/min, respectively. The insetted Raman spectra of 1350cm<sup>-1</sup> of D mode and 1598cm<sup>-1</sup> of G mode peaks as shown in Figure 6-6(b) indicate the grown singular CNT is a multi-walled tube which could be resulted by large seed size. Nevertheless, the size can be further reduced for single-walled CNT synthesis applications via high temperature anneal in a pure Ar ambient to make a part of seed vaporize [131].

The aforementioned model to describe the movement of Co droplet along an inclined surface is based on the condition of droplet rolling instead of sliding which is, in fact, the only way to realize the ultimate agglomeration of Co seeds like the phenomenon we have shown in Figure 6-6. According to (6-8), the droplet cannot roll along the inclination once its size is larger than a critical value. In that case, the large droplet will be locally deformed by gravity to form a corner shaped droplet, and then stick on the inclination to prevent the formation of agglomeration due to the force balance between the surface tension, gravity, and friction force applied on the droplet [125]. Because the purely rolling behavior is associated with the size, density, and surface tension of the droplet and the interfacial energies of the droplet to the



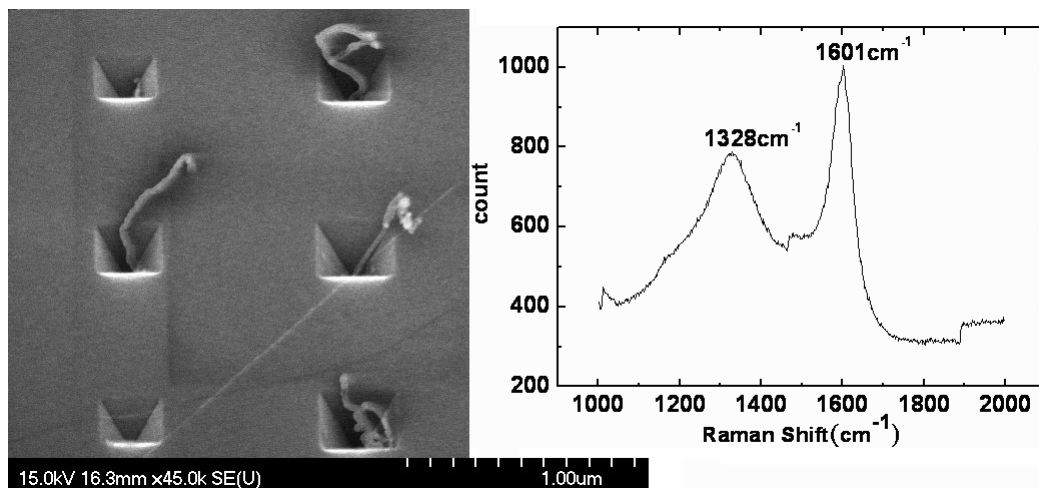
(a)



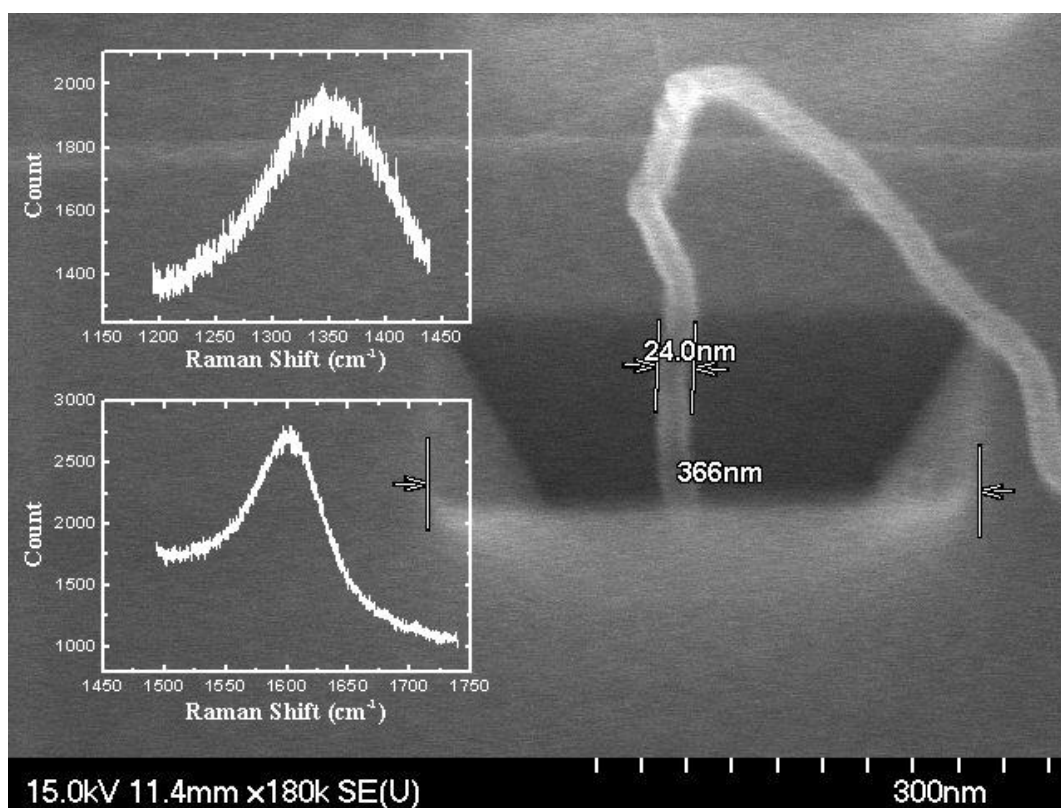
(b)

Figure 6-5: Auger line scanning spectrum across the region shown in the inset. The inset is an enlarged SEM view on an inverted pyramid with the bottom length of 290nm inside which a singular Co seed is formed with the size of 190nm in diameter [132,133].

contact surface material, and it only happens while the liquid droplet flows with minute Reynolds and Capillary numbers both indicating low movement speed of droplet [126],



(a)



(b)

Figure 6-6: (a) Array of the singular CNT. (b) SEM micrograph of a singular CNT grown from a Co seed formed by the proposed seeding scheme which is reflowed with a 6nm Co seed layer. The insetted Raman spectra both in (a) and (b) indicate the CNTs are a multi-walled carbon nanotubes [133].

further investigations are required for process optimization and seed size control to ensure the unity of Co seed, such as the characterization of the temperature-dependent viscosity and surface tension of liquid Co to the surface of inverted silicon nano-pyramid, the correlation of

Co droplet size distribution to the thickness of deposited film at different thermal reflowing temperature, and the reflowing time control for low rolling speed.

## 6.5 A Microsystem using 1D material

### 6.5.1 Miniaturization of the Microsystem

One of the frequently expectation using a 1D material in a microsystem is to achieve the goal of the miniaturization for intensive 3DIC-design and applications. The integration of 3DICs and MEMS devices using 1D materials could easily satisfy the demanding of products of multi-functionalities in electric market, such as high capacity memory and high speed digital switch using vertical MOSFET, high density transmission lines, circuitry with high transfer efficiency of electric-sound-pressure transformation used in hearing aids, and field-ionizer for atom and particle detection, and so on. Thus, in an intensive microsystem, the 1D material opens a way for not only building 3D microelectronic system but also the interconnections between circuitry and MEMS devices. For efficient manufacturing the 1D material, for instance, the carbon nanotubes (CNTs), the theoretical equations are summarized as follows:

$$\frac{\sqrt{2}g_s}{g_v} \sqrt{f(\theta_a) + f(\theta_r)} \leq R \leq \frac{1}{3\sqrt{5}} \sqrt{\frac{1.93 - 0.00033(T - T_m)}{\rho g}} \sqrt{\frac{\sin 2\theta}{13 + 12\sin \phi}}, \quad (6-13)$$

$$v \sim \frac{[1.93 - 0.00033(T - T_m)]^{3/2} \sin \phi}{0.033 \exp\left(\frac{8.2 \times 10^5}{RT}\right) \cdot R(\rho g)^{1/2}}, \quad (6-14)$$

and

$$R_C = \left[ \frac{3\sqrt{3}}{4\pi} \cdot t \cdot L^2 \right]^{\frac{1}{3}}. \quad (6-15)$$



By combining the upper limit of (6-13) with (6-14), we can find that the viscosity of the metal liquid is correlated with the inclined angle of surface and the temperature of thermal reflow:

$$v \propto \sin \phi \sqrt{13 + 12 \sin \phi} [1.93 - 0.00033(T - T_m)] \exp(-T). \quad (6-16)$$

Therefore, the rolling speed could be enhanced by slightly raising the reflowing temperature for a shorter reflow time for the seed aggregation. In comparison with the two morphologies as shown in Figure 6-3(a) and (b), the appearance of large coalescences of seeds in the inverted pyramid confirms the tendency via 100°C reflowing temperature increase.

Meanwhile, the radius of seed coalescence ( $R_C$ ) can be calculated using (6-15). Obviously, this radius simply depends on the bottom edge length of inverted pyramid and the thickness of deposited metal film. As shown in Figure 6-4, the calculation provides a good size prediction suggesting the seed size can be further reduced by reducing the thickness of deposited Co and the size of pyramid. Once the location and edge length of the inverted silicon nano-pyramid, the thickness of deposited Co film, and the temperature of the thermal reflow are all definitely determined, the location, diameter size, and length of the CNTs can be also easily controlled. Therefore, the miniaturization of the microsystem could be realized by means of using the seeding control scheme adequately. In order to reveal the ingenuity of determining the locations of each seed using the scheme under some prescribed limits, for instance, the arrangement of field-ionizer, an application of 3D CNT array is employed as an example in the following section.

### **6.5.2 Application of 3D CNT Array**

Nanotechnology development has been a major research topic in our country. One of research direction of nanotechnology is to find new application, where 3D-CNT array is also a key nanotechnology to advance the nanoelectronics and microsystems. Via achieving a group

of stand-alone and well-aligned semiconducting CNTs on a substrate, the development of 3D CNTFET IC can be further realized. As aforementioned, previous investigations have shown that the synthesis methods, growth conditions, as well as catalytic seed varieties and sizes play important roles in determining the diameter and chirality of a SWCNT, i.e. the semi-conductivity of a SWCNT, and further pointed out that one of the research efforts should move toward precisely catalytic seed sizing and positioning control to pave the way for the future nanoelectronic fabrication of SWCNTs. It is our belief that this technique will be useful for future SWCNT growth control and practical for micro- and nano-electronic CNTFET IC fabrication. In the section, as a suitable example, the foundation and advantages of a 3D-CNT array based field-ionizer will be clarified theoretically and experimentally.

The fundamental of 3D-CNT array based field-ionizer in this case is to provide high energy electron beam to ionize helium atoms to form  $\text{He}^{(e)}$  ions that will transfer electrons later to channeltron electron multiplier (CEM) for counting. The typical value of the field strength for the helium ionization is about  $1.5\sim 4 \text{ V/\AA}$  that can be formed on a tungsten tip with the diameter of 50 nm while the tip is applied with 6kV at 295K. Previously, the tungsten tip was fabricated from ordinary tungsten wire of 0.1 mm diameter. A short length of this wire was generally crimped in a small piece of copper tube with 1.5 mm outer diameter, 0.65 mm inner diameter, and 10 mm long. The tips were then electrolytically etched by following fairly standard practices [136]. Specifically, the copper tube was mounted in a holder placed above a glass beaker filled with a 2M NaOH solution. A power supply (2V dc) was connected to the copper tube on the one side and to a platinum electrode in the beaker on the other side. The wire was lowered into the solution and continuously moved up and down over a few millimeters by means of a manual translational drive. This motion distributed the preferential etching of the fluid-air interface that produces a gentle rather than an abrupt taper. The wire was monitored through magnifying glass lenses during this process. For few minutes later, when a visible indentation appeared in the wire, a series of short current pulses would be

applied by flicking the power supply on and off. By flicking bias voltage to finish the etch-through of the wire, a tip with a radius of curvature of typically 10-20 nm can be formed. Since the process is very complicated and hard for making a dense array, it is a critical research topic in the development of matter-wave microscope by implementing wafer batch process combined with nanofabrication technique to have a cost-effective solution for the fabrication of high performance field-ionizer.

Furthermore, the tips suffered with very high bias voltage, such as 6 KV in the case, will have a large erosion rate i.e. low operation lifetime. In general, the stability as well as the lifetime of the tips is directly and strictly proportional to their own electric conductivity and thermal conductivity. Previously, copper and tungsten are commonly adopted in the tip materials of microscope techniques due to their good thermal and electrical conductivity and high melting point as compared with the other solid metals. Experimental results have shown that the total erosion of copper and tungsten under applied 0.3 KV biased voltage is about  $0.1\mu\text{g}/^\circ\text{C}$  [137]. In comparison with the thermal and electrical properties of the possible materials as ionizer tip listed in Table 6-1, it seems that the thermal conductivity of CNTs is an order of magnitude larger than that of Cu and W at least. Much longer lifetime could be expected in the operation of processes of the field ionization due to the unusually high thermal conductivity of the CNTs. Thus, the employment of CNT tips could mechanically provide a

Table 6-1  
Thermal and electric properties of the possible tip materials

Tip material	Work function (eV)	Thermal conductivity (W/m-K) @100K	Electrical Resistivity ( $\Omega$ -m) @300K
Tungsten	4.5	208	$5.7 \times 10^{-8}$
Copper	4.5	482	$1.7 \times 10^{-8}$
Carbon nanotubes	4.5~5.1 [138-141]	6600 [142]	$5.1 \times 10^{-8}$ [143]

very stable and long-term observation and time-depended image trace.

Based on the aforementioned analysis, the proposed 3D-CNT array based field-ionizer requires the following critical feature for high resolution performance of helium detector (1) singular CNT tips in a form of array in an economic way, (2) uniform CNT emission property, (3) each CNT tip can be controlled individually which can further enhanced ionization efficiency. Previous investigation regarding the work function at the tip of individual single-walled CNTs (SWCNTs) and multi-walled CNTs (MWCNTs) has shown no significant relation with tip size as listed in Table 6-1. Experimental results [138,141] indicated there are no significant differences of work function of MWCNTs in the diameter ranging 15~60 nm as listed in Table 6-2, in which the values of work function are 4.5~4.9 eV. Additionally, the work function of the SWCNTs with diameter about 1 nm [139,140] roughly has a fixed value of 4.8~5.1 eV. Thus, it can be safely to assume that there is no significant relation and sufficient expressions between the diameter of a CNT and its own work function while the  $D$  is lower than 61 nm. It is noted that these values of a CNT is very close to the work functions of Cu and W. According to Fowler-Nordheim theory (F-N theory) [141], similar emission characteristics can be expected.

On the other hand, the electric field,  $E$ , nears the tip should be governed by the tip

Table 6-2  
Systematic field emission data [141]

Sample No.	$l$ ( $\mu\text{m}$ )	$d$ ( $\mu\text{m}$ )	$D$ (nm)	$\phi$ (eV)
1	0.32	2.16	52.4	4.60
2	3.9	4.3	31.7	4.51
3	3.9	4.3	31.7	4.78
4	11.2	16.9	61.1	4.58
5	6.4	8.2	46.4	4.60

The symbols used above  $l$ ,  $d$ ,  $D$ , and  $\phi$  are length of a CNT, distance from substrate to electrode, diameter of a CNT, and the work function, respectively.

morphology and the applied voltage,  $V$ . The first approximation is expressed as follows [136,144]:

$$E = \frac{V}{\kappa R}, \quad (6-17)$$

where  $R$  and  $\kappa$  are the tip radius of curvature and the field factor with a value typically of 3~8 that depends on the tip material and the geometry, respectively. For instance, if we apply a voltage of 10 kV on the tip with radius about 50 nm, the strength of the electric field with value of 2~5 V/Å will be induced. The smaller the radius as well as the diameter of the tip is, the stronger the strength of the electric field will be. It is noted that the parameter  $\kappa$  strongly relies on the adopted material and geometry of tip and it could be only alternatively determined by tailor-made measurements or F-N plot [ $\ln(I/V^2)$  vs.  $1/V$ , where  $I$  is emission current and  $V$  is applied voltage]. Meanwhile, in F-N theory, the field emission current can be determined by  $\beta$  which is called field enhancement factor and the work function  $\varphi$ :

$$I = \frac{K(\beta E)^2}{\varphi} \exp\left(-\frac{B\varphi^{3/2}}{\beta E}\right), \quad (6-18)$$

where  $K$  is a constant,  $B=6.83 \times 10^9 \text{V eV}^{-3/2} \text{m}^{-1}$ , and  $E$  is electric field. Thus, the field enhancement factor  $\beta$  can be determined by means of the slope of the F-N plot,  $m$ , as the follows [141]:

$$\beta = -\frac{1}{B} \varphi^{-3/2} \frac{E}{V} m. \quad (6-19)$$

The measurements are to trace a slope of F-N plot as shown in Figure 6-7 for the case of CNTs. According to the measurements, high field-emission phenomenon as well as high field enhancement factor,  $\beta$ , only happens when the tubes with high aspect ratio (height: diameter ~3: 1) are separated from each other at about the distance that corresponds to their height as shown in Figure 6-8, which is called field-screening effect [145].

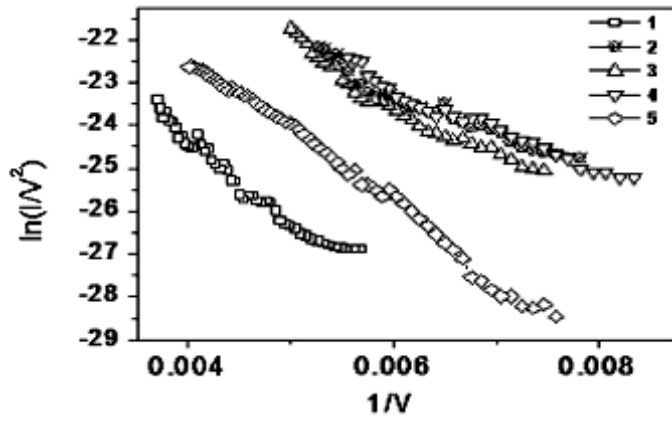


Figure 6-7: The corresponding measured F-N plot for CNTs [141].

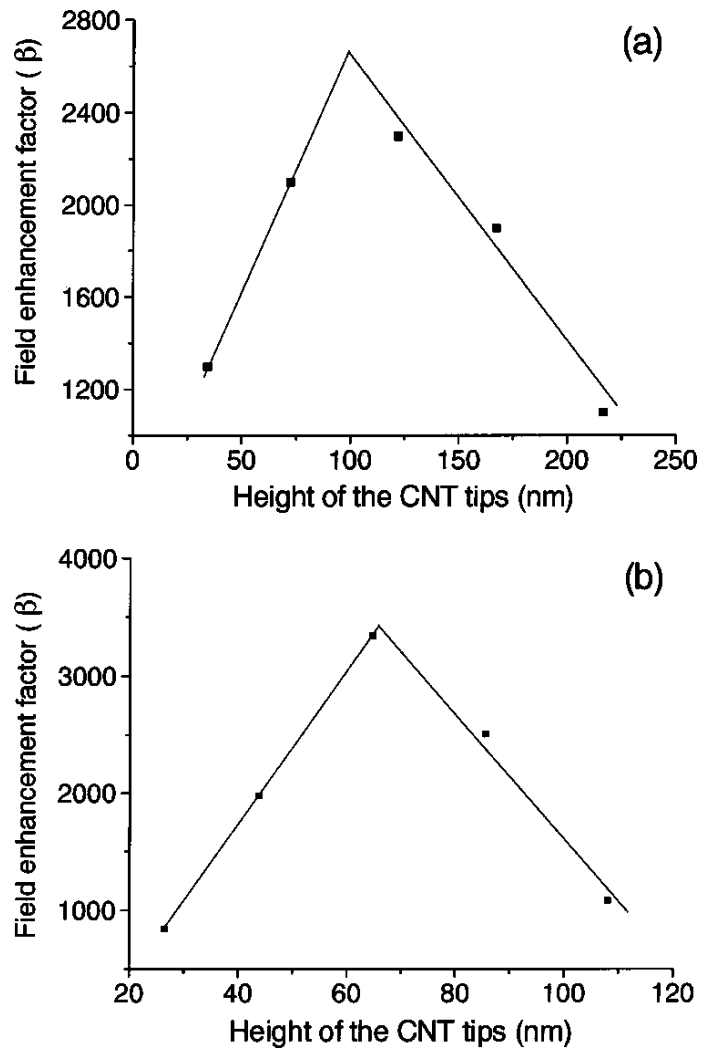


Figure 6-8: Enhancement factor vs. the tube height for CNTs whose intertube distances are (a) 104 and (b) 65 nm [145].

Thus, the efficiency of the detection will be significantly depending on tip aspect ratio and the corresponding spacing with each other. Previous investigation has shown that catalytic seed varieties and sizes can play an important role in determining the diameter and property of CNT in addition to the synthesis methods and growth conditions. For realizing the research objective, the first technical challenge to fabricate the 3D-CNT array based field-ionizer as well as the 3DICs embedded in a micor- or nano-electronic system is to satisfy the requirement of a particular method useful for 1D material seeding control. Both physically and experimentally, the developed scheme in Chapter 6 should be one of the candidates for achieving the particular requirement.

## 6.6 Summary

This chapter presents a seeding control scheme by utilizing gravity force to form an agglomeration of molten Co seeds on a patterned inverted silicon nanopyramid. Nanometer sized molten Co seeds formed on a nonwetttable inverted pyramid surface can roll along the inclination followed by aggregation to form a singular seed with the size depending on the pyramid size and the thickness of as-deposited Co film inside the pyramid. The proposed scheme allowing the formation of well-aligned catalytic seeds with manipulated size will promise the control growth of 1-D material for practical integrated microelectronic device fabrication.



## ***Chapter 7 Conclusion***

For the purpose to preliminarily explore the world of micro-electro-mechanical system, physical analyses of main MEMS component structures, including a micromachined spiral inductor, patterned dielectric fins, a hybrid biomimetic directional microphone, a thermal analysis of a heating microsystem, and a precise seeding control scheme for 1D material growth, are achieved for optimal microsystem designs in this dissertation. Inductor is an indispensable component used extensively in analog circuits and signal processing for wireless communication. An associated model using the Kramers-Kronig relations is proposed for MEMS RF passive applications. Models of self-resonant frequency and frequency-dependent inductances have been well developed and can exactly predict physical characteristics of a freely suspended micromachined polygonal spiral inductor. Developing Green's function could qualitatively describe the influence from grounded pads to the interesting circuitry or system. Meanwhile, in order to eliminate the undesired substrate coupling effects, a practical substrate loss reduction method, patterned nitride/oxide/nitride/air fins support, is demonstrated using CMOS-compatible fabrication process for high performance MEMS RF passive component fabrication. An equivalent circuit model has been also developed and validated by HFSS simulation for the circuit designers to well predict the high frequency characteristics of a CPW for CMOS RF MEMS design. Comparison of simulation results between the substrate loss of a spiral inductor deposited on nitride/oxide/nitride/air fins and that on conventional silicon based substrate shows the practicality of the proposed fins structure in RF MEMS optimization.

A new hybrid biomimetic microphone with a central floating joint design for sound source localization has been well analyzed to develop the next generation acoustic sensing and tracking microsystems like hearing aids, robots, and bionic military devices. By means of the dynamic analysis and the comparison of the microphones with the conventional designs,

two significant important features are revealed: (1) the clover-stem-like gimbal central-supported structure with a fourfold rotation axial symmetry can compensate the deformation due to gravity and residual stresses for exact sound source localization, and (2) central floating joint makes the sensing diaphragm of the microphone more flexible for better sound pressure sensitivity. The proposed hybrid central-supported structure can effectively enhance sound source localization ability of the MEMS-typed biomimetic microphones with a potential application for hearing aids. Additionally, the quality factors and air damping effect are also discussed theoretically.

To entirely analyze and manage the thermal distribution with a extensive chipset or microsystem, a method of thermal analysis is physically and conceptually presented by means of a general electrothermal network  $\pi$ -model in system level and an associated mathematical technique, the Green's theorem. By decomposing the heating system into three main components, a complicated heating structure can be efficiently simplified without degrading the analytical accuracy. The derived heat conduction and convection equations in integral forms could help the designers and engineers realize the thermal behaviors within the integrated circuits and the thermal interconnections between the systems and the external surrounding surfaces. By finding the isothermal surfaces within the heating source components, the hottest spot and the probable paths of the thermal flow can be uniquely determined, so the heating system could be further optimized to avoid the device failure or break-down. Furthermore, the associated equivalent electrothermal circuit model can be readily used for design optimization via CAD programming in terms of the structure geometry and physical characteristics of materials used in the MEMS device or microsystem. The model can also lead a way for structure simplification and system optimization with high accuracy and achieve the goal of CPU time-saving in 3-D FEA simulation without complex mesh studying or scaling.

Furthermore, to definitely inherit the three generic and distinct merits for MEMS devices:

miniaturization, microelectronics integration, and mass production with precision, the unity and localization of the catalytic seed for 1D material growth application has been realized by utilizing the effects of gravitational force on the nanometer sized liquid seeds to form an aggregated singular seed in a patterned inverted silicon nano-pyramid with a specific location. Rolling along an inclined surface is the key mechanism to the coalescence of seeds at the bottom. By well adjusting the thermal reflowing temperature and process time of the catalytic film deposited on the pyramid, the size of the aggregated seed can be controlled by the deposited film thickness and the pyramid size. The result has also revealed the first step to realize the possible scheme of vertical 3DICs using the 1D material.

Meanwhile, by considering the cooperation with the EDA technique, Fig. 7-1 visually shows the connection between the developed physical behavior models and the EDA programming, in which the mechanical or electric inputs could be conceptually converted to the required electric output signals. In the future, other physical characteristics of the on-chip inductor, such as quality factor, energy loss mechanics, parasitic capacitances and resistances must be developed and discussed in details. Response functions (i.e., the Green's function) connected to the correlation between the grounded pads effect and interesting system would be definitely clarified. A Smith chart constructed by the promoted model with strongly physical senses should be presented to achieve the goals of optimized microsystem designs in views of both engineering and physics. Additionally, accompanying with an implemented circuitry, a multi-channels MEMS acoustic sensor with superior sensitivity and directivity could be fabricated for human hearing aids, voiceprint recognize, and cochlear prosthesis. Issue of the thermal accumulation within the MEMS component structures, the microsystem, and the implement circuitry could be sufficiently resolved by means of the well developed Green's theorem-base algorithm. Furthermore, intensive circuitry system, such as retinal prosthesis, micro-robots for clinical diagnosis, and 3D stacked tissues, could be realized and buildup using the proposed method of 1D material seeding controlling for

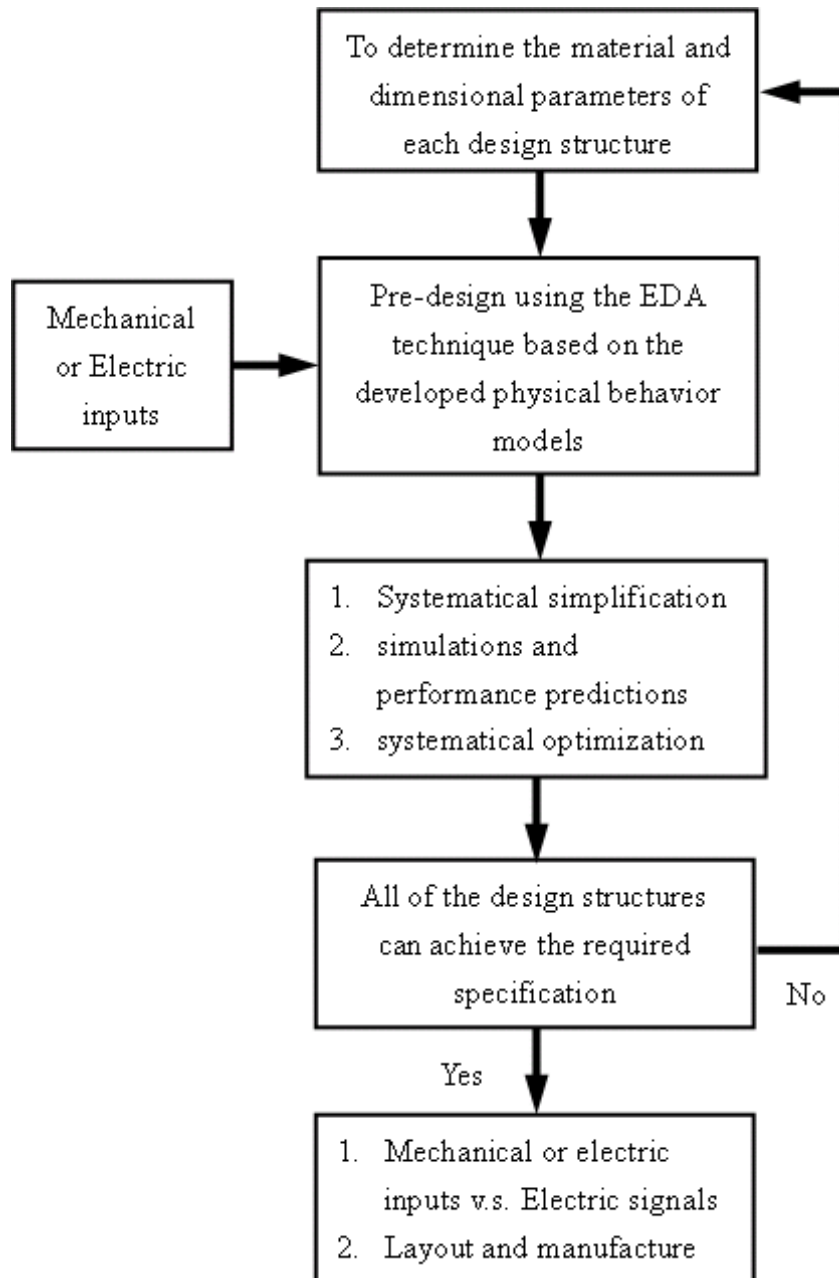


Figure 7-1: A flow chart of microsystem optimization using the EDA technique and the associated physical behavior models.

engineering and BioMEMS applications. More functionality could be included in a tiny package to effectively reduce propagating delay in the future. Eventually, physical analyses of MEMS component structures for optimal microsystem designs are completely presented in this dissertation.

## Reference

- [1] R. P. Feynman, "There's plenty of room at the bottom," *Journal of Microelectromechanical System*, Vol. 1, pp.60-66, 1992.
- [2] R. P. Feynman, "Infinitesimal machinery," *Journal of Microelectromechanical System*, Vol. 2, pp.4-14, 1993.
- [3] C. Liu, Foundations of MEMS, Illinois ECE series, Pearson Prentice Hall, 2006.
- [4] C. C. Chen, J. K. Huang, and Y. T. Cheng, "A Closed-Form Integral Model of the Spiral Inductor Using Kramers-Kronig Relations," *IEEE Microwave Component Letter*, Vol. 15, pp.778-780, 2005.
- [5] C. C. Chen, Cheng-De Lin, and Y. T. Cheng, "Model to Determine the Self-Resonant Frequency of Micromachined Spiral Inductors," *Appl. Phys. Lett.*, Vol. 89, pp. 103521-103523, 2006.
- [6] C. C. Chen, Ssu-Ying Chen, and Y. T. Cheng, "A Patterned Dielectric Support Process for High Performance Passive Fabrication," *IEEE Microwave Component Letter*, Vol. 18, pp.82-84, 2008.
- [7] C. C. Chen and Y. T. Cheng, "Physical Analysis of a Biomimetic Microphone with a Central-Supported (C-S) Circular Diaphragm for Sound Source Localization," has been submitted to *JMEMS*.
- [8] C. C. Chen, Lun-Hao Hsu, Kai Rern, Y. T. Cheng, Yi-Fan Hsieh, and Pu-Wei Wu, "Gravity-Assisted Seeding Control for One-Dimensional Material Growth," *IEEE Transactions on Nanotechnology*, Vol. 8, pp.427-430, 2009.
- [9] C. C. Chen, Y. C. Chen, Chin-Ta Chen, Hsu-Liang Hsiao, Chia-Chi Chang, Y. T. Cheng, and Mount-Learn Wu, "Thermal Analysis: VCSELs on a SiOB," *IEEE Journal of Selected Topics in Quantum Electronics*, in proofreading.
- [10] K. Puttaswamy and G. H. Loh, "Thermal analysis of a 3D die-stacked high-performance microprocessor," *Proceedings of the 16th ACM Great Lakes symposium on VLSI*

- (GLSVLSI), Philadelphia, PA, USA, pp. 19-24, Apr. 2006.
- [11] B. Goplen and S. Sapatnekar, "Thermal via placement in 3D ICs," *in. Proc. Int. Symp. Phys. Des. (ISPD)*, San Francisco, CA, USA, pp. 167-174, Apr. 2005.
- [12] J. Cong and Y. Zhang, "Thermal Via Planning for 3-D IC's," *Proceedings of the 2005 IEEE/ACM International Conference on Computer Aided Design*, San Jose, CA, USA, pp. 744-751, Nov. 2005.
- [13] W. Huang, E. Humenay, K. Skadron and M. Stan. "The Need for a Full-Chip and Package Thermal Model for Thermally Optimized IC Designs". *Intl. Symp. on Low Power Electronic Desig (ISLPED)*, San Diego, USA, pp. 245-250, Aug. 2005.
- [14] E. W. Wong, P. E. Sheehan, and C. M. Lieber, "Nanobeam Mechanics: Elasticity, Strength, and Toughness of Nanorods and Nanotubes," *Science*, Vol. 277, pp. 1971-1975, 1997.
- [15] X. M. H. Huang, C. A. Zorman, M.n Mehregany, and M. L. Roukes, "Nanoelectromechanical Systems: Nanodevice Motion at Microwave Frequencies," *Nature*, Vol. 421, pp.496, 2003.
- [16] J. Liu, A. G. Rinzler, H. Dai, J. H. Hafner, R. K. Bradley, P. J. Boul, A. Lu, T. Iverson, K. Shelimov, C. B. Huffman, F. R.-Macias, Y.-S. Shon, T. R. Lee, D. T. Colbert, R. E. Smalley, "Fullerene Pipes," *Science*, Vol. 280, pp.1253-1256, 1998.
- [17] D. W. Carr, S. Evoy, L. Sekaric, H. G. Craighead, and J. M. Parpia, "Measurement of Mechanical Resonance and Losses in Nanometer Scale Silicon Wires," *Applied Physics Letters*, Vol. 75, pp.920-922, 1999.
- [18] H. M. Greenhouse, "Design of planar rectangular microelectronic inductor," *IEEE Trans. Parts, Hybrids, Packag.*, Vol. PHP-10, no. 2, pp. 101-109, Jun. 1974.
- [19] S. Jenei, B. K. J. C. Nauwelaers, and S. Decoutere, "Physics-based closed-form inductance expression for compact modeling of integrated spiral inductors," *IEEE J. Solid-State Circuits*, Vol. 37, no. 1, pp. 77-80, Jan. 2002.



- [20] S. Asgaran, "New accurate physics-based closed-form expressions for compact modeling and design of on-chip spiral inductors," in *Proc. 14th Int. Conf. Microelectronics (ICM)*, Beirut, Lebanon, pp. 247-250, Dec. 2002.
- [21] S. S. Mohan, M. M. Hershenson, S. P. Boyd, and T. H. Lee, "Simple accurate expressions for planar spiral inductance," *IEEE J. Solid-State Circuits*, Vol. 34, no. 10, pp. 1419-1424, Oct. 1999.
- [22] A. M. Niknejad and R. G. Meyer, Design, Simulation and Applications of Inductors and Transformers for Si RF ICs. Boston, MA: Kluwer, 2000.
- [23] Y. Koutsoyannopoulos et al., "A generic CAD model for arbitrary shaped and multilayer integrated inductors on silicon substrates," in *Proc. of the 27th European Solid-State Device Research Conference (ESSDRC)*, Stuttgart, Germany, pp. 320-323, Sep. 1997.
- [24] J. R. Long and M. A. Copeland, "The modeling, characterization and designed monolithic inductors for silicon RF ICs," *IEEE J. Solid-State Circuits*, Vol. 32, no. 3, pp. 357-369, Mar. 1997.
- [25] A. M. Niknejad and R. G. Meyer, "Analysis, design and optimization of spiral inductors and transformers for Si RF ICs," *IEEE J. Solid-State Circuits*, Vol. 33, no. 10, pp. 1470-1481, Oct. 1998.
- [26] C. A. Brau, Modern Problems in Classical Electrodynamics, New York: Oxford Univ., 2004.
- [27] J. D. Jackson, Classical Electrodynamics, 3rd New York: Wiley, 1998.
- [28] C. Kittel, Introduction to Solid State Physics, 7th Ed. New York:Wiley, 2004.
- [29] N. W. Ashcroft and N. D. Mermin, Solid State Physics, New York: Holt-Sanders, 1976.
- [30] G. B. Arfken and H. J. Weber, Mathematical Methods for Physicists, HP, 2001.
- [31] A. S. Kronfeld and B. Nižić, "Nucleon Compton scattering in perturbative QCD," *Physics Review D*, Vol. 44, pp. 3445-3465, 1991.
- [32] F. J. Federspiel, R. A. Eisenstein, M. A. Lucas, B. E. MacGibbon, K. Mellendorf, A. M.



- Nathan, A. O'Neill, and D. P. Wells, "Proton Compton effect: A measurement of the electric and magnetic polarizabilities of the proton," *Physics Review Letters*, Vol. 67, pp. 1511-1514, 1991.
- [33] J. Y. Park and M. G. Allen, "High Q spiral-type microinductors on silicon substrates," *IEEE Transactions on Magnetics*, Vol. 35, no. 5, pp. 3544-3546, 1999.
- [34] Jr-Wei Lin, "An Optimum Design of the Micromachined RF Inductor," National Chiao Tung University, Master Thesis, 2004.
- [35] Ansoft-HFSS, <http://www.ansoft.com/products/hf/hfss/>
- [36] Manual of Ansoft HFSS, conf. NCHC, R. O. C.
- [37] B. Wagner, and W. Benecke, "Microfabricated actuator with moving permanent magnet," pp. 27-31, in *Proceedings IEEE Micro Electro Mechanical Systems*, Nara, Japan, 1991.
- [38] B. Rejaei, M. Vroubel, Y. Zhuang, and J. N. Burghartz, "Assessment of ferromagnetic integrated inductors for Si-technology," *Digest of Papers 4<sup>th</sup> Topical Meeting on Silicon Monolithic Integrated Circuits in RF Systems*, near Garmisch, Southern Germany, pp.100-103, 2003.
- [39] D. G. Han, and G. M. Choi, "Computer simulation of the electrical conductivity of composites: the effect of geometrical arrangement," *Solid State Ionics*, Vol. 106, pp. 71-87, 1998.
- [40] B. D. Cullity, Introduction to Magnetic Materials, New York, Addison-Wesley, 1973.
- [41] P. Cizeau, S. Zapperi, G. Durin, and H. E. Stanley, "Dynamics of a ferromagnetic domain wall and the Barkhausen effect," *Physical Review Letter*, Vol. 79, pp. 4669-4672, 1997.
- [42] Yu Wen Huang, Tzu-Yuan Chao, C. C. Chen, and Y. T. Cheng, "Power consumption reduction scheme of magnetic microactuation using electroplated Cu-Ni nanocomposite," *Applied Physics Letters*, Vol. 90, pp. 244105-1-244105-3, 2007.
- [43] N. J. Tang, W. Zhong, W. Liu, H. Y. Jiang, X. L. Wu, and Y. W. Du, "Synthesis and complex permeability of Ni/SO<sub>2</sub> nanocomposites," *Nanotech.*, Vol. 15, pp.1756-1758,

2004.

- [44] Jr-Wei Lin, C. C. Chen, and Yu-Ting Cheng, “A Robust High-Q Micromachined RF Inductor for RFIC Applications”, *IEEE Transactions on Electron Devices*, Vol. 52, pp. 1489-1496, July 2005.
- [45] K. T. Chan, C. Y. Chen, Albert Chin, J. C. Hsieh, J. Liu, T. S. Duh, and W. J. Lin, “40-GHz Coplanar Waveguide Bandpass Filters on Silicon Substrate”, *IEEE Microwave and Wireless Components Letters*, Vol. 12, pp. 429-431, Nov. 2002.
- [46] C. Patrick Yue and S. Simon Wong, “On-Chip Spiral Inductors with Patterned Ground Shields for Si-Based RFIC’s”, *IEEE J. of Solid State Circuits*, Vol. 33, pp. 743-752, May 1998.
- [47] Mina Raieszadeh, Pejman Monajemi, Sang-Woong Yoon, Joy Laskar, and Farrokh Ayazi, “High-Q Integrated Inductors on Trenched Silicon Islands”, *Micro Electro Mechanical Systems 18th IEEE International Conference*, Miami, pp. 199-202, Jan. 2005.
- [48] L. J. Fernandez, E. Berenschot, J. Sese, R. J. Wiegerink, J. Flokstra, H. V. Jansen, and M. Elwenspoek, “Fabrication of Thick Silicon Nitride Blocks for Integration of RF Devices”, *IEEE Electronics Letters*, Vol. 41, pp. 124-125, Feb. 2005.
- [49] Ssu Ying Chen, “A CMOS Compatible Patterned Dielectric Support Process for Beyond 20GHz Silicon RFIC Applications,” National Chiao Tung University, Master Thesis, 2006.
- [50] K. C. Gupta, Microstrip lines and slotlines, 2nd Ed, Artech House Antennas and Propagation Library, 1996.
- [51] M. S. Kushwaha, P. Halevi, and G. Martinez, “Theory of acoustic band structure of periodic elastic composites”, *Physical Review B*, Vol. 49, pp. 2313-2322. Jan. 1994.
- [52] I. J. Bahl and D. K. Trivedi, “A Designer’s Guide to Microstrip Line”, *Microwaves*, Vol. 16, pp. 174-182, May 1977.
- [53] D. M. Pozar, Microwave Engineering, John Wiley&Sons, 2nd Ed.

- [54] H. Lakdawala, X. Zhu, H. Luo, S. Santhanam, L. R. Carley, and G. K. Fedder, "Micromachined high Q inductors in 0.18- $\mu\text{m}$  Cu interconnect low-K CMOS," in *Proc. IEEE Custom Integrated Circuits Conf.*, San Diego, CA, USA, pp. 579-582, May 2001.
- [55] Y. C. Chen, C.-H. Li, J. K. Huang, C.-N. Kuo, and Y. T. Cheng, "Low Power 3~8 GHz UWB Tunable LNA Design Using SiP Technology," *IEEE Int. Conference on Electronics, Circuits and Systems Proc.*, Nice, FR, pp. 1026-1029, Dec. 2006.
- [56] Chun-Hsing Li, Chang Tsung Fu, Tzu-Yuan Chao, Chien-Nan Kuo, Y. T. Cheng, and D.-C. Chang "Broadband Flip-Chip Interconnects for Millimeter-Wave Si-Carrier System-on-Package", *IEEE IMS-MTT*, pp. 1645-1648, June 2007.
- [57] D. Robert, R. N. Miles, and R. R. Hoy, "Directional hearing by mechanical coupling in the parasitoid fly *Ormia Ochracea*," *Journal of Comparative Physiology A*, Vol. 179, pp. 29-44, July 1996.
- [58] R. N. Miles, D. Robert, and R. R. Hoy, "Mechanically coupled ears for directional hearing in the parasitoid fly *Ormia Ochracea*," *Journal of the Acoustical Society of America*, Vol. 98, pp. 3059-3070, June 1995.
- [59] D. Robert, J. Amoroso, and R. R. Hoy, "The evolutionary convergence of hearing in a parasitoid fly and its cricket host," *Science*, Vol. 258, pp. 1135-1137, November 1992.
- [60] D. Robert, R. N. Miles, and R. R. Hoy, "Tympanal mechanics in the parasitoid fly *Ormia ochracea*: intertympanal coupling during mechanical vibration," *Journal of Comparative Physiology A*, Vol. 183, pp. 443-452, June 1998.
- [61] D. Robert, R. N. Miles, and R. R. Hoy, "Tympanal hearing in the Sarcophagid Parasitoid Fly *Emblemasoma* SP.: the biomechanics of directional hearing" *The Journal of Experimental Biology*, Vol. 202, pp. 1865-1876, June 1999.
- [62] D. Robert and M. C. Göpfert, "Acoustic sensitivity of fly antennae," *Journal of Insect Physiology*, Vol. 48, pp. 189-196, February 2002.
- [63] G. U. C. Lehmann and K.-G. Heller, "Bushcricket song structure and predation by the

- acoustically orienting parasitoid fly *Therobia leonidei* (Diptera: Tachinidae: Ormiini),” *Behav. Ecol. Sociobiol.*, Vol. 43, pp. 239-245, March 1998.
- [64] U. Köhler and R. Lakes-Harlan, “Auditory behaviour of a parasitoid fly (*Emblemasoma auditrix*, Sarcophagidae, Diptera),” *Journal of Comparative Physiology A*, Vol. 187, pp. 581-587, September 2001.
- [65] A. C. Mason, M. L. Oshinsky, and R. R. Hoy, “Hyperacute directional hearing in a microscale auditory system,” *Nature*, Vol. 410, pp. 686-690, April 2001.
- [66] J. Sueur, E. J. Tuck, and D. Robert, “Sound radiation around a flying fly,” *Journal of the Acoustical Society of America*, Vol. 118, pp. 530-538, July 2005.
- [67] N. Ono, A. Saito, and S. Ando, “Design and experiments of bio-mimicry sound source localization sensor with gimbal-supported circular diaphragm,” in *Proceedings of the 12th International Conference on Solid-State Sensors, Actuators and Microsystems*, pp. 935-938, 2003.
- [68] N. Ono, A. Saito, and S. Ando, “Bio-mimicry Sound Source Localization with Gimbal Diaphragm,” *T. IEE Japan*, Vol. 123-E, pp. 92-97, 2003.
- [69] L. Tan, R. N. Miles, M. G. Weinstein, R. A. Miller, Q. Su, W. Cui, and J. Gao, “Response of a biologically inspired MEMS differential microphone diaphragm,” in *Proc. of SPIE*, Vol. 4743, pp. 91-98, 2002.
- [70] W. Cui, B. Bicen, N. Hall, S.A. Jones, F. L. Degertekin, and R.N. Miles, “Optical sensing in a directional MEMS microphone inspired by the ears of the parasitoid fly, *Ormia ochracea*,” in *Proceedings of the 19th IEEE International Conference on Micro Electro Mechanical Systems*, pp. 614-617, 2006.
- [71] H. Liu, X. Zhang, and M. Yu, “Understanding fly-ear inspired directional microphones” in *Proc. of SPIE*, pp. 2M1-2M11, 2009.
- [72] S. Chowdhury, M. Ahmadi, and W. C. Miller, “Nonlinear effects in MEMS capacitive microphone design,” in *Proceedings of International Conference on MEMS, NANO and*

*Smart Systems*, pp. 297-302, 2003.

- [73] J. Reinke, A. Jajoo, L. Wang, G. Fedder, and T. Mukherjee, "CMOS-MEMS Variable Capacitors with Low Parasitic Capacitance for Frequency-Reconfigurable RF Circuits," *IEEE Radio Frequency Integrated Circuits Symposium*, pp. 509-512, 2009.
- [74] Y. Zhang, Q. Ren and Y.-P. Zhao, "Modelling analysis of surface stress on a rectangular cantilever beam," *J. Phys. D: Appl. Phys.*, Vol. 37, pp. 2140-2145, 2004.
- [75] CoventorWare 2008, <http://www.coventor.com/>, version 2008.
- [76] H. Liu, L. Currano, D. Gee, B. Yang, and M. Yu, "Fly-ear inspired acoustic sensors for gunshot localization," in *Proc. of SPIE*, pp. 73210A-1-73210A-8, 2009.
- [77] Marison Thornton, Classical dynamics of particles and systems, Chapter 3, pp.116-131, 4th ed., Harcourt, 1995.
- [78] L. D. Landau and E. M. Lifshitz "Mechanics," Vol. 1, Chapter 5, 3rd ed., Butterworth-Heinemann.
- [79] Z. Hao, R. Clark, J. Hammer, M. Whitley, and B. Wingfield, "Modeling air-damping effect in a bulk micromachined 2D tilt mirror," *Sensors and Actuators A: Physical*, Vol. 102, pp. 42-48, 2002.
- [80] M. Bao and H. Yang, "Squeeze film air damping in MEMS," *Sensors and Actuators A: Physical*, Vol. 136, pp. 3-27, 2007.
- [81] M. Bao, H. Yang, H. Yin, and Y. Sun, "Energy transfer model for squeeze-film air damping in low vacuum," *J. Micromech. Microeng.*, Vol. 12, pp. 341-346, 2002.
- [82] H. J. Liu, M. Yu, and X. M. Zhang, "Biomimetic optical directional microphone with structurally coupled diaphragms," *Applied Physics Letters*, Vol. 93, pp. 243902-1-243902-3, 2008.
- [83] L. J. Currano, H. Liu, D. Gee, B. Yang, and M. Yu, "Microscale implementation of a bio-inspired acoustic localization device," in *Proc. of SPIE*, pp. 73210B-1-73210B-8, 2009.

- [84] Keng-Yu Lin, National Chiao Tung University, Master Thesis, 2010.
- [85] A. M. Darwish, A. J. Bayba, and H. A. Hung, "Accurate Determination of Thermal Resistance of FETs," *IEEE Transactions on Microwave Theory and Techniques*, Vol. 53, pp. 306-313, 2005.
- [86] A. H. Ajami, Kaustav Banerjee, and M. Pedram, "Modeling and Analysis of Nonuniform Substrate Temperature Effects on Global ULSI Interconnects," *IEEE Transactions on Computer-Aided Design of Integrated Circuits and Systems*, Vol. 24, pp. 849-861, 2005.
- [87] F. Tamigi, N. Nenadović, V. d'Alessandro, L. K. Nanver, N. Rinaldi, and J. W. Slotboom, "Modeling of thermal resistance dependence on design parameters in silicon-on-glass bipolar transistors," in *Proc. IEEE 24th International Conference on Microelectronics*, Vol. 1, Niš, Serbia-Montenegro, pp.257-260, May 2004.
- [88] B. Goplen and S. Sapatnekar, "Thermal Via Placement in 3D ICs," *Proceedings of the 2005 international symposium on Physical design*, pp.167-174, April 2005.
- [89] K. Vanmeensel, A. Laptev, J. Hennicke, J. Vleugels, and O. V. der Biest, "Modeling of the temperature distribution during field assisted sintering," *Acta Materialia*, Vol. 53, pp.4379-4388, August 2005.
- [90] A. J. Kemp, G. J. Valentine, J.-M. Hopkins, J. E. Hastie, S. A. Smith, S. Calvez, M. D. Dawson, and D. Burns, "Thermal Management in Vertical-External-Cavity-Surface-Emitting Lasers: Finite-Element Analysis of a Heatspreader Approach," *IEEE Journal of Quantum Electronics*, Vol. 41, pp.148-155, February 2005.
- [91] C. C. Chen, C. Singh, Y. C. Chen, Hsu-Liang Hsiao, Chia-Yu Lee, Mount-Learn Wu, and Y. T. Cheng, "Equivalent Electrothermal Circuit Model for Vertical-Cavity Surface-Emitting Lasers on Silicon Optical Bench," *15th International Workshop on Thermal investigations of ICs and Systems (THERMINIC)*, Leuven, Belgium, pp. 8-12, Oct. 2009.
- [92] I. P. Kaminow and T. L. Koch, Optical fiber telecommunications IIIB, Boston: Academic



Press, 1997, Vol. 2, Chap. 8.

- [93] C. Schuster, D. M. Kuchta, E. G. Colgan, G. M. Cohen, and J. M. Trehwella, "Package design and measurement of 10 Gbps laser diode on high-speed silicon optical bench," *IEEE 12th Topical Meeting on Electrical Performance of Electronic Packaging*, Princeton, New Jersey, pp. 63-66, Oct. 2003.
- [94] H.-L. Hsiao, H.-C. Lan, C.-C. Chang, C.-Y. Lee, S.-P. Chen, C.-H. Hsu, S.-F. Chang, Y.-S. Lin, F.-M. Kuo, J.-W. Shi, and M.-L. Wu, "Compact and passive-alignment 4-channel  $\times$  2.5-Gbps optical interconnect modules based on silicon optical benches with 45° micro-reflectors," *Optics Express*, Vol. 17, pp. 24250-24260, Dec. 2009.
- [95] VCSEL Technology, BeamExpress, SA, "Wafer-fused VCSELs shape up for enterprise applications," *Compound Semiconductor*, pp.25-27, 2005. Available: <http://www.beamexpress.com/publications.php>
- [96] W. Nakwaski, "Principles of VCSEL designing," *Opto-Electronics Review*, Vol. 16, pp.18-26, 2008.
- [97] W. Nakwaski and M. Osiński, "III. Thermal Properties of Vertical-Cavity Surface-Emitting Lasers," *Progress in Optics*, Vol. 38, pp.165-262, 1998.
- [98] L. Piskorski, R. P. Sarzala, M. Wasiak, and W. Nakwaski, "Tuning effects in optimization of GaAs-based InGaAs/GaAs quantum-dot VCSELs," *Optics Communications*, Vol. 281, pp.3163-3170, 2008.
- [99] M. Osiński and W. Nakwaski, "Effective thermal conductivity analysis of 1.55- $\mu$ m InGaAsP/InP vertical-cavity top-surface-emitting microlasers," *Electronics Letters*, Vol. 29, pp.1015-1016, May 1993.
- [100] W. Nakwaski, "Thermal conductivity of binary, ternary, and quaternary III-V compounds," *Journal of Applied Physics*, Vol. 64, pp.159-166, 1988.
- [101] J. Piprek, T. Tröger, B. Schröter, J. Kolodzey, and C. S. Ih, "Thermal Conductivity Reduction in GaAs–AlAs Distributed Bragg Reflectors," *IEEE Photonics Technology*



- Letters*, Vol. 10, pp.81-83, 1998.
- [102] W. Nakwaski and M. Osiński, "Heat source distribution in etched-well surface-emitting semiconductor lasers", *IEEE Photonics Technology Letters*, Vol. 3, pp.979-981, Nov. 1991.
- [103] R. Bialecki and A. J. Nowak, "Boundary value problems in heat conduction with nonlinear material and nonlinear boundary conditions," *Applied Mathematical Modelling*, Vol. 5, pp. 417-421, Dec. 1981.
- [104] M.-N. Sabry, "Static and dynamic thermal modeling of ICs," *Microelectronics Journal*, Vol. 30, pp. 1085-1091, Nov. 1999.
- [105] W. Greiner, Classical Electrodynamics, New York: Springer-Verlag, 1991.
- [106] G. D. Mahan, Many-Particle Physics, New York: Plenum Press, 1981.
- [107] F. P. Incropera and D. P. Dewitt, Introduction to Heat Transfer, John Wiley & Sons, Inc., 1996.
- [108] 5 Gb/s 1310 nm waveband VCSEL, PRELIMINARY Datasheet, BeamExpress, SA. Available: <http://www.beamexpress.com>.
- [109] Gilbert Strang, Introduction to applied mathematics, Wellesley-Cambridge Press, USA, 1986.
- [110] C. J. Lee, T. J. Lee, S. C. Lyu, Y. Zhang, H. Ruh, and H. J. Lee, "Growth mechanism and field emission properties of inject-like ZnO nanostructure," *Appl. Phys. Lett.*, Vol. 81, pp. 3648-3650, 2002.
- [111] A. Javey, J. Guo, Q. Wang, M. Lundstrom, and H. Dai, "Ballistic carbon nanotube field-effect transistors," *Nature*, Vol. 427, pp. 654-657, 2003.
- [112] M. Law, H. Kind, F. Kim, B. Messer, and P. Yang, "Photochemical sensing of NO<sub>2</sub> with SnO<sub>2</sub> nanoribbon nanosensors at room temperature," *Angew. Chem. Int.*, Vol. 41, pp. 2405-2408, 2002.
- [113] Y. Xia, P. Yang, Y. Sun, Y. Wu, B. Mayers, B. Gates, Y. Yin, F. Kim, and H. Yan,

- “One-dimensional nanostructures: synthesis, characterization, and applications,” *Adv. Mater.*, Vol. 15, pp. 353-389, 2003.
- [114] J. Haruyama, I. Takesue, and T. Hasegawa, “Anomalous localization effects associated with excess volume of cobalt catalyst in multiwalled carbon nanotubes,” *Appl. Phys. Lett.*, Vol. 81, pp. 3031-3033, 2002.
- [115] R. Vajtai, B. Q. Wei and P. M. Ajayan, “Controlled growth of carbon nanotubes,” *Phil. Trans. R. Soc. Lond.*, Vol. A362, pp. 2143-2160, 2004.
- [116] H. Chik, and J. M. Xu, “Nanometric superlattices: non-lithographic fabrication, materials, and prospects,” *Mater. Sci. and Engin. R*, Vol. 43, pp.103-138, 2004.
- [117] M. Ishida, H. Hongo, F. Nihey and Y. Ochiai, “Diameter-controlled carbon nanotubes grown from lithographically defined nanoparticles,” *Jpn. J. Appl. Phys.*, 43, pp. L1356-1358, 2004.
- [118] D. Richard and D. Quéré, “Viscous drops rolling on a tiled non-wettable solid,” *Europhys. Lett.*, Vol. 48, pp.286-291, 1999.
- [119] L. Mahadevan and Y. Pomeau, “Rolling droplets,” *Phys. Fluids*, Vol. 11, pp.2449-2453, 1999.
- [120] D. Quéré, M-J Azzopardi, and L. Delattre, “Drops at rest on a tilted plane,” *Langmuir*, Vol. 14, pp.2213-2216, 1998.
- [121] H.-Y. Kim, H. J. Lee, and B. H. Kang, “Sliding of Liquid Drops Down an Inclined Solid Surface,” *Journal of Colloid and Interface Science*, Vol. 247, pp.372-380, 2002.
- [122] F. D. D. Santos and T. Ondarçuhu, “Free-running droplets,” *Phys. Rev. Lett.*, Vol. 75, pp.2972-2975, 1995.
- [123] R. F. Allen and P. R. Benson, “Rolling drops on an inclined plane,” *Journal of Colloid and Interface Science*, Vol. 50, pp.250-253, 1975.
- [124] U. Thiele, M. G. Velarde, K. Neuffer, M. Bestehorn, and Y. Pomeau, “Sliding drops in the diffuse interface model coupled to hydrodynamics,” *Phys. Rev. E*, Vol. 64,

pp.061601-1-12, 2001.

- [125] T. Podgorski, J.-M. Flesselles, and L. Limat, “Corners, Cusps, and Pearls in Running Drops,” *Phys. Rev. Lett.*, Vol. 87, pp.036102-1-4, 2001.
- [126] J. D. Carter, Y. Qu, R. Porter, L. Hoang, D. J. Masiel and T. Guo, “Silicon-based nanowires from silicon wafers catalyzed by cobalt nanoparticles in a hydrogen environment”, *Chem. Comm.*, Vol. 17, pp. 2274-2276, 2005.
- [127] Y.-M. Chiang, D. P. Birnie, III, and W. D. Kingery, Physical Ceramics: principles for Ceramic Science and Engineering, John Wiley & Sons Inc., 1997.
- [128] K. Nakajima,” Liquid–solid interface free energies for metals from free-volume method and interface structural model”, *ISIJ International*, Vol. 46, pp. 795-800, 2006.
- [129] R. Sangiorgi, M. I. Muolo, D. Chatain, and N. Eustathopoulos, “Wettability and work of adhesion of nonreactive liquid metals on silica”, *J. Am. Ceram.*, Vol. 71, pp. 742-748, 1988.
- [130] W. J. Yao, X. J. Han, M. Chen, B. Wei and Z. Y. Guo, “Surface tension of undercooled liquid cobalt,” *J. Phys. Condens. Matter.*, Vol. 14, pp.7479-7485, 2002.
- [131] G.-H. Jeong, S. Suzuki, Y. Kobayashi, A. Yamazaki, H. Yoshimura, and Y. Homma, “Size control of catalytic nanoparticles by thermal treatment and its application to diameter control of single-walled carbon nanotubes,” *Appl. Phys. Lett.*, Vol. 90, pp. 043108-3, 2007.
- [132] Kai Rern, “Gravity Field Assisted Seeding Control for CNT Growth Application,” National Chiao Tung University, Master Thesis, 2008.
- [133] Lun-Hao Hsu, “Process Optimization of Gravity Assisted Seeding Control Scheme for 1-D Material Growth,” National Chiao Tung University, Master Thesis, 2009.
- [134] E. F. Kukovitsky, S. G. L’vov, N. A. Sainov, V. A. Shustov, and L. A. Chernozatonskii, “Correlation between metal catalyst particle size and carbon nanotube growth,” *Chem. Phys. Lett.*, Vol. 355, pp. 497-503, 2002.

- [135] G. T. A. Kovacs, Micromachined Transducers Sourcebook, McGraw Hill, 1998.
- [136] R. B. Doak, a Y. Ekinici, B. Holst, J. P. Toennies, T. Al-Kassab and A. Heinrich, "Field ionization detection of supersonic molecular beams," *Rev. Sci. Inst.*, Vol. 75, pp. 405-414, Feb. 2004.
- [137] R. Schmoll, "Analysis of the interaction of cathode microprotrusions with low-temperature plasmas," *J. Phys. D: Appl. Phys.*, Vol. 31, pp. 1841-1851, 1998.
- [138] R. Gao, Z. Pan, and Z. L. Wang, "Work function at the tips of multiwalled carbon nanotubes," *Applied Physics Letters*, Vol. 78, pp.1757-1759, 2001.
- [139] M. Shiraishi and M. Ata, "Work function of carbon nanotubes," *Carbon*, Vol. 39, pp. 1913-1917, 2001.
- [140] S. Suzuki, C. Bower, Y. Watanabe, and O. Zhou, "Work functions and valence band states of pristine and Cs-intercalated single-walled carbon nanotube bundles," *Applied Physics Letters*, Vol. 76, pp. 4007-4009, 2000.
- [141] Z. Xu, X. D. Bai, E. G. Wang, and Z. L. Wang, "Field emission of individual carbon nanotube with in situ tip image and real work function," *Applied Physics Letters*, Vol.87, pp. 163106-3, 2005.
- [142] S. Berber, Y.-K. Kwon, and D. Tománek, "Unusually High Thermal Conductivity of Carbon Nanotubes," *Physical Review Letters*, Vol. 84, pp. 4613-4616, 2000.
- [143] T. W. Ebbesen, H. J. Lezec, H. Hiura, J. W. Bennett, H. F. Ghaemi, and T. Thio, "Electrical Conductivity of individual carbon nanotubes," *Nature*, Vol. 382, pp. 54-56, 1996.
- [144] J. Piskur, L. Borg, A. Stupnik, M. Leisch, W. E. Ernst, and B. Holst, "Field ionization of free helium atoms: Correlation between the kinetic energy of ionized atoms and probability of their field ionization," *Applied Surface Science*, Vol. 254, pp. 4365-4369, 2008.
- [145] J. S. Suh, K. S. Jeong, J. S. Lee, and I Han, "Study of the field-screening effect of

highly ordered carbon nanotube arrays,” *Applied Physics Letters*, Vol. 80, pp. 2392-2394, 2002.



## Appendix A Mathematical details of Green's function in Cartesian and Cylindrical Systems

### 1.1 Mathematical details of Green's function in Cartesian Coordinates

First, an expression of potential energy of a rectangular micromachining spiral inductor with a limited-distance grounded plane is derived using the Green's function in Cartesian coordinate, in which original potential of the inductor is set to be  $\Phi_0$ . Starting from the general definition of the Green's function

$$G(\bar{r}, \bar{r}') = G_0(\bar{r}, \bar{r}') + G_i(\bar{r}, \bar{r}') = \frac{1}{4\pi|\bar{r} - \bar{r}'|} + G_i(\bar{r}, \bar{r}'), \quad (\text{A-1})$$

where  $G_0(\bar{r}, \bar{r}')$  and  $G_i(\bar{r}, \bar{r}')$  are the fields generated by the charge sources and induced by the surface charge densities on the surrounding boundary, respectively. In the Cartesian coordinate, the expression of the  $G_i(\bar{r}, \bar{r}')$  is

$$G_i(\bar{r}, \bar{r}') = \frac{1}{4\pi|\bar{r} - \bar{r}'|} = \frac{1}{4\pi [(x-x')^2 + (y-y')^2 + (z-z')^2]^{1/2}}. \quad (\text{A-2})$$

Meanwhile, the  $G_i(\bar{r}, \bar{r}')$  could be assumed to be zero due to the interesting volume is a source free space. Thus, the Green's function becomes

$$G(\bar{r}, \bar{r}') = \frac{1}{4\pi [(x-x')^2 + (y-y')^2 + (z-z')^2]^{1/2}}, \quad (\text{A-3})$$

then

$$\left. \frac{\partial G(\bar{r}, \bar{r}')}{\partial n'} \right|_s = - \left. \frac{\partial G(\bar{r}, \bar{r}')}{\partial z'} \right|_{z'=0} = \frac{1}{4\pi [(x-x')^2 + (y-y')^2 + z^2]^{1/2}}. \quad (\text{A-4})$$

Thus, combining the result of (2-63) with (2-59) above, the potential energy in any observed point at the upper half plane can be expressed as:

$$\Phi_s(\vec{r}) = \frac{z}{2\pi} \int_{-\frac{l_{\max}}{2}}^{\frac{l_{\max}}{2}} dx' \int_{-\frac{l_{\max}}{2}}^{\frac{l_{\max}}{2}} \frac{\Phi_0}{[(x-x')^2 + (y-y')^2 + z^2]^{3/2}} dy'. \quad (\text{A-5})$$

Letting  $W' = x' - x$  and  $U' = y' - y$ , and using the integral formula

$$\int \frac{dU}{\left[ U^2 \pm \left( \frac{l_{\max}}{2} \right)^2 \right]^{3/2}} = \frac{U}{\pm \left( \frac{l_{\max}}{2} \right)^2 \sqrt{U^2 \pm \left( \frac{l_{\max}}{2} \right)^2}} + C, \quad (\text{A-6})$$

(2-64) becomes

$$\Phi_s(\vec{r}) = \frac{z\Phi_0}{2\pi} \int_{-\frac{l_{\max}}{2}-x}^{\frac{l_{\max}}{2}-x} \left[ \frac{l_{\max}/2 - y}{(W'^2 + z^2)[(l_{\max}/2 - y)^2 + W'^2 + z^2]^{1/2}} + \frac{l_{\max}/2 + y}{(W'^2 + z^2)[(l_{\max}/2 + y)^2 + W'^2 + z^2]^{1/2}} \right] dW', \quad (\text{A-7})$$

Again letting  $b' = b \pm y$  and  $x'^2 = W'^2 + z^2$ , then we have  $dW' = (x'/W')dx'$  and  $W'^2 = (x'^2 - z^2)^{1/2}$ . Using the integral formula

$$\int \frac{dU}{U \sqrt{U^2 - (l_{\max}/2)^2} \sqrt{(l_{\max}/2)^2 - U^2}} = \frac{12}{l_{\max}} \tan^{-1} \left( \sqrt{\frac{U^2 - (l_{\max}/2)^2}{(l_{\max}/2)^2 - U^2}} \right) + C, \quad (\text{A-8})$$

we eventually obtain the potential energy in any observable point outside the spiral inductor:

$$\Phi_s(\vec{r}) = \frac{\Phi_0}{2\pi} \sum_{\pm, \mp} \left\{ \cot^{-1} \left( \frac{(l_{\max}/2 \pm x)(l_{\max}/2 \pm y)}{z[(l_{\max}/2 \pm y)^2 + (l_{\max}/2 \pm x)^2 + z^2]^{1/2}} \right) + \cot^{-1} \left( \frac{(l_{\max}/2 \pm x)(l_{\max}/2 \mp y)}{z[(l_{\max}/2 \mp y)^2 + (l_{\max}/2 \mp x)^2 + z^2]^{1/2}} \right) \right\}. \quad (\text{A-9})$$

## 1.2 Mathematical details of Green's function in Cylindrical Systems

For any point source  $(\rho', \phi', z')$  inside the cavity, the scalar Green's function satisfies the inhomogeneous equation as follows:



$$\frac{1}{\rho} \frac{\partial}{\partial \rho} \left( \rho \frac{\partial G}{\partial \rho} \right) + \frac{1}{\rho^2} \frac{\partial^2 G}{\partial \varphi^2} + \frac{\partial^2 G}{\partial z^2} = -\frac{1}{\rho'} \delta(\rho - \rho') \delta(\varphi - \varphi') \delta(z - z'), \quad (\text{A-10})$$

where the expansions of the  $\delta(\varphi - \varphi')$  and  $\delta(z - z')$  are as follows:

$$\delta(\varphi - \varphi') = \frac{1}{2\pi} \sum_{m=-\infty}^{\infty} e^{im(\varphi - \varphi')}, \quad (\text{A-11})$$

and

$$\delta(z - z') = \frac{2}{d} \sum_{n=1}^{\infty} \exp\left(\frac{n\pi}{d}(z - z')\right). \quad (\text{A-12})$$

Thus, the generalized solution of the Green's function has the form:

$$G(\rho, \rho') = \frac{1}{d\pi} \sum_{m=-\infty}^{\infty} \sum_{n=1}^{\infty} g_{mn}(\rho, \rho') e^{im(\varphi - \varphi')} \sinh\left(\frac{n\pi}{d}z\right) \sinh\left(\frac{n\pi}{d}z'\right). \quad (\text{A-13})$$

Substituting (A-11), (A-12), and (A-13) into (A-10), we obtain the inhomogeneous modified Bessel function:

$$\frac{1}{\rho} \frac{\partial}{\partial \rho} \left( \rho \frac{\partial g_{mn}}{\partial \rho} \right) - \frac{m^2}{\rho^2} g_{mn} - \frac{n^2 \pi^2}{d^2} g_{mn} = -\frac{1}{\rho'} \delta(\rho - \rho'). \quad (\text{A-14})$$

When  $\rho \neq \rho'$  the  $g_{mn}$  satisfies the homogeneous equation  $\nabla_{\rho}^2 g_{mn}(\rho - \rho') = 0$ , so that the general solution of the modified Bessel function can be expressed as:

$$g_{mn}(\rho, \rho') = \begin{cases} AI_m\left(\frac{n\pi}{d}\rho\right), & 0 < \rho < \rho' \\ BI_m\left(\frac{n\pi}{d}\rho\right) + CK_m\left(\frac{n\pi}{d}\rho\right), & \rho' < \rho < a \end{cases}. \quad (\text{A-15})$$

Using the two prescribed boundary conditions

$$g_{mn}(a, \rho') = 0, \quad (\text{A-16a})$$

and

$$g_{mn}(\rho, \rho') \Big|_{\rho=\rho'_-} = g_{mn}(\rho, \rho') \Big|_{\rho=\rho'_+}, \quad (\text{A-16b})$$

we obtain

$$\left. \begin{aligned} BI_m\left(\frac{n\pi}{d}a\right) + CK_m\left(\frac{n\pi}{d}a\right) &= 0 \\ AI_m\left(\frac{n\pi}{d}\rho'\right) &= BI_m\left(\frac{n\pi}{d}\rho'\right) + CK_m\left(\frac{n\pi}{d}\rho'\right) \end{aligned} \right\}, \quad (\text{A-17})$$

Thus,

$$g_{nm}(\rho, \rho') = \begin{cases} C \frac{I_m\left(\frac{n\pi}{d}a\right)K_m\left(\frac{n\pi}{d}\rho'\right) - I_m\left(\frac{n\pi}{d}\rho'\right)K_m\left(\frac{n\pi}{d}a\right)}{I_m\left(\frac{n\pi}{d}a\right)I_m\left(\frac{n\pi}{d}\rho'\right)} I_m\left(\frac{n\pi}{d}\rho\right), & 0 < \rho < \rho' \\ C \frac{I_m\left(\frac{n\pi}{d}a\right)K_m\left(\frac{n\pi}{d}\rho\right) - I_m\left(\frac{n\pi}{d}\rho\right)K_m\left(\frac{n\pi}{d}a\right)}{I_m\left(\frac{n\pi}{d}a\right)}, & \rho' < \rho < a \end{cases}, \quad (\text{A-18})$$

In order to determine the rest coefficient, both sides of (A-14) were multiplied by  $\rho'$  then integrated within  $(\rho' - \varepsilon, \rho' + \varepsilon)$ , where  $\varepsilon$  is an arbitrary number:

$$\begin{aligned} \lim_{\varepsilon \rightarrow 0} \int_{\rho' - \varepsilon}^{\rho' + \varepsilon} \frac{\rho'}{\rho} \frac{\partial}{\partial \rho} \left( \rho \frac{\partial g_{nm}}{\partial \rho} \right) - \rho' \frac{m^2}{\rho^2} g_{nm} - \rho' \frac{n^2 \pi^2}{d^2} g_{nm} d\rho' \\ = \lim_{\varepsilon \rightarrow 0} \int_{\rho' - \varepsilon}^{\rho' + \varepsilon} -\delta(\rho - \rho') d\rho' \end{aligned}, \quad (\text{A-19})$$

thus we obtain

$$\left[ \rho \left( \frac{\partial g_{nm}}{\partial \rho} \Big|_+ - \frac{\partial g_{nm}}{\partial \rho} \Big|_- \right) \right]_{\rho=\rho'} = -1. \quad (\text{A-20})$$

Substituting (A-18) into (A-20)

$$I_m\left(\frac{n\pi}{d}\rho'\right)K_m\left(\frac{n\pi}{d}\rho'\right) - I_m\left(\frac{n\pi}{d}\rho'\right)K_m\left(\frac{n\pi}{d}\rho'\right) = \frac{I_m\left(\frac{n\pi}{d}\rho'\right)}{C} \frac{d}{n\pi\rho'}, \quad (\text{A-21})$$

and comparing with the Wronskian formula

$$K_n(x)I_n'(x) - I_n(x)K_n'(x) = \frac{1}{x}, \quad (\text{A-22})$$

the rest coefficient eventually can be defined as:

$$C = I_m\left(\frac{n\pi}{d}\rho'\right). \quad (\text{A-23})$$

Now, by setting a combinational function

$$W(\alpha, \beta) = I_m\left(\frac{n\pi}{d}\alpha\right)K_m\left(\frac{n\pi}{d}\beta\right) - I_m\left(\frac{n\pi}{d}\beta\right)K_m\left(\frac{n\pi}{d}\alpha\right), \quad (\text{A-24})$$

the general solution of the Green's function in (2-72) can be finally determined:

$$G(\rho, \rho') = \frac{1}{d\pi} \sum_{m=-\infty}^{\infty} \sum_{n=1}^{\infty} e^{im(\varphi-\varphi')} \exp\left(\frac{n\pi}{d}(z-z')\right) \left[ \frac{I_m\left(\frac{n\pi}{d}\rho\right)W_{mm}(a, \rho')}{I_m\left(\frac{n\pi}{d}a\right)}, \rho' < \rho < a \right. \\ \left. \times \frac{W_{mm}(a, \rho)I_m\left(\frac{n\pi}{d}\rho'\right)}{I_m\left(\frac{n\pi}{d}a\right)}, 0 < \rho < \rho' \right]. \quad (\text{A-25})$$

Assuming the original point of the cylindrical coordinate is set at the central point of the freely suspended spiral inductor and considering the simplest case that the charge density is accumulated at the outermost edge of the circular-like inductor and the inductor is axial symmetry ( $m=0$ ), thus the distribution of the charge density,  $\sigma(\rho')$ , could be expressed using the two-dimensional  $\delta$ -function:

$$\sigma(\rho') = \frac{1}{2\pi b} \delta(\rho' - b) \delta(z' - d). \quad (\text{A-26})$$

Thus, the special solution of the potential energy is

$$\begin{aligned} \Phi_V(\rho) &= \frac{1}{\epsilon_0} \int_V G(\rho, \rho') \sigma(\rho') dV' \\ &= \frac{q}{\epsilon_0 b \pi} \sum_{m=-\infty}^{\infty} \sum_{n=1}^{\infty} \exp\left(\frac{n\pi}{d}(z-d)\right) \times \begin{cases} \frac{I_m\left(\frac{n\pi}{d}\rho\right) W_{nm}(a, b)}{I_m\left(\frac{n\pi}{d}a\right)}, \rho' < \rho < a \\ \frac{W_{nm}(a, \rho) I_m\left(\frac{n\pi}{d}b\right)}{I_m\left(\frac{n\pi}{d}a\right)}, 0 < \rho < \rho' \end{cases} \end{aligned} \quad (\text{A-27})$$



## Appendix B Successive over-relaxation (SOR) with red-black ordering

The algorithm provided below only indicates the method for deriving the thermal resistances and the required mathematical skill, Successive over-relaxation (SOR) with red-black ordering.

```
%Define input power
V_INPUT= 2; % unit : V
I_INPUT= 8e-3; % unit : A

%Define materials
AIR=0;
SILICON=1;
BCB=2;
GOLD=3;
GAAS=4;

th_r=[ 1e10, 1e-3, 1.20, 1.47, 19.48/4]; % k=thermal conductivity unit W/um-K
k=[ 2.57e-7, 1.48e-4, 2.9e-7, 3.18e-4, 0.44e-4]; % k=thermal conductivity unit W/um-K
% Make AIR k close to zero

%Define steps
STEP=100;
ITERATIONS=1000;

%Define dimensions
%SiOB
SIOB_X=4700;
SIOB_Y=2350;
SIOB_Z=625;
%Dielectric Unit
DIELECTRIC_UNIT=133;
DIELECTRIC_Z=3;
%Ground
GROUND_Z=10;
%VCSEL
VCSEL_X_TO_BORDER=DIELECTRIC_UNIT*6;
VCSEL_X=350;
VCSEL_Y=250;
VCSEL_Z=150;
VCSEL_X_LENGTH=floor( ( VCSEL_X_TO_BORDER + VCSEL_X )/STEP) - floor(VCSEL_X_TO_BORDER/STEP)+1;
VCSEL_Y_LENGTH=floor( (SIOB_Y /2. + VCSEL_Y *2 )/STEP) - floor( (SIOB_Y /2. - VCSEL_Y *2 )/STEP) +1;
VCSEL_switch=[ 1, 0, 0, 0 ]; % VCSEL switch -- control on/off of a VCSEL
%For heating source (GaAs)
% {
2mA---->2.66mW
4mA----->7.41
6mA----->12.18
8mA----->17.94
10mA----->24.304
12mA----->30.056
% }
%Int Range
RANGE=5;

R_VCSEL = 10 ; % S = 0.1 S/m
EFFICIENCY_VCSEL = 0.857 ; % the electric-thermal energy transfer efficiency = 85.7%

QV = I_INPUT * I_INPUT / 1000 / 1000 * R_VCSEL * EFFICIENCY_VCSEL

%THERMAL_VIA
THERMAL_VIA_X=90;
THERMAL_VIA_Y=90;
THERMAL_VIA_Z=12;

%Contact Pad
CONTACT_PAD_X=178;
CONTACT_PAD_Y=178;
CONTACT_PAD_Z=10;

x=0:STEP:SIOB_X;
```



```

y=0:STEP:SIOB_Y;
z=0:STEP:(SIOB_Z+VCSEL_Z);
material=zeros(length(x),length(y),length(z)); % material types
%k=zeros(length(x),length(y),length(z)); % k=thermal conductivity
Temp=ones(length(x),length(y),length(z)); % k=thermal conductivity
Temp_pre=ones(length(x),length(y),length(z)); % k=thermal conductivity
%th_resistor=zeros(length(x),length(y),length(z)); % thermal resistor
th_resistor=ones(length(x),length(y),length(z)); % thermal resistor
%heat_source_factor=zeros(length(x),length(y),length(z)); % heat source factor
%TODO : precise heat source factor
Temp=Temp*25;

simple_heat_source_factor=[1 1 1];
for index_vcsel=1:1:4
    for f_index=index_vcsel+1:1:4
        if(VCSEL_switch(f_index)==1)
simple_heat_source_factor(index_vcsel)=simple_heat_source_factor(index_vcsel)+10/(abs(f_index-index_vcsel))^2;
            end;
        end
        for f_index=index_vcsel-1:-1:1
            if(VCSEL_switch(f_index)==1)
simple_heat_source_factor(index_vcsel)=simple_heat_source_factor(index_vcsel)+10/(abs(f_index-index_vcsel))^2;
            end;
        end
    end
end

%Calculate R
disp('Calculate R');

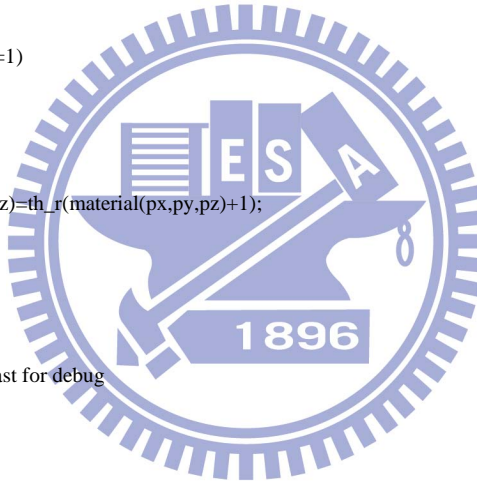
if(USE_KNOWN_TH_RESISTOR==1)

%fix R value
for pz= 1:1:length(z)
    for py= 1:1:length(y)
        for px= 1:1:length(x)
            th_resistor(px,py,pz)=th_r(material(px,py,pz)+1);
        end
    end
end
material(:, :,length(z)-1);
th_resistor(:, :,length(z)-1);
else
%for pz= length(z)-2:1:length(z) % fast for debug
for pz= 1:1:length(z)
    pz=length(z)
    pz
    for py= 1:1:length(y)
        for px= 1:1:length(x)

            if(material(px,py,pz)==GAAS)
                for pzp= max ( z-RANGE , 1 ) :1: min ( z+RANGE , length(z) )
                    for pyp= max ( y-RANGE , 1 ) :1: min ( y+RANGE , length(y) )
                        for pxp= max ( x-RANGE , 1 ) :1: min ( x+RANGE , length(x) )

                            if( ~(pxp==px & pyp==py & pzp==pz) )
                                r= 3 / ( 4 * pi * k(material(px,py,pz)+1) ) * STEP / (sqrt( (pxp-px)^2 +
                                (pyp-py)^2 + (pzp-pz)^2 )) - 1 / ( 4 * pi * k(material(px,py,pz)) ) * STEP / (sqrt( (pxp-px)^2 + (pyp-py)^2 +
                                (pzp-pz)^2 )) );
                                th_resistor(px,py,pz) = th_resistor(px,py,pz) + r/(STEP * RANGE*2)^3 * ( STEP *
                                10^-6)^3;
                            end;
                        end
                    end
                end
            else
                th_resistor(px,py,pz)=0;
                for pzp= max ( z-RANGE , 1 ) :1: min ( z+RANGE , length(z) )
                    for pyp= max ( y-RANGE , 1 ) :1: min ( y+RANGE , length(y) )
                        for pxp= max ( x-RANGE , 1 ) :1: min ( x+RANGE , length(x) )
                            if( ~(pxp==px & pyp==py & pzp==pz) )
                                r2= 1 / ( 4 * pi * k(material(px,py,pz)+1) ) / (sqrt( (pxp-px)^2 + (pyp-py)^2
                                + (pzp-pz)^2 )) );
                                th_resistor(px,py,pz) = th_resistor(px,py,pz) + r2 ;%/(STEP * RANGE*2)^3 * ( STEP )^3;
                            end;
                        end
                    end
                end
            end
        end
    end
end

```



```

end;
end
end
end;
end
end
end

```

```

end;
%th_resistor(:,length(z)-1)
%th_resistor
%disp('>>>print th_resistor');
%th_resistor
disp('>>>print material');
material
disp('>>>print th_resistor');
th_resistor
th_resistor=abs(th_resistor);

```

%Remove constant temp plate

```

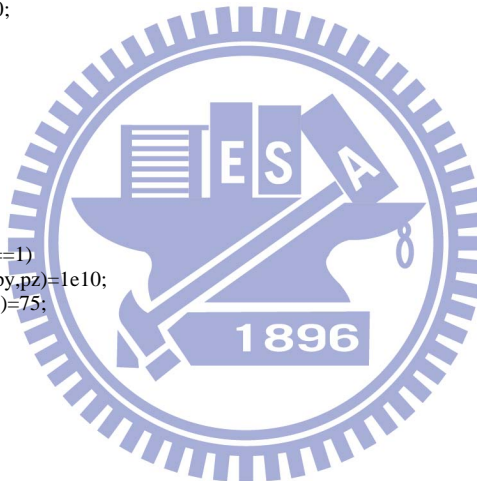
for pz= 2:1:length(z)-1
for py= mod(pz,2)+2:1:length(y)-1
for px= mod(pz,2)+2:1:length(x)-1
Temp_pre(px,py,pz)=0;
end
end
end

```

```

for py= 1:1:length(y)
for px= 1:1:length(x)
for pz= 1:1:length(z)
if(Temp_pre(px,py,pz)==1)
th_resistor(px,py,pz)=1e10;
Temp(px,py,pz)=75;
end;
end
end
end

```



%Set bottom temp

```

for pz= 1:1:3
for py= 1:1:length(y)
for px= 1:1:length(x)
Temp(px,py,pz)=75;
end
end
end

```

%Calculate Temp

%Successive overrelaxation (SOR) with red-black ordering

%Ref <http://beowulf.lcs.mit.edu/18.337-2004/hw1/>

%The method of solution that we will use here is successive overrelaxation (SOR) with red-black ordering.

%Calculate Power and transient time

```

%do iterations
for iter= 1:1:ITERATIONS
Power_in=0;
%delta Temp at 4 VCSELS
% delta Temp = Power * thermal resistor
% Temp at 4 VCSELS equals to max ( near by Temp + thermal resistor * Power ) <= MAKE SURE TEMP IS ASCENDING

```

```

%Power = V_INPUT * I_INPUT (W)
%POWER_INPUT = V_INPUT * I_INPUT;

```

```

%input power R= 2um/(0.1*65um*65um) 2um/ S * A
RP_INPUT=2/(0.1*65*65);

```



```

POWER_INPUT = I_INPUT^2 * RP_INPUT;
CONTACT_AERA = STEP * STEP;

T_DELTA=POWER_INPUT*CONTACT_AERA*EFFICIENCY_VCSEL*4000;

    px= floor( ( VCSEL_X_TO_BORDER + VCSEL_X/2. ) /STEP);
    pz= floor( ( SIOB_Z + VCSEL_Z ) /STEP);
%for py= floor( (SIOB_Y /2. - VCSEL_Y *2 + VCSEL_Y /2. )/STEP) :floor(VCSEL_Y/STEP):floor( (SIOB_Y /2. + VCSEL_Y
*2 )/STEP)
for index_vcsel=1:1:4
if(VCSEL_switch(index_vcsel)==0)
continue;
end;
%py= floor( (SIOB_Y /2. - VCSEL_Y *2 + VCSEL_Y /2. + ( index_vcsel -1 ) * VCSEL_Y )/STEP) ;
py= floor( (SIOB_Y /2. - VCSEL_Y *2 + VCSEL_Y /2.)/STEP) + ( index_vcsel -1 ) *floor( VCSEL_Y /STEP);
%    Y_M1=th_resistor(px,py-1,pz);
%    Y_P1=th_resistor(px,py+1,pz);
%    Y_MAX=max (Temp_pre(px,py-1,pz)+th_resistor(px,py-1,pz)*POWER_INPUT ,
Temp_pre(px,py+1,pz)+th_resistor(px,py+1,pz)*POWER_INPUT );
%    X_MAX=max( Temp_pre(px-1,py,pz) + th_resistor(px-1,py,pz)*POWER_INPUT, Temp_pre(px+1,py,pz)
+th_resistor(px+1,py,pz)*POWER_INPUT );
%    Z_MAX= Temp_pre(px,py,pz-1)+th_resistor(px,py,pz-1)*POWER_INPUT ;
%    XY_MAX=max(X_MAX,Y_MAX);
%    Temp(px,py,pz)=max( XY_MAX , Z_MAX );

%    Temp( floor(( VCSEL_X/2. - 65/2 )/STEP),py,pz) = Temp_pre( floor(( VCSEL_X/2. - 65/2 )/STEP)-1,py,pz) + T_DELTA *
th_resistor( floor(( VCSEL_X/2. - 65/2 )/STEP)-1,py,pz);
%    Temp( floor(( VCSEL_X/2. + 65/2 )/STEP),py,pz) = Temp_pre( floor(( VCSEL_X/2. + 65/2 )/STEP)+1,py,pz) + T_DELTA
* th_resistor( floor(( VCSEL_X/2. + 65/2 )/STEP)+1,py,pz);
%
Temp( px-1,py,pz) = Temp_pre( px-2,py,pz) + T_DELTA * th_resistor( px-2,py,pz) *
simple_heat_source_factor(index_vcsel) ;
Power_in= Power_in + T_DELTA * simple_heat_source_factor(index_vcsel) ; % T/R
Temp( px+1,py,pz) = Temp_pre( px+2,py,pz) + T_DELTA * th_resistor( px+2,py,pz) *
simple_heat_source_factor(index_vcsel) ;
Power_in= Power_in + T_DELTA * simple_heat_source_factor(index_vcsel) ;
Temp( px,py-1,pz) = Temp_pre( px,py-2,pz) + T_DELTA * th_resistor( px,py-2,pz) *
simple_heat_source_factor(index_vcsel) ;
Power_in= Power_in + T_DELTA * simple_heat_source_factor(index_vcsel) ;

Temp( px,py+1,pz) = Temp_pre( px,py+2,pz) + T_DELTA * th_resistor( px,py+2,pz) *
simple_heat_source_factor(index_vcsel) ;
Power_in= Power_in + T_DELTA * simple_heat_source_factor(index_vcsel) ;
Temp( px,py,pz) = Temp_pre( px,py,pz-1) + T_DELTA * th_resistor( px,py,pz-1) * simple_heat_source_factor(index_vcsel) ;
Power_in= Power_in + T_DELTA * simple_heat_source_factor(index_vcsel) ;
%Power calculation section
%Temp( px,py,pz+1) = Temp_pre( px,py,pz+2) + T_DELTA * th_resistor( px,py,pz+2);

end

Power_in
%Set bottom temp

for pz= 1:1:3
for py= 1:1:length(y)
for px= 1:1:length(x)
Temp(px,py,pz)=75;
end
end
end
end

Temp_pre=Temp;

%Calculate Red points

%Formula ( A/Ra + B/Rb + C/Rc + D/Rd ) / ( 1/Ra + 1/Rb + 1/Rc + 1/Rd )
for pz= 2:1:length(z)-1
for py= mod(pz,2)+2:1:length(y)-1
for px= mod(pz,2)+2:1:length(x)-1
if(mod(px+py,2)==0)
Temp(px,py,pz)= ( Temp_pre(px-1,py,pz)/th_resistor(px-1,py,pz) + Temp_pre(px+1,py,pz)/th_resistor(px+1,py,pz) +

```

```

Temp_pre(px,py-1,pz)/th_resistor(px,py-1,pz) + Temp_pre(px,py+1,pz)/th_resistor(px,py+1,pz) +
Temp_pre(px,py,pz-1)/th_resistor(px,py,pz-1) + Temp_pre(px,py,pz+1)/th_resistor(px,py,pz+1) ) / ( 1/th_resistor(px-1,py,pz) +
1/th_resistor(px+1,py,pz) + 1/th_resistor(px,py-1,pz) + 1/th_resistor(px,py+1,pz) + 1/th_resistor(px,py,pz-1) + 1/th_resistor(px,py,pz+1) );
    if(Temp(px,py,pz)<0)
        Temp(px,py,pz)=0;
    end
end
end;
end
end
end
end

```

```
Temp_pre=Temp;
```

```
%Calculate Black points
```

```
%Formula ( A/Ra + B/Rb + C/Rc + D/Rd ) / ( 1/Ra + 1/Rb + 1/Rc + 1/Rd )
```

```

for pz= 2:1:length(z)-1
    for py= 2:1:length(y)-1
        for px= 2:1:length(x)-1
            if(mod(px+py,2)==1)
                Temp(px,py,pz)= ( Temp_pre(px-1,py,pz)/th_resistor(px-1,py,pz) + Temp_pre(px+1,py,pz)/th_resistor(px+1,py,pz) +
Temp_pre(px,py-1,pz)/th_resistor(px,py-1,pz) + Temp_pre(px,py+1,pz)/th_resistor(px,py+1,pz) +
Temp_pre(px,py,pz-1)/th_resistor(px,py,pz-1) + Temp_pre(px,py,pz+1)/th_resistor(px,py,pz+1) ) / ( 1/th_resistor(px-1,py,pz) +
1/th_resistor(px+1,py,pz) + 1/th_resistor(px,py-1,pz) + 1/th_resistor(px,py+1,pz) + 1/th_resistor(px,py,pz-1) + 1/th_resistor(px,py,pz+1) );
                if(Temp(px,py,pz)<0)
                    Temp(px,py,pz)=0;
                end
            end
        end
    end;
end
end
end
end
end

```



# Curriculum Vitae

陳健章 (Chien-Chang Chen)

*Ph. D. Candidate*

*Department of Electronics Engineering & Institute of Electronics*

*National Chiao Tung University*

*HsinChu, Taiwan, R.O.C.*

E-mail: [gettgod.ee92g@nctu.edu.tw](mailto:gettgod.ee92g@nctu.edu.tw)

**Chien-Chang Chen** was born in Hualien, Taiwan. He received the B.S. degree in physics from the National Central University, Jhongli, Taiwan, in 2003, and graduated with highest honor. In 2006, he received the M.S. degree in electrical engineering from the National Chiao Tung University, Hsinchu, Taiwan. His master thesis was entitled “A Closed-Form Integral Model of Spiral Inductor Using the Kramers-Kronig Relations.” Fortunately, he will soon earn his Ph.D. degree in the Department of Electronics Engineering & Institute of Electronics, National Chiao Tung University, where he is working on creating physical behavior models for solid-state N/MEMS devices, electromagnetic-thermal-field theory, and generalized Green’s theorem-based theory. His Ph.D. dissertation focuses on the physical analyses of N/MEMS (Nano- and Micro-Electro-Mechanical Systems) component structures for optimal microsystem design. Currently, his group-mate and he are successfully establishing a Green’s theorem-based algorithm for thermal analysis of a 3D optical stacking structure, the VCSELs on a SiOB. In the future, the developed algorithm will be introduced into the 3D-nanoelectronic circuitry system and 3D-N/MEMS devices for further thermal management and structural optimization. Meanwhile, he is the winner of the *Excellent Achievement of 2010 Ph.D. Dissertation* in Institute of Electronics, National Chiao Tung University.

## **Biography**

09/2008~at present, Ph.D. Student, Department of Electronics Engineering & Institute of Electronics, National Chiao Tung University, Hsinchu City, Taiwan.

M.S., Department of Electronics Engineering & Institute of Electronics, National Chiao Tung University, Hsin Chu City, Taiwan, 2006.

B.S., Department of Physics, National Central University, Jhongli City, Taiwan, 2003.

## Research Interests

- Condensed Matter Field Theory
- Physical Behavior Models in Micro- and Nano-systems
- MEMS Modeling, Design, Simulation, and Optimization
- Computational Electromagnetic and Thermal Fields
- Electromagnetic-Thermal-Chip for Tissue Engineering

## Publications

### Journals:

1. C. C. Chen and Y. T. Cheng, "Physical Analysis of a Biomimetic Microphone with a Central-Supported (C-S) Circular Diaphragm for Sound Source Localization," submitted to *IEEE JMEMS*.
2. Y. C. Chen, C. C. Chen, W. Tu, Y. T. Cheng, and F. G. Tseng, "Design and fabrication of a microplatform for the proximity effect study of localized ELF-EMF on the growth of in-vitro HeLa and PC-12 Cells," *J. Micromech. Microeng.*, Vol. 20, 125023, 2010.
3. C. C. Chen, Y. C. Chen, Chin-Ta Chen, Hsu-Liang Hsiao, Chia-Chi Chang, Y. T. Cheng, and Mount-Learn Wu, "Thermal Analysis: VCSELs on a SiOB," *IEEE Journal of Selected Topics in Quantum Electronics*, in proofreading.
4. C. C. Chen, Lun-Hao Hsu, Kai Rern, Y. T. Cheng, Yi-Fan Hsieh, and Pu-Wei Wu, "Gravity-Assisted Seeding Control for One-Dimensional Material Growth," *IEEE Transactions on Nanotechnology*, Vol. 8, pp.427-430, 2009.
5. Jingkuang Chen, Xiaoyang Cheng, C. C. Chen, P.-C. Li, J.-H. Liu, and Y. T. Cheng, "A Capacitive Micromachined Ultrasonic Transducer Array for Minimally Invasive Medical Diagnosis," *IEEE Journal of Microelectromechanical Systems*, Vol. 17, pp.599-610, 2008.
6. C. C. Chen, Ssu-Ying Chen, and Y. T. Cheng, "A Patterned Dielectric Support Process for High Performance Passive Fabrication", *IEEE Microwave Component Letter*, Vol. 18, pp.82-84, 2008.

7. Yu Wen Huang, Tzu-Yuan Chao, C. C. Chen, and Y. T. Cheng, "Power consumption reduction scheme of magnetic microactuation using electroplated Cu–Ni nanocomposite", *Appl. Phys. Lett.*, Vol. 90, pp. 244105-244107, 2007.
8. C. C. Chen, Cheng-De Lin, and Y. T. Cheng, "Model to Determine the Self-Resonant Frequency of Micromachined Spiral Inductors", *Appl. Phys. Lett.*, Vol. 89, pp. 103521-103523, 2006.
9. C. C. Chen, J. K. Huang, and Y. T. Cheng, "A Closed-Form Integral Model of the Spiral Inductor Using Kramers-Kronig Relations", *IEEE Microwave Component Letter*, Vol. 15, pp.778-780, 2005.
10. J. W. Lin, C. C. Chen, and Y.-T. Cheng "A Robust High Q Micromachined RF Inductor for RFIC Applications", *IEEE Trans. on Elec. Dev.*, Vol. 52, pp. 1489-1496, 2005.

Conference Proceedings:

1. C. C. Chen, Yu-Sian Liu, Y. C. Chen, and Y. T. Cheng, "A New Technique of Thermal Analysis for 3-D MEMS Applications," submitted to *TRANSDUCER 2011*.
2. Yu-Sian Liu, C. C. Chen, Y. T. Cheng, and Kuei-Ann Wen, "Successive Overrelaxation Method for 3D-Stacking Structures Thermal Analysis," submitted to *DAC2011*.
3. C. C. Chen, Y. C. Chen, Keng-Yu Lin, and Y. T. Cheng, "Hybrid Biomimetic Directional Microphone for the Full Space Sound Source Localization," *Solid-State Sensors, Actuators, and Microsystems Workshop*, Hilton Head Island, South Carolina, June 6-10, 2010, pp. 96-97.
4. C. C. Chen, C. Singh, Y. C. Chen, Hsu-Liang Hsiao, Chia-Yu Lee, Mount-Learn Wu, and Y. T. Cheng, "Equivalent Electrothermal Circuit Model for Vertical-Cavity Surface-Emitting Lasers on Silicon Optical Bench," *15<sup>th</sup> International Workshop on Thermal investigations of ICs and Systems (THERMINIC)*, Leuven, Belgium, 7-9 October, 2009, pp. 8-12.

5. C. C. Chen, Y. C. Chen, Keng-Yu Lin, and Y. T. Cheng, "A Novel Design and Analytical Model for Biomimetic Microphone with Floating Center-Supported Gimbal Circular Diaphragm," *13<sup>th</sup> NMC*, Hsinchu, Taiwan, 9-10 July, 2009.
6. C. C. Chen, Y. C. Chen, Hsu-Liang Hsiao, Chia-Yu Lee, Mount-Learn Wu, and Y. T. Cheng, "Equivalent Electrothermal Circuit Model and Thermal Analysis for Vertical-Cavity Surface-Emitting Lasers on Silicon Optical Bench," *13<sup>th</sup> NMC*, Taiwan, 9-10 July, 2009.
7. C. C. Chen, Lun-Hao Hsu, and Y. T. Cheng, "Formation, Rolling, and Agglomeration of a Co Seed Droplet in Patterned Inverted Silicon Nano-Pyramid," *IEEE 9<sup>th</sup> International Conference on Nanotechnology digset*, Genoa, Italy, 26-30 July, 2009.
8. Y. C. Chen, C. C. Chen, W. T. Tu, Y. T. Cheng, and F. G. Tseng, "The Investigation of the Proximate Effect of Time-Variant Magnetic Field on the Growth of In-Vitro Hela and PC-12 Cells Using On-Glass Spiral Inductor," *5<sup>th</sup> International Conference on Microtechnology in Medicine and Biology*, Canada, April 2009.
9. Y. C. Chen, C. C. Chen, Wen Hao Ching and Y. T. Cheng, "Design and Fabrication of High Performance Biomimetic Microphone Using Oxalis-Like Sensing Diaphragm for Sound Localization", *APCOT*, Taiwan, 2008.
10. X. Cheng, J. Chen, T. Zhang, C. C. Chen, Y. T. Cheng, and M. Wang, "An Implantable Ultrasonic Doppler Blood Flowmeter," *IEEE Ultrasonics Symposium*, Oct. 2-6, 2006, pp.808-811.
11. Jr-Wei Lin, C. C. Chen, J. K. Huang, and Y. T. Cheng, "An Optimum Design of The Micromachined RF Inductor", *IEEE Radio Frequency Integrated Circuits (RFIC) Symposium*, June 6-8, 2004, pp. 639-642.

## **Patents**

1. C. C. Chen and Y. T. Cheng, "Method for predicting inductance and self-resonant frequency of a spiral inductor", U.S. 7,451,415 B2.
2. C. C. Chen and Y. T. Cheng, "一種預測雙埠晶片懸浮螺旋式電感之感值與共振頻率的方法," Taiwan, R.O.C. No.200734927.



## Experience

- 06/2007 ~ At present

### 經濟部學界科專計畫：平行化高速光連接技術開發四年計畫

在高速光通訊傳送過程中，電訊號傳送至光通訊端，由發光模組做電-光轉換後，經由光纖傳送到接收端，再由檢光模組做光電轉換，將光訊號還原為電訊號。因此發光模組在高速光通訊系統中扮演極為重要的角色。本計畫中，中央大學光電所伍茂仁教授以矽光學平台為基礎研發出了一套光學連結模組，其中使用了垂直共振腔面射雷射 (Vertical Cavity Surface Emitting Laser, VCSEL) 做為模組的發光源，其優點將表現在與光纖的耦合上。為了充分發揮此光學連結模組的通訊能力，並在綦振瀛院長以及指導教授鄭裕庭老師之期望下，本人利用 Green's theorem 的數學架構與物理原則，成功首次推演出熱傳導、對流與熱阻的廣義積分式。藉由此積分式，吾人便可輕易計算出光學連結模組中 VCSELs 的熱耗散與溫度響應分布方程式。同時，本方法亦首次從理論上驗證了 Fourier 熱傳導定律。此外，本人亦和指導之大學部專題生合作，成功研發出一套 Green's theorem-based 演算法。此演算法不僅在結構分析與計算步驟上優於目前常用的有限元素分析法 (Finite Element Method)，同時亦將計算時間大幅縮減 400 倍之多。此法將以外掛方式與 C 語言以及 Verilog-A 語言為基礎的商業模擬軟體耦合，使其能在處理光學行為模擬時，亦同時將熱耗散影響以及在高速資料傳輸時的熱串音效應考慮至系統模組中。最終，此演算法將運用於 3D 奈微米電子元件與微機電結構中，以實現並提出系統結構熱分布分析及結構、材料最佳化處理方針。此發展之演算法相關研究已發表在 THERMINIC 2009 國際研討會 (ORAL)、IEEE JSTQE 國際期刊、投稿至 DAC 2011 國際研討會、TRANSDUCER 2011 國際研討會，以及申請專利中。

- 08/2007~07/2008

### 國科會專題研究計畫：助聽器晶片及設計--微機電式聲學元件暨助聽器異質整合

麥克風在助聽器與人工電子耳以及微型機械人中扮演著接收訊息與方位判斷的角色，若有較強的訊號雜訊比 (SNR) 以及音源定位能力，將有助於提升各項運用元件的品質。本計畫中，將利用仿生式的音源定位機制過濾出訊息的來源方向，並企望經由電路運算降低四周的雜音，進而提聲音源訊號之 SNR。在仿生式的微機電結構上，本人首創結合了蒼蠅的音源定位機制以及酢醬草的葉膜與莖的彈性耦合概念，因而設計出了中央懸浮樞紐結點耦合薄膜機械結構。在與實驗室兩位博、碩班學弟分工合作以及國



家晶片系統設計中心的協助下，此種創新結構之頻率響應、動態行為分析與靜態結構分析已充分獲得。且相較於傳統音源定位麥克風，此設計大幅提升元件自身之頻率響應範圍、靈敏度、方向性等指標性需求。此結構之相關物理與動力學分析之相關研究已發表在 Hilton Head 2010 國際研討會 (ORAL)，並投稿至 IEEE JMEMS 國際期刊。

## **Honors**

National Novel Creation Awards in R.O.C., in 1995 & 1998.

Academic Achievement Award in NCU (graduation with highest honor, 2003)

Excellent Achievement of 2010 Ph.D. Dissertation in Institute of Electronics, National Chiao Tung University.

## **References**

Professor Tai-Sone Yih, Department of Physics, National Central University, No.300, Jhongda Rd., Jhongli City, Taoyuan County, Taiwan (R.O.C.) 320. E-mail: [tsyih@phy.ncu.edu.tw](mailto:tsyih@phy.ncu.edu.tw).

Professor Yu-Ting Cheng, IEEE Senior Member, Department of Electronics Engineering and Institute of Electronics, National Chiao Tung University, No.1001 Ta Hsueh Road, Hsinchu City, Taiwan (R.O.C.) 300. E-mail: [ytcheng@faculty.nctu.edu.tw](mailto:ytcheng@faculty.nctu.edu.tw).

Associate Professor Jingkuang Chen, Department of Electrical and Computer Engineering, The University of New Mexico, Albuquerque, NM 87131 USA. E-mail: [jingkuang@yahoo.com](mailto:jingkuang@yahoo.com).